Karlsruhe Institute of Technology

Investigations of background due to secondary electron emission in the KATRIN-experiment

Zur Erlangung des akademischen Grades eines

Doktors der Naturwissenschaften

von der Fakultät für Physik
des Karlsruher Instituts für Technologie
genehmigte Dissertation

von

Dipl.-Phys. Benjamin Leiber

aus Tuttlingen

Erstgutachter:	Prof. Dr. G. Drexlin Institut für Experimentelle Kernphysik, KIT
Zweitgutachter:	Prof. Dr. H. Blümer Institut für Experimentelle Kernphysik, KIT

Tag der mündlichen Prüfung: 17. 07. 2014

Erklärung

Hiermit bestätige ich, dass ich die vorliegende Arbeit selbst verfasst und keine anderen als die angegebenen Quellen und Hilfsmittel verwendet und diese im Text kenntlich gemacht habe.

Benjamin Leiber, Juni 2014

Abstract

The determination of the absolute scale of the neutrino mass in a laboratory experiment is of major importance for cosmological models and our fundamental understanding of particles.
The **KA**rlsruhe **TRI**tium **N**eutrino experiment (KATRIN) is a next-generation direct neutrino mass experiment that is targeted to determine the effective mass of the electron anti-neutrino with a sensitivity of 200 meV (90% C.L.). To do so, KATRIN will scan the tritium-β-spectrum close to the endpoint energy of 18.6 keV with unprecedented precision. The energy analysis is based on a tandem setup of spectrometers based on the principle of magnetic adiabatic collimation with an electrostatic filter (MAC-E filter). As only a small fraction of 10^{-13} of all β-decay electrons fall in the region-of-interest close to the β-decay endpoint, a very low background rate of 0.01 counts per second is necessary during the long-term measurement to achieve the design sensitivity.
The focus of this work lies on the detailed investigation of one of two main background sources of the experiment: the emission of secondary electrons from the large 690 m^2 inner surface of the stainless steel vessel. As measurements at predecessor experiments have shown, this emission process is caused by cosmic ray muons and environmental radiation accounts for a major part of the expected background rate in spectrometers of the MAC-E filter type. The mechanisms that allow secondary electrons emitted from the wall to cause background in the inner sensitive parts is investigated in detail.
An essential cornerstone of background investigation and studies to optimize the electromagnetic properties of the spectrometers is formed by the Kassiopeia software package, to which this thesis has contributed significantly. A special focus is put on advanced field calculation methods, including discrete computation methods that allow for true-to-reality modeling of geometries, as well as axisymmetric methods which allow for fast computation speed. The mathematical methods and approximations further refined in this work form the basis for the calculation of particle trajectories in Kassiopeia. This allows to perform large-scale Monte-Carlo (MC) simulations where the creation and transport mechanisms of background electrons due to secondary emission in the KATRIN spectrometers are modeled in detail.
In order to independently study the production and transport mechanisms of muon-induced secondary electrons at the experiment, a set of muon detector systems has been installed and commissioned at the monitor and main spectrometer. The detailed depiction of these systems focuses on key parameters like timing accuracy of the data acquisition (DAQ) and long-term stability of the measured muon rate.
In the course of the measurements of the first commissioning phase of the spectrometer and detector section, first information has been obtained on the correlation of secondary electron emission with the rate of incident comic muons. Measurements

with different electrostatic offsets at the wire electrodes of the main and monitor spectrometer were then used to deduce the energy distribution of secondary electrons. In addition, other emission characteristics such as event topologies and electron multiplicity distributions help to constrain the origin of secondary emission.
As a "byproduct" of the extensive studies of cosmic ray induced background, the phenomenon of field emission was studied at the main and monitor spectrometer as well. The well-defined Fowler-Nordheim (F-N) behavior of field emission and the localized emission region of this well-understood process help to better understand complex electron transport processes by $\vec{E} \times \vec{B}$ and $\nabla\vec{B} \times \vec{B}$ drift processes into the inner parts of the flux tube. Field emission processes contribute to the overall background and thus emphasize the importance of a proper setup of electromagnetic fields in the experiment.
This work concludes with a discussion of the impact of the observed background rate due to secondary electron emission on the neutrino mass sensitivity of the KATRIN experiment. In this context, both the absolute rate (about 0.5 cps) as well as its characteristics (small non-Poissonian component) call for further detailed studies of this background class to retain the neutrino mass sensitivity of KATRIN.

Zusammenfassung

Die Bestimmung der absoluten Größenordnung der Neutrinomasse in einem Labor-Experiment ist von zentraler Bedeutung sowohl für kosmologische Modelle als auch für unser fundamentales Verständnis der Teilchenphysik.
Das **KA**rlsruhe **TRI**tium **N**eutrino Experiment (KATRIN) ist ein Zerfallsexperiment der neusten Generation, welches eine direkte Messung der effektiven Masse des Elektronantineutrinos mit einer Genauigkeit von 200 meV (90% C.L.) durchführen wird. Um dies zu erreichen, wird KATRIN den Bereich nahe der Endpunktsenergie ($E_0 = 18.6$ keV) des Tritium-β-Spektrums mit noch nie dagewesener Präzision vermessen. Die Energieanalyse im Experiment wird durch einen Aufbau mit zwei Spektrometern realisiert. Diese nutzen das Prinzip der magnetisch-adiabatischen Kollimation gepaart mit einem elektrostatischen Filter (MAC-E Filter). Lediglich ein kleiner Anteil von 10^{-13} aller Zerfallselektronen fallen in das Energiefenster nahe dem Endpunkt. Dies bedingt eine strenge Anforderung an den Untergrund, welcher während der Langzeitmessung unter 0.01 Elektronen pro Sekunde liegen muss.
Das Hauptaugenmerk dieser Arbeit liegt auf der detaillierten Untersuchung einer der beiden Hauptuntergrundquellen im Experiment: der Emission von Sekundärelektronen von der 690 m^2 großen inneren Oberfläche der Edelstahltanks. Messungen an Vorgängerexperimenten haben gezeigt, dass diese Emission, die durch kosmische Myonen und natürliche Hintergrundstrahlung verursacht wird, in MAC-E Filtern für den Großteil der zu erwartenden Untergrundrate verantwortlich ist. Die Mechanismen, die es solchen Sekundärelektronen ermöglichen das empfindliche Innere der Spektrometer zu erreichen, werden detailliert beschrieben.
Ein Eckpfeiler, welcher die genauen Untergrund- und Optimierungsstudien die elektromagnetischen Eigenschaften der Spektrometer betreffend ermöglicht, bildet das Kassiopeia software Paket, zu welchem diese Arbeit wesentlich beigetragen hat. Ein spezieller Fokus wurde hierbei auf die Methoden zur Feldberechnung gelegt, welche sowohl diskrete Methoden, die eine realitätsgetreue Modellierung ermöglichen, als auch axialsymmetrische Methoden, welche eine schnelle Berechnung mit sich bringen, umfassen. Im Rahmen dieser Arbeit wurden mathematische Methoden und Näherungen weiter verfeinert, die die Basis für die Teilchenbahnberechnung in Kassiopeia bilden. Diese Simulationswerkzeuge machen große MC Berechnungen möglich, in denen die Enstehungs- und Transportmechanismen von Untergrundelektronen aus Sekundärelektronen detailliert in den KATRIN Spektrometern modelliert werden können.
Um unabhängig davon die Entstehungs- und Transportmechanismen der myoninduzierten Sekundärelektronen im Experiment zu studieren, wurden am Haupt- und am Monitorspektrometer jeweils ein Myondetektorsystem aufgebaut und in Betrieb genommen. Die detaillierte Charakterisierung dieser Systeme konzentriert sich auf ihre wichtigsten Aspekte, wie die Genauigkeit der Zeitbestimmung in der Datener-

fassung, die Langzeitstabilität der einzelnen Module sowie die zeitliche Änderung der Myonrate.
Im Zuge der ersten Inbetriebnahme-Messungen am Hauptspektrometer wurden erste Korrelationsanalysen zwischen der Rate der Sekundärelektronen und der der kosmischen Myonen durchgeführt. Messungen mit unterschiedlichen Offset-Spannungen auf den Drahtelektroden von Haupt- und Monitorspektrometer wurden benutzt, um auf die Energieverteilung der emittierten Sekundärelektronen zurückzuschließen. Zusätzlich wurden weitere Emissionschrakteristiken, wie Detektor-Topologien und Elektronenmultiplizität untersucht, welche ergänzende Aussagen über die Natur der Sekundäremission ermöglichen.
Als Nebenprodukt der umfassenden Messungen an myoninduzierten Sekundärelektronen wurde das Phänomen der Feldemission an Haupt- und Monitorspektrometer untersucht. Die Emissionsrate in Abhängigkeit der Spannung folgt dabei der bekannten F-N-Form. Ebenso tritt die Feldemission stark lokalisiert auf und ermöglicht somit eine Betrachtung der komplexen Transportprozesse, welche dafür sorgen, dass ein Elektron durch $\vec{E} \times \vec{B}$ und $\nabla \vec{B} \times \vec{B}$ Driften in das Innere des magnetischen Flussschlauch gelangen kann.
Abschließend werden die Auswirkungen des bisher gemessenen Sekundärelektronenuntergrunds auf die Neutrinomassensensitivität des KATRIN Experiments erörtert. Dabei wird sowohl auf die absolute Rate (ca. 0.5 cps) als auch auf die Eigenarten des Untergrunds (kleine nicht-Poisson-verteilte Komponente) eingegangen. Beide diese Eigenschaften erfordern weitere, detaillierte Untersuchungen dieser Art von Untergrund, um die angepeilte Neutrinomassensensitivität von KATRIN sicherzustellen.

Contents

1. Neutrino Physics

Since their postulation in 1930 by W. Pauli, neutrinos have been the subject of great scientific interest. Due to their elusive nature, the observation and investigation of neutrinos is a challenging branch of astroparticle physics. The observation of the oscillation of atmospheric neutrinos in 1998 by the Super-Kamiokande experiment turned out to be the cornerstone for a new generation of neutrino experiments. These intend to further investigate the properties of neutrinos, and in particular to measure the masses of the neutrinos.
This chapter will give a short overview of the status and open issues in neutrino physics and thereby focus on the status of key experiments in this field. At first the compelling evidence for massive neutrinos will be discussed, as being provided by various experiments. This is followed by a brief introduction to the concept of neutrino oscillations and the determination of key oscillation parameters. The chapter will close with a description of the main aspects relevant in direct and indirect measurements of neutrino masses.

1.1. Postulation and discovery of the neutrino

Between the theoretical postulation of the neutrino by Wolfgang Pauli and its discovery in the series "Poltergeist" experiments by Clyde Cowan and Frederick Reines a time span of 26 years passed, underlining the challenges in experimental neutrino physics. In 1995 Reines received the Nobel prize in physics for his discovery.

1.1.1. Postulation of the neutrino

In 1914 James Chadwick was among the first [1] to investigate the energy spectrum of electrons stemming from nuclear β-decays. At that time the energy spectra of other types of radioactivity, α- and γ-decays, were already known to show characteristic mono-energetic lines. Thus the expectation was to also measure a mono-energetic line for the β-decay electrons. Yet, he measured a continuous β^--energy spectrum, which was in apparent contradiction to energy and angular momentum conservation if a two-body decay was assumed.
This finding was corroborated by many subsequent works and was finally explained

on December 4^{th} 1930 by W. Pauli in his famous letter [2]. He solved the mystery by postulating a neutral spin $^1/_2$ particle that is produced together with the electron in the β-decay, and which he called the *neutron*. Pauli's postulation transformed β-decays to a three-body-decay in which energy and momentum conservation was granted.
Shortly later, when Chadwick discovered the neutron in 1932 [3], it was evident that the mass of the newfound neutron was to high to be the missing particle from the β-decay. It was Enrico Fermi who introduced the name *neutrino* for the particle, when he published his theoretical description of β-decays in 1934 [4]. Fermi derived a description for the energy spectrum of the decay electrons still valid and in use today. From comparison with the available experimental data he already reasoned, that the mass of the neutrino must be much smaller than the electron mass or even be zero.

1.1.2. First discovery of the neutrino

The first experiment that obtained a signal from neutrinos was the suite of experiment often dubbed "Poltergeist" by C. Cowan and F. Reines. The first detector of the project was located at the Hanford reactor site. Unfortunately, the rather high background in this experimental arrangement prevented an unambiguous detection of a neutrino signal. Shortly thereafter they set up an improved detector at the Savannah river reactor, where they finally discovered the neutrino [5, 6] via the now classical inverse β-decay:

$$\bar{\nu_e} + p \rightarrow n + e^+ \tag{1.1}$$

The detector consisted of a water target, surrounded by liquid scintillator tanks equipped with photomultiplier (PMT)s. The emitted positron from the reaction in 1.1 nearly instantly annihilates with an electron in the water, thereby releasing two gamma rays which subsequently produce scintillation light via Compton scattering that is detected by the PMTs.
Due to rather high background rates it was not until some cadmium-chloride was added to the water that the scientists were finally able to see a distinct neutrino signal. The presence of Cd added a second, delayed signal component: The released neutron scatters off protons from H_2O, thereby losing energy, until being slow enough to be captured by a Cd-nucleus. The excited Cd*-nucleus releases gamma ray when decaying back to the ground-state. The prompt and delayed signals form a distinct delayed coincidence signature of an inverse β-decay occurring in the H_2O-target, thereby giving proof of a neutrino interacting in the target.

1.1.3. Discovery of the ν_μ

Another eight years passed until, in 1962, L.M. Lederman, M. Schwartz and J. Steinberger found the second neutrino flavor state, the muon-neutrino ν_μ, at the Brookhaven Alternating Gradient Synchrotron [7]. They were investigating the pion decay:

$$\pi^+ \rightarrow \mu^+ + \nu_\mu \tag{1.2}$$

For neutrino detection, a spark chamber made of 10 t of aluminum was employed. The muons from the decay were shielded so that only the neutrinos were able to reach the detector. The result was that only tracks of muons and no electron-showers as expected from the ν_e were detected. Their conclusion was that these neutrinos (ν_μ),

produced together with a muon in pion decay were a different kind of particle than the already known electron-neutrino (ν_e). All three lead authors of [7] were awarded the Nobel prize in 1988 for this discovery.

1.1.4. Discovery of the ν_τ

Finally in the year 2000 the third, so called tau-neutrino (ν_τ) was detected in the DONUT (Direct Observation of Nu Tau) experiment at Fermilab [8]. In this experiment a particle accelerator produced a beam of protons with energies up to 800 GeV. The beam was then directed onto a tungsten target where the protons collided with the target material to produce, among many pions and kaons, also charmed particles whose subsequent decay produced tau-neutrinos. A combination of strong magnets and high-density materials was then used to collimate charged mesons and to shield all particles, respectively. The DONUT detector consisted of stainless steel and emulsion plates in alternating order. A ν_τ-interaction in the detector will produce a τ-lepton which, due to its short lifetime will only produce a short track in the emulsion followed by a characteristic kink, marking its decay.
Before this direct observation, a strong, indirect evidence for the existence of three neutrino generations was given by the ALEPH experiment (and others) at LEP (CERN) in 1989 [9, 10]: The measured decay width of the Z^0-boson was compared to theoretical predictions and the best agreement was found for the case of three weakly interacting neutrinos with masses below ∼45 GeV.

1.2. Neutrino oscillations

Until about two decades ago no compelling experimental evidence for non-zero neutrino masses existed. The discovery of neutrino oscillations in 1998 finally gave convincing proof that neutrinos are in fact not massless, as expected in the Standard Model (SM). The oscillation of flavor eigenstates requires neutrinos to have mass and mixing, implying that mass and flavor eigenstate are different. Correspondingly, the measurement of mass splittings in neutrino-oscillation experiments gives a lower mass bound, if the lightest neutrino is assumed to be almost massless.

1.2.1. The solar neutrino problem

The first hint for non-zero neutrino masses was provided by solar neutrinos originating within the sun. These astrophysical neutrinos are of special interest, because, on the one hand, they yield information about the inner core of the sun and the ongoing fusion processes there. On the other hand, they allow to study neutrino properties in a unique regime. Solar neutrinos have relatively low energies ($\langle E_\nu \rangle \approx 0.3$ MeV) and travel a long way, first through the solar matter and then in vacuum through the space between Earth and sun. The vast majority of neutrinos inside the sun are produced through the famous thermo-nuclear fusion of hydrogen to helium:

$$\begin{aligned} 4p &\rightarrow {}^4\mathrm{He} + 2e^+ + 2\nu_e, \\ &\text{the } e^+ \text{ annihilate quasi-instantly with } e^-: \\ 2e^- + 4p &\rightarrow {}^4\mathrm{He} + 2\nu_e + 26.73 \text{ MeV} \end{aligned} \tag{1.3}$$

This so called *pp*-reaction takes place in the inner core of the sun. On an average, only 2% of the energy is emitted in neutrinos. The abundant *pp*-neutrinos have a

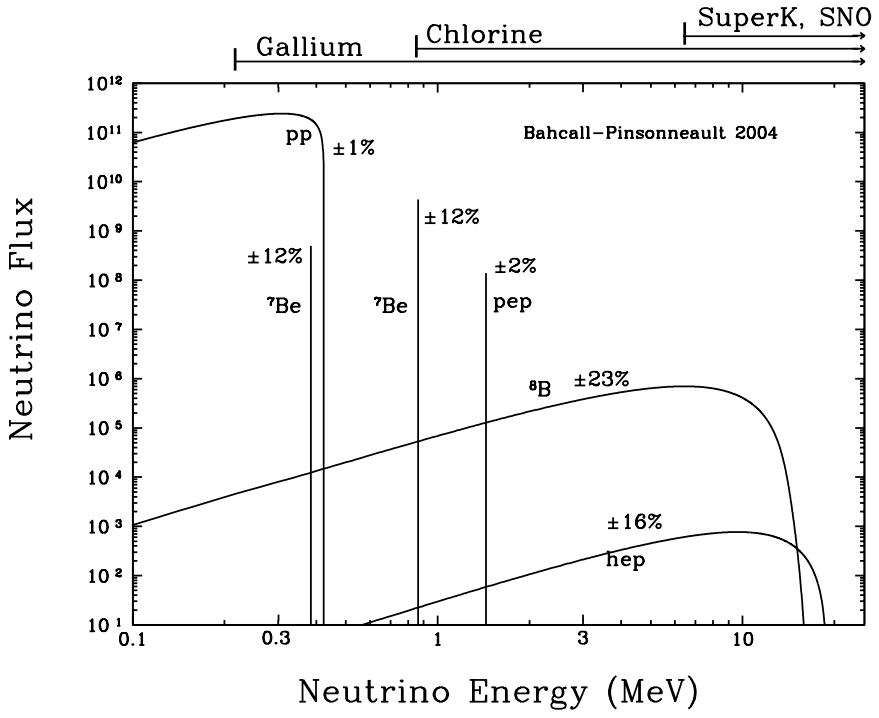

Figure 1.1.: **Solar neutrino energy spectrum according to the SSM** The markers on the top indicate the energy threshold of the individual experiments. For each solar neutrino branch the theoretical uncertainties are given as 1σ errors. Figure taken from [11].

distinct energy signature (see figure 1.1) together with the ^{7}Be- and ^{8}B- neutrinos from other *pp*-chains, that however have a far smaller contribution to the total solar neutrino flux. On Earth solar neutrinos account for a flux of 60 billion per cm^2 per second.

In 1964 J. Bahcall and R. Davis Jr. proposed an experiment to count the number of electron neutrinos ν_e, emitted by the sun. Their goal was to validate the newly established SSM based on equation 1.3. Their experiment was finally realized in the form of a 600 t tank of perchloroethylene, containing the isotope ^{37}Cl, which was set up deep underground in the Homestake mine, USA. When a neutrino from the sun interacts with a ^{37}Cl nucleus it is radiochemically transmuted into an excited ^{37}Ar atom:

$$^{37}\mathrm{Cl} + \nu_e \rightarrow \ ^{37}\mathrm{Ar} + e^- \tag{1.4}$$

After several weeks of measurement the produced ^{37}Ar are extracted by radiochemical methods from the tank into a small proportional counter. ^{37}Ar atoms extracted subsequently decayed via electron capture to excited states of ^{37}Cl, which then deexcites via Auger emission. These Auger electrons were finally detected in the proportional counter. Surprisingly, they only found about a third of the neutrino flux predicted by the SSM [12, 13]. This deficit established the so called *solar neutrino problem*, which was later confirmed by other experiments. Subsequent experiments made use either of radiochemical detection methods like the gallium-based experiments GALLEX [14], GNO [15] and SAGE [16], or provided real-time informa-

tion via neutrino-electron scattering in large water-based Cherenkov detectors like Kamiokande [17].
Possible explanations for the disappearance of ν_e were either based on the assumption of an incorrect SSM or on the concept of neutrino flavor oscillations. The latter phenomenon implies that neutrinos undergo a flavor change on their way from the center of the sun to the Earth. The above-mentioned experiments were almost exclusively sensitive to ν_e charged current reactions only and therefore were unable to measure neutrinos of other flavor that could have appeared due to oscillations.

1.2.2. The solution for the solar neutrino problem

The SNO experiment [18] finally was able to measure the total solar neutrino flux of all three flavors. During the first measurement phase, the detector was filled with 10^3 t of pure heavy water (D_2O). The choice of this unique target (deuterons) allowed to observe elastic scattering (ES) processes of electrons as well as neutral (NC) and charged current (CC) interactions on deuterons:

$$\begin{array}{lcll} \nu_e + d & \rightarrow & p + p + e^- & \textbf{C}\text{harged }\textbf{C}\text{urrent, } \nu_e \text{ only} \\ \nu_\alpha + d & \rightarrow & p + n + \nu_\alpha & \textbf{N}\text{eutral }\textbf{C}\text{urrent, all flavors} \\ \nu_\alpha + e^- & \rightarrow & \nu_\alpha + e^- & \textbf{E}\text{lastic }\textbf{S}\text{cattering, predominantly } \nu_e \end{array} \tag{1.5}$$

The three different reactions each give rise to a specific signal. This allows to measure the total neutrino flux via NC processes and the ν_e flux separately via CC reactions. The two additional experimental phases of SNO, apart from the first pure D_2O phase, were used to cross-check the initial results for the NC reaction using different detection schemes for neutrons. In the second phase salt (NaCl) was added to the D_2O to boost γ-energies from the neutron capture, and in the third phase ^{3}He counters were installed in the detector for separate detection of neutrons. The experimental data give evidence to the fact that only one third of the electron neutrinos originating from the Sun still retain their initial flavor state when reaching the detector [19, 20]:

$$\frac{\phi(\nu_e)}{\phi(\nu_e) + \phi(\nu_{\mu,\tau})} = 0.340 \pm 0.023^{+0.029}_{-0.031} \tag{1.6}$$

This implies that the missing two thirds of the ν_e-flux has oscillated into another flavor state on their way from the sun to the Earth. Furthermore, the data showed that the integral flux provided by the NC-induced deuteron breakup is consistent with the flux of ^{8}B neutrinos predicted by the SSM (shown in figure 1.2), thereby solving the solar neutrino problem that existed for almost 40 years.

1.2.3. Atmospheric neutrino anomaly

Final proof of the concept of neutrino oscillation was provided by atmospheric neutrinos which are produced in interactions of cosmic rays with atomic nuclei in the upper atmosphere. They originate mainly from pion and subsequent muon decays leading to a 2:1 ratio of ν_μ to ν_e for neutrino energies above the GeV scale. Experiments like Kamiokande [21] and Super-Kamiokande [22] that used water-based Cherenkov detectors and Soudan 2 [23], Frejus [24] and NUSEX [25] which used iron calorimeters, measured the flux of atmospheric ν_μ and ν_e with directional resolution.

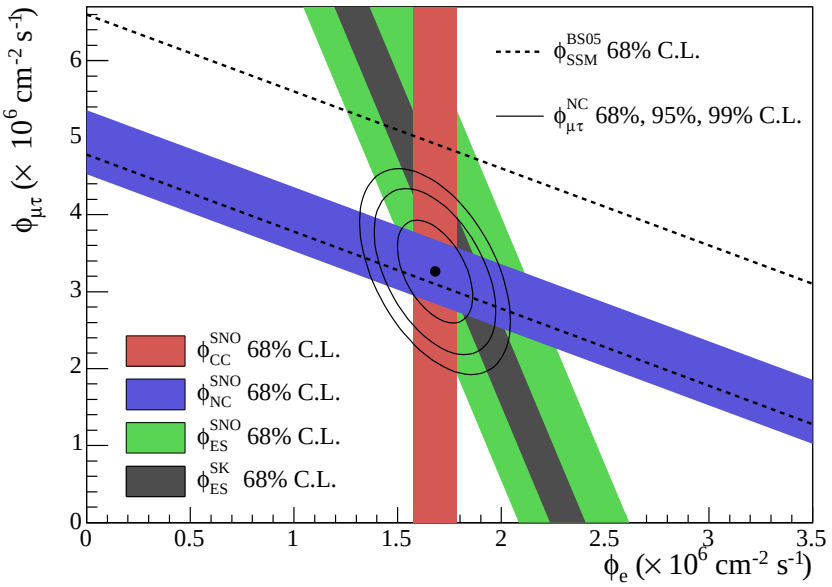

Figure 1.2.: **Flavor composition of neutrinos from the sun** Here, the solar neutrino fluxes $\phi_{\mu\tau}$ versus ϕ_e as measured by the SNO and Super-Kamiokande experiments are displayed. The dashed lines mark the neutrino flux predicted by the SSM. The flux ϕ_e is given by the CC-flux (marked by a point and lines, that represent various confidence levels) and $\phi_{\mu\tau}$ by the difference of the fluxes NC - CC. Figure taken from [20].

It was finally shown by Super-Kamiokande that the flavor ratio $r = \nu_\mu/\nu_e$ variated with the zenith-angle (see figure 1.3). The ratio r_b of atmospheric neutrinos that travel through Earth and reach the detector from below was found to be smaller than the ratio r_a of atmospheric neutrinos that travel a much smaller distance coming directly from above. This was the first irrevocable evidence of ν_μ oscillating into ν_e.

1.2.4. Theoretical description

Neutrino oscillations originate from the fact that neutrinos can be described by two fundamental sets of eigenstates. The first set are the *flavor-eigenstates* $|\nu_\alpha\rangle$ ($\alpha = e, \mu, \tau$) which are defined by weak interactions; while the second set are the *mass-eigenstates* $|\nu_i\rangle$ ($i = 1, 2, 3$) which are defined by their mass. Hence, the neutrino states coupling to weak interactions are not identical to the states propagating. The weak interaction eigenstates of the neutrinos can thus be expressed as superposition of mass eigenstates:

$$|\nu_\alpha\rangle = \sum_i U_{\alpha i} |\nu_i\rangle \tag{1.7}$$

with $U_{\alpha i}$ being the Maki-Nakagawa-Sakata-Pontecorvo mixing-matrix. It contains three mixing angles Θ_{ij} that describe the contribution of the mass-eigenstates to a specific flavor-eigenstate, the complex Dirac-phase (CP-violating) δ_D and, in principle, the two complex Majorana-phases $\delta_{\mathrm{M}i}$. These phases can cause CP-violation in the lepton sector [27], but are only of interest in double-β-decay. The matrix U can be decomposed into Euler-rotation matrices that describe the mixing between the

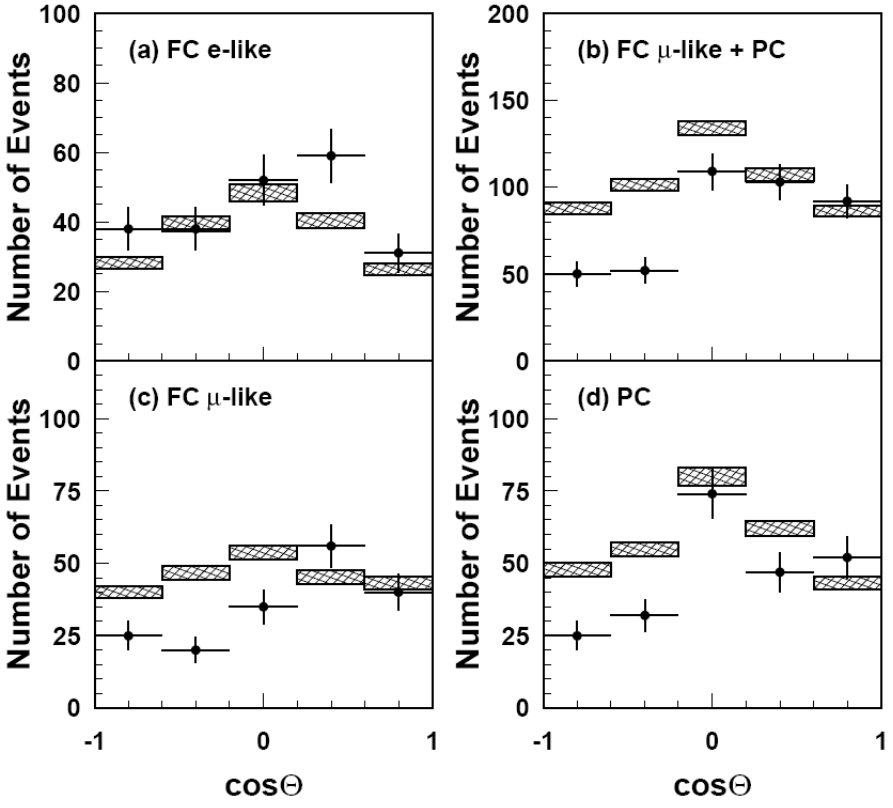

Figure 1.3.: **Evidence for atmospheric neutrino oscillations** The zenith angle distributions as measured by Super-Kamiokande are displayed for: (a) e-like events, (b) μ-like fully- and partially-contained events, (c) μ-like events and (d) all partially-contained events. The angle $\cos\Theta = 1$ corresponds to down-going neutrinos. The histograms with the shaded error bars show the MC-predictions with their statistical uncertainties. Figure taken from [26].

single states ν_i:

$$U = \begin{pmatrix} 1 & 0 & 0 \\ 0 & \mathrm{c}_{23} & \mathrm{s}_{23} \\ 0 & -\mathrm{s}_{23} & \mathrm{c}_{23} \end{pmatrix} \begin{pmatrix} \mathrm{c}_{13} & 0 & \mathrm{s}_{13}e^{-i\delta_\mathrm{D}} \\ 0 & 1 & 0 \\ \mathrm{s}_{13}e^{-i\delta_\mathrm{D}} & 0 & \mathrm{c}_{13} \end{pmatrix} \begin{pmatrix} \mathrm{c}_{12} & \mathrm{s}_{12} & 0 \\ -\mathrm{s}_{12} & \mathrm{c}_{12} & 0 \\ 0 & 0 & 1 \end{pmatrix} \begin{pmatrix} e^{-i\delta_{\mathrm{M}1}} & 0 & 0 \\ 0 & e^{-i\delta_{\mathrm{M}2}} & 0 \\ 0 & 0 & 1 \end{pmatrix}$$

where s_{ij} (c_{ij}) denote $\sin\Theta_{ij}$ ($\cos\Theta_{ij}$).
The mass eigenstates $|\nu_i\rangle$ are stationary and can be propagated into time-dependent form:

$$|\nu_i(t)\rangle = e^{-iE_it}|\nu_i\rangle \tag{1.8}$$

A pure flavourstate $|\nu_\alpha\rangle$ at the time $t = 0$ propagates into:

$$|\nu(t)\rangle = \sum_i U_{\alpha i}e^{-iE_it}|\nu_i\rangle = \sum_{i,\beta} U_{\alpha i}U^*_{\beta i}e^{-iE_it}|\nu_\beta\rangle \tag{1.9}$$

For the transition probability from flavor $\alpha \to \beta$ we find the amplitudes [28, 29]:

$$\begin{aligned} P_{\nu_\alpha\to\nu_\beta}(t) = |\langle\nu_\beta(t)|\nu_\alpha(t)\rangle|^2 &= \left|\sum_i U^*_{\alpha i}e^{-iE_it}U_{\beta i}\right|^2 \\ &= \sum_{i,j} U^*_{\alpha i}U_{\beta i}U_{\alpha j}U^*_{\beta j}e^{-i(E_i-E_j)t} \end{aligned} \tag{1.10}$$

In the ultra-relativistic limit, assuming $p_i = p = E$ we get the transition amplitudes:

$$P_{\nu_\alpha\to\nu_\beta}(L/E) = \sum_{i,j} U^*_{\alpha i}U_{\beta i}U_{\alpha j}U^*_{\beta j}e^{-i\frac{\Delta m^2_{ij}L}{2E}} \tag{1.11}$$

where the oscillation phase is given through the mass splitting terms $\Delta m^2_{ij} \equiv m^2_i - m^2_j$, while L corresponds to the distance between source and detector and E to the energy of the neutrino. This model is able to describe the disappearance of neutrinos of a certain flavor α as a function of their energy and oscillation length, as well as the appearance of neutrinos of a flavor β different from the flavor α which was emitted at the source.

1.2.5. Measurements of the parameters of neutrino oscillation

In order to determine the full set of the neutrino mixing parameters, neutrinos from different sources have to be observed. For a particular experiment, the experiment-specific L/E-ratio translates into a sensitivity for a combination of mass-splittings Δm_{ij} and mixing angles Θ_{ij}.

Atmospheric neutrinos

As mentioned in 1.2.3, high-statistics data from the Super-Kamiokande experiment showed that the number of atmospheric ν_μ that reached the detector depends on the incident zenith angle. The muon neutrinos that come from below have to travel a longer path through the Earth and therefore have a greater possibility to oscillate into tau neutrinos. With the available experimental data, the parameter Θ_{23} of the mixing matrix U was determined to [30, 27]:

$$\sin^2(2\Theta_{23}) \geq 0.92 \text{ (90\%C.L.)} \tag{1.12}$$

and the mass difference Δm^2_{23} was narrowed down to the range:

$$1.9 \times 10^{-3}\mathrm{eV}^2 < \Delta m^2_{23} < 2.6 \times 10^{-3}\mathrm{eV}^2 \text{ (90\%C.L.)} \tag{1.13}$$

Table 1.1.: Current limits on Θ_{13}

Experiment	$\sin^2(2\Theta_{13})$	$\sigma_{\text{stat.}}$	$\sigma_{\text{syst.}}$
Daya Bay [35]	0.089	0.010	0.005
Double Chooz [33]	0.109	0.030	0.025
RENO [34]	0.113	0.013	0.019

Reactor neutrinos

Fission reactors are a copious source of electron anti-neutrinos that are produced in the β-decays of neutron-rich nuclei following nuclear fission in the reactor core. These $\bar{\nu}_e$ are produced by a large number of different chains of β-decays of the fission products.
A typical modern nuclear power plant has a reactor core with a thermal power of the order of 3 GW_{th}. On average, each fission produces 200 MeV of energy with the release of about 6 $\bar{\nu}_e$. This translates into a flux of $\bar{\nu}_e$ of about 2×10^{20} s^{-1} per GW_{th}. Although the anti-neutrino flux is very high, it is isotropic and thus decreases rapidly with distance. As the released $\bar{\nu}_e$ are relatively low in energy (in the order of a few MeV), their oscillation length is rather short, of the order of 2 km (Θ_{13}) or 60 km (Θ_{12}) only.
Reactor anti-neutrinos are detected through the inverse beta decay, as described in equation 1.1.
KamLAND is a long-baseline-experiment that has observed the $\bar{\nu}_e$-flux from all Japanese reactors with an average distance of about 180 km. For these distances, the transition probability mainly depends on Θ_{12} and Δm^2_{12}. Figure 1.4 exhibits the result that clearly shows not only the disappearance of electron anti-neutrinos but also the expected oscillation pattern as a function of L/E. The analysis of the measured data yields [31]:

$$\sin^2(2\Theta_{12}) = 0.87 \pm 0.03 \qquad \text{and} \qquad \Delta m^2_{12} = 7.59 \pm 0.20 \times 10^{-5}\text{eV}^2 \tag{1.14}$$

On the other hand, for short distances (< 5 km) the influence of Θ_{12} and Δm^2_{12} is negligible, and the transition probability mainly depends on Θ_{13} and Δm^2_{13}. Short-baseline-experiments like Double CHOOZ [32, 33], RENO [34] and Daya Bay [35] make use of this fact to determine Θ_{13}. They typically set up two detectors, one at a short distance of less than 400 m, the other far detector at a distance of 1-2 km from the nuclear reactor core to look for the disappearance of $\bar{\nu}_e$. Their results are given in table 1.1.

Accelerator neutrinos

The neutrino beams in accelerator experiments are produced through pion decay-in-flight or by muon decay-at-rest in the beam dump. These experiments are therefore sensitive to the oscillation channel $\nu_\mu \leftrightarrows \nu_\tau$, a fact that at first allowed the determination of Θ_{23} and Δm^2_{23}.
In the Japanese K2K experiment an almost pure ν_μ-beam was sent over a distance of 250 km from the KEK laboratory to the Super-Kamiokande detector. Under the assumption of maximum mixing, $\sin^2(2\Theta_{23}) = 1$, the experimental data yield a best-fit value of the 2-3 mass splitting of [36]:

$$1.9 \times 10^{-3}\text{eV}^2 \leq \Delta m^2_{23} \leq 3.5 \times 10^{-3}\text{eV}^2 \text{ (90\%C.L.)} \tag{1.15}$$

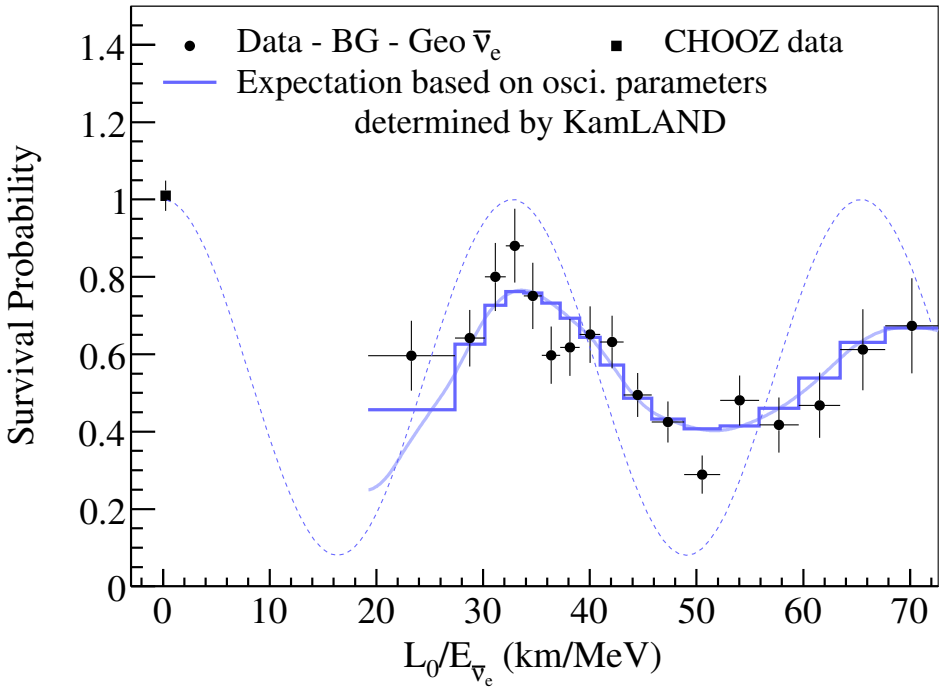

Figure 1.4.: **Results of KamLAND** Survival probability of reactor neutrinos $\bar{\nu}_e$ as a function of distance over energy. Different neutrino-energies were observed, allowing for a variation of the L/E ratio. In addition a point derived from CHOOZ data is shown. Figure taken from [31].

Future experiments like T2K [37] and NoVa [38] will have the primary objective to study $\nu_\mu \leftrightarrows \nu_e$ oscillations in these beams. Such a measurement would give information on the element U_{e3} of the neutrino mixing matrix in complementary to reactor oscillation studies.

1.2.6. Conclusions

The phenomenon of neutrino oscillations has been studied in detail by a wide selection of experiments. All major oscillation parameters such as mixing angles and differences of squared masses have been measured rather precisely. In figure 1.5 a summary of the data presently available is shown. However, some main issues remain unsolved:

- **Absolute mass scale**: as oscillation experiments are only sensitive to the parameter Δm^2_{ij}, the abolute mass scale is still to be determined.
- **Mass hierarchy**: at present, the ordering of mass eigenstates of the neutrinos is not known, this could be hierarachical ($m_1 < m_2 < m_3$) or inverted hierarachical ($m_3 < m_2 < m_1$), or even quasi-degenerate ($m_3 \approx m_2 \approx m_1$), where a fundamental mass scale of neutrinos would be measured

1.3. Measurements of neutrino mass

As stated above, oscillation experiments only yield information on neutrino mass splittings, information on the absolute values of neutrino masses has to be provided by other methods.

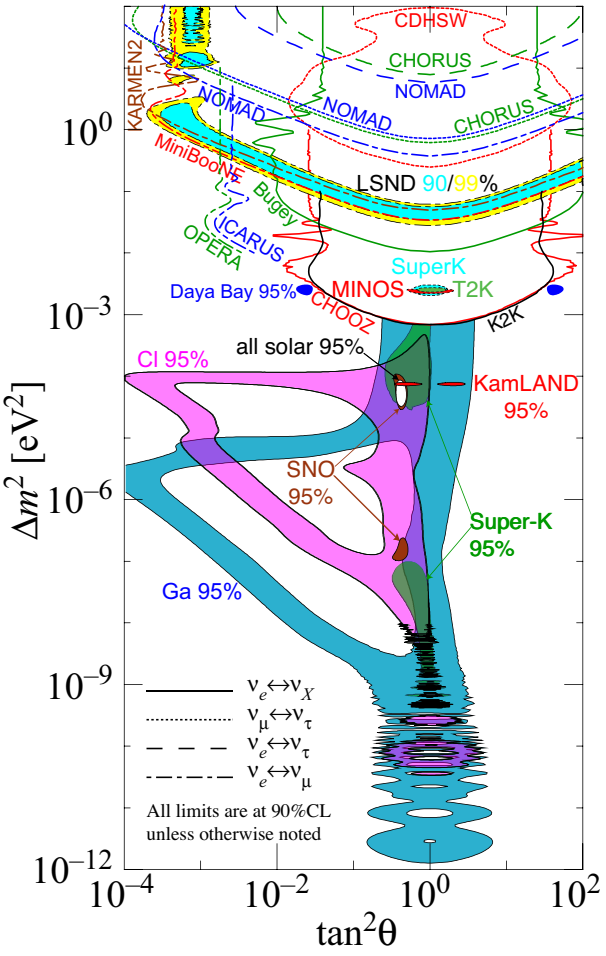

Figure 1.5.: **Parameters of neutrino oscillations** This plot gives an overview of Δm^2 and $\tan^2\Theta$ of a large number of ν-oscillation experiments. The filled areas highlight the preferred values of Δm^2 and $\tan^2\Theta$ measured in different experiments. Figure taken from [39].

In general, two different approaches exist to measure the masses of the neutrinos: they are labeled as indirect and direct methods. The indirect methods rely on model assumptions such as on the CP-properties of neutrinos, whereas direct methods investigate kinematics of decay processes where neutrinos are involved.

1.3.1. Supernova neutrinos

Core-collapse supernovae (SN) represent a very strong source of neutrinos, so their time-of-flight can be used to investigate neutrino masses. When the nuclear fusion chain in the core of a massive star of several solar masses has reached the stage of silicon burning to iron, the core can no longer resist the gravitational force of the outer shells. It collapses in a free fall, thereby transforming into a hot proto-neutron star. During the collapse, a large number of neutrinos is generated by the following processes (neutronization burst and thermal cooling of the hot proto-neutron star):

$$\begin{aligned} e^- + p &\rightarrow n + \nu_e \\ \gamma \leftrightarrows e^- + e^+ &\leftrightarrows \nu_\alpha + \bar{\nu_\alpha} \end{aligned} \tag{1.16}$$

When the re-bouncing matter shock wave of the core hits the infalling outer shell of the star, it is stalled, however, current SN-models point to a "delayed explosion" via neutrino-heating. The total duration of the neutrino emission after the collapse is only of the order of 10 s. On their way out of the core the neutrinos undergo scattering processes because of the enormous density $\mathcal{O}(10^{11}$ g/cm$^3)$ of the cooling neutron star. The exact shape of the neutrino pulse emitted thus depends on model assumptions of neutron star formation and collective neutrino processes.
The supernova SN1987A in the Large Magellanic Cloud emitted a neutrino-burst which was detected by several underground detectors in Baksan, Russia [40], the Morton-Thiokol salt mine, USA [41] and the Kamioka mine, Japan [42], opening up the door to low-energy neutrino astrophysics and marking the birth of astroparticle physics. The time-of-flight T_ν of a neutrino from the supernova to the detector is given by:

$$T_\nu \approx \frac{L_\nu}{c}\left(1 + \frac{{m_\nu}^2 c^4}{2{E_\nu}^2}\right) \tag{1.17}$$

where m_ν and E_ν denote the neutrino mass and energy and $L = 1.5 \times 10^{21}$ m denotes the distance of the source (here SN1987A) to the detector. The imprint of a non-zero neutrino mass m_ν on T_ν is such that T_ν depends on E_ν, with different energies $E_{\nu,1}$ and $E_{\nu,2}$. The time difference Δt between the arrival of the two neutrinos thus is:

$$\Delta t = \Delta t_0 + \frac{L{m_\nu}^2 c^4}{2c}\left(\frac{1}{E_{\nu,2}} - \frac{1}{E_{\nu,1}}\right) \tag{1.18}$$

The parameter Δt_0 is the time-difference between the emission of the two neutrinos and is a model-independent parameter [43, 44], which seriously affects the sensitivity of SN-time-of-flight studies with regard to measuring m_ν in the sub-eV mass scale. For the model case of SN1987A, a new, detailed analysis yields an upper limit for the neutrino mass of [45]:

$$m_{\nu_e} < 5.8 \text{ eV} \quad (90\% \text{ C.L.}) \tag{1.19}$$

1.3.2. Cosmology

Cosmological studies offer several interesting pathways to determine the neutrino mass, i. e. the sum of ν-masses. However, most approaches are very model-specific.

Cosmic Microwave Background

In the early universe, shortly after the Big Bang, temperatures were high enough for particles to be in perfect thermal equilibrium [46]. As the universe expanded and cooled the temperature became low enough (3000 K) for photons to decouple from matter. At this point, about 3.8×10^5 years after the Big Bang, neutral atoms were forming and photons started to stream freely. During the expansion of the universe, the free-streaming photons cooled further so that today they form a black-body spectrum with an effective temperature of ~ 2.7 K [47]. This is the Cosmic Microwave Background (CMB) which was first discovered in 1965 [48].

Satellite-based CMB-experiments have discovered small anisotropies in this radiation, the latest being the Planck [49] observer which measured these anisotropies

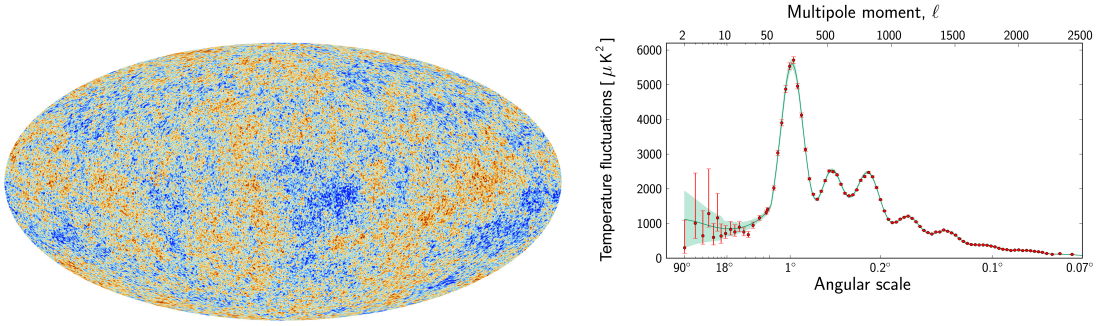

(a) PLANCK-skymap (b) PLANCK-power-spectrum

Figure 1.6.: **CMB measured by Planck** The red dots in (b) show the multipole-expansion for (a). The blue line represents the fit to the ΛCDM-model. Figures taken from [49].

to very high precision. The observed fluctuations are shown in figure 1.6(a). For analysis, they are expanded into spherical harmonics, with figure 1.6(b) exhibiting the resulting power spectrum. The form of this power spectrum is well described by the so called ΛCDM-concordance model and strongly constrains cosmological parameters like the baryonic mass density Ω_b, dark energy density Ω_Λ and dark matter density Ω_DM.

Cosmic neutrinos can be described in a rather similar fashion to the CMB-photons. Once the weak interaction rate Γ_ν fell below the expansion rate of the universe [50], relic neutrinos decoupled and were able to free-stream while being redshifted due to the expansion of the universe.
At present there is no direct experimental signature for relic neutrinos, but standard hot BigBang cosmology allows to calculate their density n_ν ($\approx 56\ \nu_e/\ \mathrm{cm}^3$ [51]) is in close relation to the density of CMB-photons n_γ:

$$n_\nu = \frac{3}{11} n_\gamma \tag{1.20}$$

With this the contribution of neutrinos to the total energy density of the universe is constrained by the sum of the masses of all non-relativistic neutrinos:

$$\Omega_\nu = \frac{\rho_\nu}{\rho_\mathrm{crit}} = \frac{\sum_i m_{\nu_i}}{93.14 \cdot h^3\ \mathrm{eV}} \tag{1.21}$$

where h denotes the dimensionless Hubble parameter and ρ_crit the critical energy density corresponding a flat universe. Analyses of the PLANCK data within the ΛCDM-model [52] result in a (conservative) upper limit of:

$$\sum_i m_{\nu_i} < 1.1\ \mathrm{eV} \quad (95\%\ \mathrm{C.L.}) \tag{1.22}$$

Structure formation

Even with small rest masses, the free-streaming of neutrinos leaves an imprint on the distribution of galaxies and thereby the matter distribution in the universe we

observe today.
The Sloan Digital Sky Survey (SDSS) [53] has imaged more than a quarter of the sky in its eight years of operation until today. It has observed large-scale structures of galaxies and revealed the filament-like matter distribution. Cosmologists are able to reproduce this observed pattern with numerical simulations on the basis of the ΛCDM or comparable models [54, 55]. In these simulations, the sum of the neutrino masses is a free parameter. In the early universe, when these structures formed, neutrinos were floating unimpeded, equalizing primordial density fluctuations and thus washing-out small-scale structures on the galactic scale.
The ability of neutrinos to wash-out structures depends on their summed mass $\sum_i m_{\nu_i}$. Therefore a comparison of the simulations of structure formation with the observed data allows to obtain information on neutrino masses. Combining analyses of structure formation with CMB data yields upper limits for the sum of the neutrino masses ranging from

$$\sum_i m_{\nu_i} < 0.5 \quad - \quad 1 \text{ eV}, \tag{1.23}$$

depending on the priors that were used [56, 57]. In view of the considerable scatter of the results, it is much preferable to measure the neutrino mass in the laboratory and to use it as input in cosmological studies.

1.3.3. Neutrinoless double-β-decay

Neutrinoless double-β-decay ($0\nu\beta\beta$) experiments allow to investigate the Majorana-nature [58] of neutrinos. In addition, such experiments offer the possibility to determinate of the absolute neutrino mass scale and to investigate the mass pattern of neutrinos.
Neutrinoless double-β-decay processes of the types

$$\begin{aligned} \mathcal{N}(A,Z) &\rightarrow \mathcal{N}(A,Z+2) + 2e^- \quad (2\beta^-_{0\nu}) \\ \mathcal{N}(A,Z) &\rightarrow \mathcal{N}(A,Z-2) + 2e^+ \quad (2\beta^+_{0\nu}) \end{aligned} \tag{1.24}$$

are forbidden in the SM due to lepton number conservation. If neutrinos are massive Majorana-particles, a nucleus decaying via the $2\beta_{2\nu}$ process can also decay through a $2\beta_{0\nu}$ process, albeit with a different (and much longer) lifetime.
There is a large number of experiments looking for $0\nu\beta\beta$ events. The GERDA experiment [59] used well shielded Germanium diodes to look for the $2\beta^-$ decay of the isotope ^{76}Ge into ^{76}Se. Figure 1.7 shows the hypothetical spectrum of such a decay. After an exposure of 21 kg·years, no signal of $0\nu\beta\beta$ was found, yielding [60]:

$$\tau_{0\nu} > 2.1 \times 10^{25} \text{ a} \quad (90\%\text{C.L.}) \tag{1.25}$$

This result does not confirm the claim of a subgroup of the previous Heidelberg-Moscow experiment [61]. A part of the experiment's collaboration claimed to have evidence that neutrinos are massive Majorana-particles and estimated an effective Majorana-neutrino mass of [62]:

$$\langle m_\nu \rangle = 0.39^{+0.45}_{-0.34} \text{ eV} \tag{1.26}$$

The claimed mass lies in a scale accessible to KATRIN in the near future. When comparing $0\nu\beta\beta$ searches and β-decay experiments one has to keep in mind however

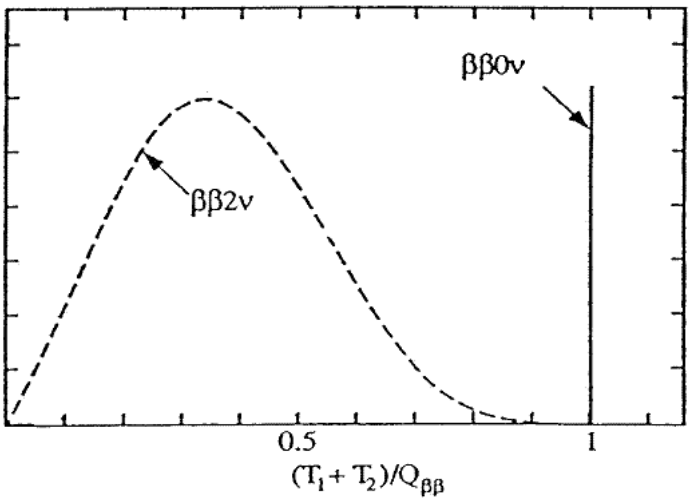

Figure 1.7.: **Energy spectrum of a double-β-decay process** The $2\nu\beta\beta$ continuum represents the summed energy of both charged leptons. The monoenergetic line at the total energy E_0 of the transition corresponds to the $0\nu\beta\beta$-decay, which violates lepton-number conservation by 2 units ($\Delta L = 2$). Figure taken from [63].

the significant model dependence of $0\nu\beta\beta$-results: the complex Majorana-phases that enter into the observable, the effective Majorana-neutrino mass $\langle m_{0\nu\beta\beta}\rangle$, are not known, and calculation of the nuclear transition matrix is notoriously difficult to obtain with sufficient precision. Finally there can be other mechanisms contributing to neutrinoless double β-decay than the one involving massive neutrinos, as for example super symmetric particles or right-handed weak couplings.

1.3.4. β-decay

Today the most sensitive method to measure the effective mass of the electron (anti-)neutrino in a model-independent way is by measuring the electron energy spectrum of a nuclear β-decay

$$\mathcal{N}(A, Z) \rightarrow \mathcal{N}(A, Z+1) + e^- + \bar{\nu_e} \tag{1.27}$$

where A and Z are the mass and atomic numbers of the parent nucleus.
As described in equation (1.7) the electron neutrino, does not have a definite mass, but is a mixture of mass eigenstates.

Fermi's Golden Rule can be used to describe the transition probability T for the decay:

$$T \propto |\mathcal{M}|^2 \, \rho(E) \tag{1.28}$$

implying that the decay probability depends on the overlap between the initial- and final-state wave functions. In case of so called "allowed" β-decays, the final-state wave functions of the electron and the anti-neutrino largely overlap and the nuclear matrix element $|\mathcal{M}|^2$ does not depend on energy. With the density of the available final states ρ [4], one obtains a decay rate as a function of the electron energy E [29]:

$$\frac{\mathrm{d}\dot{N}}{\mathrm{d}E} = R(E)(E_0 - E)\sqrt{(E_0 - E)^2 - m_{\bar{\nu}_e}^2 c^4} \; \Theta\left(E_0 - E - m_{\bar{\nu}_e} c^2\right) \tag{1.29}$$

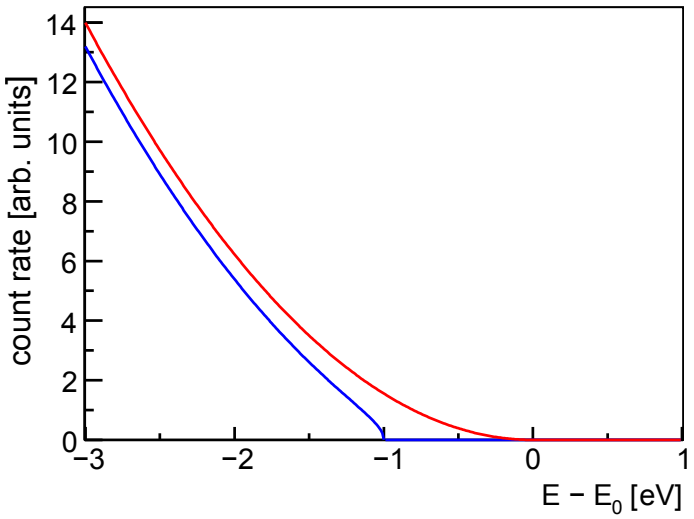

Figure 1.8.: **Spectra arround the β-decay endpoint** $E-0$ for 0 (red) and 1 eV (blue) $\bar{\nu}_e$-mass. Figure taken from [64]

The step function

$$\Theta\left(E_0 - m_e c^2 - m_{\bar{\nu}_e} c^2\right) \tag{1.30}$$

guarantees energy conservation. $R(E)$ is a product of numerical factors and kinematic variables of the electron, given by:

$$R(E) = \frac{G_{\mathrm{F}}^2}{2\pi^3 \hbar^7} \cos^2\theta_{\mathrm{C}} \left|\mathcal{M}\right|^2 F(Z+1, E) p(E + m_e c^2), \tag{1.31}$$

where G_{F} is the Fermi coupling constant, θ_{C} is the Cabibbo angle, $\mathcal{M}$ is the nuclear matrix element, E and p are the electron kinetic energy and momentum. $F(Z+1, E)$ is the Fermi function that describes the electromagnetic interaction of the β-electron with the Coulomb field of the nucleus in the final state.
The figure of interest in equation (1.29) is of course $m_{\bar{\nu}_e} c^2$, which gives access to the effective electron neutrino mass. In case of a non-zero value, the endpoint of the β-spectrum will be shifted to a lower energy. In the region of high count rates, the effect of the neutrino mass on the shape is insignificant due to the ultra-relativistic nature of neutrinos there. The spectrum close to E_0 is plotted in figure 1.8.

As mentioned above, when taking into account the effects of neutrino mixing, we can express the electron neutrino as a weighted superposition of mass eigenstates:

$$\nu_e = \sum_i U_{ei} \nu_i \tag{1.32}$$

Incorporating this to the β-decay spectrum gives:

$$\frac{\mathrm{d}\dot{N}}{\mathrm{d}E} = R(E) \sum_i \left|U_{ei}\right|^2 (E_0 - E) \sqrt{(E_0 - E)^2 - m_i^2 c^4}\, \Theta\left(E_0 - E - m_i c^2\right) \tag{1.33}$$

This results in a fine structure of the β-decay spectrum, which, up to now, cannot be resolved in measurements due to the very small mass splittings Δm_{ij}^2 (see 1.2.5). Accordingly, in current measurements only an incoherent sum, the effective electron

neutrino mass, is observable:

$$m_{\nu_e}^2 = \sum_{i=1}^{3} |U_{ei}|^2 \, m_{\nu_i}^2 \tag{1.34}$$

Note that only the square $m_{\nu_e}^2$ is measured.
Most of the theoretical parameters of the spectrum described in (1.33) are well known. In view of this, kinematic searches for m_{ν_e} are highly model-independent, because the only unknown quantities that have to be taken into account are m_{ν_e} and the endpoint energy E_0.

1.3.5. π- and τ-decay

For historical reasons, we briefly outline former analyses and methods to access the neutrino mass experimentally: these are kinematic analyses of pion- and tau-decays. In view of modern oscillation results the resulting experimental constraints are much less stringent than those obtained in β-decay experiments. Still these pion- and tau-decay experiments can be used to constrain the mixing of ν_μ and ν_τ with heavy neutrinos beyond three-neutrino mixing.
Measurements of the kinematics in the decay of charged pions can give information on the neutrino masses. The most sensitive experiment up to now was performed at Paul-Scherrer-Insitut (PSI) in Switzerland and has used the following decay:

$$\pi^+ \to \mu^+ + \nu_\mu. \tag{1.35}$$

Since this decay has a two-body final state, the mass of the neutrino can be determined by energy-momentum conservation if the momenta of the pion and muon can be measured with sufficient accuracy. In case of neutrino mixing, the ν_μ is a superposition of different massive neutrinos. A measurement of the neutrino mass forces the superposition to collapse on the massive neutrino whose mass has been measured. Therefore, in analogy to (1.33), peaks should appear corresponding to the values of the neutrino masses, which are given by

$$m_i^2 = m_\pi^2 + m_\mu^2 - 2m_\pi \sqrt{m_\mu^2 + |\vec{p}_\mu|^2} \quad (i = 1, 2, 3) \tag{1.36}$$

for pions decaying at rest.
The value of the muon momentum measured at the PSI is [65, 66]:

$$|\vec{p}_\mu|^2 = 29.79200 \pm 0.00011 \ (\mathrm{MeV/c})^2 \tag{1.37}$$

leading to upper limits of m_i (at 90% C.L.)

$$m_i < 0.17 \ \mathrm{MeV} \quad (i = 1, 2, 3) \tag{1.38}$$

At CERN, the ALEPH experiment has used tau-decays for a corresponding measurement of neutrino masses. The decays

$$\tau^- \to 2\pi^- + \pi^+ + \nu_\tau \quad \text{and} \quad \tau^- \to 3\pi^- + 2\pi^+ + \nu_\tau + \pi^0 \tag{1.39}$$

have been studied, with the result (at 95%C.L.) [67]:

$$m_i < 18.2 \ \mathrm{MeV} \quad (i = 1, 2, 3) \tag{1.40}$$

It is unlikely that in the future the measurements of neutrino masses with pion- and tau-decay experiments may improve so much to reach a precision at the eV- or sub-eV-level, comparable to the one of β-decay experiments. As mentioned before, their interest lies mainly in the possibility of constraining the admixture of the ν_μ and ν_τ with heavy neutrinos beyond the standard three-neutrino mixing.

2. The KATRIN experiment

The goal of the KATRIN experiment [68] is to determine the effective mass of the electron (anti-)neutrino by examining the shape of the tritium-β-spectrum close to its endpoint. With approximately 1000 net days of data-taking, the experiment will be able to achieve a mass sensitivity down to 200 meV/c^2 (90% C.L.).
The following chapter will give a short introduction to the experiment. First an overview is given on general selection criteria for a β-source highlighting the advantages of tritium as β-emitter. Then, the experimental set-up and the main components will be reviewed. This will be followed by a in-depth description of the working principle of a MAC-E filter. The chapter will close with an overview of the experimental setup and give details on the SDS-I commissioning phase that took place from May to September of 2013, where a significant body of experimental data was collected, forming the main body of the present thesis.

2.1. The tritium β-decay

KATRIN is built to perform an ultra-precise measurement of the kinematics of β-decay electrons close to E_0, making the choice of a β-source of special importance. The KATRIN experiment uses the decay of the unstable hydrogen-isotope tritium (^{3}H),

$$^3_1\mathrm{H} \rightarrow {}^3_2\mathrm{He}^+ + e^- + \bar{\nu}_e \tag{2.1}$$

due to the following key advantages:

- **low endpoint energy** The β-spectrum of tritium has an endpoint-energy of $E_0 = 18.57$ keV thus being the β-emitter (after ^{187}Rh) with the second lowest energy E_0 of all relevant β-emitters. As the relative fraction of electrons with energies near the endpoint decreases with E_0 ($\sim {E_0}^{-3}$), a low endpoint energy yields the advantage of a relatively high count-rate of electrons in the energy region of interest, despite the fact that the decay rate scales with $\sim {E_0}^5$.
- **super-allowed transition** The tritium β-decay is of super-allowed type due to the fact that the transition is between mirror nuclei. Thus the nuclear matrix

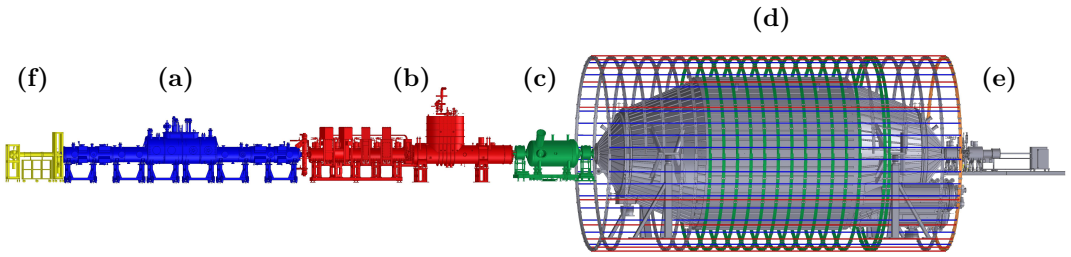

Figure 2.1.: **Overview of the KATRIN experimental setup** the tritium source WGTS (a), the transport section (b), the pre-spectrometer (c), the main spectrometer (d), the detector (e) and the rear section (f).

element is energy independent and no corrections from the nuclear transition matrix elements $\mathcal{M}$ have to be taken into account. As a consequence, tritium is a rather short-lived isotope, featuring a half-life of only 12.3 a. This has the distinct advantage of requiring less source material in order to reach an adequate count rate for a reasonable measurement time.

- **simple electron shell** The atomic shell configurations of tritium and its daughter $^3He^+$ are rather simple, also with regard to molecular (excited) states. The atomic and molecular corrections and corrections due to interactions of the emitted electron with the source thus can be computed precisely [69, 70].
- **small inelastic scattering probability** As tritium features a nuclear charge $Z = 1$ the probability for inelastic scattering of emitted β-decay electrons within the source will be small.

An alternative to tritium would be the β-emitter ^{187}Re, which has the lowest endpoint energy (2.47 keV) of all known β-decay nuclei [71]. The MARE experiment [72, 73] has used arrays of low-temperature calorimeters to measure the Rhenium-187 β-spectrum. It aims for a sensitivity comparable to the current $m^2_{\bar{\nu}_e}$-limits set by the Mainz and Troitsk experiments. Another very promising approach is to investigate the electron capture on ^{163}Ho [74] in the framework of the ECHo [75, 76] and HoLMES [77] projects. The calorimetric approach followed by these collaborations offers scalability and all plan to reach a sub-eV sensitivity in the long-term future.

2.2. Basic setup

2.2.1. WGTS

KATRIN will make use of a Windowless Gaseous Tritium Source (WGTS), as source β-decay electrons. In the WGTS, ultra-cold (27 K) molecular tritium gas with high isotopic purity (>95%) will be injected at the center of the 10 m long source tube, which then diffuses towards both ends. The beam tube has a diameter of 90 mm. AT either end of the beam tube two pump ports housing two turbo-molecular pump (TMP)s reduce the gas flow out of the WGTS. By carefully controlling the temperature and the injection rate, the column density within the tube will be fixed to the reference value $\rho\, d = 5{\times}10^{17}$ molecules/cm^2, which grants optimal conditions with regard to high luminosity and small probability of scattering of β-electrons off

residual gas molecules. The entire source tube is surrounded by superconducting solenoids that generate a strong magnetic field (3.6 T) to adiabatically guide the β-electrons out of the source towards the transport section.

2.2.2. Transport section

While β-decay electrons travel from the source to the SDS, the tritium gas injected into the source is not contained by a physical barrier, hence why it is called "windowsless". However, with respect to background reduction it is crucial that the amount of tritium gas penetrating from the source to the SDS part of the experiment is constrained to extremely low levels. Therefore, the gas flow from the source will be reduced by 14 orders of magnitude, from the initial injection rate in the WGTS of 1.8 mbar·ℓ/s to a value of only 10^{-14} mbar·ℓ/s at the entrance of the pre-spectrometer. For this purpose, two different pumping sections are being implemented between the source and the spectrometers: The Differential Pumping Section (DPS) which houses TMPs to reduce the gas flow and the Cryogenic Pumping Section (CPS), where the inner beam tube is covered by argon frost, so that residual gas molecules are absorbed. In addition, the beam tube in both pumping elements contains a chicane to avoid the beaming effect in molecular gas flow„ which in turn increases the efficiency of the residual gas removal. Similar to the WGTS, the electrons in the transport section are guided by a strong magnetic field (up to 5.6 T) generated by superconducting solenoids.

2.2.3. Spectrometers

The β-decay electrons originating from the source will be analyzed by a tandem set-up of electrostatic retarding spectrometers of the MAC-E-Filter type. Only those electrons with a large starting energy will pass this filter system, while all others will be rejected. This principle will be described in detail in section 2.3.

2.2.4. Focal Plane Detector

With the precision energy filtering being performed by the tandem set-up of the spectrometer system, the main task of the detector in principle is to count the β-electrons that pass the main spectrometer. However, the detector must show a good energy resolution in order to discriminate signal- from and background-electrons. In particular, the detector has to meet the following stringent requirements:

- low intrinsic background level ($\sim$ 1 mcps)
- ability to operate in high magnetic fields ($B_{\mathrm{max}} = 6$ T)
- ability to cope with high rates of more than 1 kcps during calibration phases
- good spatial resolution, to map the potential variation in the analyzing plane and to yield information on background processes in the spectrometers at different flux tube values (0-210 T cm^2)

On that account, a silicon PIN diode array will be used with a resolution of around 1.5 keV for electron energies of 18.6 keV [78, 79]. Due to the rather low count rates expected very close to the endpoint E_0, the detector itself must be well shielded to suppress background radiation. To achieve spatial resolution, the detector is segmented into 148 pixels, each of them covering a part of the flux tube with the same area (see figure 2.2(b)).

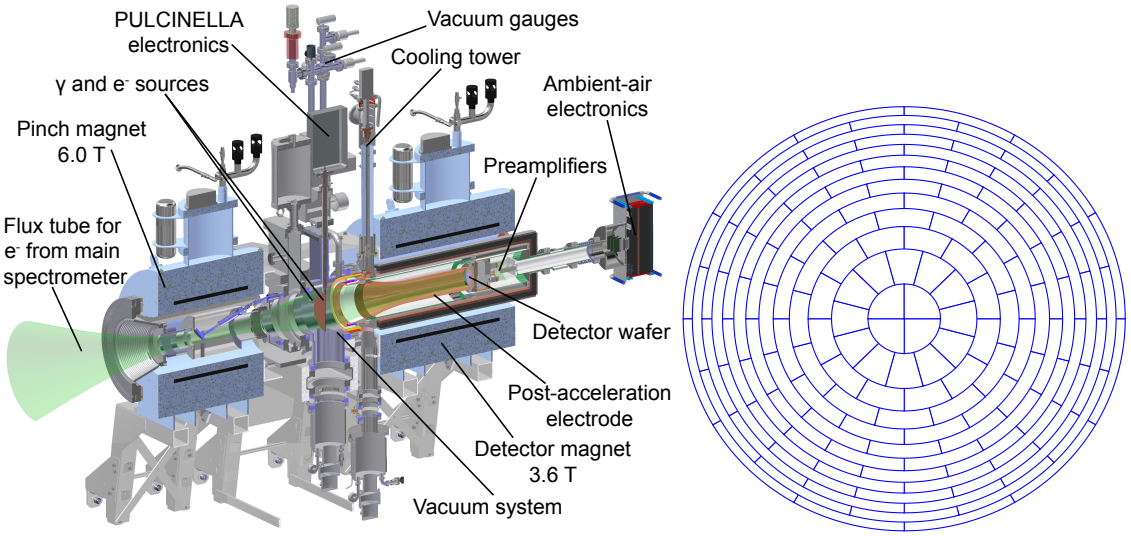

(a) sketch of detector-system

(b) separated pixels of detector

Figure 2.2.: **Detector system** Overview of the detector system and sketch of the detector-wafer showing all 148 separated pixels.

2.3. MAC-E filter

Most of the information on the experimental observable $m^2_{\nu_e}$ is contained in the narrow region just a few eV below the endpoint E_0. As only a fraction 10^{-12} to 10^{-13} of all β-decays reside in a region of 1 eV below E_0, the energy-filtering by the spectrometer must be achieved with a large angular acceptance and a narrow width. The KATRIN spectrometers fulfill these requirements as they rely on the principle of magnetic adiabatic collimation followed by an electrostatic filter, or short: the MAC-E filter.

2.3.1. Principle

The MAC-E-filter principle is based on the idea of adiabatically guiding the β-decay electrons from the source to detector (see figure 2.3) on a cyclotron motion along magnetic field lines [80, 81, 82]. In the spectrometer region in between, the strength of the magnetic field decreases slowly, so that the momentum of electrons perpendicular to the magnetic field lines $p_\perp$ is being transformed into the momentum parallel to the magnetic field lines $p_\parallel$. An electrostatic retarding potential is then used to filter $p_\parallel$. At the position of minimal magnetic field strength $B_{\min}$ the electrostatic retarding potential reaches its maximum absolute value U_0. Transmission is only achieved by those electron which retain a greater-than-zero parallel momentum $p_\parallel$. The transmission condition thus requires for the minimum parallel kinetic energy

$$E_\parallel > qU_0 \tag{2.2}$$

Hence the MAC-E-filter acts as a so called high-pass filter and cyclic variation of U_0 will deliver an integrated spectrum. Furthermore, the adiabatic guiding of electrons along the magnetic field lines implies that β-decay electrons always move in the same part of the flux tube. With the transported magnetic flux being constant, the flux tube becomes larger for weaker magnetic fields. For these reasons, a MAC-E-filter needs to have the largest ($\varnothing = 10$ m) radius in the area of the minimal magnetic field strength ($B_{\min} = 3 \times 10^{-4}$ T).

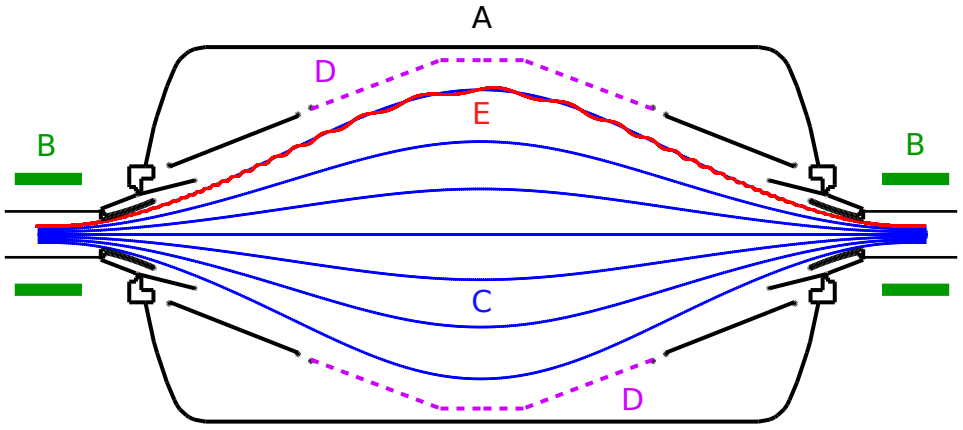

Figure 2.3.: **MAC-E filter principle** Sketch of the KATRIN-pre-spectrometer as an example for the MAC-E filter principle.The spectrometer vessel (A) is put on a negative high potential, whereas the superconducting solenoids (B) provide the guiding magnetic field (C). The inner wire-electrodes (D) are used to fine-tune the electrostatic retarding potential. An exemplary electron trajectory (E) is displayed, showing its cyclotron motion.

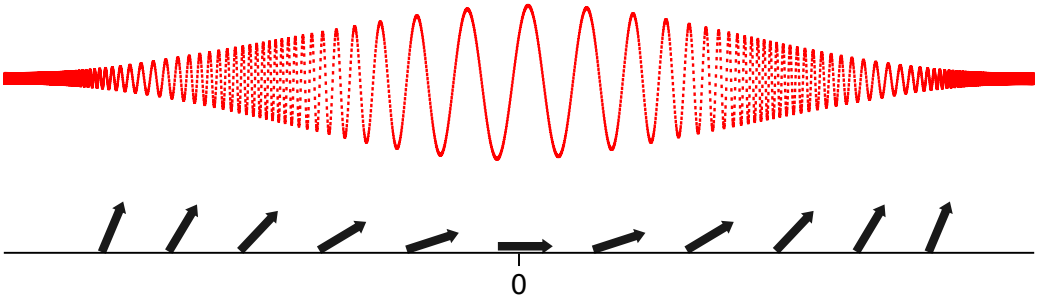

Figure 2.4.: **Cyclotron motion** This figure shows an exaggerated cyclotron motion of an electron transmitted through the spectrometer. The arrows below indicate the momentum of the electron with respect to the magnetic field, neglecting the change of the momentum due to the electrostatic retarding field (or corresponding to the case of $U_0 = 0$ V).

2.3.2. Characteristics

Adiabacity

In a non-relativistic approximation, $E_\perp$ and $E_\parallel$ can be expressed as follows:

$$\begin{aligned} E_{\text{kin}} &= \frac{p^2}{2m} = E_\parallel + E_\perp, \\ E_\parallel &= E_{\text{kin}} \cdot \cos^2\theta, \\ E_\perp &= E_{\text{kin}} \cdot \sin^2\theta. \end{aligned} \tag{2.3}$$

If the magnetic flux enclosed by the gyrating trajectory of the electron is constant, the motion is called adiabatic. Adiabatic electron motion is achieved, if the change of the magnetic field along the cyclotron motion is small. The magnetic field strength and electric potential vary along the electron path, hence the cyclotron radius is resized, which contains a constant flux. With the prerequisite of a conservation of the enclosed magnetic flux, the adiabatic invariant is defined as:

$$\Phi = \int \vec{B}\mathrm{d}\vec{A} = \text{const.} \qquad \Longrightarrow \qquad B r_c^2 = \text{const.} \tag{2.4}$$

Another formulation for adiabatic motion is the conservation of the product of the absolute value of the orbital magnetic moment $|\vec{\mu}|$ and the Lorentz-factor $\gamma = \frac{1}{\sqrt{1-\frac{v^2}{c^2}}}$

$$\gamma\mu = \text{const.} \tag{2.5}$$

In the β-decay of tritium, the maximum occurring Lorentz factor is γ =1.04 for electrons with a kinetic energy $E_{\text{kin}} = E_0$. Consequently, equation (2.5) can be approximated by only considering the magnetic moment:

$$\mu = \frac{E_\perp}{B} = \text{const.} \tag{2.6}$$

Energy resolution

As denoted earlier in 2.3.1, the momentum and the kinetic energy of electrons performing a cyclotron motion along the magnetic field lines can be split into a longitudinal component, parallel to the magnetic field lines ($p_\parallel, E_\parallel$) and a transversal component, perpendicular to the magnetic field lines ($p_\perp, E_\perp$). These components are defined by the polar (pich) angle θ between the momentum of the electron $\vec{p}$ and the magnetic field at its position $\vec{B}$ see figure 2.5.

With these definitions, an expression for the so called "energy resolution ΔE" of a MAC-E filter can be derived. It is assumed that the motion is adiabatic and the electron has its maximum kinetic energy $E_{\text{kin,max}}$ stored in the perpendicular component at the point with maximum magnetic field B_{max} ($\theta = 90°$). Then the remaining energy $\Delta E_\perp$ that is still stored in the perpendicular momentum at the point of minimum magnetic field B_{min} is given by the relation

$$\frac{E_{\text{kin,max}}}{B_{\text{max}}} = \frac{\Delta E_\perp}{B_{\text{min}}}. \tag{2.7}$$

Thus, the remaining transversal energy $\Delta E_\perp$ is not analyzed by the the potential barrier. For the KATRIN main spectrometer the maximum magnetic field strength

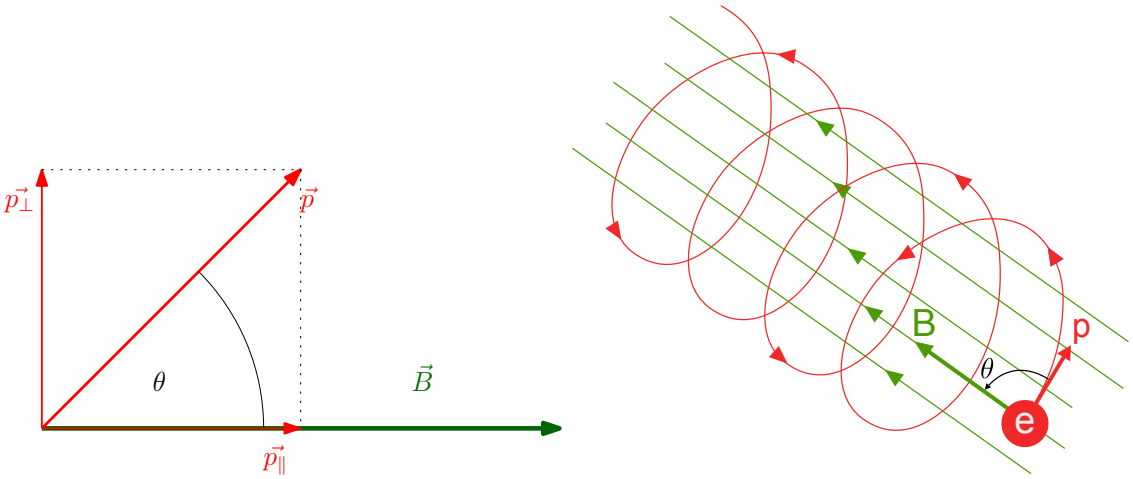

(a) angle θ between $\vec{p}$ and $\vec{B}$-field (b) cyclotron motion

Figure 2.5.: **Definition of the pitch angle** θ of an electron undergoing cyclotron motion in a magnetic field $\vec{B}$.

is $B_{\text{max}} = 6$ T at the pinch magnet, whereas the minimum value $B_{\text{min}} = 3 \times 10^{-4}$ T is present in the middle of the spectrometer, the so called *analyzing plane*. For the tritium endpoint energy at $E_0 = 18.6$ keV we thus obtain an "energy resolution" of:

$$\Delta E_\perp = \frac{B_{\text{min}}}{B_{\text{max}}} E_0 = \frac{3 \times 10^{-4}\ \text{T}}{6\ \text{T}} \cdot 18.6\ \text{keV} = 0.93\ \text{eV}. \tag{2.8}$$

While transversal energy is transformed into longitudinal energy it is important in a MAC-E filter that the electrostatic retardation field to analyze $E_\parallel$ is not applied too early.

Transmission function

One of the most important attributes of a MAC-E filter is the *transmission function* which describes the transmission probability of electrons (usually with isotropic angular distribution) with specific kinetic energy E for a specific retarding potential U_0 (see figure 2.6). Ideally this would be a step function, but as the spectrometer has a finite filter this typically looks like the example shown in figure 2.6.

To determine the transmission function of a MAC-E filter we have to investigate which initial conditions an electron has to fulfill at the entrance of the spectrometer in order to pass the filter. This is mainly defined by the relation between the initial transversal energy $E_{\perp,\text{start}}$ of the electron (which can be expressed in terms of the initial angle θ_{start} with respect to the magnetic field) and the retarding potential U_0 at the position where the electron will pass the filter. Following equation (2.2) only electrons that retain a positive longitudinal energy can pass the spectrometer:

$$\begin{aligned} E_{\parallel,B_{\text{min}}} > 0 \quad \Longrightarrow \quad E_{\parallel,B_{\text{min}}} &= E_{\text{kin},B_{\text{min}}} - E_{\perp,B_{\text{min}}} \\ &= E_{\text{kin},B_{\text{min}}} - E_{\perp,B_{\text{start}}} \frac{B_{\text{min}}}{B_{\text{start}}} \\ &= E_{\text{kin},B_{\text{start}}} - qU_0 - E_{\text{kin},B_{\text{start}}} \sin^2\theta_{\text{start}} \frac{B_{\text{min}}}{B_{\text{start}}} \\ \Longrightarrow \quad qU_0 &> E_{\text{kin},B_{\text{start}}} \left(1 - \sin^2\theta_{\text{start}} \frac{B_{\text{min}}}{B_{\text{start}}}\right). \end{aligned} \tag{2.9}$$

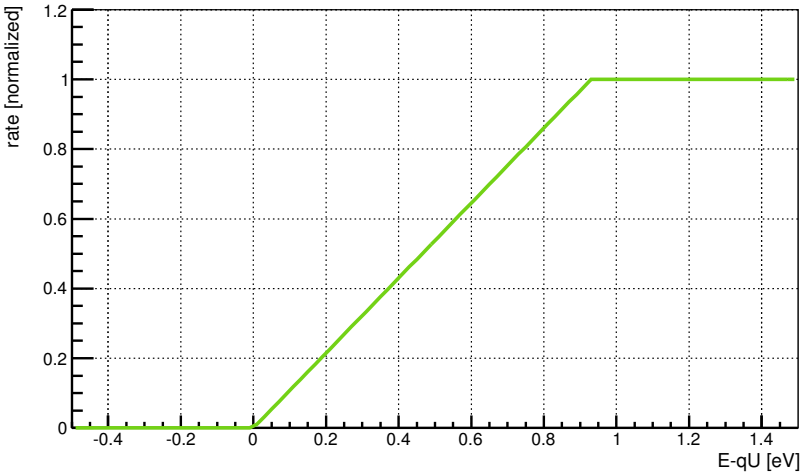

Figure 2.6.: **Theoretical transmission function of a MAC-E filter** for isotropically emitted β-decay electrons at the source.

Here, the indices "min" and "start" describe the conditions in the analyzing plane and at the entrance of the filter, respectively. The maximum accepted angle θ of transmitted electrons is limited to:

$$\Longrightarrow \quad \theta_{\text{start}} \leq \arcsin \sqrt{\frac{E_{\text{kin}} - qU_0}{E_{\text{kin}}} \frac{B_{\text{start}}}{B_{\text{min}}}}. \tag{2.10}$$

Only electrons with an angle smaller than θ_{start} at the entrance of the filter are able to pass the potential barrier. When calculating the fraction of electrons passing the filter and comparing this number to the total number of incoming electrons, the transmission function can be determined.
From equation (2.10) we also obtain the solid angle $\Delta\Omega$. Comparing $\Delta\Omega$ with the maximal solid angle 2π (forward direction) gives the fraction of electrons that are accepted by the filter:

$$\frac{\Delta\Omega}{2\pi} = 1 - \cos\theta. \tag{2.11}$$

Combining these two equations we obtain the transmission function $\mathcal{T}(E_{\text{kin}}, U_0)$ of the MAC-E filter:

$$\mathcal{T}(E_{\text{kin}}, U_0) = \begin{cases} 0 & \text{for} \quad E_{\text{kin}} < qU_0 \\ 1 - \sqrt{1 - \frac{E_{\text{kin}} - qU_0}{E_{\text{kin}}} \frac{B_{\text{start}}}{B_{\text{min}}}} & \text{for} \quad qU_0 \leq E_{\text{kin}} \leq \frac{qU_0}{1 - \frac{B_{\text{min}}}{B_{\text{start}}}} \\ 1 & \text{for} \quad \frac{qU_0}{1 - \frac{B_{\text{min}}}{B_{\text{start}}}} \leq E_{\text{kin}} \end{cases} \tag{2.12}$$

In order to measure the transmission function, it is advantageous to employ monoenergetic electron sources. To do so, either the retarding potential U_0 has to be varied or an additional, variable acceleration potential has to be applied to the electron source. From equation (2.12) it is evident that in the case of a perfectly monoenergetic source the width of the transmission function solely depends on the ratio $\frac{B_{\text{min}}}{B_{\text{start}}}$ of the magnetic fields. The width increases if a source with an energy distribution of finite width is used. In this case the transmission function has to be convoluted with respect to the intrinsic distribution.

For realistic setups, we have to apply specific corrections to the transmission function in order to describe the filter characteristics correctly. In the case of the KATRIN experiment the maximum magnetic field occurs at the pinch magnet, but not within the source. Therefore, some β-decay electrons will be reflected by the magnetic mirror effect before they reach the spectrometer. A particle moving from a region with lower magnetic field strength into a region with higher magnetic field strength is reflected if the polar angle exceeds a critical value:

$$\theta_{\mathrm{crit}} = \arcsin \sqrt{\frac{B_{\mathrm{start}}}{B_{\mathrm{max}}}} \tag{2.13}$$

where B_{start} is the magnetic field strength at the starting point. Taking this effect into account and with B_{S} denoting the magnetic field strength in the source, one obtains a modified transmission function:

$$\mathcal{T}'(E_{\mathrm{kin}}, U_0) = \begin{cases} 0 & \text{for} \quad E_{\mathrm{kin}} < qU_0 \\ \frac{1-\sqrt{1-\frac{E_{\mathrm{kin}}-qU_0}{E_{\mathrm{kin}}}\frac{B_{\mathrm{start}}}{B_{\mathrm{min}}}}}{1-\sqrt{1-\frac{B_{\mathrm{S}}}{B_{\mathrm{max}}}}} & \text{for} \quad qU_0 \leq E_{\mathrm{kin}} \leq qU_0 \frac{B_{\mathrm{max}}}{B_{\mathrm{max}}-B_{\mathrm{min}}} \\ 1 & \text{for} \quad qU_0 \frac{B_{\mathrm{max}}}{B_{\mathrm{max}}-B_{\mathrm{min}}} \leq E_{\mathrm{kin}} \end{cases} \tag{2.14}$$

It is challenging and indeed difficult to reproduce this form of the transmission function exactly, as there are typically additional factors such as like detector and background effects, which modify the shape of this function.

Electric potential sag

It is evident that the electric potential across the analyzing plane of a MAC-E filter can not be homogeneous (see figure 2.7). This effect due to the finite geometry is called *potential sag*. As a result, the transmission condition of a signal β-electron depends on its radial distance to the spectrometer axis. Therefore, the detector of the KATRIN experiment is separated into 148 pixels (see section 2.2.4) in 12 rings plus a central bulls eye to determine the radial position of detected electrons. In the offline analysis, individual transmission functions for each pixel will have to be taken into account.

Magnetic field variation

Analogously, the magnetic field is not homogeneous in the analyzing plane (see figure 2.7), a fact that again leads to a radial dependence of the filter width. In the main spectrometer, this deviation is of the order of about 2%, in the smaller pre-spectrometer this increases to 25% of the value in the center of the analyzing plane.

2.3.3. KATRIN spectrometers

The KATRIN experiment houses three different spectrometers of the MAC-E filter type, namely the pre- and main spectrometer, which are integral parts of the beam line to analyze the tritium β-decay spectrum, and the monitor spectrometer that forms a separate beam line to monitor the stability of the main spectrometer retarding potential.

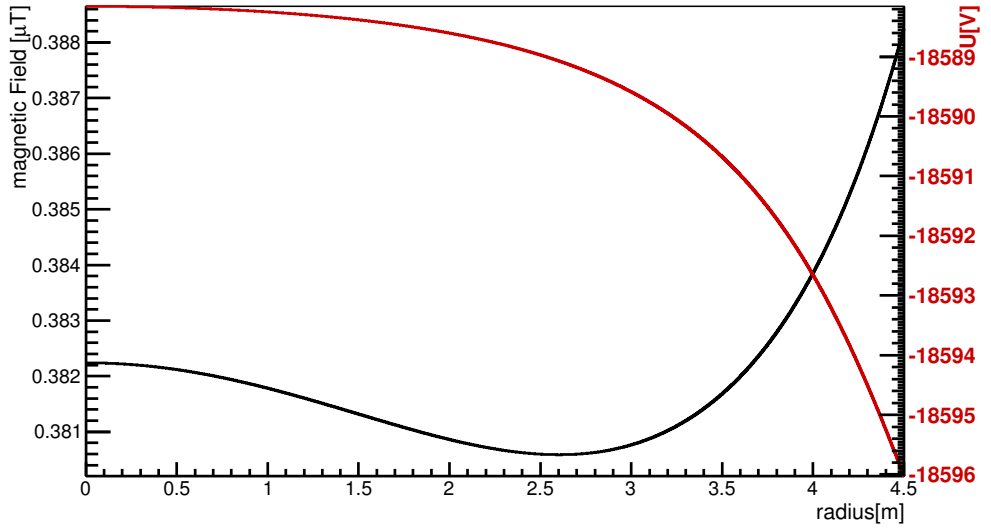

Figure 2.7.: **Radial dependence** of the electrostatic retarding potential (red) and the magnetic field (black) in the analyzing plane of the KATRIN main spectrometer.

Monitor spectrometer

The backwork of a 200 meV/c^2 sensitivity for the neutrino mass requires the retarding potential in the analyzing plane of the main spectrometer to be known with a precision of better than 4 ppm at 18.6 kV. In order to control this, a real-time calibration experiment will run in parallel to the main beam line. Here the so called monitor spectrometer will detect and monitor high-voltage (HV) fluctuations by observing count rate fluctuations of a nuclear standard (^{83m}Kr).
Large parts of the monitor beam line were already utilized in the Mainz Neutrino Mass Experiment [83, 84] to analyze the β-decay spectrum of a condensed tritium film. After the Mainz set-up was transferred to the KATRIN experimental site in late 2009, the set-up has undergone significant hardware upgrade. During long-term operation, the monitor spectrometer will be fed by the retarding potential of the main spectrometer, analysing an electron source from a well-known nuclear standard close to the tritium endpoint E_0 [85, 86, 87].
At the same time the monitor spectrometer, after commissioning, has been used as test facility for test experiments before their application at the main spectrometer. For example, it has been equipped with a muon-dectector system for background studies. This system will be characterized in more detail in chapter 6. A picture of the monitor spectrometer is shown in figure 2.8 and a sketch showing the field and electrode configuration is shown in figure 2.9.

Pre-spectrometer

The pre-spectrometer is an integral part of the KATRIN beam line. Before the on-going system integration it served as a prototype for the main spectrometer by investigating novel vacuum concepts such as the heating- and cooling-system, and by optimizing electromagnetic design features especially with respect to background [88]. Later, during the long-term ν-mass measurements the pre-spectrometer will

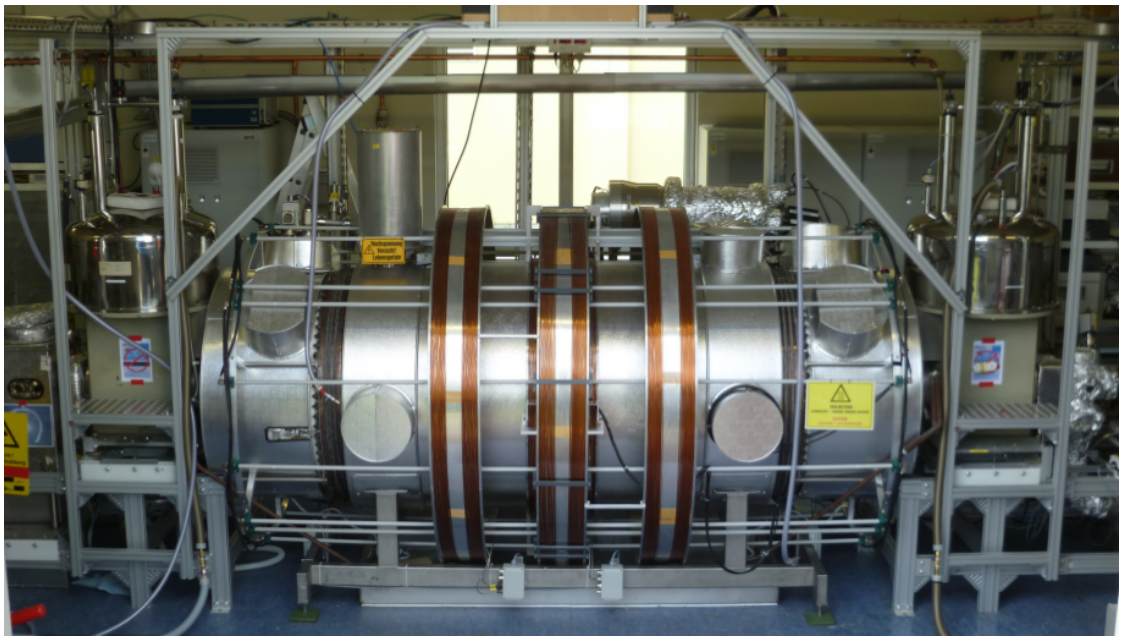

Figure 2.8.: **Photograph of the monitor spectrometer** The vacuum tank is enclosed by the 3 sets of air coils. At each end of the spectrometer a superconducting solenoid is situated. On the top of the picture the bottom paddle of the muon detector system is visible. Picture taken from [85].

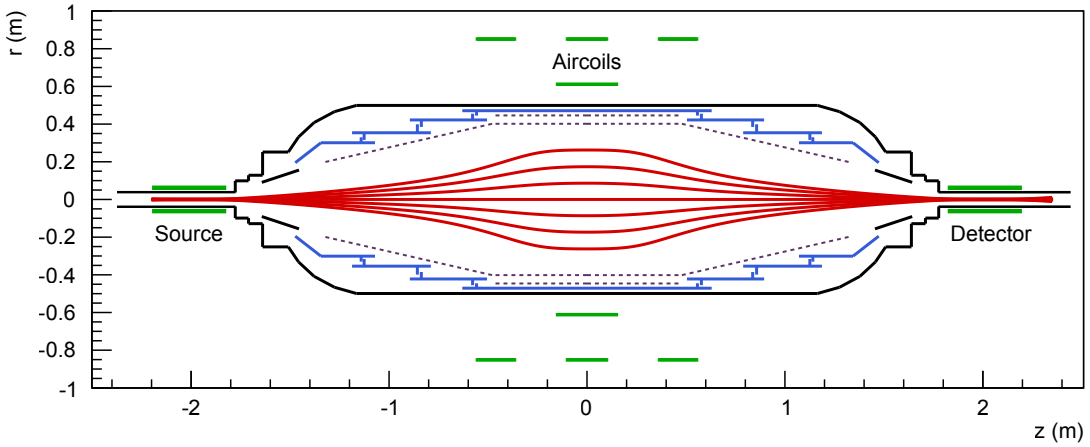

Figure 2.9.: **Sketch of the electromagnetic field setup of the monitor spectrometer** The magnetic flux tube is generated by two superconducting solenoids (Detector,Source) and a set of 3 air coils (green). The electrode system comprises of a solid electrode (blue) and a wire electrode (violet). Note that the wire electrode has two layers in the cylindrical part. Figure taken from [87].

serve as additional MAC-E filter, offering the option to filter out all electrons with energies $E \lesssim E_0 - 300$ eV. This would result in a reduction-factor of 10^6 for β-decay electrons that reach the main spectrometer.
The pre-spectrometer will also serve as an additional pump for the tritium from the source, lowering the ^{3}H-partial-pressure from $1{\times}10^{-20}$ mbar to $1{\times}10^{-22}$ mbar in the main spectrometer. The pre-spectrometer is a 3.4 m long stainless steel vessel with a diameter of 1.7 m which will be operated with a pressure of about 10^{-11} mbar. It achieves an energy resolution of $\Delta E \approx 100$ eV. It arrived at Karlsruhe Institute of Technology (KIT) Campus North (CN) already in late 2003 and since then has been used for extensive tests until 2011.

Main spectrometer

The precision MAC-E filter and measuring tool of the KATRIN experiment is the main spectrometer. It is about 23 m long and has a radius of 5 m, its surface are accounts to 610 m^2 and encloses a volume of about 1240 m^3. To achieve an operating pressure of below 10^{-11} mbar, it is equipped with a rather complex and potent vacuum system. It features six TMPs and over 3000 m of non-evaporable getter (NEG) strips which are located at the 3 large pump-ports. To shield-off single radon atoms emanated from the NEG-strips, a Liquid Nitrogen (LN2)-cooled baffle system was installed between the pump ports and the spectrometer volume (see figure 2.11) [89, 90].
Analogous to the pre-spectrometer, the stainless steel vessel can be put on high voltage. A central design element of the main spectrometer is an inner electrode system of wire electrodes for potential shaping and background reduction. Two superconducting solenoids are positioned at the ends of the spectrometer to provide the magnetic guiding field. Furthermore, the spectrometer is surrounded by a system of cable loops, the so called the *aircoil system* which is responsible for fine-tuning the magnetic field shape and strength and compensation of magnetic stray fields [91, 92]. With a maximum magnetic field of 6 T within the superconducting coils and a minimum magnetic field of about $3{\times}10^{-4}$ T in the analyzing plane the spectrometer features an energy resolution of $\Delta E = 0.93$ eV.

2.3.4. Aircoil system

In the low magnetic field region close to the analyzing plane of the main spectrometer, the Earth magnetic field is not negligible and has a strong influence on the orientation and strength of magnetic field inside the spectrometer. The homogeneous Earth field results in a deformation of the flux tube, which if uncorrected, would lead to the loss of signal electrons. And, at the same time it would imply a strong increase of background electrons that are directly guided from the wall towards the detector (see figure 2.12).
To avoid such a distortion, the KATRIN main spectrometer features a so called air coil system consisting of the Earth Magnetic field Compensation System (EMCS) and the low-field coil system (LFCS) [93]. The EMCS will compensate the vertical and horizontal, non-axisymmetric component of the Earth's magnetic field. It consists of 16 vertical and 10 horizontal cosine coils. To have the flux-tube fit into the main spectrometer in the region close to the analyzing plane, the LFCS contribute an axisymmetric magnetic field enhancing the stray field of the superconducting solenoids at the entrance and exit ports (see figure 2.12). The LFCS consists of

Figure 2.10.: Photograph of the main spectrometer including the air-coil mounting-structure. The author can be seen on the very right.

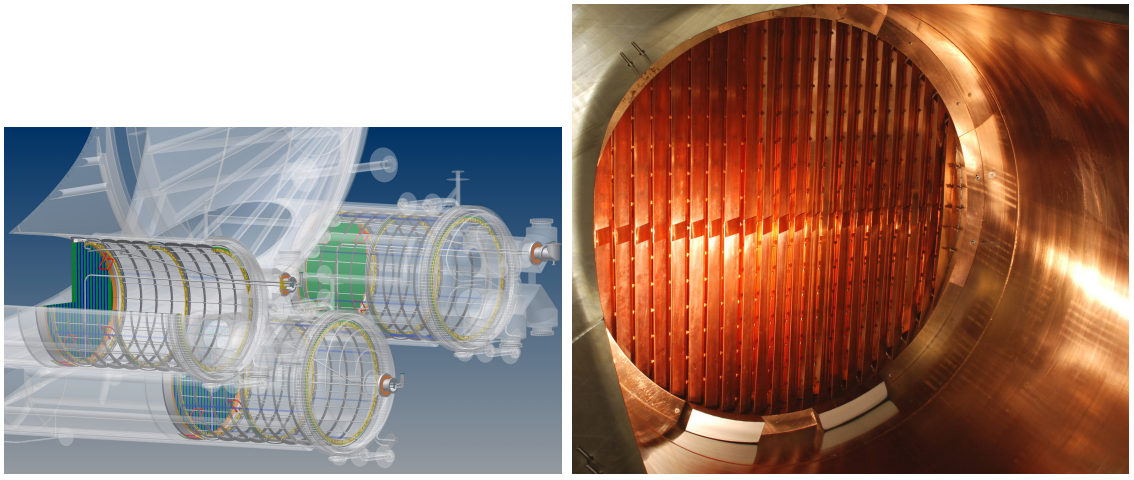

(a) CAD-drawing pump-ports

(b) Photograph of copper-baffle

Figure 2.11.: Spectrometer pump ports and LN2-cooled baffle system.

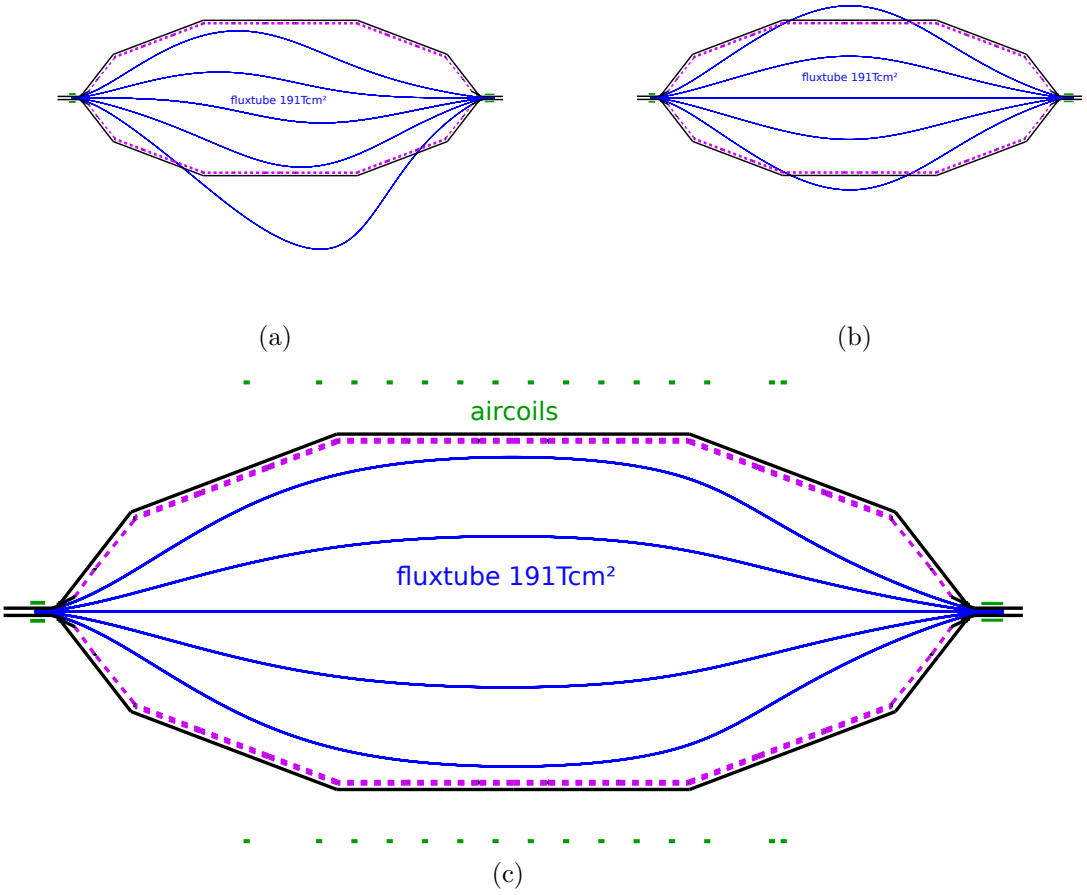

Figure 2.12.: **Magnetic flux-tube with LFCS and EMCS corrections** Flux tube geometry in the main spectrometer without any magnetic filed compensation (a), with the EMCS compensating the Earth magnetic field (b) and in an ideal configuration with EMCS and LFCS powered up (c). It is clearly visible that the flux tube only fits into the spectrometer with the help of the air coils.

15 large coils, whose rotational symmetry axis is the beamtube. They are powered individually with up to 1500 Ampere-turns and thus are a vital tool to shape the desired flux tube into a form that fits into the spectrometer [94].

2.4. SDS-Phase I comissioning measurements

In the second half of 2013 a series of long-term measurements of the first SDS-commissioning phase took place [95]. It was the first test where the KATRIN main spectrometer and the focal plane detector (FPD) were connected and taking data together. It also was the first joint test for many complex systems at the main spectrometer together, as for example the HV supplies, the magnet system, consisting of four superconducting coils and air coils of large diameter, the vacuum system of the main spectrometer and detector, and finally the muon-detector system, which will be described in more detail in chapter 6.
Also, to perform first measurements of the transmission function, an electron-gun was mounted on the source-side of the spectrometer. An illustration of the experimental setup is shown in figure 2.13.

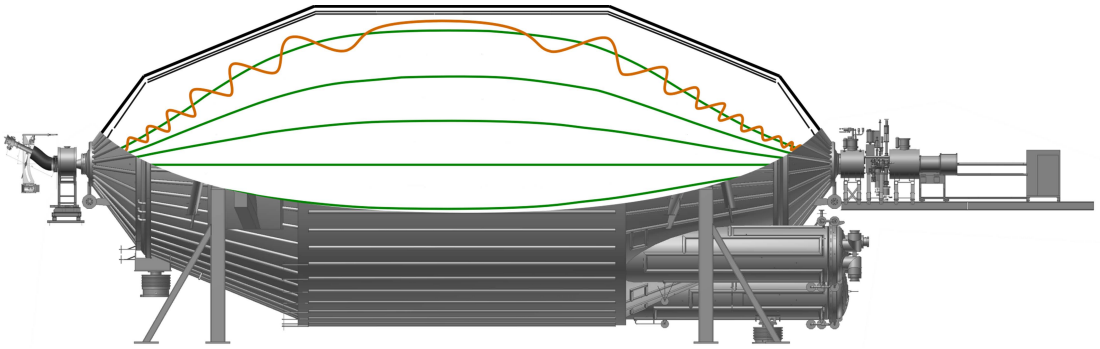

Figure 2.13.: **Experimental overview of the SDS-phase I in the 2nd half of 2013** Overview of the experimental setup during the first phase of the SDS commissioning-measurements. Shown is the KATRIN main spectrometer with an electron gun attached to the left and the FPD-system attached to the right. Inside the spectrometer the magnetic field-lines and a sample electrode trajectory are displayed.

Not all components were fully operational during the SDS-I-phase: The pinch magnet, sitting on the detector-facing part of the main spectrometer was not stable when operating at its full nominal field of 6 T. Instead, it had to be operated at 5 T, a fact which, together with the non-perfect alignment of the detector system with respect to the main spectrometer resulted in a partial shadowing of detector pixels [79]. In figure 2.14 a map of the detector pixels shows that only 118 of the total of 148 pixels were operational during these commissioning measurements.

Furthermore, the wire-electrode was not working under nominal conditions, as its two layers were short-circuited by a thermal softening of at the CuBe-rods of the HV feed system.

The vacuum system was fully operational during the commissioning phase. The LN2-based cooling system of the baffles, to adsorb emanated radon atoms from the NEG-strips was only operational for very short periods of time [89, 90]. As a consequence, it was not possible to suppress radon-induced background by the baffles for the entire measurement period.

All measurements that will be presented later in this thesis in chapter 8 were obtained during the SDS-I-commissioning phase. Due to the narrow time periods allocated to specific measurements not all measurements could be extended to an optimal time period to minimize statistical errors.

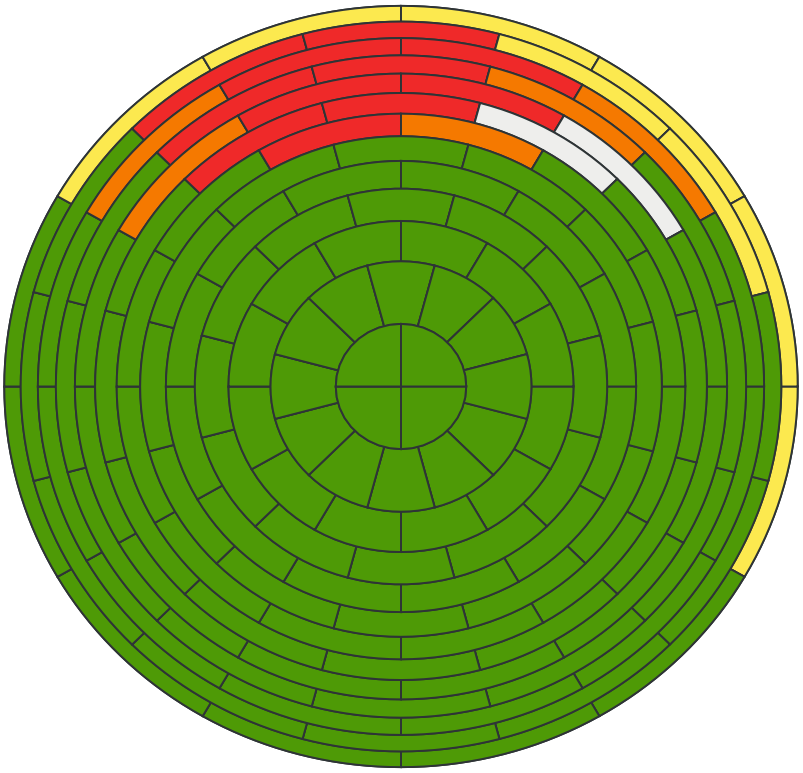

Figure 2.14.: **Status of detector-pixels during SDS-phase I** In this front view of the segmented PIN diode array, green-colored pixels were working without restrictions. The red and orange colored pixels were (partly) shaded by the flapper-valve of the detector system, the yellow ones by the PAE. The two white pixels were short-circuited on the wafer. A total of 118 out of 148 pixels could be used for the measurements (see [79]).

3. Background in the KATRIN spectrometers

In spectrometers of the MAC-E-Filter type several non-negligible mechanisms occur that result in the creation of background electrons. The following chapter will give an overview over these mechanisms and. where possible, we investigate a specific background source by simulations. In addition, rejection mechanisms inherent in MAC-E filters for suppression of background due to secondary electron emission will be discussed. Also, light will be shed on the experimental factors that can allow electrons to circumvent these mechanisms and create background, in particular we study the case of non-axially symmetric magnetic fields.
In general, there are three main sources of background electrons present in electrostatic spectrometers: Ionization of residual gas, either by

(a) signal electrons

(b) or particles stored in Penning traps and the magnetic bottle of the filter,

(c) and secondary electrons emitted from the vessel hull.

It is important to note that the time scales of ionization of residual gas will be significantly enlarged due to the very low operating pressure of 10^{-11} mbar or less inside the spectrometer vessels. This fact has already been tested by predecessor experiments and test measurements at the pre-spectrometer.

3.1. Penning traps

The first measurements at the pre-spectrometer with applied high-voltage and with design magnetic field ($B_{\text{solenoid}} = 4.5$ T) resulted in a strong discharge and electric breakdown with large increases of pressure and leakage current [96]. Simulations of the electric- and magnetic field revealed the presence of so called Penning traps at the entrance and exit regions of the pre-spectrometer to be the cause of this behavior. Penning traps are created in areas with an axial magnetic field for charged particle guiding, and where a minimum in the electrostatic potential occurs. In the case of a flaw in the electrode design, several Penning traps can co-exist within a MAC-E

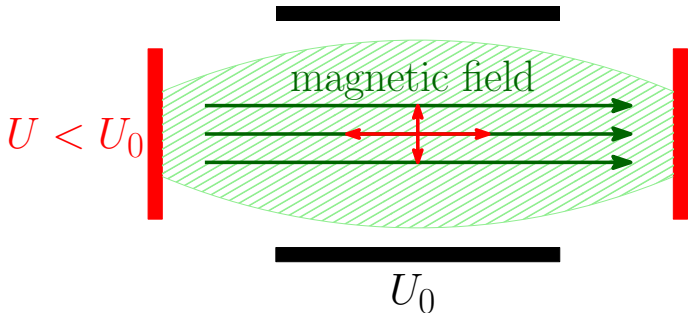

Figure 3.1.: **Sketch showing the principle of a Penning trap** The magnetic field constrains the particle vertically, whereas the potential minimum constrains it horizontally

filter. The particles stored within the traps (see fig. 3.1) can initiate enormous background rates through ionization of residual gas. This is caused by messenger-particles in the form of electrons and photons which are emitted by photo-emission from the traps. To prevent this, one has to be very careful when designing the electrode-geometry and one must pay special attention to avoid formation of even shallow Penning traps.

3.2. Stored electrons

Electrons from a few eV up to several hundreds of keV can be created inside the spectrometer by various background processes. It is rather unlikely that ionizing radiation, such as cosmic ray muons or environmental gamma-rays interact with the residual gas to create an electron in the inner spectrometer volume due to the excellent ultra-high vacuum (UHV) conditions, i. e. the probability for the environmental gamma-rays to create one ionization electron by scattering on residual gas molecules in the course of the entire KATRIN measurement period (1000 days) accounts to $p_{\gamma \to e} = 5 \times 10^{-3}$ [97].
The dominant mechanism to create stored electrons are nuclear decays of radioactive atoms or molecules like tritium or radon inside the active part of the flux tube [98, 99, 100]. Another possibility are secondary electrons from the wall that can reach the sensitive volume, they can change their trajectories by scattering on residual gas molecules or other (non-adiabatic) interactions. If the electrons are created in the low-magnetic field regions of the spectrometer volume, they usually are stored due to the magnetic mirror effect.
Figure 3.2 shows that the electrons over a vast dynamic range mainly cool down via subsequent inelastic scattering off residual gas molecules, thereby creating further *tertiary* electrons. For example, an electron with 100 eV kinetic energy has a close to maximum total inelastic scattering cross-section of about $\sigma \approx 10^{-16}$ cm^2 [101]. With the particle density in the main spectrometer corresponding to $n = 2.4 \times 10^{11}$ 1/m^3, the mean free path of an electron is:

$$\lambda = \frac{1}{\sigma \cdot n} \approx 4 \times 10^8 \text{m} \tag{3.1}$$

Based on an average energy-loss per scattering of 37 eV, a 100 eV electron is able to travel a total path-length of about 1×10^9 m, creating about three tertiary electrons

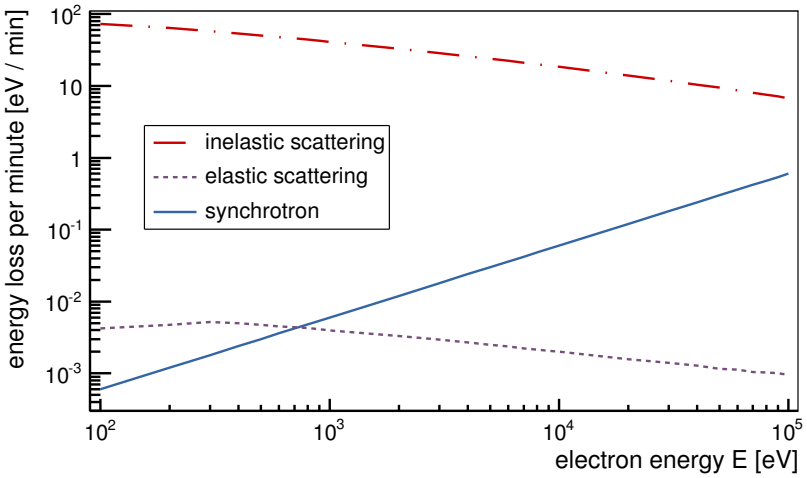

Figure 3.2.: **Kassiopeia-simulation of cooling-processes of stored electrons** Here, the energy-loss per unit time as a function of the start energy of electrons stored in the main spectrometer is shown. The predominant process via which the electrons cool down is inelastic scattering on residual gas (dash-dotted line). Cooling by elastic scattering on these molecules (dashed line) and cooling by emission of synchrotron radiation (solid line) only play a minor role.

and being stored over a time period of several minutes. Depending on their energies, storage times for those electrons may reach up to several hours [102] for nominal pressure (10^{-11} mbar) in the main spectrometer. In this time they can create thousands of tertiary electrons. These tertiaries are created with an isotropic distribution of angles. Hence, they are not necessarily stored but can reach the detector over short time scales if they are created in the sensitive flux tube volume. It is these short-trapped tertiary electrons which reach the detector quickly that make stored electrons a quite serious source of background in the KATRIN experiment.

3.3. Secondary electrons from the wall

Environmental radioactivity and in particular the rather large flux of cosmic rays are of great concern for a low-background experiment like KATRIN, as they can induce a large number of background processes. Due to the large spectrometer size and the required tritium infrastructure, it is impossible to operate the experiment in an underground laboratory. Thus the spectrometer is exposed to the normal sea-level flux of cosmic muons and environmental radiation.
Cosmic rays, environmental radiation, intrinsic radioactivity and field-emission can lead to the emission of secondary electrons from the vessel hull and inner electrodes. The field emission can be significantly reduced by careful electrode design. However, as mentioned above, a MAC-E filter has inherent shielding against external radiation. This radiation, consisting of cosmic ray muons and environmental rays, can interact in the stainless steel vessel and thereby induce secondary electron emission. When upscaling measurements from predecessor experiments [103], we expect an emission rate of up to 10^5 secondary electrons per second which originate from the vessel-wall

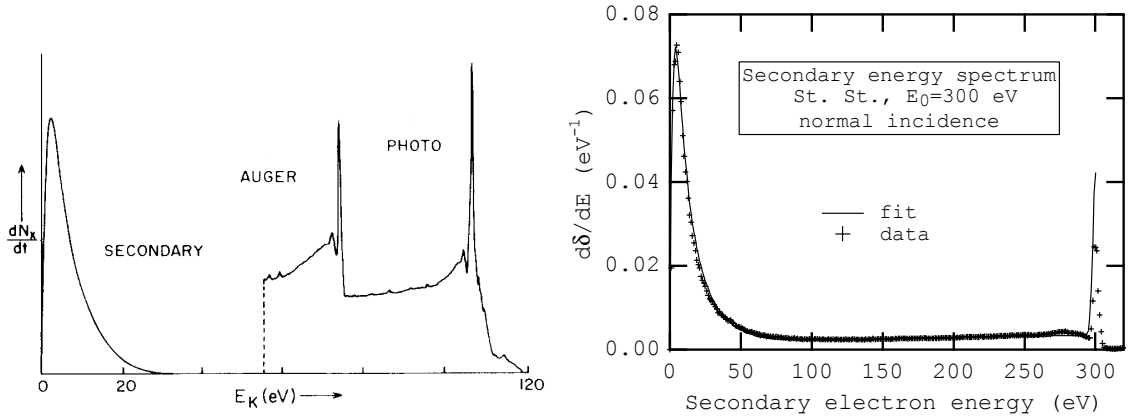

(a) typical photoemission-spectrum (b) spectrum of true secondaries for stainl. steel

Figure 3.3.: **Energy spectra of secondary electrons** In (a) a typical electron emission-spectrum for X-ray photons is shown (picture taken from [104]). The spectrum comprises of the low-energetic true secondary electrons and the fast secondary electrons that are created through Auger- and Photo-effect and have energies close to the photon energy. In (b) the true secondary electron spectrum for stainless steel is shown for incident mono-energetic electron irradiation ($E_e = 300$ eV). The true secondaries peak at $E_{\mathrm{sec}} = 1.22$ eV and mostly have energies below 20 eV. Figure taken from [108]

and electrodes. This calls for highly efficient shielding mechanisms of 10^7 or better to achieve a background rate of < 0.01 cps.

3.3.1. Creation mechanism

When ionizing radiation interacts in the stainless steel vessel of the main spectrometer, in general two classes of secondary electrons are emitted: High-energy, so-called *fast* secondary electrons, with energies up to the keV scale, and low-energy, so called *slow* or *true* secondary electrons with energies below 50 eV [104].
The fast secondary electrons result from Auger- and Photo-emission of electrons in a small boundary layer of 10^{-8} to 10^{-9} m distance to the inner surface. These electrons have enough energy to leave the solid state. The slow secondaries originate from interactions deeper in the material, and accordingly, they undergo numerous scattering processes in the solid. If they can reach the above-mentioned boundary layer, the slow secondary electrons can overcome the potential barrier at the surface and emerge into the vacuum [105]. In general, the emission rate of slow secondary electrons is much larger than the rate of fast secondaries, although the exact ratio depends on the thickness of the target material and the energy of the incident radiation [106, 107]. A typical photoemission spectrum and an example true secondary electron energy-spectrum for stainless steel are shown in figure 3.3.
The angular distribution of the true secondary electrons is independent of the direction of the primary particle, as they undergo a large number of scattering processes in the solid and thereby loose their initial direction information. It is also independent of the electron energy and can be described by the angular distribution function $f(\theta) = \cos\theta$, where θ denotes the angle perpendicular to the emitting surface. For

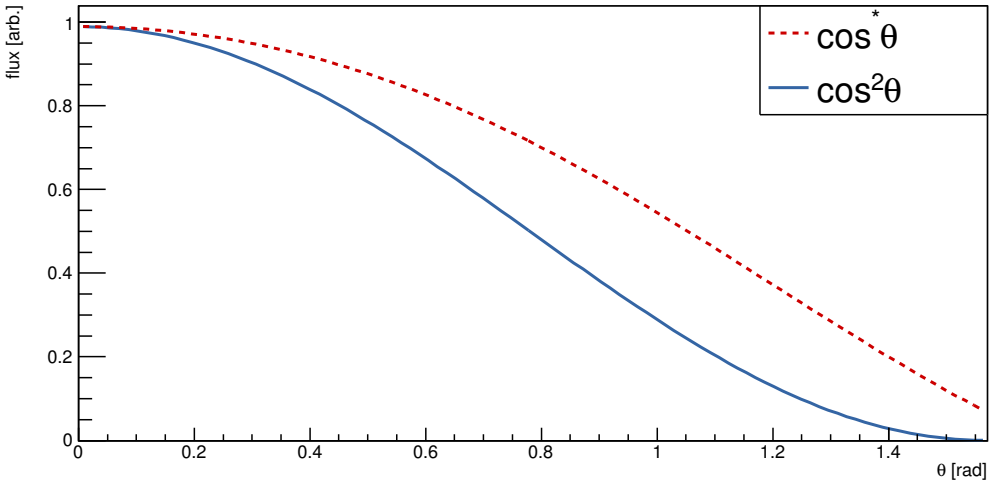

Figure 3.4.: **Angular distribution of cosmic muon flux** Comparison of the muon flux following a $\cos^2\theta$- (solid line) and a $\cos^*\theta$-angular-distribution (dashed line). The $\cos^*\theta$-distribution includes muons of very high energies (E > 4 GeV) that account for a higher relative flux from flat angles where the muon has to travel a long way through the atmosphere.

fast secondaries this is not the case, their emission-direction is highly correlated to the direction of the primary particle [109].

3.3.2. Cosmic rays

The flux of cosmic ray muons on sea level, where the main spectrometer is located, accounts to 189 muons/m^2/s. Muons, as minimum ionizing particles, are able to pass the stainless steel vessel and thin electrodes thereby loosing energy corresponding to the Bethe-Bloch-formula [110]. The energy-loss causes ionization and excitation in the metal, leading to secondary electron emission at the inner wall surfaces and electrodes of the spectrometers. If a muon loses enough energy in the solid, it can be stopped and, in case it is a μ^-, it can be captured into an atomic orbit by an iron nucleus. The capture is followed by fast de-excitation, as the muon's orbital levels decrease. This is accompanied by emission of Auger electrons and X-rays from the atom [111, 112]. If such a capture with subsequent significant emission of electrons and X-rays happens close enough to the inner surface it will result in an event where multiple electrons reach the detector over a relatively short timespan.
It can roughly be estimated that less that 10^{-2} of the overall muon flux or about 10^2 muons per second are stopped in the material of the main spectrometer [113]. In this case, only an estimated number of about 1 muon per second is stopped in a layer close enough to the inner surface to cause secondary electron emission.
The angular distribution of cosmic ray muons at sea level can roughly be described by a $\cos^2\theta$-distribution for energies smaller than $E_\mu = 4$ GeV [114]. A more comprehensive description is given by the so called $\cos^*\theta$ distribution, which is expected to be valid up to very high muon energies [115]. A comparison of both angular distributions is displayed in figure 3.4.

Based on this information about the muon flux, a dedicated MC simulation includ-

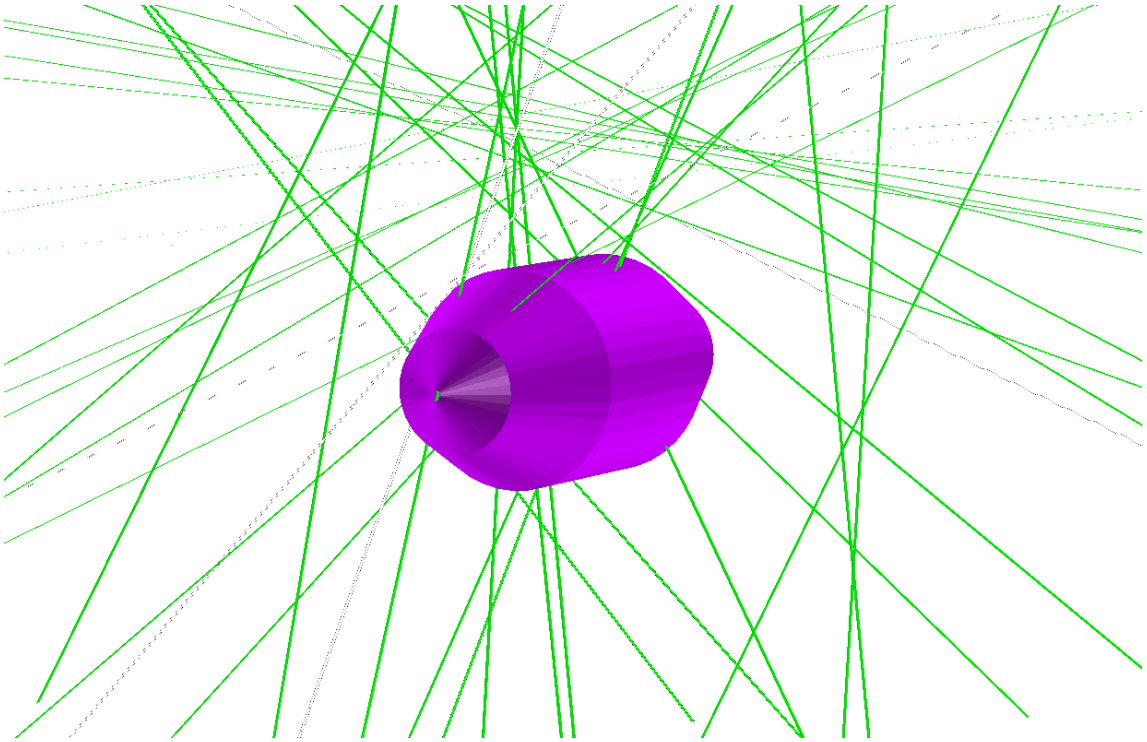

Figure 3.5.: **Geometry simulation for muon-flux** MC simulation of muons hitting the KATRIN main spectrometer. Muons were created in a 100 m×100 m plane 20 m above the spectrometer with random angles following $\cos^2\theta$- and $\cos^*\theta$-angular-distributions.

ing the detailed spectrometer geometry was performed. In doing so, random muon paths were created and at first a fast check was performed to ensure that only muon tracks were considered which pass through the main spectrometer.
The simulation has yielded a muon flux of 37.4×10^3 muons per second hitting the main spectrometer for $\cos^2\theta$-angular-distribution and 39.4×10^3 muons per second assuming a $\cos^*\theta$-angular-distribution. A non-stopping muon passes the surface twice, by entering and leaving the volume. The main spectrometer has a surface of about 610 m^2, translating to a muon flux of 122 to 129 muons / m^2 / s on the surface. Figure 3.5 shows a picture of the utilized geometry together with 40 muon tracks of a simulation run.

The literature gives reliable values for the overall flux and the energy distribution of cosmic muons. On the other hand, we are not interested in muons but in the energy spectrum of muon-induced fast secondary electrons. Former works [116] have obtained the energy spectrum of fast secondary electrons with the help of GEANT4 [117, 118] and PENELOPE [119, 120]. These simulations have included the following interactions: ionization, photo-emission, bremsstrahlung, elastic scattering, pair-production and -annihilation. Their results are summed up in the energy spectrum shown in figure 3.6.

The simulated spectrum shows that secondary electrons are created by muon-vessel interactions with energies ranging from 1 keV up to several MeV which follow a power law $\frac{dN}{dE} \sim E^{-2.1}$. With a total production rate of μ-induced fast secondary electrons of about 2000 events per second a large background rate can be expected.

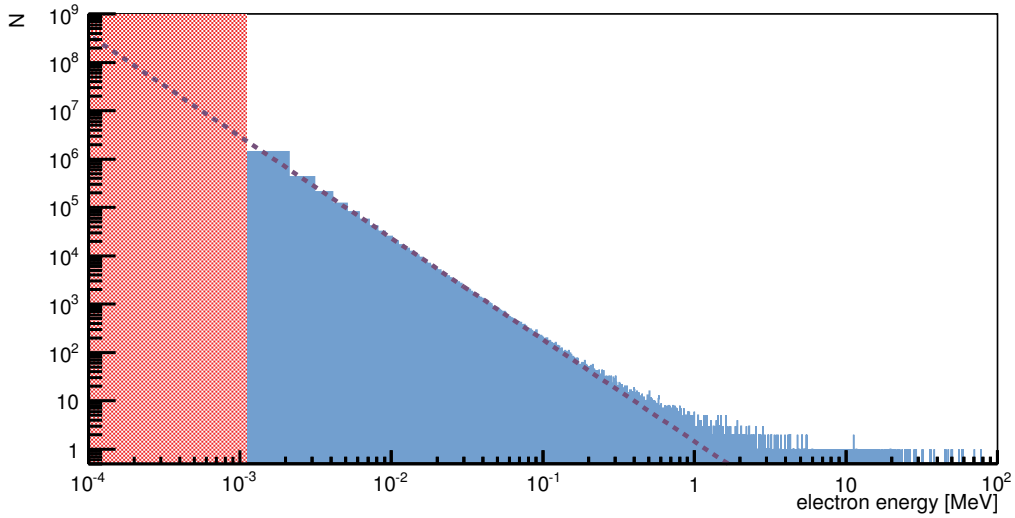

Figure 3.6.: **Fast secondary spectrum from a Geant4-simulation** The simulated electron energy spectrum for muon interactions in the stainless steel of the tank-hull does not include electron energies below 1.1 keV (shaded area) as GEANT4 and PENELOPE can not provide reliable data for such low energies. For a large part of the spectrum, secondary electron energies follow a power law $\mathrm{d}N/\mathrm{d}E \sim E^{-2.1}$ (dashed line).

However, the before-mentioned simulation-packages are not able to give results on the production rates and energies for electrons with energies below 1 keV. Moreover, the rather rare but high-multiplicity muon-capture processes were not included in these simulations.
Measurements at the Mainz experiment [121] have shown that low-energy true secondary electrons make up for the vast majority of the secondary emission, explaining the factor of 50 between the expectation and the simulated production rate.
At the University of Münster a dedicated experiment was conducted to investigate the muon-induced secondary electron emission. The experiment resulted in an average secondary-electron yield of 0.98×10^{-2} electrons per incident muon [122]. At present, it is not clear if this experimental result includes the true secondary emission present in the spectrometers of MAC-E-filter type.

3.3.3. Environmental and intrinsic radiation

The so called environmental radiation consists of gamma-rays that originate almost exclusively from the decays of ^{40}K and ^{208}Tl from the Thorium-decay-chain and ^{214}Bi from the Uranium-decay-chain [123]. Accordingly, these gammas do not exhibit a discrete spectrum, as they interact mainly via Compton-scattering on their way through the surrounding matter. The gamma flux strongly depends on the local geometry and the materials used for construction.
Previous measurements with an X-ray-gun at the Mainz experiment and the KATRIN pre-spectrometer showed experimentally that gamma-rays can in fact generate secondary electrons on the inner surfaces of electrodes and that these can enter the spectrometer volume [121, 124]. To reduce gamma radiation near the experiment, the spectrometer hall was built with low-activity concrete. Also, due to stability requirements, the wall thickness of the stainless steel of the main spectrometer vessel

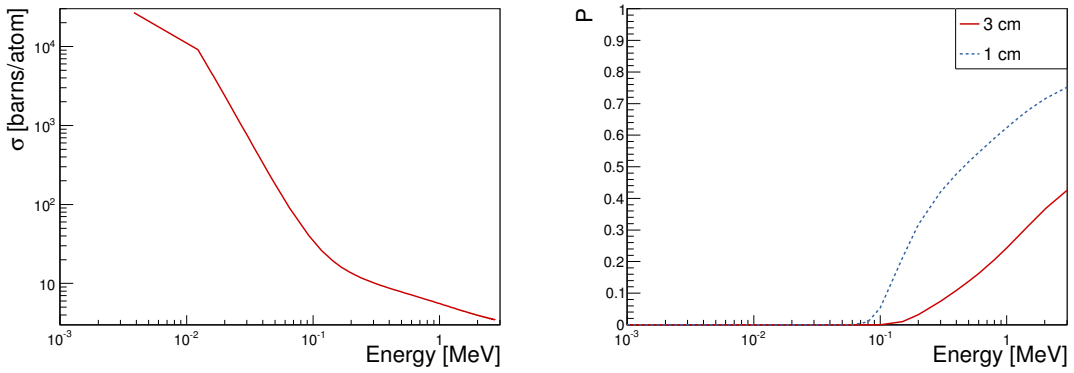

(a) Total attenuation

(b) Probability for penetration

Figure 3.7.: **Attenuation of γ-rays by vessel hull** Total photon attenuation in ^{26}Fe including coherent scattering (a) and probability of a photon penetrating the vessel hull as a function of energy (b). In (b) a comparison of wall-thicknesses of the pre-spectrometer (1 cm, dashed line) with the main spectrometer (3 cm, solid line) is displayed. Cross-sections are taken from [97].

was raised to 3 cm, compared to 1 cm wall thickness in the Mainz experiment and pre-spectrometer. When comparing the flux of environmental gammas, this has to be taken into account.
Accordingly, only photons with enough energy to penetrate the 3 cm stainless steel of the vessel wall are considered, as these are able to create secondary electrons on the inside. The probability P that a photon can penetrate a wall of thickness x cm without being absorbed in it is given by:

$$P(x, E) = \mathrm{e}^{-\sigma(E)\cdot\rho_{\mathrm{atom}}\cdot x} \quad \text{with} \quad \rho_{\mathrm{atom}} = \frac{N_{\mathrm{A}}\cdot\rho_{\mathrm{Fe}}}{M} \tag{3.2}$$

where $\sigma(E)$ describes the energy-dependent absorption cross section of the photon in steel in cm^2/atom, N_{A} denotes the Avogadro-constant, ρ_{Fe} the density of steel in g/cm^3 and M the molar mass in g/mol. Figure 3.7(a) shows the absorption cross section as function of the energy, whereas figure 3.7(b) shows a comparison between the energy-dependent penetration probability for a 1 cm and a 3 cm steel absorber.

With the help of figure 3.7(b) it also becomes obvious that measurements with an existing X-ray-gun at the main spectrometer have to be redesigned in view of the photon energies of around 140 keV. Their probability to penetrate the spectrometer-tank is below 2% which would call for long measurement times, if compared to the pre-spectrometer.

In April 2008 an NaJ-detector was used to perform gamma spectroscopy of the environmental activity inside the KATRIN hall, as well as to measure the absolute gamma-activity in the region from 1-3000 keV [125]. The resulting energy spectrum of photons is shown in figure 3.8. The plot also shows the calculated flux suppression of the γ-spectrum through a 3 cm steel absorber. The spectrometer vessel reduces X-ray-photons ($E_\gamma < 150$ keV) by approximately 98% and the total gamma-radiation by 92.5%.

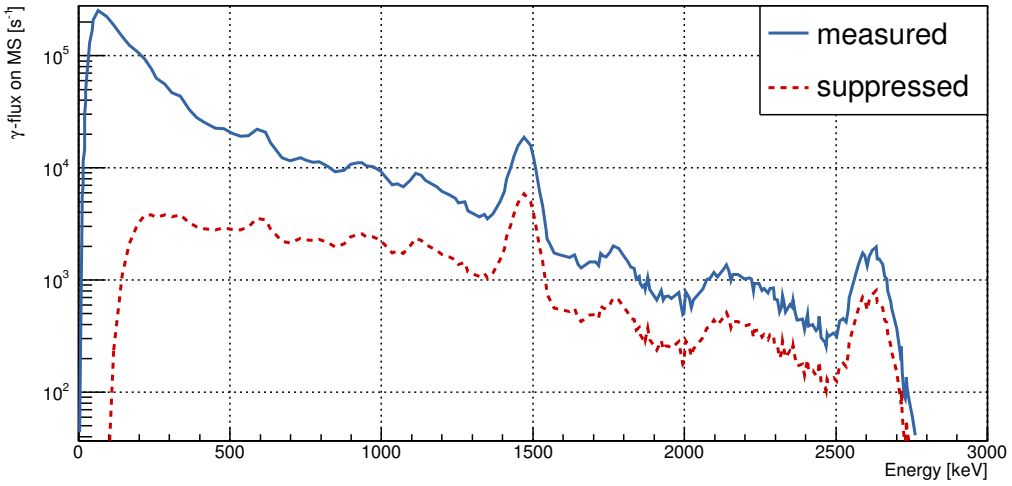

Figure 3.8.: **Environmental radiation-spectrum KATRIN hall** Measured spectrum of environmental gamma radiation in the KATRIN hall (solid line) and spectrum of dampened radiation inside the main spectrometer (dashed line). Some γ-peaks of ^{40}K (1.46 MeV), ^{208}Tl (2.61 MeV) and ^{214}Bi (0.58 MeV) are clearly visible in both spectra. Energies taken from [126].

The average measured rate in the KATRIN hall accounts to (5172±1509) γ s^{-1}m^{-2}, at the former pre-spectrometer site to (4483±1432) γ s^{-1}m^{-2} and at the Mainz experimental site to (7648±860) γ s^{-1}m^{-2}. Accordingly, the background radiation in the KATRIN hall is lower as at the Mainz experimental site due to the low-activity concrete that was used there. The former pre-spectrometer experimental site at building 245 at KIT CN had the lowest background radiation, probably due to the architecture of the building, as two of the four walls are almost exclusively made of glass instead of concrete.
The measurement at the KATRIN hall, together with the calculations for a 3 cm thick stainless steel vessel result to (389±114) γ s^{-1}m^{-2} that are able to create secondary electrons on the inner surface of the main spectrometer. This number appears to be high, but the secondary electron yield of photons in this energy range is typically around 10^{-4} to 10^{-3} e/γ [127]. Taking into account these yields, an estimated secondary electron rate of (2.6±0.8) cps/m^2, with electron energies partly around the primary-γ-energies and partly below 50 eV, arises from this environmental radiation. When integrating this rate over the whole surface of the main spectrometer of about 610 m^2, this results in (1.6×10^3) electrons s^{-1}. This result hast to be compared to the expected overall secondary emission rate of 10^5 electrons s^{-1}-From this ratio of rates it is evident that the environmental radiation is only of minor concern for background stemming from secondary electrons in the spectrometers.

The rate of secondary electrons due to the intrinsic radioactivity of the stainless steel vessel is even lower. A measurement done at the Low Background Facility of the Lawrence Berkeley National Laboratory (LBNL) [128] resulted into an activity of $<$ 32 mBq / kg for the steel of the main spectrometer vessel. Assuming that

only radioactive decays in the inner layer of 1 mm can produce γ-rays that in turn could create electrons at the surface, the total active mass of relevance amounts to about 6.7 t of stainless steel. With the above-mentioned typical electron yields of the photons this would correspond to an upper limit for the additional secondary electron rate of about 3.5×10^{-4} cps/m^2. This rate is several orders of magnitude smaller than the above-given rates expected from environmental radiation and can therefore be neglected.

3.3.4. Field Emission

In experiments where components are elevated to a negative high-voltage under vacuum-conditions, while other parts remain grounded, field electron emission from parts such as electrodes is a pretty common occurrence. In this case, electron emission from metal electrodes occurs in regions with high electric field: If a high potential is applied to an electrode, the work function E_w that electrons in the bulk need to leave the crystal is lowered. Simultaneously, the potential barrier at the surface of the crystal is narrowed, because of the strong negative potential outside. The narrow potential barrier now allows for tunneling of electrons from the crystal to the outside. The principle is sketched in figure 3.9.

The theory of field emission was first described in the works by R.H. Fowler and L.W. Nordheim in 1928 [129]. Their work formulated the now so called *Fowler-Nordheim*-equation that describes the local emission current density J (in A/m^2) as a function of the unreduced work function ϕ and electric field F:

$$J = \frac{a}{\phi}F^2 \exp\left(\frac{-b\phi^{3/2}}{F}\right) \tag{3.3}$$

where a and b denote "constants" with a very weak dependency on the material [130, 131].

$$a \approx 1.541434 \times 10^{-6}\ \text{AeV/V}^2 \text{ and } b \approx 6.830890 \times 10^{9}\text{V}\cdot\text{eV}^{-3/2}/\text{m}. \tag{3.4}$$

However, F-N theory does give a description of the precise energy spectrum of the emitted electrons directly after tunneling, i. e. before acceleration by the potential. Typically, field electron emission occurs punctual on rough edges, spikes and unpolished electrode surfaces, often as spark discharge. It thereby depends on the surface condition of the emitter. This is expressed by the surface enhancement factor $\beta = F/\mathcal{E}$ that describes the field amplification due to the surface conditions [130].
Usually field emission discharges are used to "weld" the surface smooth high current densities are produced that heat up the emitting materials. This procedure is also known as *conditioning* [132] and is intentionally used for surface treating in preparation of high-voltage measurements.
In the main spectrometer the rather complicated wire electrode system with its sometimes rather sharp-edged holding structure is likely to be a source of field electron emission in case of strong electrostatic field between the electrodes and the vessel wall. It is planned to condition the solid electrodes and optimize the potential settings to avoid field electron emission during measurement operation.

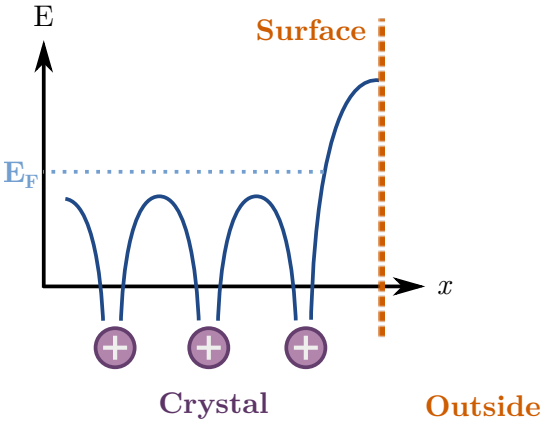

(a) electron energy inside the crystal

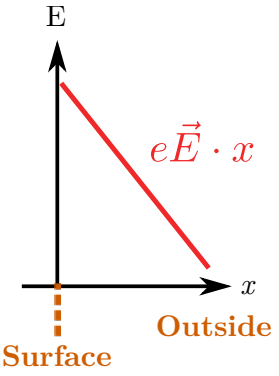

(b) electron energy outside the crystal

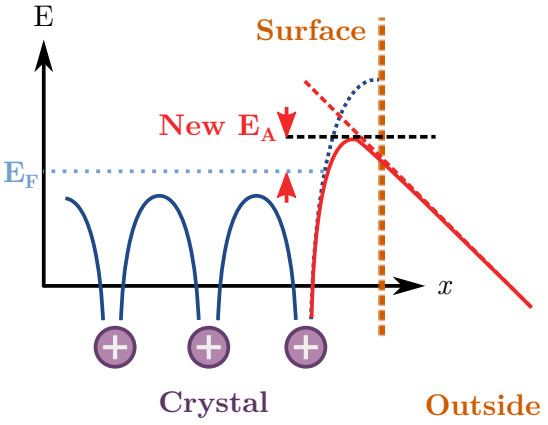

(c) new workfunction

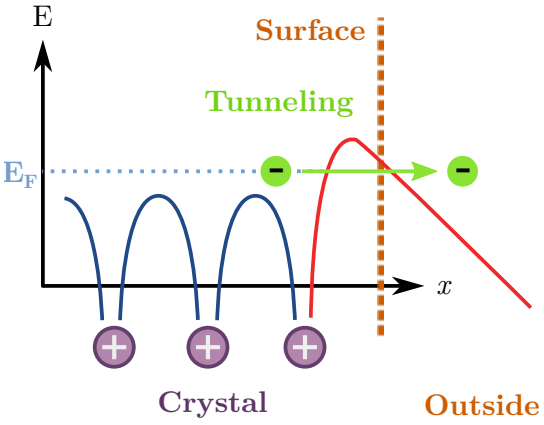

(d) electron tunnelling

Figure 3.9.: **Model for of field emission** Sketch of electron energies inside of the bulk (a) potential of the atomic grid, (b) field outside of the crystal due to the electric potential applied to the crystal. The applied potential leads to a new, lowered workfunction (c). Bound electrons in the crystal can overcome this lowered workfunction by tunnelling (d) and are thereby released into the vacuum.

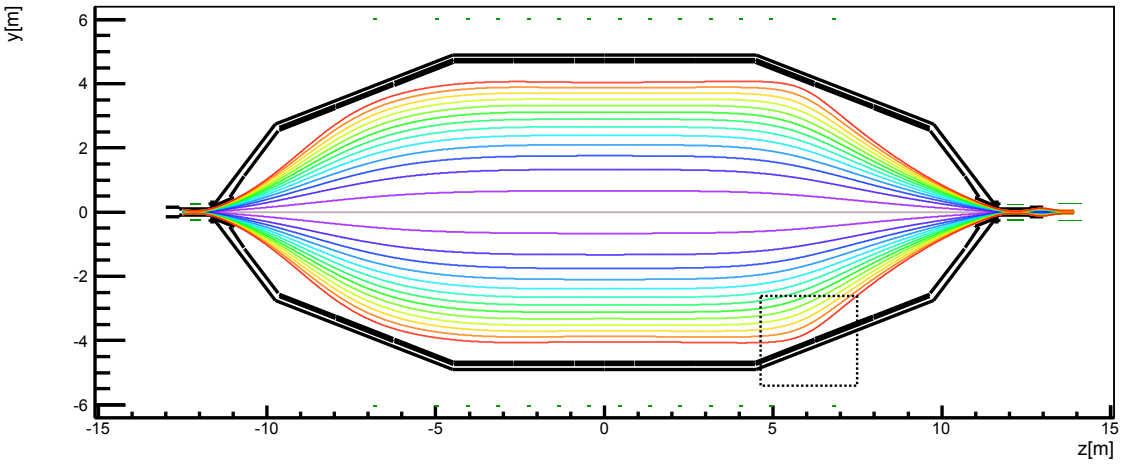

(a) field lines in a 3.8 G setup

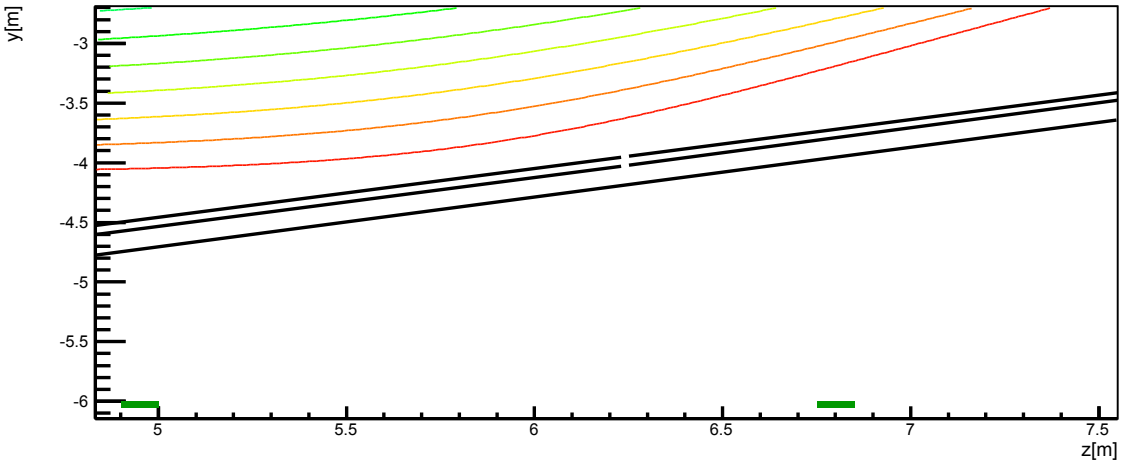

(b) zoom in of the dashed box in (a)

Figure 3.10.: **The sensitive magnetic flux tube at 3.8 G in the center** The outermost line (red) of the sensitive magnetic flux tube encloses 210 T cm^2 in the 3.8 G configuration (a). This is the reference configuration for the measurements with the largest extent of the magnetic flux tube. In (b) a the picture is zoomed in on the section with the smallest distance between the flux tube and the electrodes.

3.4. Magnetic shielding

In the introduction of this chapter it was briefly mentioned that a spectrometer of the MAC-E-Filter-type has inherent background suppression features. The first and most effective one is the so called *magnetic shielding*.
In the spectrometer setup, the guiding magnetic field is produced by two superconducting solenoids with co-axial coild that create an axially symmetric field. In the main spectrometer this field changes from 4.5 T at the entrance to 3.8×10^{-4} T in the central analyzing plane to 6 T at the exit of the spectrometer. The magnetic field lines do not connect the detector to any part of the wall and the transported flux tube of 191 T cm^2 keeps a minimum distance to it of about 30 cm, see fig. 3.10.

Typically, true secondary electrons from the wall have rather low energies. They experience a Lorentz-force and thus follow a cyclotron motion along the magnetic

field lines. Only in areas, where the magnetic field lines are not exactly parallel to the electrodes surface emitted electrons are not instantly reflected back by the Lorentz-force to the surface. In case they have a small enough angle relative to the surface and are also emitted with low energies, they can form relatively long trajectories which can be described in three categories:

- Electrons are guided along the magnetic field lines well outside the sensitive flux tube. In this case they do not hit the detector, because they are not able to advance into the sensitive volume of the magnetic flux tube. Also, their cyclotron radius in the region of the detector is very small ($\leq$1 mm), confining them to non-sensitive parts there.

- If electrons pass regions with a high electric combined with a low magnetic field they can gain a considerable amount of kinetic energy within a few cyclotron periods. This leads to a non-adiabatic motion of the electron which can result in a change of its cyclotron angle and corresponding shifts of the gyration center [133].

- Electrons that start in a relatively low magnetic field in the central region of the spectrometer can be reflected both, at the entrance and exit of the spectrometer due to the magnetic mirror effect. As result, they will be stored inside the spectrometer for at least one magnetron period. Figure 3.14 shows such a stored electron, here with a higher starting energy.

Fast secondary electrons can be injected into the inner volume with energies up to several keV. In the low magnetic fields close to the analyzing plane of the main spectrometer these high energies imply cyclotron radii of several meters. When they start from the wall they will be immediately reflected back due to the magnetic field. But, as a consequence of their large cyclotron radii, they are able to fly through a considerable part of the sensitive flux tube in the cause of their motion from the wall and back. The process is illustrated in figure 3.11. One can easily estimate the probability for such an electron to actually ionize residual gas molecules inside the sensitive flux tube. If we assume a maximum cyclotron radius of 4 m this would correspond to an electron of about 400 keV and an estimated distance of Δx =12 m which the electron could travel inside the sensitive flux tube when starting on the wall of the cylindrical spectrometer section. The ionization cross-section drops for larger electron energies and at 400 keV electron energy it amounts to $\sigma \approx 10^{-15}$ cm^2. Correspondingly, when making use of equation 3.2 one can calculate a scattering probability of:

$$P(x, E) = 1 - \mathrm{e}^{\sigma(E)\cdot\Delta x\cdot n} = 2.9 \times 10^{-8} \tag{3.5}$$

with $n(= 2.4 \times 10^{11}$ 1/m^3, at $p = 10^{-11}$ mbar) is the particle density inside the main spectrometer. This estimated probability is tiny and illustrates that this process will make only a very small contribution to the overall background in the experiment. Still, we can use the total fast secondary electron rate of $2{\times}10^3$ per second obtained by the GEANT4 simulations and combine them with the result to get an expected ionization rate of $5.8{\times}10^{-5}$ per second in the experiment. Compared to the other background mechanisms this will be a very minor contribution, but underlines the requirement of maintaining excellent UHV conditions.

In order to estimate the magnetic shielding factor for the main spectrometer, individual measurements of the background rate originating from electrode surfaces

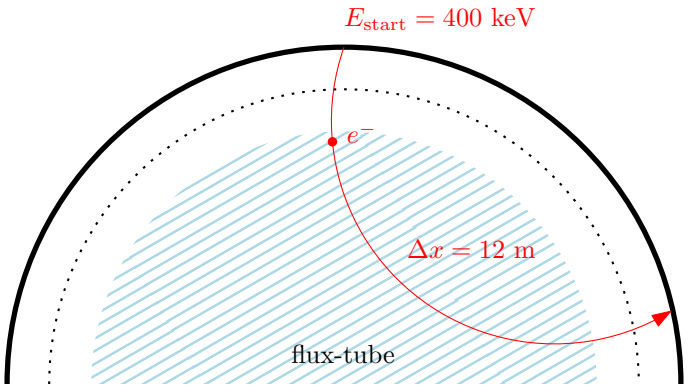

Figure 3.11.: **Electron traversing the flux tube** Sketch of a high-energy electron emitted from the wall flying through parts of the sensitive magnetic flux tube (shaded area).

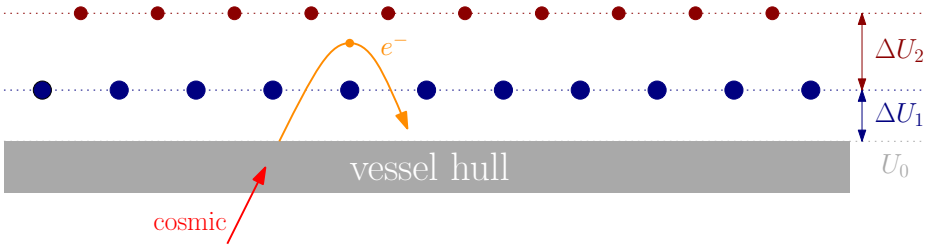

Figure 3.12.: Working principle of the wire electrodes.

at the pre-spectrometer and Mainz spectrometer [134, 135] can be scaled up. The magnetic shielding factor is then expected to be of the order of $s_{\text{mag}} = 10^5$, if similar levels of axial symmetry can be obtained for the very large spectrometer dimensions.

3.5. Electric shielding

The main spectrometer is equipped with a further shielding mechanism to obtain the benchmark of a background rate of 0.01 cps. It features an inner wire-electrode system, consisting of 148 modules which mostly feature two wire layers, an outer one where the wires are at a distance of 15 cm from the vessel-surface, and an inner one where the wires are at a distance of 22 cm from the vessel hull. The previous layers can be elevated to different potential relative to each other and/or the tank, with a maximum up to 1000 V. In order to shield electrons, they have to be set on a more negative potential than the tank. For example, if they are elevated on a potential 100 V more negative than the tank, they should electrostatically reflect all electrons from the walls with energies smaller than 100 eV. A sketch of the underlying working principle is shown in figure 3.12. In normal operation the inner wire layer will be set onto a more negative potential than the outer, to shield the wire-holding-structure, which are on the potential of the outer layer. The electric shielding factor is expected to be of the order $s_{\text{el}} = 10^2$, so that a combined shielding factor of $s_{\text{com}} = 10^7$ can be achieved.

3.6. Penetration of shielding and background production mechanism

A part of the secondary electrons from the walls will have enough energy to overcome the potential barrier of the wire electrode. In addition, secondary electrons will be created on the surface of the wires and their holding structure as well. These electrons can be stored in the volume of the spectrometer by the magnetic mirror. If their energies are high enough, they will traverse the sensitive volume of the spectrometer due to the large cyclotron radii. In case of a perfectly axial symmetric magnetic- and electric-field, the electrons would be stored in a stable condition, usually outside of the volume of the sensitive flux tube. However there is a two step process, that allows these electrons to create background in the inner parts of the flux tube:

1. The presence of non-axially symmetric fields leads to a radial drift of the stored electrons inwards into the sensitive volume of the magnetic flux tube.
2. Once trapped inside the sensitive volume they can start to produce tertiary electrons via ionization and inelastic scattering on residual gas molecules. These electrons are stored only for very short periods of time and reach the detector very fast.

The mechanism to allow stored electrons to create background at the detector was already discussed in section 3.2. In the following, the origin of the radial drift that enables electrons to overcome the magnetic shielding will be described in more detail.

In case of non-axially symmetric electric and magnetic fields in a MAC-E filter, a magnetron drift $\vec{v}_d$ of stored electrons is initiated. It is driven by two components [136, 137] :

$$\vec{v}_d = \vec{v}_{\vec{\mathcal{E}}\times\vec{B}} + \vec{v}_{\nabla B} \tag{3.6}$$

where the first component is called the $\vec{\mathcal{E}} \times \vec{B}$ **drift**:

$$\vec{v}_{\vec{\mathcal{E}}\times\vec{B}} = \frac{\vec{\mathcal{E}} \times \vec{B}}{|\vec{B}|^2} \tag{3.7}$$

and the second component is called the **gradient**$\vec{B}$ **drift**:

$$\vec{v}_{\nabla B} = \frac{(E_\perp + 2E_\parallel)}{|\vec{B}|^3} \left(\nabla B \times \vec{B}\right) \tag{3.8}$$

which, for positively charged particles, actually would have the opposite sign. $\vec{\mathcal{E}}$ and $\vec{B}$ denote the electric and magnetic field in SI-units, and $E_\perp$ and $E_\parallel$ are the transversal and longitudinal components of the kinectic energy of the electron in eV.

The radial electric and magnetic field components arise from field variations due to the finite spectrometer size in the lateral plane. In principle, they are not harmful for the experiment as they only lead to an azimuthal drift of the electron. This drift is called *magnetron motion*, and a visualization can be seen in figure 3.14.

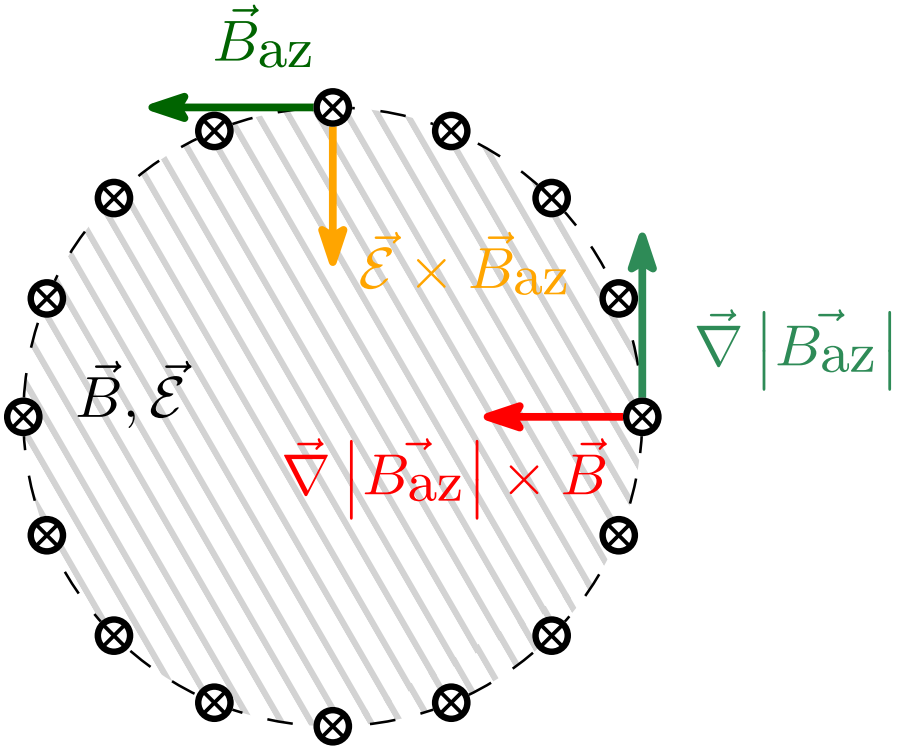

Figure 3.13.: **Principle of adiabatic drifts** Here, the two inward drift processes of an $\vec{\mathcal{E}} \times \vec{B}$ drift (yellow) and a gradient $\vec{B}$ drift (red) are shown. Azimuthal $\vec{B}$ and $\vec{\nabla} \left| \vec{B} \right|$ components cause a radial drift.

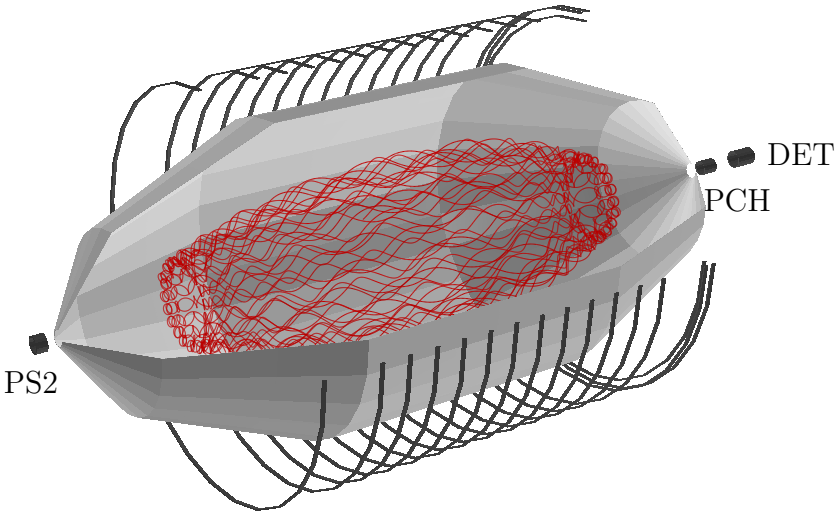

Figure 3.14.: **Path of a stored electron** KASSIOPEIA trajectory simulation of a stored electron inside the main spectrometer. The superconducting solenoids (PS2, PCH, DET) and air coils are shown in black.

In the case of axially symmetric fields $\vec{\mathcal{E}}$, $\vec{B}$ and ∇B are parallel within the zr-meridian plane. As a result, the magnetron drift of the electron is perpendicular to this plane and implies no axial or radial component, i. e. only an azimuthal one. As a result the electron does not change its mean radial position r in the course of a magnetron drift. Therefore, the electron will circle with constant radius in the lateral plane and not be able to enter the sensitive flux tube.
In case there is, however, a non-axially symmetric magnetic field contribution, this distortion would manifest in a non-zero azimuthal field $\vec{B}_{\mathrm{az}}$ as well as a field gradient component ∇B_{az}. This more dangerous field configuration then would lead to radial drifts of the electrons, as shown in figure 3.13.
Theory requests that an electron describes a closed path after one magnetron period. This is of major importance: if an electron does not advance into the sensitive flux tube within one single magnetron drift, it will remain stored outside the sensitive volume. It is thus of central importance that drift processes are slow with respect to magnetron motion.

3.6.1. Non-axially symmetric magnetic field contributions

There is a variety of sources which can cause non-axially symmetric magnetic fields. All these distortions have to be taken into account for the KATRIN-experiment. The most significant ones are the Earth's magnetic field, stray fields from magnetic materials within construction materials of the walls of the building and magnetic stray fields caused by the small non-axial symmetry of coils, and finally due to off-axis and tilted superconducting solenoids. The Earth's magnetic field is very homogeneous over the spectrometer size and can, to a very high degree, easily be compensated with a cosine coil system. This task is performed by the EMCS [93]. The other distorting components are less homogeneous and have to be modeled locally when investigating the axial symmetry of the magnetic field within the spectrometers.

Deformed LFCS

The aluminum mounting structure on which the field-generating air-coil system Al-cables are installed exhibits some deviations from a perfect circular shape due to mechanical tolerances. These deviations have been measured by a theodolite to a precision of ± 0.5 cm at 36 points on the mounting rings.

Figure 3.15 exemplarily shows the measured deviations at one ring. To take this into account, a polynomial function was fitted to the data. Then, the ring was discretized into line segments with a radius as obtained from the polynomial fit. Afterwards, the resulting discrete model was compared with actual field measurements to validate it [138].

Magnetic materials in the building's walls

Magnetized steel bars within the walls and the floor of the KATRIN hall can cause a relatively strong, inhomogeneous magnetic field. These magnetic stray fields within the KATRIN hall have been measured [138]. On the basis of these measurements a model for the distribution of magnetic dipole bars has been created [139] to estimate

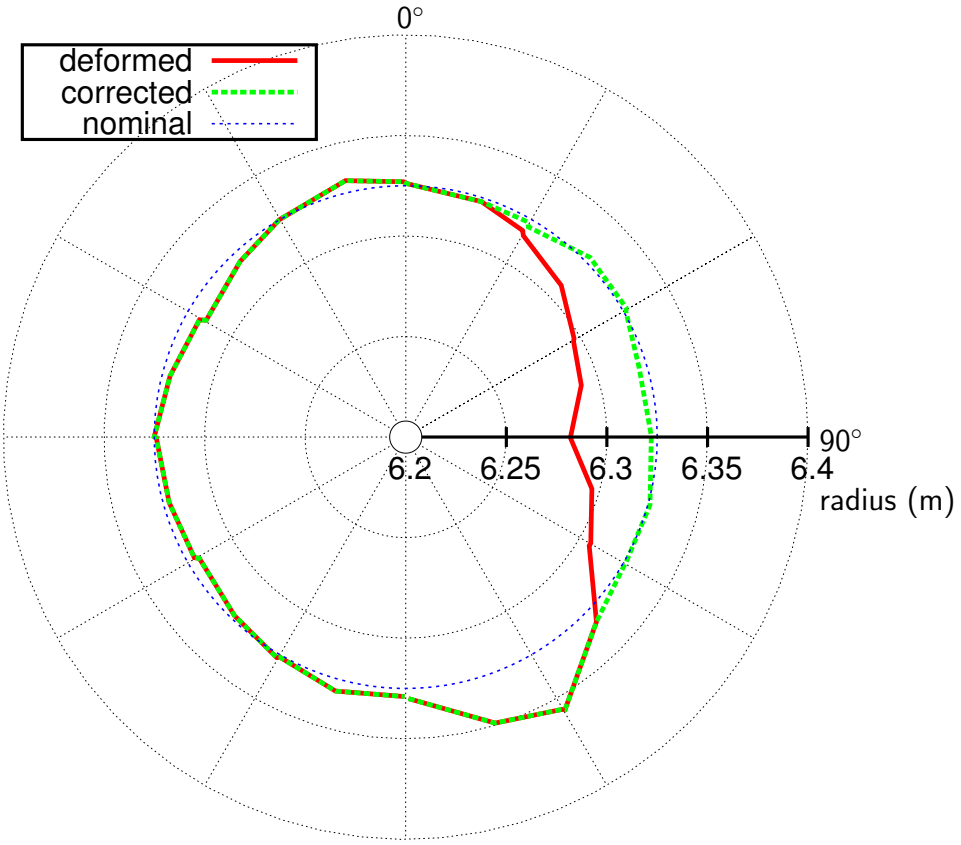

Figure 3.15.: **Deformation of LFCS-ring 5** Measured radial variation at 36 points as a function of the azimuth angle of LFCS mounting ring 5. The radius along the holding structure was measured before (red) and after (green) radial correction. The thin dashed line denotes the nominal radius of r =6.325 m.

the influence of structural materials. At this point it is important to note that this model was also validated by additional measurements, to ensure a true-to-reality description of the magnetic materials.

In figure 3.16 some field calculations of the magnetic stray field in the analyzing plane are shown. AT a radial distance of 4.5 m from the center, at azimuthal angles of 12° and 320°, the deviation is of the order of 1.5 µT. This localized effect is mostly caused by magnetic materials. For a low-energy electron of 1 eV this distortion will result in drift velocities of around 10 m/s. As these drift velocities are rather small, compared to the average time that eV-scale electrons spend within the main spectrometer ($\approx 10^{-6}$ s), only low energy electrons that are stored within the spectrometer can drift into the sensitive flux tube.

Off-axis and misaligned solenoids

In chapter 2 it was outlined, that the KATRIN beamline features bends at the DPS (20°) and the CPS (15°) to avoid any beaming effects in the tritium molecular flow from the source to the spectrometer section. These bends imply that there are several superconducting solenoids in an off the axis position relative to the main beamline, so that electrons are guided through this chicane. The azimuthal magnetic field that they introduce into the flux tube however accounts to less than 0.01 µT in the analyzing plane of the spectrometer, which is of no concern here.
Finally, the alignment of the solenoids of the pinch- and detector magnet to the beamline can only be done with finite precision. Therefore, small misalignments of the solenoids will remain and cause non-axially symmetric magnetic field components. In this case the azimuthal magnetic field due to these misalignments was estimated to be 0.3 µT in the analyzing plane [140]. As shown in figure 3.16(c) the inhomogeneities that are introduced by magnetic materials in the building and deformed air-coils are 2 to 4 orders of magnitude larger than the ones introduced by misalignment and off-axis positions of solenoids. Hence the latter two effects are less important for the magnetic shielding ,however, they are nonetheless considered in magnetic-field computations.

3.6.2. Non-axially symmetric electric field contributions

Similar to non-axially symmetric magnetic field contributions, non-axially symmetric electric fields can cause electrons to drift into the sensitive volume of the flux tube, see fig. 3.13. Of special concern here are symmetry-breaking electric dipole fields. This effect can manifest due to the HV design of the main spectrometer where the wire electrodes are arranged in two halves (east-west, see fig. 3.17) and weight-induced distortions, resulting in a "flattening" of the spectrometer tank. So in case of problems with the calibration, or, as a result of vessel deformations, electric dipoles are likely to be formed inside the experiment.

3.6.3. Particle tracks influenced by non-axisymmetric magnetic fields

The non-axisymmetric magnetic field contributions manifest in the spectrometer were implemented in the simulation framework Kassiopeia using methods described in chapter 4.1.1. This makes it possible to add them to standard axisymmetric magnetic field contributions of the experiment and calculate particle

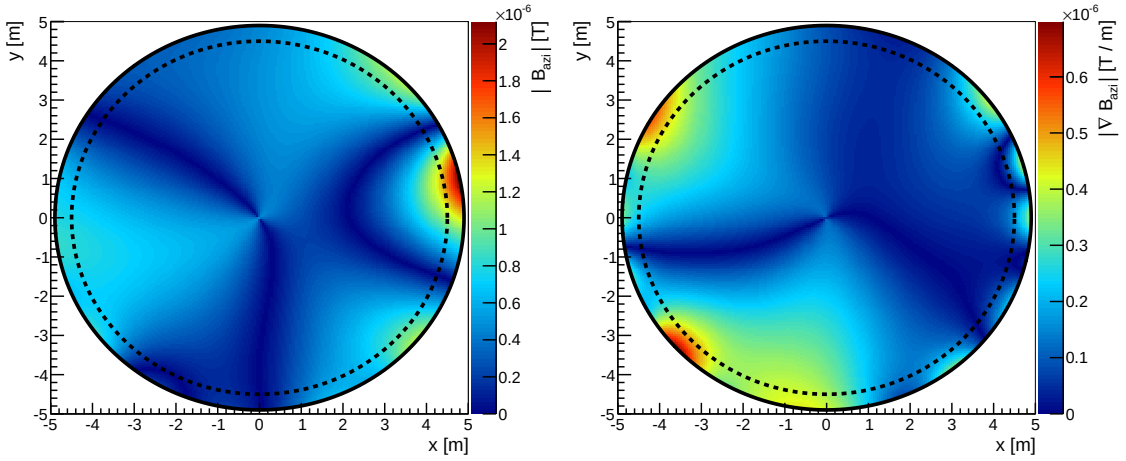

(a) $\vec{B}_{\mathrm{azi}}$ (b) ∇B_{azi}

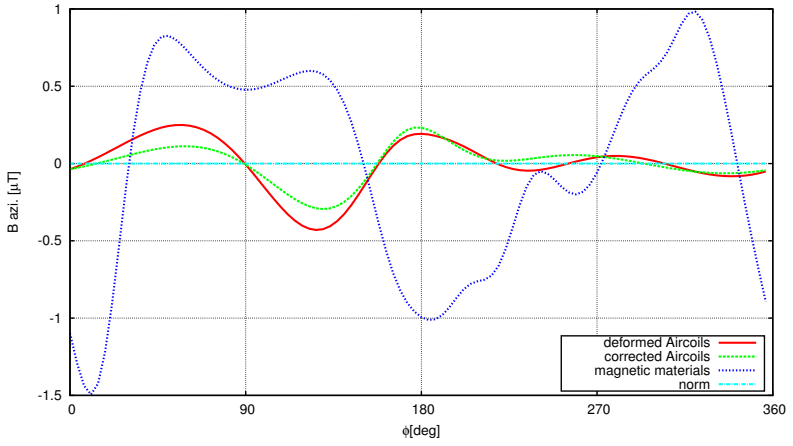

(c) $\vec{B}_{\mathrm{azi}}$

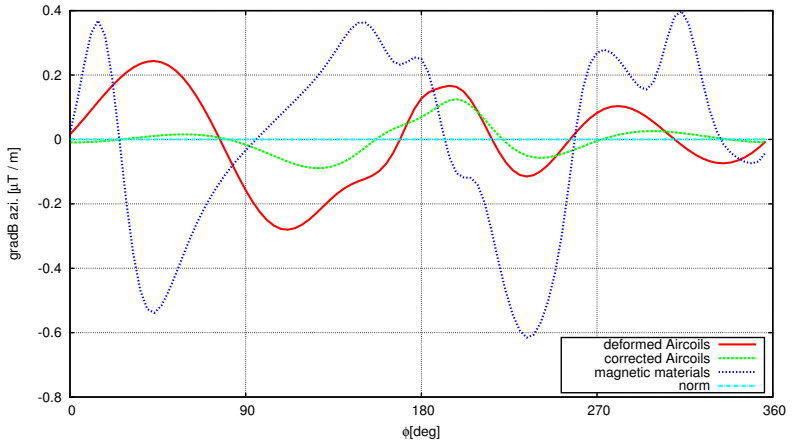

(d) ∇B_{azi}

Figure 3.16.: **Magnetic field distortions** Azimuthal magnetic field components in the analyzing plane of the main spectrometer. In (a) and (b) the black circle denotes the vessel hull and the dashed circle line denotes a radius of 4.5 m where the curves in (c) and (d) were calculated.

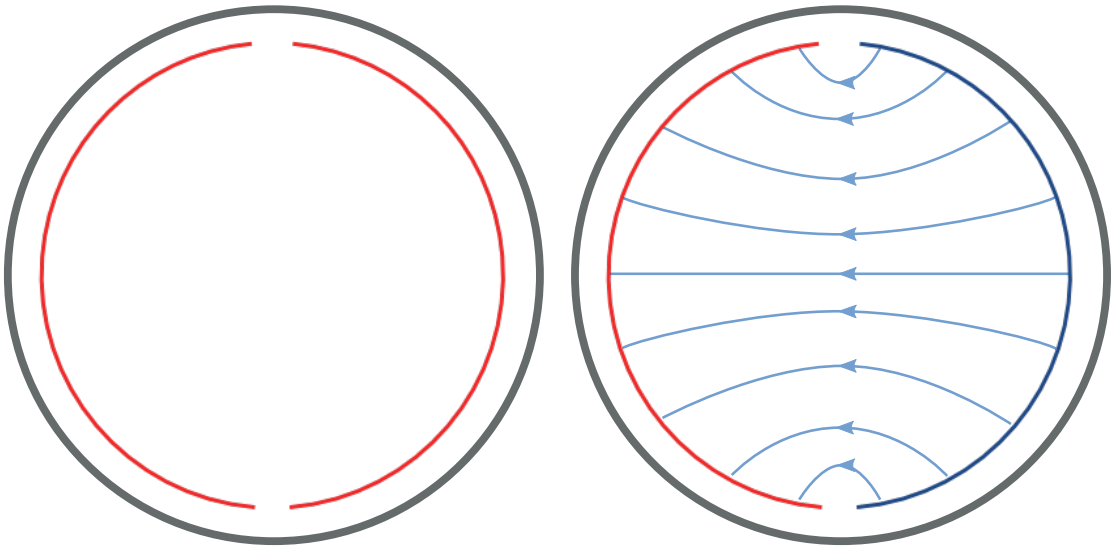

(a) no dipole (b) potential offset

Figure 3.17.: **Electric dipole field in the MS** Cross section through the main spectrometer illustrating (a) an undistorted field layout with short-circuited electrodes and (b) the formation of an electric dipole inside the experiment: Here a dipole-field is formed due to a potential offset between the dipole halves.

trajectories using a non-symmetric magnetic field. With the primary emphasis of these investigations focused on these background electrons that enter the flux tube, we have to investigate trajectories of low-energy electrons starting from the surface which then are stored in the main spectrometer.
Figures 3.18 and 3.19 examplarily show an electron that actually enters the flux tube and which would be able to initiate background processes. As a result of scattering or residual gas ionization tertiary electrons can now be guided to the sensitive area of the detector. The average time for such a particle to reach the outer sensitive parts of the flux tube is only of the order of milliseconds. To reach the inner parts of the flux tube an electron can take up to several seconds. Over this rather long period of time a scattering will almost certainly happen, as low-energy electrons populate the maximum of the cross-section for residual gas ionization. Unfortunately, this exceedingly long storage time leads to a computation time of days to weeks for one trajectory. To speed this up, an interpolation grid of the magnetic stray field was created and used for particle tracking, resulting in a reduction of computation time down to a few days [141].

These calculations for selected test cases that it is possible for background electrons with energies of several eVs to advance into the sensitive part of the flux tube and, correspondingly, it can be assumed that they will create background particles there.

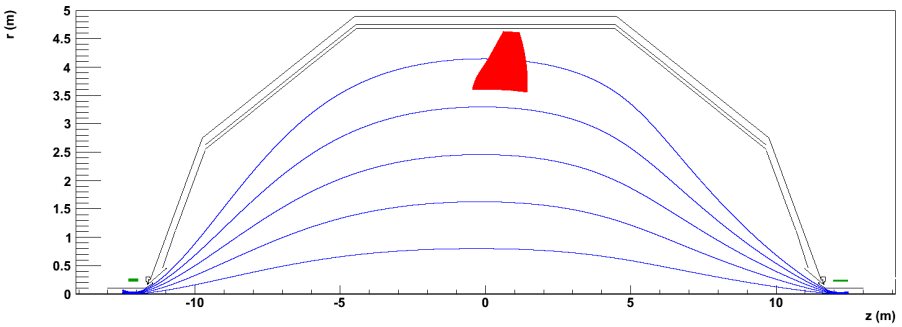

Figure 3.18.: Electron trajectory in the z-r plane (red). In this test case, an electron started from the vessel hull with 2 eV of kinetic energy. The track was stopped well inside the flux tube (blue) after a scattering event happened.

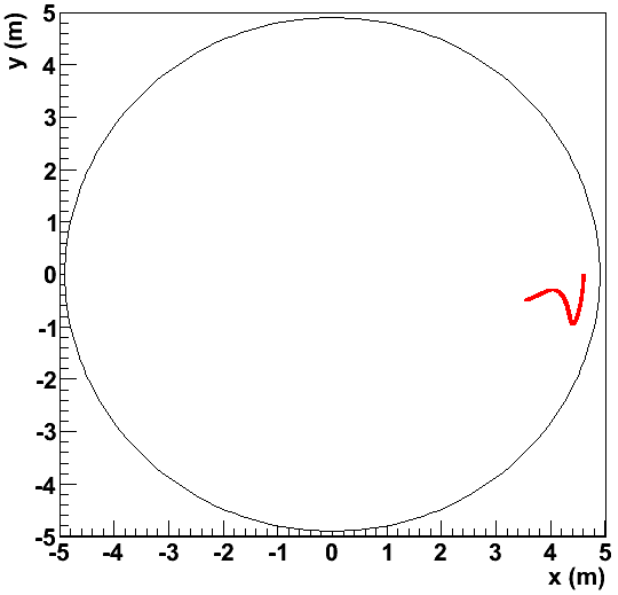

Figure 3.19.: The same electron trajectory as shown in figure 3.18 in the x-y plane (red). The black circle marks the vessel hull.

4. Methods for electric and magnetic field-calculation

The ability to calculate electric and magnetic field configurations with extraordinary precision, taking into account diverse types of geometries and field-shaping bodies is very important for an experiment whose central principle of spectroscopy is based on a well-defined interplay of electric and magnetic fields. Field simulation tools are an essential cornerstone of electromagnetic design calculations. They are also of key importancefor investigations of trajectories of charged particles, as for example, investigations of Penning traps or simulations of transmission functions.
Most of the methods presented in this chapter were originally developed and implemented in C-code by Dr. Ferenc Glück [142, 143] at KIT. The pre-existing code has been rewritten, restructured and improved in the context of this thesis and was transformed into an object-oriented shape, allowing it to interface with simulations of the tritium source [144] and detector [145]. The methods developed here were also implemented in the software Kassiopeia [146], which is a program package developed and maintained by members of the KATRIN-Collaboration. Kassiopeia includes a full computational description of electron processes in the KATRIN experiment.

4.1. Magnetic field calculation

The magnetic fields in the KATRIN experiment are of special interest, as they guide the electrons through the experiment and have to be shaped so that an adiabatic transformation of the electron momentum in the spectrometers takes place. Depending on the field-generating component, there are several ways to calculate the resulting magnetic field: *discrete* methods are able to emulate complex forms by composing them of numerous small elements, thus being flexible but their computational speed is rather slow. In contrast *axisymmetric* methods are very fast, but need pre-calculations and are only applicable to rotational-symmetric geometries. This section will give an introduction to both methods, explaining the underlying physical and mathematical principles they are based on.

4.1.1. Discrete methods

In section 3.6 it was explained that already small deviations of the magnetic field from axialsymmetry can cause a breach of the magnetic shielding. To study the efficiency of the dominant magnetic shielding, it is very important to accurately model all components that can introduce non-axisymmetric magnetic stray fields and not to just approximate them by simple geometric shapes. A standard approach in the description of realistic geometric shapes is to discretize them into many small elements of simple form. This method is quite common, because it offers the opportunity to scale the discretization of the emulated object. The user can choose either a less accurate model with just a few elements that is relatively fast to compute, or a very accurate model, consisting of many elements which thus takes a lot of computation time.

4.1.1.1. Integrated Biot-Savart

In the KATRIN beamline, there are several field-generating components with a relatively simple shape, consisting of conductor-cables that are wound in a distinct way. These components include the cables of the air-coil system (see also 2.3.4): the EMCS, that consists of several *cosine coils* and the LFCS that features 14 coils with small deviations from the circular shape. Further applications also include the calculation of the magnetic field of the dipole coils in the Differential Pumping Section 1-Rear (DPS1-R), Differential Pumping Section 1-Forward (DPS1-F) and the Rear Section adjacent to the WGTS. To compute their effects on the magnetic field in the experiment, the integrated Biot-Savart method is used [147].
The magnetic field that is generated by any current-carrying component can be described using Biot-Savart's law: From an infinitely long conductor segment with current I, an infinitesimally small segment $\mathrm{d}\vec{l}$ in direction of the current generates at the position $\vec{r}$ a magnetic field:

$$\mathrm{d}\vec{B} = \frac{\mu_0}{4\pi}\frac{I\mathrm{d}\vec{l}\times\hat{r}}{r^2}. \tag{4.1}$$

When discretizing our objects down to finite line-current-segments, similar to the example shown in figure 4.1, we have to integrate along a line current segment $\mathrm{d}\vec{l}$ and get:

$$\begin{aligned} \vec{B}_i &= \frac{\mu_0}{4\pi}\mathrm{d}\vec{L}\times\vec{I} \qquad \text{with} \\ \mathrm{d}\vec{L} &= \left(\frac{\hat{r}_1+\hat{r}_2}{R+l} - \frac{\hat{r}_1+\hat{r}_2}{R-l}\right), \\ R &= |\vec{r}_1|+|\vec{r}_2|, \qquad l = |\vec{r}_2-\vec{r}_1| \qquad \text{and} \qquad \hat{r}_i = \frac{\vec{r}_i}{|\vec{r}_i|}. \end{aligned} \tag{4.2}$$

In doing so we are able to use the superposition principle, i. e. it is possible to approximate complex shapes by discretizing them into numerous line current segments and simply sum up their individual field contributions $\vec{B}_i$ to obtain the overall resulting magnetic field:

$$\vec{B}_{\text{total}} = \sum_i^N \vec{B}_i \tag{4.3}$$

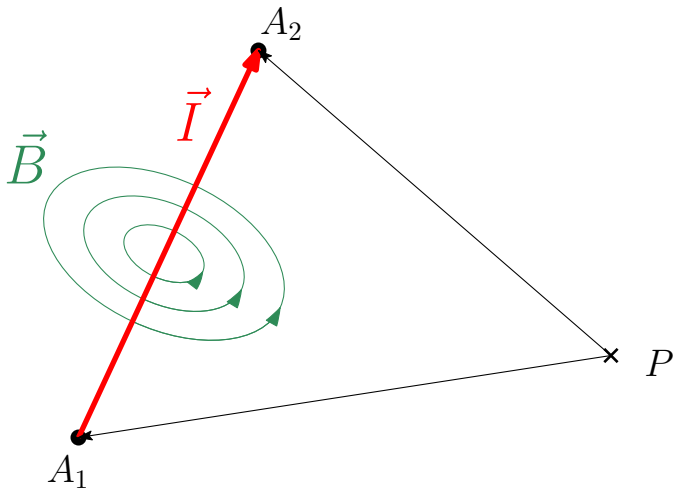

Figure 4.1.: **Line-current segment in the Biot-Savart-method** A line-current segment is defined by a start point A_1, an endpoint A_2 and the magnitude of the current $\vec{I}$ that flows from A_1 to A_2 so that the value of the $\vec{B}$ field can be calculated at point P.

Geometries which are composed of such line current segments can easily be tested by checking the validity of the Maxwell-equations. If, for example, the curl of the magnetic field $\vec{\nabla} \times \vec{B}_{\text{total}}$ is non-zero in vacuum, this result is a hint that a current loop is not closed and that one has to check the discretization.

4.1.1.2. Magnetic dipole-bars

The spectrometer hall consists mainly of concrete and steel reinforcement, both in stainless and normal steel [148]. The non-austenitic steel rods inside the floor and the walls of the experimental hall give rise to non-negligible and highly non-homogeneous magnetic stray fields. For financial reasons, part of the reinforcements are non-austenitic, giving rise to a non-negligible magnetic component located at the outer parts of the walls of the spectrometer hall.
It is well known however, in which direction the obstructed steel bars are magnetized: namely along their symmetry axis. In this case, one can make the simplifying approximation of a magnetic dipole with two magnetic charges $Q_{\text{a}} = Q_{\text{b}}$ at both ends of the bar (see figure 4.2).
The magnetic field of such a dipole can easily be calculated in analogy to Coulomb's law:

$$\vec{B}_i(P) = Q\frac{\mu_0}{4\pi}\left(-\frac{\vec{r}_{\text{a}}}{|\vec{r}_{\text{a}}|^3} + \frac{\vec{r}_{\text{b}}}{|\vec{r}_{\text{b}}|^3}\right) \qquad \text{with} \qquad Q = |\vec{M}| \cdot \pi R^2 \tag{4.4}$$

Here, $\vec{M}$ denotes the magnetization and R the radius of the dipole-bar. Again, to get the total magnetic field from all dipole-bars their individual contributions B_i have to be summed up. However, the steel in the buildings is enclosed by concrete and thereby it is not readily accessible for direct measurements of the magnetization, it is quite complicated to build a model to describe them [139].
In order to get an appropriate model, many magnetic field measurements near the walls of the KATRIN hall are necessary. With these data and an assumption of an equidistant distribution of the steel bars in the wall, one can post a set of linear equations. The solution of these linear equations leads to a good model for the

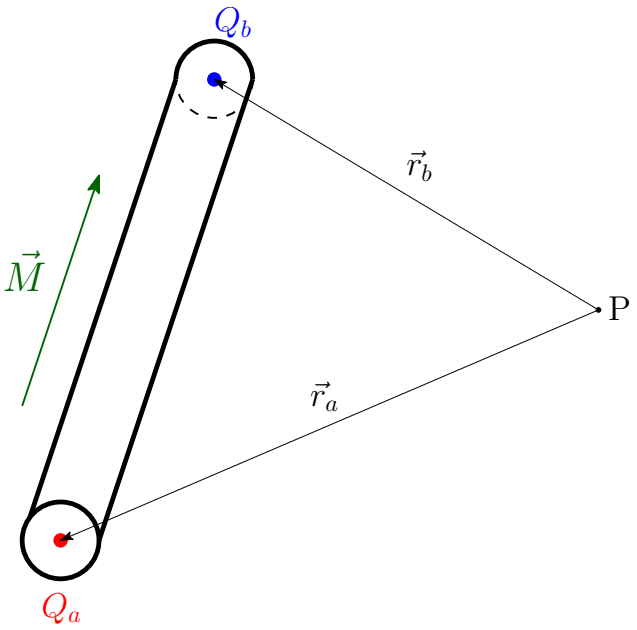

Figure 4.2.: **Parameters of a magnetic dipole bar** The magnetic dipole bars are characterized by two magnetic charges Q_a, Q_b at the ends of the bar, resulting in a magnetization $\vec{M}$ of the bar.

magnetization which enables the calculation of the magnetic field due to magnetic materials in the spectrometer hall.

4.1.2. Axisymmetric methods

The KATRIN beamline contains over 40 superconducting solenoids. They consist of quite rigid material and can very well be approximated as being rotational symmetric. In the following section the method used to calculate these axisymmetric solenoids will described, namely the calculation method based on *elliptic integrals* and a further simplification, the *Legendre polynomial expansion* that allows for a tremendous speed gain in the calculation of the magnetic fields from solenoids.

4.1.2.1. Elliptic Integrals

Each superconducting solenoid can be discretized into simple circular current loops, with a rotational symmetry axis (compare fig. 4.3).
The Biot-Savart law (4.1) for a thin coil can then be expressed in terms of the complete elliptic integrals:

$$
\begin{aligned}
K(k) &= \int_0^{\frac{\pi}{2}} \frac{\mathrm{d}\varphi}{\sqrt{1-k^2\sin^2\varphi}} && \text{(I)} \\
E(k) &= \int_0^{\frac{\pi}{2}} \mathrm{d}\varphi \sqrt{1-k^2\sin^2\varphi} && \text{(II)} \\
\Pi(c,k) &= \int_0^{\frac{\pi}{2}} \frac{\mathrm{d}\varphi}{(1-c^2\sin^2\varphi)\sqrt{1-k^2\sin^2\varphi}} && \text{(III)}
\end{aligned}
\tag{4.5}
$$

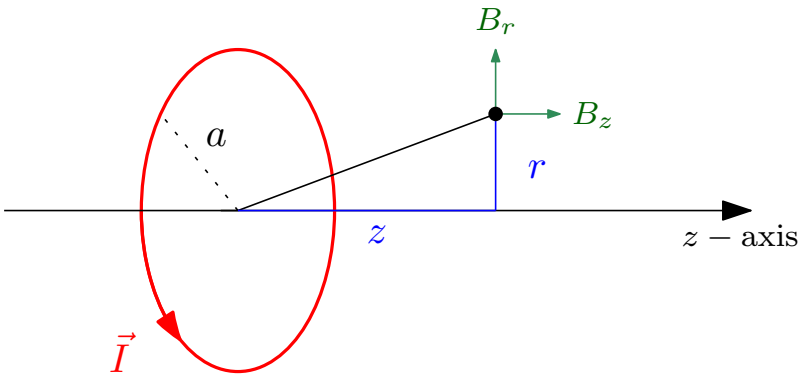

Figure 4.3.: **Circular current loop** A loop with the a and current $\vec{I}$ running through it generates a magnetic field $\vec{B}$

These expression can be used for an analytical computation of the magnetic field [149]:

$$\begin{aligned} B_r &= \frac{I}{c}\frac{2z}{r\sqrt{(a+r)^2+z^2}}\left[-K(k)+\frac{a^2+r^2+z^2}{(a+r)^2+z^2}E(k)\right] \\ B_\varphi &= 0 \\ B_z &= \frac{I}{c}\frac{2}{r\sqrt{(a+r)^2+z^2}}\left[K(k)+\frac{a^2-r^2-z^2}{(a+r)^2+z^2}E(k)\right] \end{aligned} \tag{4.6}$$

where $k^2 = \frac{4ar}{z^2+(a+r)^2}$. For real coils, of finite length, the third integral is also needed for a description of the magnetic field. Usually, the parameters $K(k)$, $E(k)$ and $\Pi(c,k)$ are expressed via Carlson's elliptic integrals R_F, R_J, R_D [150]:

$$\begin{aligned} K(k) &= (R_F, 0, 1-k^2, 1) \\ E(k) &= (R_F, 0, 1-k^2, 1) - k^2\frac{1}{3}(R_D, 0, 1-k^2, 1) \\ \Pi(c,k) &= (R_F, 0, 1-k^2, 1) - c^2\frac{1}{3}(R_J, 0, 1-k^2, 1, 1-c^2) \end{aligned} \tag{4.7}$$

These solutions are valid everywhere implying that the magnetic field can be calculated even inside the coils. In addition, Carlson's elliptic integrals offer a relatively fast numerical computation method. But still a numerical integration is necessary, which usually means summing over many numbers. To speed things up, a solution has to be found that is fast to compute: in our case, zonal harmonics are appropriate solutions for axisymmetric coils. They can be computed fast and offer a variable precision, depending on the number of expansion orders that are considered.

4.1.2.2. Zonal Harmonic Expansion

The magnetic field at a point $\vec{p}(r,z)$ located close to the symmetry axis can be expressed in terms of the Legendre polynomial expansion and its derivatives at the point z_0 that lies on the symmetry axis, a so called source point. In cases where the distance of the field-point to the source point is smaller than the minimal distance of the source point to the coil body ($\rho < \rho_{\text{cen}}$, see fig. 4.4), the magnetic field is

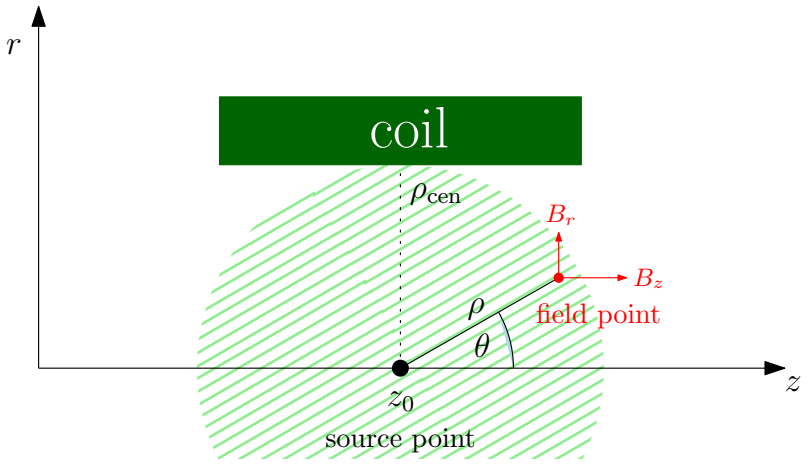

Figure 4.4.: Convergence radius of the central expansion.

given by the so called *central expansion*:

$$\begin{aligned} B_r &= -s \sum_{n=1}^{\infty} \frac{B_n^{\text{cen}}}{n+1} \left(\frac{\rho}{\rho_{\text{cen}}} \right)^n P_n'(u) \\ B_\varphi &= 0 \\ B_z &= \sum_{n=0}^{\infty} B_n^{\text{cen}} \left(\frac{\rho}{\rho_{\text{cen}}} \right)^n P_n(u) \\ &\text{where} \quad u = \cos\theta \quad \text{and} \quad s = \sin\theta \end{aligned} \tag{4.8}$$

and with B_n^{cen} being the central source coefficients and P_n the Legendre polynomials of n^{th}-grade. The minimal distance between the source point and the coil ρ_{cen} is usually called central convergence radius and equation (4.8) is only valid within it. As we want to know the magnetic field outside of the convergence radius too, a second polynomial expansion has to be introduced. This remote expansion is only valid for distances to the source point greater than the remote convergence radius ρ_{rem}, which is the maximal distance of the source point to the coil ($\rho > \rho_{\text{rem}}$, see fig. 4.5). The magnetic field is then defined by the remote expansion:

$$\begin{aligned} B_r &= s \sum_{n=2}^{\infty} \frac{B_n^{\text{rem}}}{n} \left(\frac{\rho_{\text{rem}}}{\rho} \right)^{n+1} P_n'(u) \\ B_\varphi &= 0 \\ B_z &= \sum_{n=2}^{\infty} B_n^{\text{rem}} \left(\frac{\rho_{\text{rem}}}{\rho} \right)^{n+1} P_n(u) \end{aligned} \tag{4.9}$$

with B_n^{rem} being the remote source coefficients.
These expansions now allow a very fast field-computation nearly everywhere in space. They are however not valid very close to and inside the coils, so elliptic integrals have to be used here.

4.1.2.3. Application

For the description of a system of multiple coils, the convergence radii are determined by the closest and the most remote coil, respectively. To cover a larger area

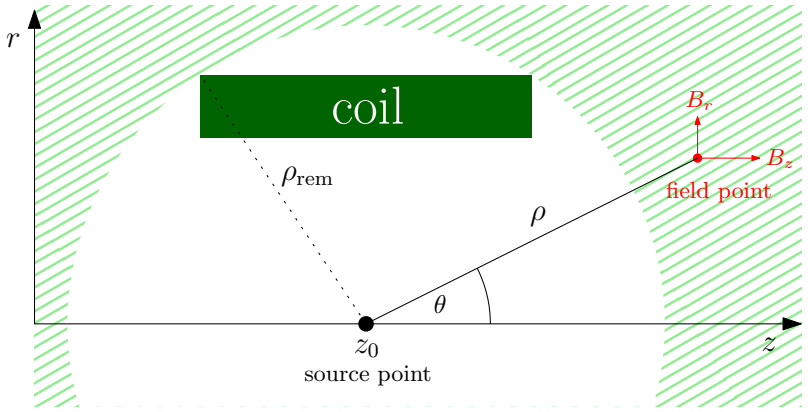

Figure 4.5.: Convergence radius of the remote expansion.

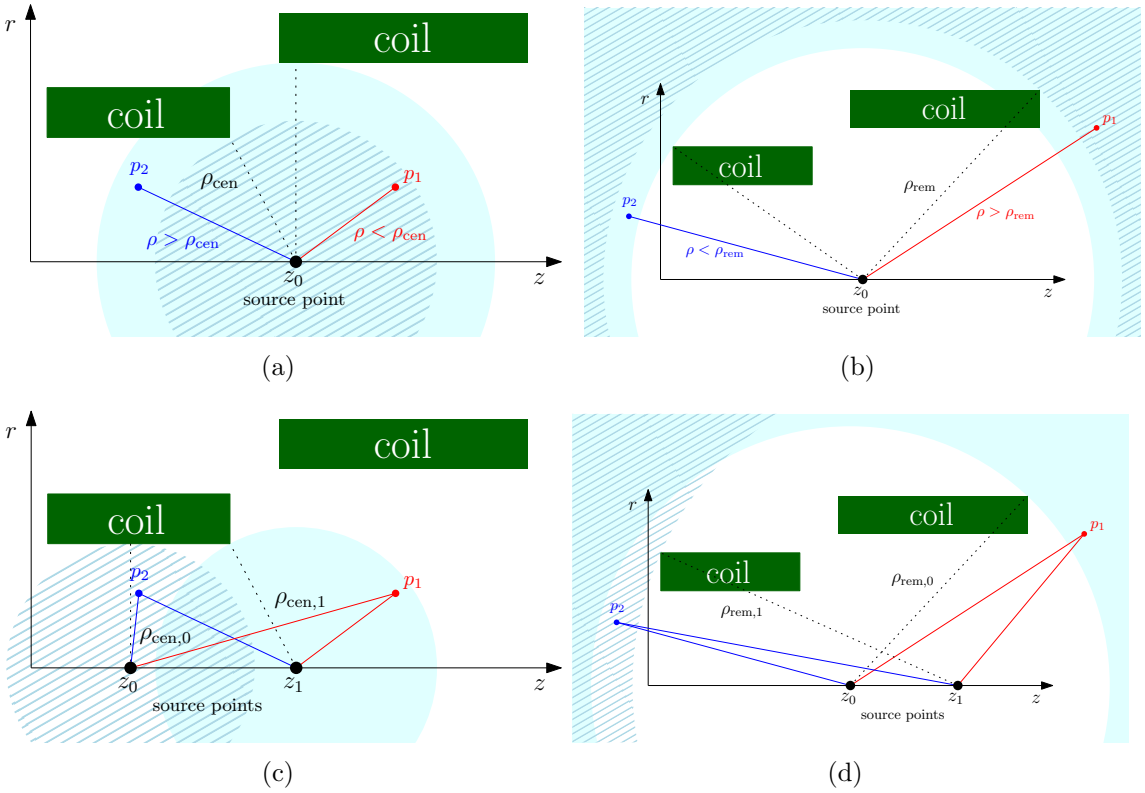

Figure 4.6.: **Application of the method of multiple source points** Displayed is the central convergence radius (a) and the remote convergence radius (b), with two coils using only one source point. The expansions converge in p_1 but not in p_2. By introducing additional source points, it is now possible to compute the magnetic field in both p_1 and p_2 with the polynomial expansion ((d),(c)).

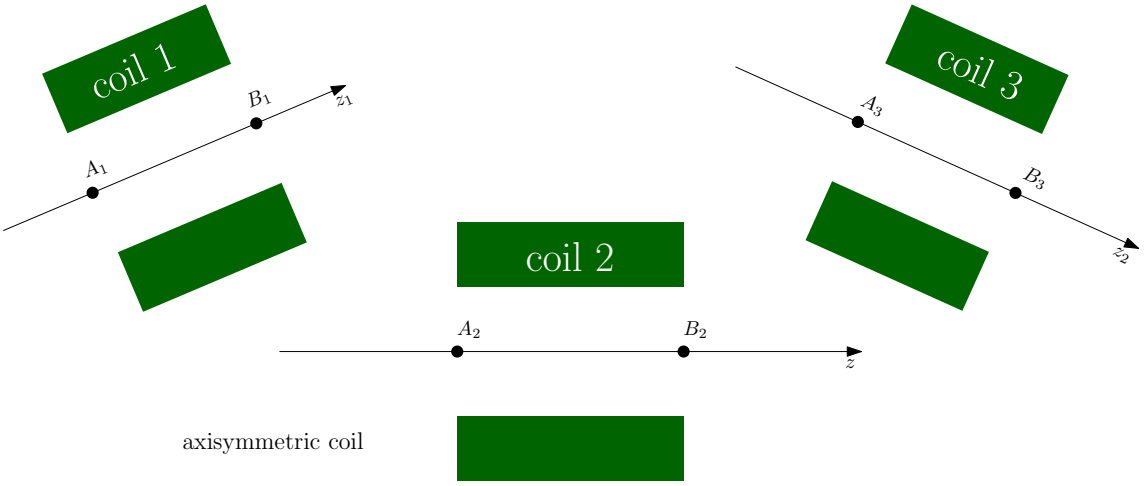

Figure 4.7.: Tilted coil configuration with different symmetry axes.

the amount of source points can simply be increased, as shown in figure 4.6.

Another benefit of making use of several source points is a faster computation, as the polynomial expansion converges faster if the fractions $\frac{\rho}{\rho_{\text{cen}}}$ and $\frac{\rho_{\text{rem}}}{\rho}$ are smaller. By choosing the source point with the smallest fraction for the field point to be calculated, a significant amount of computation time can be saved.

In preparation for the polynomial expansion, the source coefficients B_n^{cen} and B_n^{rem} need to be computed at every source point. These can be expressed by two-dimensional integrals over the coil profile:

$$\begin{aligned} B_n^{\text{cen}} &= \int_{R_{\min}}^{R_{\max}} \mathrm{d}R \int_{Z_{\min}}^{Z_{\max}} \mathrm{d}Z \; b_n(R,Z) \quad \text{and} \\ B_n^{\text{rem}} &= \int_{R_{\min}}^{R_{\max}} \mathrm{d}R \int_{Z_{\min}}^{Z_{\max}} \mathrm{d}Z \; b_n^*(R,Z), \end{aligned} \tag{4.10}$$

with

$$\begin{aligned} b_n(R,Z) &= \frac{\mu_0 I}{2A\rho_{\text{cen}}} \left(1 - \left(\frac{Z-z_0}{\rho_{ZR}}\right)^2\right) \left(\frac{\rho_{\text{cen}}}{\rho_{ZR}}\right)^{n+1} P'_{n+1}\left(\frac{Z-z_0}{\rho_{ZR}}\right), \\ b_n^*(R,Z) &= \frac{\mu_0 I}{2A\rho_{\text{rem}}} \left(1 - \left(\frac{Z-z_0}{\rho_{ZR}}\right)^2\right) \left(\frac{\rho_{\text{rem}}}{\rho_{ZR}}\right)^{n} P'_{n-1}\left(\frac{Z-z_0}{\rho_{ZR}}\right), \end{aligned} \tag{4.11}$$

where ρ_{ZR} is the distance between the source point z_0 and the point (Z,R) in the coil body while $\frac{I}{A}$ denotes the current density within the coil.

It is even possible to compute the field of multiple coils that do not have a common symmetry axis. In this case, the coils can be merged into groups with common symmetry axes (see fig. 4.7). The source coefficients are computed for the source points in their respective coordinate system. Afterwards the magnetic field is transformed back into the reference system.

4.2. Electric field calculation

Calculations of the electric field and potential turn out to be more complicated than the magnetic ones. Magnetic fields are caused by electric currents, i. e. by quantities which can be directly measured and set. The electric field and potential, however, are caused by a charge distribution that is usually not known a priori. The quantity one can set and measure on the electrodes is the applied voltage. The charge density on the electrodes dependens on the voltage, but also strongly depends on the actual geometry of the electrode itself and on its surroundings. Another spectrometer-specific requirement is the ability to handle rather large volumes which are enclosed by the electrodes. Most of the standard methods to simulate electric fields, like for example the Finite Difference [151] and Finite Element Methods [152], are not applicable in such a case, as they divide the volume into a close-meshed grid, which, for extended geometries, can not be handled without serious problems regarding computer memory.
Actually, within KATRIN, a method exists that meets these requirements: the so called Boundary Element Method (BEM).

4.2.1. Boundary element method

When working with the BEM, it is generally assumed that on a given surface part of the electrode the charge density is distributed homogeneously so that the resulting electric field can be derived from it. Analogous to the discrete line-segment methods discussed earlier in this chapter, the discretization into surface elements offers the ability to model even complex shapes out of simpler geometry elements with variable level of detail and thereby accuracy.
Accordingly, an electrode can be discretized into N sub-elements S_j. The geometry S can then be written as a sum of these sub-elements:

$$S = \sum_{j=1}^{N} S_j \tag{4.12}$$

By integrating over the charge densities σ of all subelements, we obtain the potential at the position $\vec{r}$ for the geometry S [153]:

$$\Phi(\vec{r}) = \frac{1}{4\pi\varepsilon_0} \int\limits_S \frac{\sigma(\vec{r}_S)}{|\vec{r} - \vec{r}_S|} \mathrm{d}^2\vec{r}_S \tag{4.13}$$

Although the charge-densities are assumed to be constant within one subelement, they are usually not known priori. The experimental quantities that are known are the voltages U_i which are applied to the electrodes. It is however possible to write down a system of equations which relates the charge density σ_j with the voltage applied to subelement U_i:

$$U_i = \sum_{j=1}^{N} C_{ij}(\vec{r})\sigma_j, \tag{4.14}$$

with $C_{ij} = C_j(\vec{r}_i)$ being the so called Coulomb matrix element. It can be regarded as the electric potential at the center of subelement i caused by subelement j. It is a geometrical factor given by:

$$C_j(\vec{r}_i) = \frac{1}{4\pi\varepsilon_0} \int\limits_{S_j} \frac{1}{|\vec{r}_i - \vec{r}_S|} \mathrm{d}^2\vec{r}_S \tag{4.15}$$

The equation system (4.14) can be numerically solved by using the Gauss-Jordan- or LU-decomposition-algorithm [154], providing the charge densities σ_j of the individual subelements thereby allowing us to compute the electric potential and field.

4.2.2. Axisymmetric methods

The electrodes in the main spectrometer are in good approximation rotational symmetric. This makes it easy to describe them as cones.
The electric potential of an infinitesimally thin charged ring at a field point (z, r) is given by:

$$\Phi(z, r) = \frac{Q}{2\pi^2\epsilon_0}\frac{K(k)}{S} \tag{4.16}$$

where

$$S = \sqrt{(R+r)^2 + (z-Z)^2}, \;\; k = \frac{2\sqrt{Rr}}{S}, \tag{4.17}$$

Here, Z is the axial coordinate of the ring, R its radius, Q its total charge and $K(k)$ represents the first complete elliptic integral (see eq. (4.5)).
A numerical integration of this formula allows to compute the potential of a conical subelement with constant charge density σ. This subelement is described by two points (z_a, r_a) and (z_b, r_b), and can be expressed as a sum of thin charged rings:

$$Z = z_a + (z_b - Z_a)\cdot\frac{p}{L}, \;\; R = r_a + (r_b - r_a)\cdot\frac{p}{L}. \tag{4.18}$$

Here p is the distance of the arbitrary subelement point (Z, R) from the point (z_a, r_a) that lies between 0 and L, where L denotes the length of the line segment. Taking the infinitesimal charge $\mathrm{d}Q = 2\pi\sigma R\ \mathrm{d}p$ of the ring, the potential of the cone can finally be described:

$$\Phi = \frac{\sigma}{\pi\epsilon_0}\int_0^L \mathrm{d}p\ \frac{RK(k)}{S} \tag{4.19}$$

This integral can lead to divergences, when evaluating it close to the segment. To avoid this, the integration region is divided into smaller subintervals, within which the integrand does not have any divergences.

4.2.3. Wire

Similar to the above discussed case of current-carrying cables, the thin wires of the electrode system inside the spectrometers can be represented by multiple short and uniformly charged line segments. In figure 4.8 a sketch of such a segment is shown. The potential at a point $P(z, r)$ outside a segment with the length $2c$ and the charge-density λ is given by the integral:

$$\Phi(z, r) = \frac{\lambda}{4\pi\epsilon_0}\int_{-c}^{+c}\frac{\mathrm{d}\zeta}{\sqrt{r^2 + (z-\zeta)^2}} \tag{4.20}$$

This integral is analytically solvable, see [155]. The solution for Φ is given by the expression:

$$\Phi(z, r) = \frac{\lambda}{4\pi\epsilon_0}\log_{10}\left(\frac{a+c}{a-c}\right) \tag{4.21}$$

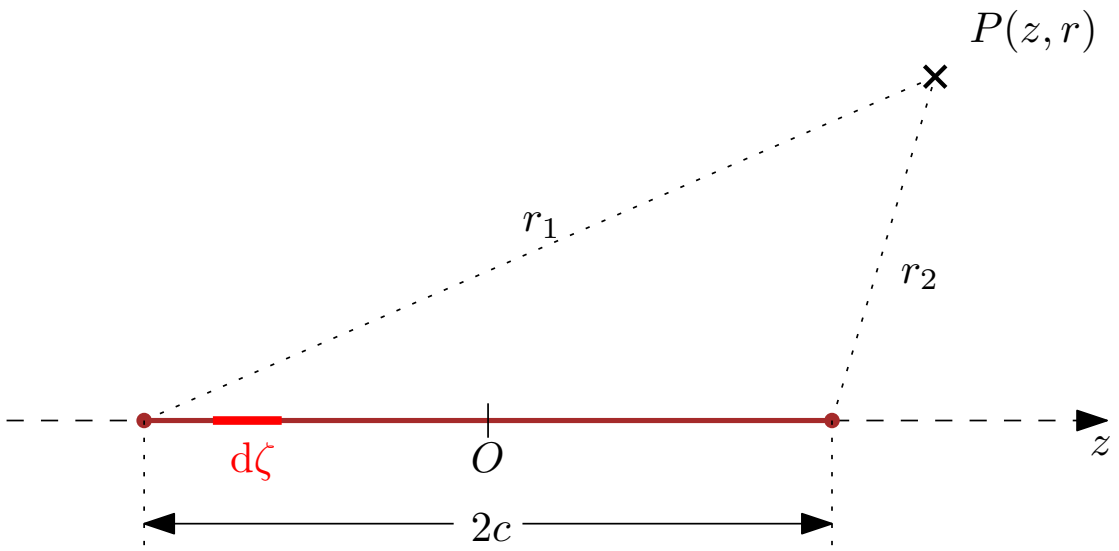

Figure 4.8.: **Calculation of the potential of a wire of the electrode system** For a uniformly charged segment of length $2c$ with field-point P, the distances of P to the two end-points are denoted by r_1 and r_2.

the mean distance of the segment-ends to the point is given by $a = \frac{r_1+r_2}{2}$. The main spectrometer features a two-layer wire electrode system, with each layer comprising of 12000 wires. Hence, the computation of the potential of the whole geometry takes a considerable amount of computation time. For distances large enough, the wire electrode can be well approximated by cones that carry the same charge as the wires, thus tremendously speeding up the computation time.

4.2.4. Trapezoid

When computing the potential and electric field in the vicinity of the electrodes, the rotational symmetric approximation no longer suffices. A detailed description of the non-rotational symmetric components of the electrode-system is required, in particular for elements such as the wire holding structure or the voltage distribution units. Existing simulation geometries of these structures composed of surfaces of rectangles and triangles.
In the context of this thesis, a method to compute the potential and electric field of uniformly charged trapezoids was implemented, as both, rectangles and triangles are special cases of trapezoids. This allows to use both geometry types with one code.
To simplify the field calculation for a trapezoid, a new coordinate system is defined with the following attributes, see fig. 4.9 :

1. The trapezoid $\mathcal{T}$ lies in the new x-y-plane.

2. The new x-axis is parallel to the segment $\overline{AB}$.

3. The field point lies on the new z-axis.

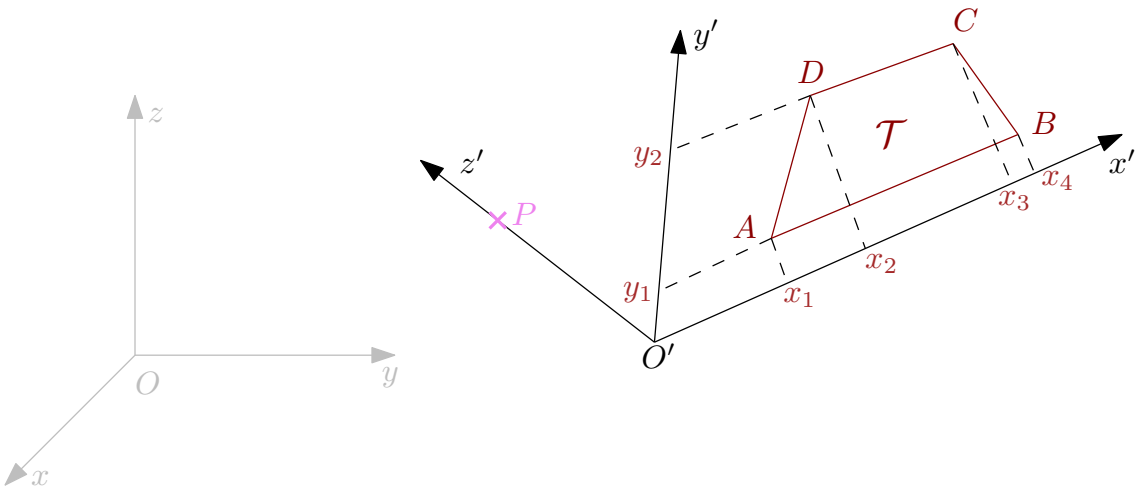

Figure 4.9.: **Calculation of the potential of a trapezoid** The red trapezoid $\mathcal{T}$ and the field-point P are represented in the new coordinate system defined by (O', x', y', z'). The original coordinate system (O, x, y, z) is shown in gray.

The potential Φ and electric field $\vec{\mathcal{E}}$ in P due to the uniformly charged trapezoid $\mathcal{T}$ is then given by the integral:

$$\begin{aligned}
\Phi(P) &= \int_{y_1'}^{y_2'} \mathrm{d}y' \int_{x_\mathrm{u}(y')}^{x_\mathrm{o}(y')} \frac{\sigma}{\sqrt{x'^2 + y'^2 + z'^2}} \mathrm{d}x' \\
\mathcal{E}_x(P) &= -\int_{y_1'}^{y_2'} \mathrm{d}y' \int_{x_\mathrm{u}(y')}^{x_\mathrm{o}(y')} \frac{x' \cdot \sigma}{\left(\sqrt{x'^2 + y'^2 + z'^2}\right)^3} \mathrm{d}x' \\
\mathcal{E}_y(P) &= -\int_{y_1'}^{y_2'} \mathrm{d}y' \cdot y' \int_{x_\mathrm{u}(y')}^{x_\mathrm{o}(y')} \frac{\sigma}{\left(\sqrt{x'^2 + y'^2 + z'^2}\right)^3} \mathrm{d}x' \\
\mathcal{E}_z(P) &= z' \int_{y_1'}^{y_2'} \mathrm{d}y' \int_{x_\mathrm{u}(y')}^{x_\mathrm{o}(y')} \frac{\sigma}{\left(\sqrt{x'^2 + y'^2 + z'^2}\right)^3} \mathrm{d}x'
\end{aligned} \tag{4.22}$$

with x_u and x_o denoting the parameterization of the segments $\overline{AB}$ and $\overline{DC}$. With this expression, the potential and electric field can be computed by numerical integration. However, for $z' \neq 0$, the integrals are analytically solvable. We define the dimensionless auxiliary variables:

$$\begin{aligned}
v_\mathrm{u}(u) &= \frac{x_\mathrm{u}(y')}{z'} = a_1 + b_1 \cdot u \qquad \text{and} \\
v_\mathrm{o}(u) &= \frac{x_\mathrm{o}(y')}{z'} = a_2 + b_2 \cdot u
\end{aligned} \tag{4.23}$$

as an expression for the parameterization which formerly went from y_1' to y_2' and now runs from u_1 to u_2. The integrations for the potential and the electric field then

result in the terms [156]:

$$\begin{aligned}
\Phi(P) &= \sigma \cdot |z'| \sum_{i,j=1}^{2} (-1)^{(1-\delta_{ij})} \cdot \mathcal{F}\left(a_i, b_i, u_j\right) \\
\mathcal{E}_x(P) &= \sigma \cdot \operatorname{sign}(z') \sum_{i,j=1}^{2} (-1)^{(1-\delta_{ij})} \cdot \mathcal{G}\left(a_i, b_i, u_j\right) \\
\mathcal{E}_y(P) &= \sigma \cdot \operatorname{sign}(z') \sum_{i,j=1}^{2} (-1)^{(1-\delta_{ij})} \cdot \mathcal{H}\left(a_i, b_i, u_j\right) \\
\mathcal{E}_z(P) &= \sigma \cdot \operatorname{sign}(z') \sum_{i,j=1}^{2} (-1)^{(1-\delta_{ij})} \cdot f_3\left(a_i, b_i, u_j\right)
\end{aligned} \tag{4.24}$$

where the functions $\mathcal{F}, \mathcal{G}$ and $\mathcal{H}$ are defined by:

$$\begin{aligned}
\mathcal{F} &= u \cdot f_1(a,b,u) + a \cdot \frac{f_2(a,b,u)}{\sqrt{b^2+1}} - f_3(a,b,u) \\
\mathcal{G} &= \frac{f_2(a,b,u)}{\sqrt{b^2+1}} \\
\mathcal{H} &= \frac{f_4}{2} - \frac{b \cdot f_2(a,b,u)}{\sqrt{b^2+1}}
\end{aligned} \tag{4.25}$$

with the auxiliary functions being defined as:

$$\begin{aligned}
f_1(a,b,u) &= \operatorname{arcsinh}\left(\frac{a+b\cdot u}{\sqrt{u+1}}\right) \\
f_2(a,b,u) &= \operatorname{arcsinh}\left(\frac{u\cdot(b^2+1)+a\cdot b}{\sqrt{1+a^2+b^2}}\right) \\
f_3(a,b,u) &= \arctan\left(\frac{a\cdot u - b}{\sqrt{(a+b\cdot u)^2+(u^2+1)}}\right) \\
f_4(a,b,u) &= \operatorname{sign}(a+b\cdot u)\cdot \operatorname{arcoth}\left(\frac{a\cdot\sqrt{\alpha(a,b)+\beta(a,b)}}{t(a,b,u)\cdot(a^2+b^2)}\right)
\end{aligned} \tag{4.26}$$

and $\alpha(a,b), \beta(a,b)$ and $t(a,b,u)$ defined by:

$$\begin{aligned}
\alpha(a,b) &= \beta\cdot(1+a^2+b^2) \\
\beta(a,b) &= \frac{a^2+b^2}{a^2} \\
t(a,b,u) &= \frac{1+\frac{u\cdot b}{a}}{u-\frac{b}{a}}
\end{aligned} \tag{4.27}$$

The analytical solution allows to calculate the potential and electric field of a trapezoidal element directly, instead via the method of numerical integration. This approach implies a significant gain of computation speed. However, in cases where the field-point lies inside the plane of the trapezoid one has to regress to numerical integration. Another advantage of the trapezoid method is that it allows for versatile meshing of objects with rectangles, parallelograms and triangles. Therefore, actual surfaces can be modeled very close to reality.

4.2.5. Legendre polynomial expansion

Similar to the approach applied to the magnetic field, the zonal harmonic expansion is applicable also for axisymmetric electric fields. Depending on the convergence ratio, the computation by expansion is much faster than by elliptic integrals. Nevertheless, the computation of charge densities by the BEM is required as input parameters, in order to compute the source coefficients at the source points.
Analogous to eq. (4.8) and (4.9) for the magnetic field, there exists a central polynomial expansion (for $\rho < \rho_{\text{cen}}$) for electric fields, given by:

$$\begin{aligned}
\Phi(z,r) &= \sum_{n=0}^{\infty} \phi_n^{\text{cen}} \left(\frac{\rho}{\rho_{\text{cen}}}\right)^n P_n(u) \\
\mathcal{E}_z(z,r) &= -\frac{1}{\rho_{\text{cen}}} \sum_{n=0}^{\infty} (n+1)\phi_{n+1}^{\text{cen}} \left(\frac{\rho}{\rho_{\text{cen}}}\right)^n P_n(u) \\
\mathcal{E}_r(z,r) &= \frac{s}{\rho_{\text{cen}}} \sum_{n=0}^{\infty} \phi_{n+1}^{\text{cen}} \left(\frac{\rho}{\rho_{\text{cen}}}\right)^n P_n'(u) \\
&\text{with} \quad u = \cos\theta \quad \text{and} \quad s = \sin\theta
\end{aligned} \tag{4.28}$$

and a remote expansion (for $\rho > \rho_{\text{rem}}$), given by:

$$\begin{aligned}
\Phi(z,r) &= \sum_{n=0}^{\infty} \phi_n^{\text{rem}} \left(\frac{\rho_{\text{rem}}}{\rho}\right)^{n+1} P_n(u) \\
\mathcal{E}_z(z,r) &= \frac{1}{\rho_{\text{rem}}} \sum_{n=1}^{\infty} n\phi_{n-1}^{\text{rem}} \left(\frac{\rho_{\text{rem}}}{\rho}\right)^{n+1} P_n(u) \\
\mathcal{E}_r(z,r) &= \frac{s}{\rho_{\text{rem}}} \sum_{n=1}^{\infty} \phi_{n-1}^{\text{rem}} \left(\frac{\rho_{\text{rem}}}{\rho}\right)^{n+1} P_n'(u)
\end{aligned} \tag{4.29}$$

where, again, $P_n(u)$ are the Legendre polynomials, ϕ_n^{rem} and ϕ_n^{cen} denote the source coefficients at the source points, and ρ_{rem} and ρ_{cen} are the convergence radii, given by the maximum and minimum distance from the source point to the electrode. The source coefficients ϕ_n^{rem} and ϕ_n^{cen} are determined by the surface and volume charge of the electrode [157].

4.3. Three-dimensional Hermite interpolation

4.3.1. Motivation

Interpolation methods are often employed when calculating the field of a static setup. The interpolation grid is then plotted once in advance and every time the field needs to be evaluated at a certain point, it is interpolated and optionally scaled using the precomputed grid. The Hermite interpolation, in contrast to the simpler linear interpolation does not only require to calculate the values at the grid points, but also their partial derivatives. This results in a longer precomputation time, but as the accuracy of the Hermite interpolation scales not just with the 2nd but with the 4th power of the grid distance, this is the preferred method of choice when interpolating with relatively large grids.

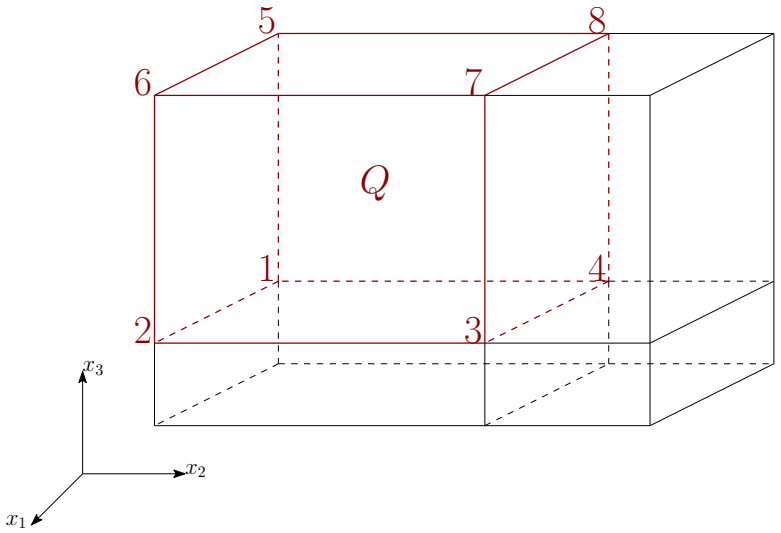

Figure 4.10.: **Interpolation cuboid** Here, the structure of an interpolation-grid for an interpolation-cuboid Q defined by its 8 corner-points is displayed.

Interpolation usually invokes a dramatic speed up of the field calculations, especially for non-axisymmetric fields while still granting a very high numeric precision. However, in axisymmetric fields, close to the symmetry axis, the Legendre-polynomial methods are faster.

4.3.2. Theory

We start by defining a rectangular, three-dimensional grid that consists of cuboids. A cuboid Q of this grid can be described as follows.

$$Q := \left\{(x_1, x_2, x_3) \ \epsilon \ \mathbb{R}^3 \ / \ x_{ui} < x_i < x_{oi} \ ; \ i = 1, 2, 3\right\} \tag{4.30}$$

Applying a coordinate-transformation of the form:

$$\begin{aligned} u_i &= \frac{x_i - x_{mi}}{a_i} \quad \text{with} \\ x_{mi} &= \frac{x_{oi} + x_{ui}}{2} \quad \text{and} \quad a_i = \frac{x_{oi} - x_{ui}}{2} \end{aligned} \tag{4.31}$$

allows to project Q to the unit-cube E:

$$E := \left\{(u_1, u_2, u_3) \ \epsilon \ \mathbb{R}^3 \ / \ -1 < u_i < 1 \ ; \ i = 1, 2, 3\right\} \tag{4.32}$$

Now we define a function $g(\vec{u})$ on E with:

$$f(\vec{x}) = g(\vec{u}(\vec{x})) \tag{4.33}$$

The goal now is to interpolate $g(\vec{u})$ within the unit-cube E. Therefore, we need to know the function values at the eight corner points $\vec{u}_i$ as well as their first partial derivatives. We combine them into a Matrix $\mathcal{G}$, where the function values fill one column:

$$\mathcal{G}_{i0} := g(\vec{u}_i) \ (i = 1, ..., 8) \tag{4.34}$$

while the others are filled by their partial derivatives:

$$\mathcal{G}_{ij} := \left\{ \frac{\partial g(\vec{u})}{\partial u_j} \right\}_{\vec{u}=\vec{u}_i} \qquad (i = 1, ..., 8\ ;\ j = 1, 2, 3) \tag{4.35}$$

The next step is to define a so called interpolation polynomial:

$$G(\vec{u}) = \sum_{i=1}^{8} \sum_{j=0}^{3} \mathcal{G}_{ij} \phi_{ij}(\vec{u}) \tag{4.36}$$

The coefficients of the polynomials ϕ_{ij} are chosen so that $G(\vec{u}_k) = \mathcal{G}_{k0}$ and $\left\{ \frac{\partial g(\vec{u})}{\partial u_1} \right\}_{\vec{u}=\vec{u}_k} = \mathcal{G}_{k1}$. This leads to the following constraints:

$$\phi_{ij}(\vec{u}_k) = \delta_{ik}\delta_{j0} \qquad \text{and} \qquad \left\{ \frac{\partial \phi_{ij}(\vec{u})}{\partial u_1} \right\}_{\vec{u}=\vec{u}_k} = \delta_{ik}\delta_{j1} \tag{4.37}$$

These are fulfilled, if we define ϕ_{ij} by:

$$\phi_{ij}(\vec{u}) := u_{ij} \prod_{k=1}^{3} \varphi_{jk}(u_{ik} \cdot \vec{u}_k) \tag{4.38}$$

where φ_{jk} is given by:

$$\varphi_{jk}(t) := \frac{1}{4} \left[\left(2 + 3t - t^3\right) + \left(-3 - 4t + t^2 + 2t^3\right) \delta_{jk} \right] \quad \text{and} \quad u_{i0} := 1 \tag{4.39}$$

In order to interpolate the function $f(\vec{x})$ within the cuboid Q, we have to follow the following steps:

1. calculate the function-values and their partial derivatives of f regarding $\vec{x}$ at all 8 corner points,
2. transform them into the unit-cube E:

$$\mathcal{G}_{ij} = \begin{cases} a_j \cdot \left\{ \frac{\partial f(\vec{x})}{\partial x_j} \right\}_{\vec{x}=\vec{x}_i} & \text{if} \quad j > 0 \\ f(\vec{x}_i) & \text{if} \quad j = 0 \end{cases} \tag{4.40}$$

3. and interpolate the function values and derivatives at any point $\vec{x}\ \epsilon\ Q$:

$$\begin{aligned} \frac{\partial f(\vec{x})}{\partial x_j} &= a_j^{-1} \cdot \frac{\partial G(\vec{u}(\vec{x}))}{\partial u_j} \qquad j = 1, 2, 3 \\ f(\vec{x}) &= G(\vec{u}(\vec{x})) \end{aligned} \tag{4.41}$$

Interpolation methods yield the very interesting possibility of scalable precision. When a high precision is needed, the distance between the grid points can be chosen arbitrarily small. In the opposite case, when a lower precision suffices, the grid distance can be chosen rather large. This has no impact on the actual computation time, just on the time needed to compute the initial grid.

5. Tracking of charged particles

This chapter describes the mathematical methods and approximations that are used to calculate the trajectories of charged particles in the KATRIN experiment. At first, the Runge-Kutta methods will be introduced, which are able to approximate the solutions of 1st order differential equation systems. This is followed by a description on how these numerical solvers can be applied to calculate particle trajectories and field lines.

5.1. The Runge-Kutta method

Runge-Kutta methods are a well-known family of implicit and explicit iterative methods for the approximation of solutions of ordinary differential equations [158]. They have proven themselves to have a very high precision. In this section, a brief introduction to the explicit 4th order Runge-Kutta (RK4) will be given. Although both the 4th order and 8th order Runge-Kutta methods are being used for particle tracking calculations in the KATRIN beamline, this section will focus only on the RK4 method in greater detail. Conclusively, there will be a short description of the generalization of the RK4 method to higher orders.

The basic idea of the RK methods is the same as for the Euler method: An exact solution $y = y(x)$ of a 1st order ordinary differential equation

$$y' = f(x; y) \tag{5.1}$$

with the given initial value $y(x_0) = y_0$ is replaced by a line in every sub-interval of length h.
The starting point is the given initial point $P_0 = (x_0; y_0)$. We replace the solution within the interval $x_0 \leq x \leq x_1$ with a line that is descibed by the equation:

$$\frac{y - y_0}{x - x_0} = m \qquad \text{or} \qquad y = y_0 + (x - x_0)m \tag{5.2}$$

In contrast to the Euler method[1], the slope m of the replacement line is taken as a weighted average of slopes of the solution, taking into account: the slope k_1

[1] In the Euler method, only the slope in the left boundary point of the interval is taken into account.

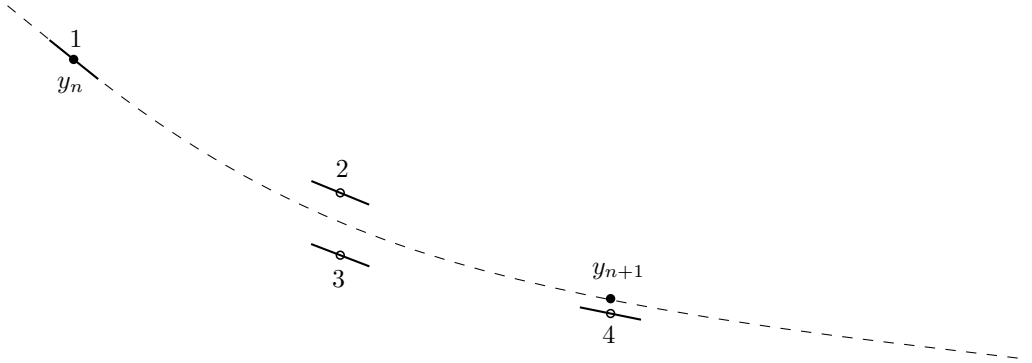

Figure 5.1.: **Graphical interpretation of the 4th order Runge-Kutta method** In each step the derivative is evaluated four times: once at the initial point, twice at trial midpoints, and once at a trial endpoint. From these derivatives the final function value (filled dot) is calculated. Figure after [150]

at the beginning of the interval, two mutually distinct computed slopes k_2,k_3 at the midpoint of the interval and the slope k_4 at the end of the interval. With these definitions the approximated solution $y(x)$ running through $P_n(x_n; y_n)$ can be computed point-wise:

$$\begin{aligned} y(x_{n+1}) \approx y_{n+1} = y_n + \frac{1}{6}\left(k_1 + 2k_2 + 2k_3 + k_4\right) \quad \text{with} \\ k_1 &= h \cdot f(x_n; y_n) \\ k_2 &= h \cdot f\left(x_n + \frac{h}{2}; y_n + \frac{k_1}{2}\right) \\ k_3 &= h \cdot f\left(x_n + \frac{h}{2}; y_n + \frac{k_2}{2}\right) \\ k_4 &= h \cdot f(x_n + h; y_n + k_3) \end{aligned} \tag{5.3}$$

The auxiliary quantities k_1, k_2, k_3 and k_4 have to be computed for each step. The error of the method can be estimated to:

$$\Delta y_k = y(x_k) - y_k \approx \frac{1}{15}(y_k - \tilde{y}_k), \tag{5.4}$$

where $y(x_k)$ is the exact solution at x_k, y_k denotes the approximate solution at x_k with step-size h and $\tilde{y}_k$ represents the approximate solution at x_k with doubled step-size $2h$. In good approximation the error is of the order $\mathcal{O}(h^{p+1})$, where p is the order of the Runge-Kutta method that is used.

The generalization for the approximate solution, taking into account s derivatives, is given by [159]:

$$y(x_{n+1}) \approx y_{n+1} = y_n + h \sum_{i=1}^{s} b_i k_i \tag{5.5}$$

with the auxiliary quantities k_i described by:

$$k_i = f\left(x_n + hc_i; h \sum_{j=1}^{s} a_{ij} k_j\right). \tag{5.6}$$

The coefficients b_i, c_i and a_{ij} are given through the so called Butcher tables [160]. Although the RK8 method needs 13 computation steps and the RK4 only 4, RK8 is the preferred method because the step size h can be chosen larger than in case of RK4 with equal numerical precision. Clever use of this advantage makes the computation about 10 times faster for RK8 than for RK4 [161].

5.2. Particle motion in general force fields

This section gives an example on how to apply the Runge-Kutta method to a physical problem. Given is a non-relativistic particle that is moving in a general force field and we aim to calculate its trajectory.
The motion of a particle in such a field can be written as a 1st order differential equation system:

$$\begin{aligned} \dot{x}_j &= v_j \\ \dot{v}_j &= \frac{1}{m} F_j(x_1, x_2, x_3; v_1, v_2, v_3; t) \qquad (j = 1, 2, 3) \end{aligned} \tag{5.7}$$

where x_1, x_2, x_3 are the Cartesian space coordinates, v_1, v_2, v_3 are the components of the particle's velocity, t is the time, m is the mass of the particle and F_j are the forces acting on it. The differential equation system (5.7) consists of 6 first order differential equations. The variables y_i $(i = 1, .., 6)$ are defined as:

$$\begin{aligned} y_i &= x_i \quad \text{for} \quad i = 1, 2, 3 \ \text{ and} \\ y_i &= v_{i-3} \quad \text{for} \quad i = 4, 5, 6. \end{aligned} \tag{5.8}$$

Equation (5.7) can now be expressed in terms of the derivative function f:

$$\begin{aligned} f(i, y_1, ..., y_6, t) &= v_i \qquad \text{for} \quad i = 1, 2, 3 \ \text{ and} \\ f(i, y_1, ..., y_6, t) &= \frac{1}{m} F_{i-3} \quad \text{for} \quad i = 3, 4, 5. \end{aligned} \tag{5.9}$$

With these realtions we are now able to calculate the trajectory of the particle via Runge-Kutta steps.

5.3. Charged particle motion in electric and magnetic fields

For the design and optimization of the KATRIN beamline, the calculation of trajectories of relativistic electrons is of central interest. Therefore a fast and precise way to compute the electron trajectories within electric and magnetic fields is of prime importance.
As is well known, a particle in an electro-magnetic field is experiencing a Lorentz force:

$$\vec{F}_{\mathrm{L}} = q \left(\vec{\mathcal{E}} + \vec{v} \times \vec{B} \right) \tag{5.10}$$

with q being the charge of the particle, $\vec{v}$ the velocity 3-vector, $\vec{\mathcal{E}}$ the electric field vector and the $\vec{B}$ magnetic field vector.

Again, we can write down a first order differential equation system, describing the motion:

$$\begin{aligned} \dot{\vec{x}} &= \vec{v} \qquad \text{and} \\ \dot{\vec{p}} &= \vec{F}_{\mathrm{L}}, \end{aligned} \tag{5.11}$$

where $\vec{v}$ and $\vec{p}$ are the velocity and momentum 3-vectors, respectively. In this case the variables y_i are defined by the momentum instead of the velocity:

$$\begin{aligned} y_i &= x_i \quad \text{for} \quad i = 1, 2, 3 \ \text{ and} \\ y_i &= p_{i-3} \quad \text{for} \quad i = 4, 5, 6. \end{aligned} \tag{5.12}$$

For the electrons we make use of the relativistic relations between velocity and momentum:

$$\begin{aligned} \vec{p} &= \frac{m\vec{v}}{\sqrt{1 - \frac{\vec{v}^2}{c^2}}} \qquad \text{and} \\ \vec{v} &= \frac{\vec{p}}{\sqrt{m^2 + \frac{\vec{p}^2}{c^2}}}, \end{aligned} \tag{5.13}$$

where m denotes the rest mass of the electron. Then the derivative functions are:

$$\begin{aligned} f(i, y_1, ..., y_6, t) &= v_i \qquad\quad \text{for} \quad i = 1, 2, 3 \ \text{ and} \\ f(i, y_1, ..., y_6, t) &= \frac{1}{m} F_{L,i-3} \quad \text{for} \quad i = 4, 5, 6. \end{aligned} \tag{5.14}$$

with v_i being calculated by making use of the relations from the equations (5.13). For further information see [162].

5.4. Field lines

When referring to of the motion of charged particles, the concept field lines might not be the first thing that comes to mind. In fact, calculation of field lines and particle trajectories are closely related to each other, as both are defined by a specific force.

In general, the calculation of field lines is a very important task in electro-magnetic simulations. It is essential when designing a new electrode geometry to optimize the electric potential along a magnetic field line to avoid Penning traps. It is even possible to approximate the actual electron trajectory with a field line, as the electrons perform a microscopic cyclotron motion around these field lines, thus saving computation time.

The differential equation system defining a field line of a three-dimensional vector field $\vec{A}$ is given by:

$$\frac{\mathrm{d}x_i}{\mathrm{d}s} = \pm \frac{A_i}{|\vec{A}|} \qquad (i = 1, 2, 3). \tag{5.15}$$

with s denoting the path. This equation system is time independent. Instead of a force that depends on location and velocity, the "force" in the case of field lines just depends on the position. As usual, we define y_i as variables for the Runge-Kutta method:

$$y_i = x_i \quad \text{for} \quad i = 1, 2, 3, \tag{5.16}$$

and the derivative functions f, which embed the "force":

$$f(i, y_1, y_2, y_3, t) = \pm \frac{A_i}{|\vec{A}|} \quad \text{for} \quad i = 1, 2, 3. \tag{5.17}$$

As the initial differential equation system (5.15) has only 3 components, the computation of field lines is pretty fast. By slightly modifying the "force", so that it points orthogonal to field vector, it is also possible to compute equipotential lines.

5.5. Adiabatic approximation

Charged particles flying through a time- and position-independent magnetic field perform a uniform cyclotron motion which can be described by a circular motion with its center moving along the magnetic field lines. If the magnetic field in fact depends on time or position, the trajectory is no longer given by an ideal cyclotron motion, but it is assumed as an approximately cyclotron-like motion. The basic idea of the *adiabatic approximation* is that the actual motion can be approximated by taking the ideal motion and adding some corrections to it.
At first the motion of the center of the cyclotron motion, the so called guiding center motion shall be described. It is very similar to the concept of field lines and given by the differential equation system:

$$\begin{aligned} \dot{\vec{x}} &= \frac{B_i}{|\vec{B}|} v_\parallel \qquad \text{and} \\ \dot{p_\parallel} &= -\frac{\mu}{\gamma} \vec{\nabla}_\parallel \vec{B} + q\mathcal{E}_\parallel, \end{aligned} \tag{5.18}$$

where $\mu = \frac{p_\perp^2}{2m|\vec{B}|}$ is the magnetic moment, $\gamma = \sqrt{1 + \frac{p_\parallel^2 + p_\perp^2}{m^2 c^2}}$ the Lorentz-factor and $\mathcal{E}_\parallel$ the electric field parallel to the magnetic field $\vec{B}$. The velocity $v_\parallel$, the momentum $p_\parallel$ and the gradient $\nabla_\parallel$ are parallel to the magnetic field as well.
The variables y_i are then defined as follows:

$$\begin{aligned} y_i &= x_i \quad \text{for} \quad i = 1, 2, 3 \quad \text{and} \\ y_i &= p_\parallel \quad \text{for} \quad i = 4. \end{aligned} \tag{5.19}$$

The derivative functions are again obtained by the force:

$$\begin{aligned} f(i, y_1, ..., y_4, t) &= \frac{B_i}{|\vec{B}|} v_\parallel \qquad \text{for} \quad i = 1, 2, 3 \quad \text{and} \\ f(i, y_1, ..., y_4, t) &= -\frac{\mu}{\gamma} \vec{\nabla}_\parallel \vec{B} + q\mathcal{E}_\parallel \quad \text{for} \quad i = 4. \end{aligned} \tag{5.20}$$

The guiding centre performs a longitudinal motion along the magnetic field lines. To approximate the real cyclotron motion, a motion transversal to the magnetic field lines has to be added.
With the adiabatic invariant $\mu = \frac{\gamma+1}{2} \frac{E_\perp}{|\vec{B}|}$ (see section 2.3.2) and the transversal momentum $p_\perp = 2\mu m |\vec{B}|$, the cyclotron radius can be expressed by:

$$r = \frac{\gamma m v_\perp}{q|\vec{B}|} = \frac{p_\perp}{q|\vec{B}|} \tag{5.21}$$

With the given step size of the Runge-Kutta step h and the cyclotron frequency $\omega = \frac{q|\vec{B}|}{m\gamma}$, the change of the azimuthal angle amounts to:

$$\Delta\varphi = \omega h \tag{5.22}$$

The cyclotron radius and the change of azimuthal angle completely describe the approximated transversal motion. They are simply added to the guiding center position at the end of the Runge-Kutta step, resulting in an adiabatic approximated step.
This approximation has proven itself to be very fast if the step size h is large. For small step sizes h, and especially when tracking close to an electrode, this approximation is often slower than the "exact" numerical solution, because it requires more electric field calculations, which are rather slow.
In general, the step size is controlled by monitoring of the energy conservation. If energy conservation within one step is not good enough, the step size is reduced and the step is redone. If it is sufficient, the step size for the next step is increased.
A gyrating electron performs an additional magnetron motion. This magnetron drift has also to be added separately to the step, for further informations see [163].

6. The KATRIN muon detector systems

In chapter 3 it was outlined that a major source of background in the KATRIN spectrometers is expected to be caused by secondary electron emission stemming from interactions of cosmic muons in the stainless steel vessel of the spectrometer tank and electrodes. Therefore it is very important for the experiment to study the nature and characteristics of the incident muons and their potential correlation with the background rate. To cover this, a muon detection system has been built, installed and commissioned at the monitor and main spectrometer experimental sites [164]. The following chapter will give a short overview of these systems and describe the properties that are of relevance in context of this work.

6.1. Scintillator

The muon detection systems at the main and monitor spectrometer are modules made of the premium-grade organic plastic scintillator Bicron BC-412. The material is composed of the synthetic polymer polyvinyltoluene doped with anthracene. The scintillator plates originate from the KARMEN [165] experiment and were refitted and, in same cases, cut for use with the KATRIN spectrometers.
A scintillator which is excited by ionizing radiation emits light via luminescence by absorbing energy from the incident particle.
Due to the anthracene-doping, this type of scintillator emits mainly blue light when charged particles like protons or cosmic ray muons pass through it, see fig. 6.1. BC-412 is designed for large area modules and thus has a long light attenuation length of 210 cm and a relatively high photon-yield of ∼8500 photons per MeV of deposited energy.

6.2. Photomultiplier

A PMT is a widely used device to detect faint light signals by photoeffect and further amplification by electron impact on a series of dynodes. It is composed of

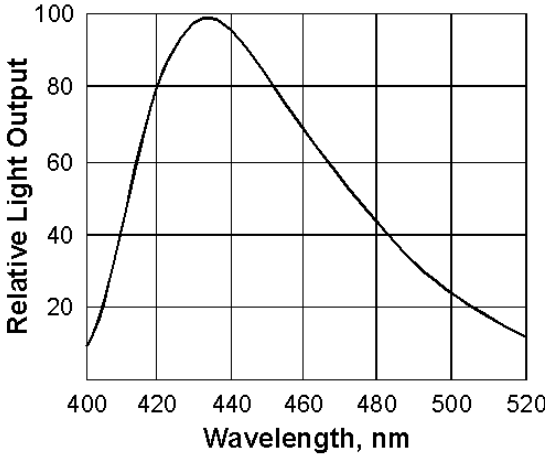

Figure 6.1.: **Scintillation-light BC-412** Emission spectrum of scintillation-light emitted by Bicron BC-412. Figure taken from the data-sheet of the scintillator [166].

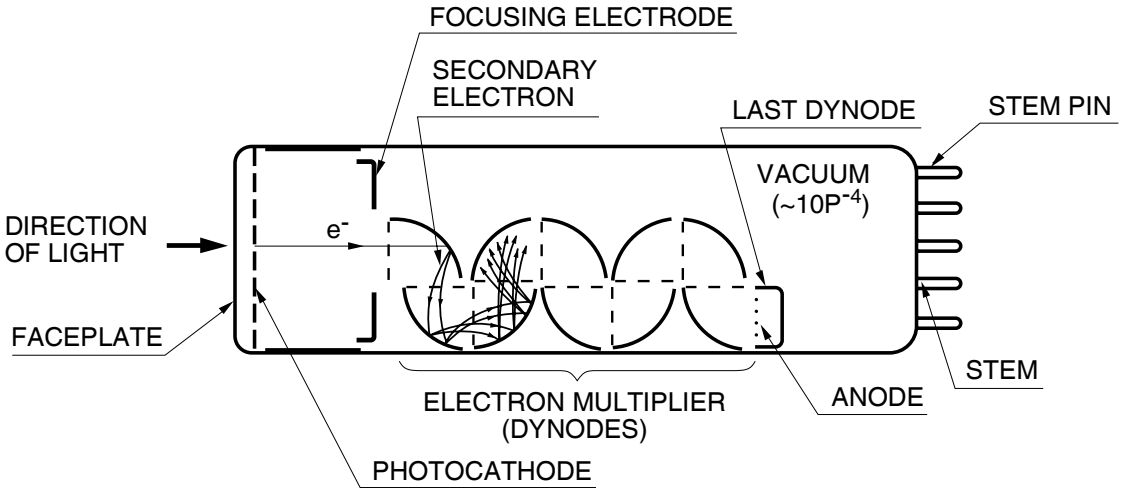

Figure 6.2.: **Working principle PMT** Sketch of a PMT taken from [167]

a photocathode with an attached electron multiplier in a vacuum casing (typically 10^{-7} to 10^{-8} mbar). When photons from the scintillation-light hit the photocathode, the bialkali emits electrons due to the photoelectric effect. The electrons have the maximal start-energy:

$$E_{\mathrm{kin,max}} = h\nu - \varphi \tag{6.1}$$

where h is the Planck-constant, ν the wavelength of the incident light and φ the work-function of the cathode-metal. The electrons enter the vacuum and are then electrostatically guided to the electron multiplier that consists of a chain of dynodes. These dynodes are each placed at a acceleration potential $U_{\mathrm{a}} = 100 - 200$ V more negative than the previous one. This results in a cascade emission of secondary electrons, as the kinetic energy of an electron rises by $e \cdot U_{\mathrm{a}}$ per pair of dynodes. The amplified signal can then be read out. Figure 6.2 shows a sketch of this working-principle and figure 6.7(a) shows an output signal of a 2-inch PMT of the type Philips Valvo XP 2262/PA in use here.

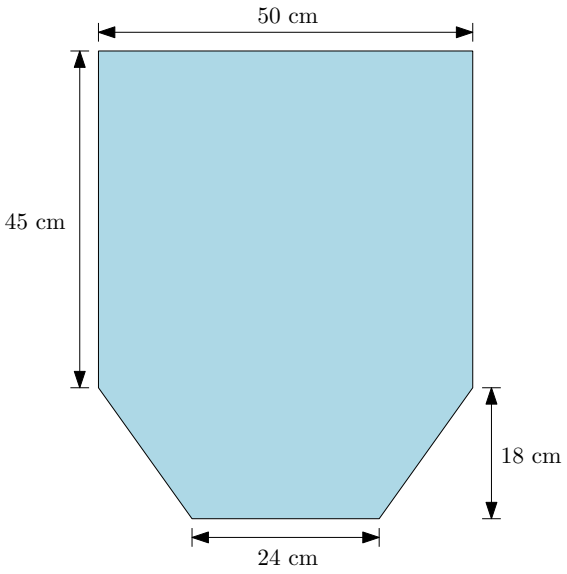

(a) Sketch of the sensitive area

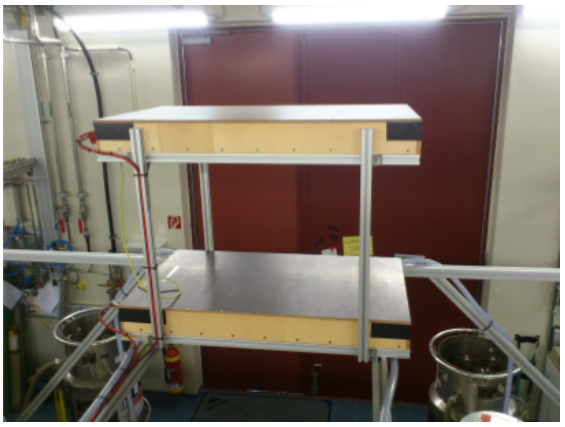

(b) Muon-paddles above monitor-spectrometer

Figure 6.3.: Pictures of the muon-paddles used at the monitor-spectrometer

6.3. Muon detector system at the monitor spectrometer

The muon detector system of the monitor spectrometer consists of two modules in flapper-like form. The BC-412 modules each have an area of 0.5 m^2 and a thickness of 5 cm. Each module has a two 2-inch PMT of the type Philips Valvo XP 2262/PA for read-out of the scintillation-light at the smaller front face.

The modules are situated 1.77 m and 2.37 m above the beam-axis of the monitor-spectrometer and are slightly closer to the source side at a maximal distance of 0.47 m to the analyzing plane. In figure 6.3 a picture of the arrangement above the monitor-spectrometer as well as a sketch of the used scintillator-piece are shown.

6.3.1. High-voltage supply and DAQ

The operation HV for the PMTs is supplied by two power supplies of the type Caen N-126, located in a Nuclear Instrumentation Module (NIM)-crate in the monitor-spectrometer DAQ-cabinet. Within the very same cabinet a IPE-Crate Mark III [168] is located, to which the output signals of the PMTs are connected via coaxial cables. Inside the crate, the signals are fed into a first level trigger (FLT)-card. The same crate also handles the electron-induced signals from the detector of the monitor spectrometer via a second FLT-card, so that all recorded events of the muon- and electron detectors share the same timing mechanism. The DAQ-crate is controlled and read-out by a PC running the object-oriented real-time control and acquisition (ORCA) software [169].

6.4. Muon detector system at the main spectrometer

The muon detector system at the main spectrometer consists of eight long scintillator modules that are arranged in three towers (see figure 6.5). similar to the system of

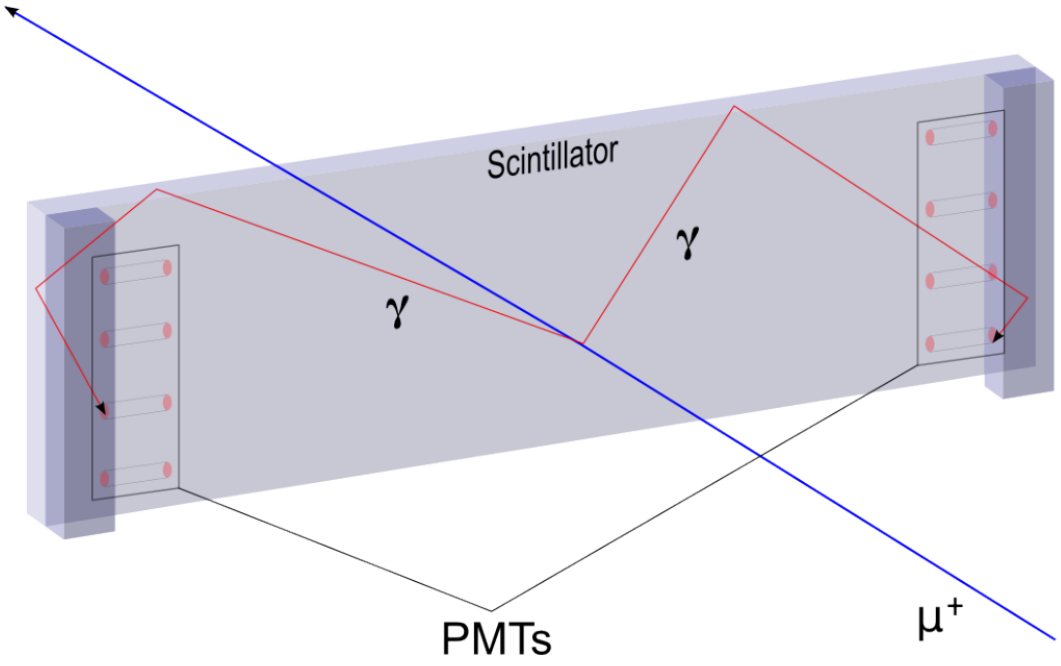

Figure 6.4.: **Sketch of muon-panel at the main spectrometer** At the short ends the light-guides and the surmounted PMTs are visible. Figure taken from [165].

the monitor spectrometer, the modules are based on the organic plastic scintillator Bicron BC-412. They are of rectangular shape with dimensions of 3.15 m × 0.65 m and a thickness of 5 cm. The resulting sensitive area of a single module accounts to 2.05 m^2.
The scintillation light is detected by an array of four 2-inch PMTs of the type Philips Valvo XP 2262/PA on each front side of the modules. To further increase the detection efficiency of the PMTs [165], they are connected to the scintillator via intermediate light-guides. Figure 6.4 shows a sketch of one module with PMTs attached.

In order to cover a large area of the main spectrometer surface, the modules are positioned very close to the LFCS. The air coils are responsible for magnetic fields up to 1 µT inside the PMTs which causes a deviation of the electron paths in the dynode system due to $\vec{\mathcal{E}} \times \vec{B}$-drift so that the amplifier cascade is interrupted. The ultimate consequence of this strong field is that the PMTs operating within it had to be shielded from the external magnetic field, by wrapping with multiple layers of permalloy-foil. This made it possible to operate the PMTs in strong magnetic fields during the measurements [170].

6.4.1. High-voltage supply and DAQ

The PMTs are fed with a high-voltage of about 1.5 kV, which is supplied by two Caen SY-127 units [171]. Each unit features 10 output lines, so that each side of a module is fed by a separate HV-line.
The signals of the PMTs are passively added during readout and guided to the DAQ-system by 25 m long coaxial-cables with 50 Ω impedance. The cables introduce a

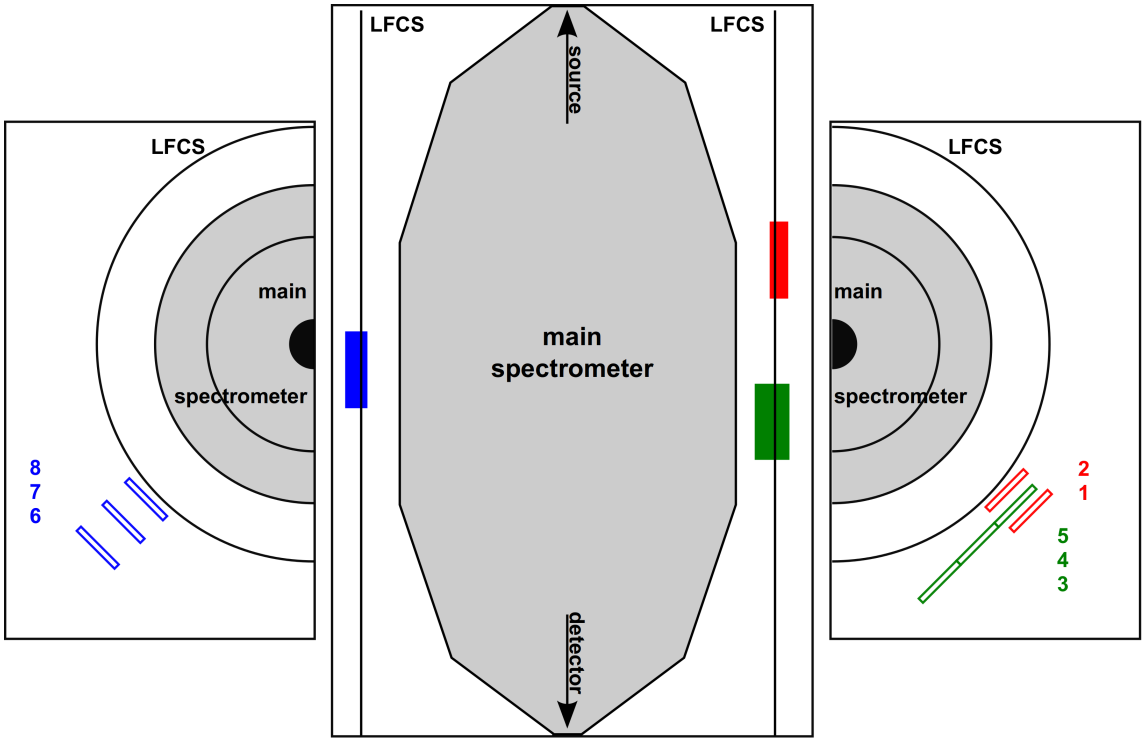

Figure 6.5.: **Muon-tower arrangement** Arrangement of the muon panels on their holding-structures around the main spectrometer. Image after [164].

signal propagation delay of about 15 ns. The signals are fed in into a so called, IPE-Crate Mark IV [168] via connector-boards. The crate is equipped with FLT-cards that have a built-in coincidence-filter: only events registered on both ends of a module are passed to the second level trigger (SLT) and from there to the DAQ-PC that is running the ORCA-software [169]. In order to allow a combined analysis of data from the muon detector and the FPD-system, a global positioning system (GPS)-clock is connected via fibers to both DAQ-crates, which synchronizes the time counters of both systems [172]. The assignment of the module-signals to the DAQ-channels can be found in table 6.1.

6.4.2. Signal processing and coincidence

The energy loss signal of cosmic ray muons in the scintillator is characterized by the well-known Landau form, an example of the Landau maximum and the high-energy

Table 6.1.: **Channel assignment muon-detector-system** Assignment of muon counter modules to FLT cards and channels.

Module	1A	1B	2A	2B	3A	3B	4A	4B
Card	3	3	3	3	6	6	6	6
Channel	0	14	3	7	0	14	3	7
Module	5A	5B	6A	6B	7A	7B	8A	8B
Card	6	6	8	8	8	8	8	8
Channel	9	23	0	14	3	7	9	23

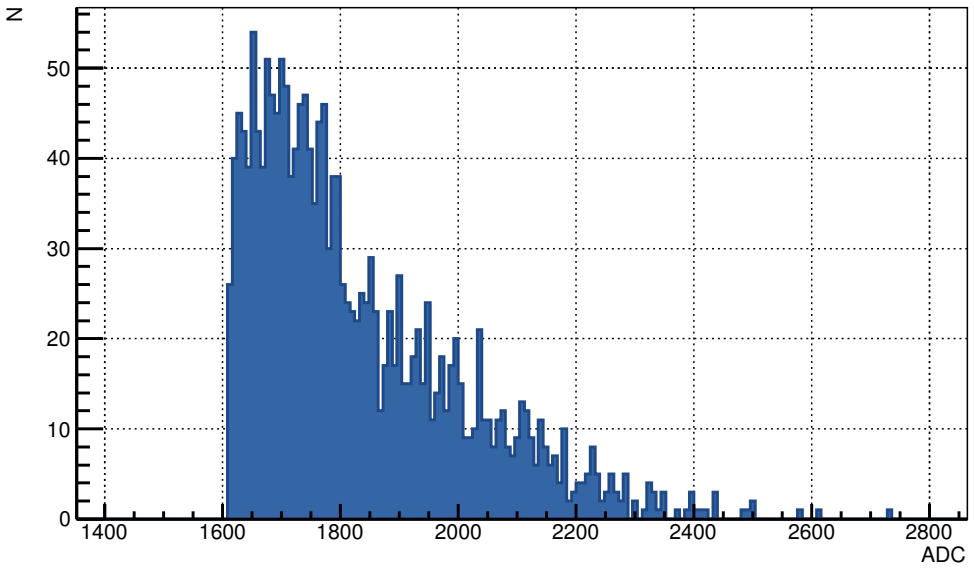

Figure 6.6.: **ADC signal of cosmic ray muons in a BC-412 module** Pulse height distribution of PMT signals in a measurement with the muon detector. The Landau maximum corresponds to 11 MeV for vertical muons.

tail of the ADC-spectrum is shown in figure 6.6. In order to study coincidences and correlations between incident muons and secondary electron emission it is important to study the time-shape of the signal.

It is evident that when searching for coincidences between muon-events and FPD a sufficiently precise determination of event times is needed. The initial triggering of the event is done by applying a so called *Boxcar*-filter. It computes a floating average of the signal in a given time-window t_{BC}. As soon as the filtered signal exceeds the threshold value the event trigger is released. The filtered signal is then run through a *Trapezoidal*-filter with the shaping length t_{T}. This filter subtracts the integral of the input signal in the first half of the time window given by the shaping length from from the integral of the input-signal in the second half. The filtered signal will feature a zero-transition. The time of this zero-transition is modified by 3/2 of the shaping length of the trapezoidal-filter is taken as the event-time of a muon event. Depending on the used time-windows t_{BC} and t_{T} and the initial signal shape this time has an uncertainty of up to $2\times t_{\mathrm{BC}}$ which during measurements typically was 0.3 µs for the muon detector system at the main spectrometer. The single signal-processing steps are shown in figure 6.7.

6.4.3. Long-term operation

When investigating muon-induced background in spectrometers, it is interesting to note that the muon flux on the surface of the Earth is not constant but exhibits fluctuations. This also means that the secondary electron emission in the main spectrometer and thereby the background in the experiment will not be constant over the entire measurement time but should follow the fluctuation of the cosmic-ray-flux.

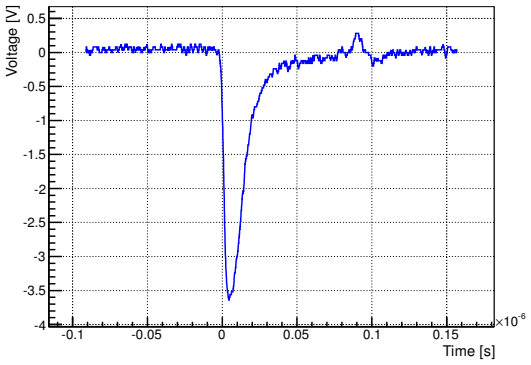

(a) signal-output of PMT

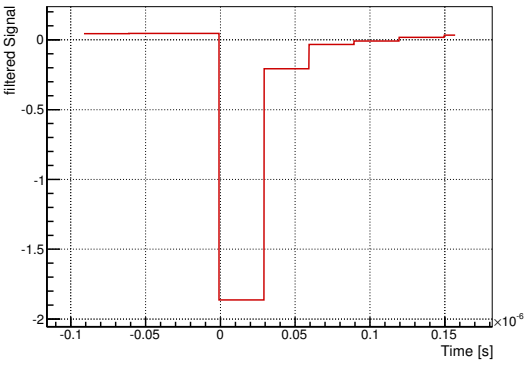

(b) boxcar-filter applied

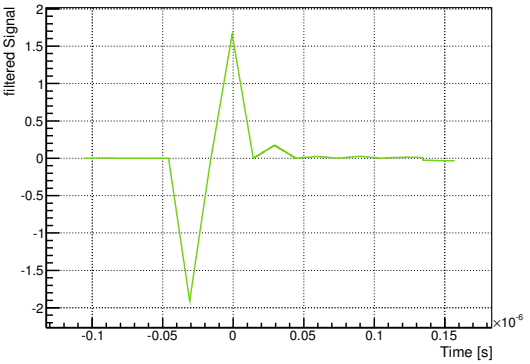

(c) trapezoidal filter applied

Figure 6.7.: **PMT time-signal processing chain** In (a) a PMT signal measured with the oscilloscope is shown. Software-filter were subsequently applied to the measured signal: In 6.7(b) a boxcar-filter was applied and then in 6.7(c) again a trapezoidal-filter was applied to the filtered signal. Figure after [173].

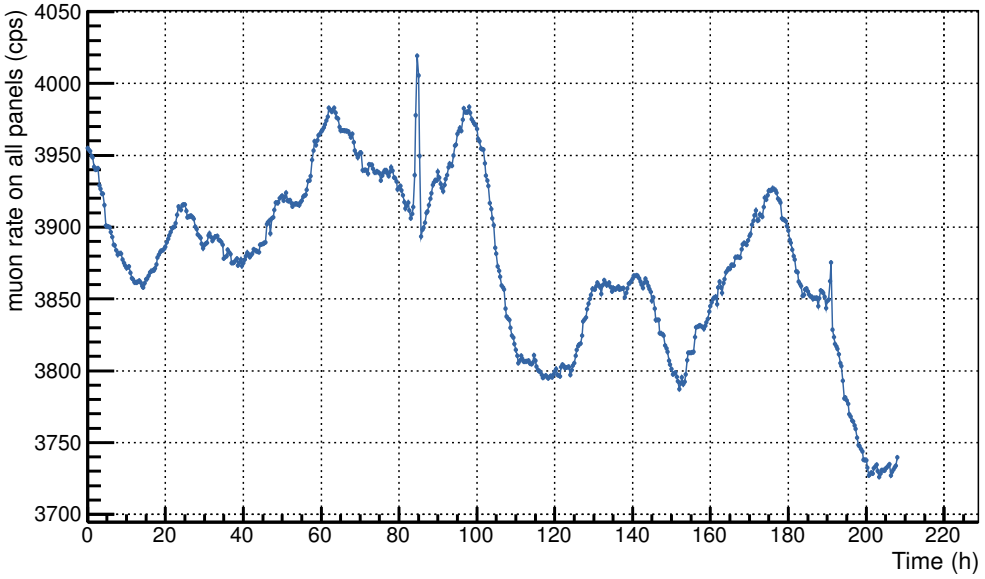

Figure 6.8.: **Longtime measurement muon-rate** Measurement of the 20 min average of the summed rates at muon panels 1-8. Measurement started at 21.12.2013, 10 am. Mean total rate was 3876 cps.

The ab-initio cosmic ray muon intensity I_{CR} depends solely on the flux of high energy cosmic particles on the Earth atmosphere, this is generally called *space weather*. However, to model the fluctuations of the intensity of flux of cosmic ray muons on sea level $I_{\mu,\mathrm{NN}}$ one has to take additional factors into account: The fluctuation is closely related to the variation of the production height Δh ($\bar{h} \approx$15 km) of the muons, which determines how long they have to travel to reach the ground. Also, the fluctuation of the atmospheric density, which is described by variations of the pressure Δp and temperature of the ΔT is important. The density determines how much energy the muons lose on their way through the atmosphere. The relation between the initial intensity I_{CR} of cosmic ray muons and its intensity at sea level I_{NN} is then given by [174]:

$$I_{\mathrm{NN}} = I_{\mathrm{CR}} \cdot (1 - \alpha_\mu \Delta p + \beta \Delta h - \gamma \Delta T) \tag{6.2}$$

Here, α_μ denotes a muon-specific barometric coefficient (2.15×10^{-3} / mmHg), β an average decay coefficient (0.005 / km) and γ a temperature coefficient (0.001 / K).

In figure 6.8 a longtime measurement of the summed rate in all muon-panels over the course of several days is shown. The mean total rate was 3876 cps with maximum fluctuations of up to 3% observable from the average.
Such a large variation can not be left unaccounted. Therefore it is planned to keep the muon detector system operational during the whole measurement-period of KATRIN to monitor the incident muon-flux. In addition, the efficiency of the panels will have to be regularly checked with calibration sources.

7. Measurments at the monitor spectrometer

The KATRIN monitor spectrometer is targeted to give precision information on the HV stability of the KATRIN experiment. It achieved operation readiness in early 2011 and since then has been a test facility for experiments and studies to be performed later at the main spectrometer. In particular, the monitor spectrometer is equipped with a muon-detector system, making it a unique testbed for measurements with symmetric and asymmetric magnetic fields to study secondary electron emission.
The beamline of the monitor spectrometer is not equipped with a PAE, this means that electrons have to obtain an energy of at least 6 keV to surpass the detection threshold. For this reason, no measurements with zero potential were performed, as incoming secondary emission electrons with typical energies below 50 eV would not have been discriminated from detector noise. All measurements in this chapter were run with a HV of -30 kV applied to the tank. In measurements where the wire-electrode voltage was varied, an additional power supply was used to apply voltages of up to -33 kV to them.

7.1. Magnetic field-setup

In preparation for the measurements extensive simulation studies were performed in the framework of this thesis. For all measurements with asymmetric field configuration it was crucial to select a magnetic field configuration where the part of the spectrometer which was monitored by the muon detector system was mapped onto the detector. At the same time, this configuration should feature a maximized magnetic field on the electrode surface under investigation to minimize the magnetic mirror effect. By doing so, a maximum number of secondary electrons from the electrode will reach the detector.
The monitor-spectrometer features two super-conducting solenoids (S_{source}, $S_{detector}$), three circular coils (C_{inner}, $C_{central}$, C_{outer}) and a set of cosine-coil systems ($EMCS_{hor}$, $EMCS_{ver}$) to compensate the horizontal and the vertical component of the Earth magnetic field. The configurations for the symmetric and asymmetric layouts are

Table 7.1.: **Magnetic field-setups monitor-spectrometer** Solenoid-, air-coil- and EMCS-current settings for measurements at the monitor spectrometer. Positive current generate magnetic fields pointing towards the detector

	S_{source}	S_{det}	C_{inner}	$C_{central}$	C_{outer}	$EMCS_{hor}$	$EMCS_{ver}$
asymmetric	0.1 A	13 A	0 A	-2 A	-2 A	0 A	0 A
asymmetric FE	0.1 A	50 A	0 A	-8 A	-8 A	1.68 A	-19.5 A
symmetric	25 A	25 A	2.5 A	-4 A	-9 A	1.68 A	-19.5 A

shown in table 7.1.
The calculated magnetic flux tubes for all three configurations are displayed in figure 7.1. As outlined, the asymmetric configurations minimize the reflection of electrons from the wall due to the magnetic mirror effect: In the "asymmetric" configuration the focus was on the mapping of the target area that is surveyed by the muon-detector. The symmetric configuration has a reduced magnetic field in order to reduce the magnetic shielding so as to maximize the number of electrons from the wall for better statistics.

7.2. Measurements of the secondary electron emission

In the following we report on the measurements with the asymmetric configuration "asymmetric" where the wire and solid electrodes were kept on the identical potentials to measure the unscreened secondary rate.

7.2.1. Secondary electron rate

Figure 7.2 shows the rate trend of this 3 h measurement. The average rate accounted to (1.33±0.01 cps) for the surveyed area of 0.16 m^2. To obtain the total emission rate over the entire monitor spectrometer surface a simulation was performed. Electrons were started equally distributed over the entire area surveyed by the flux tube and with isotropically distributed starting angles. The starting energies were selected to between 0.1 and 50 eV. A total of 5×10^5 electrons were started, of which a fraction of 7.07×10^{-2} were guided to the detector. With this probability, the true secondary emission rate should account to 120 electrons m^{-2} s^{-1}. This calculated value is compatible with the measurements from the pre-spectrometer, where an emission rate of 165 electrons m^{-2} s^{-1} was measured [103].

7.2.2. Secondary rate as function of the wire-voltage

The inner electrode of the monitor spectrometer consists of thin wires to reduce background from secondary electrons originating from the outer solid electrode. This unique configuration is of particular interest for measurements with asymmetric magnetic fields. In this case, one can look at secondary electrons from the full electrode and vary the potential of the inner electrode. Electrons with a longitudinal energy relative to the magnetic field larger than the potential difference will pass the wires and can be counted at the detector. It is thus possible to measure an integrated $E_{\parallel}$-spectrum of secondary electrons, which is closely connected to the total kinetic

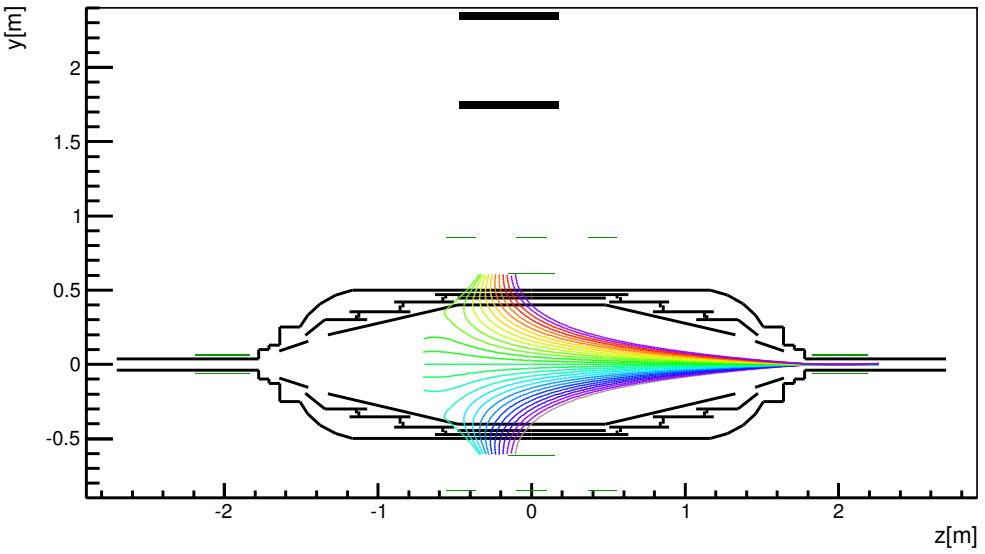

(a) "asymmetric" flux-tube with positions of the muon paddles

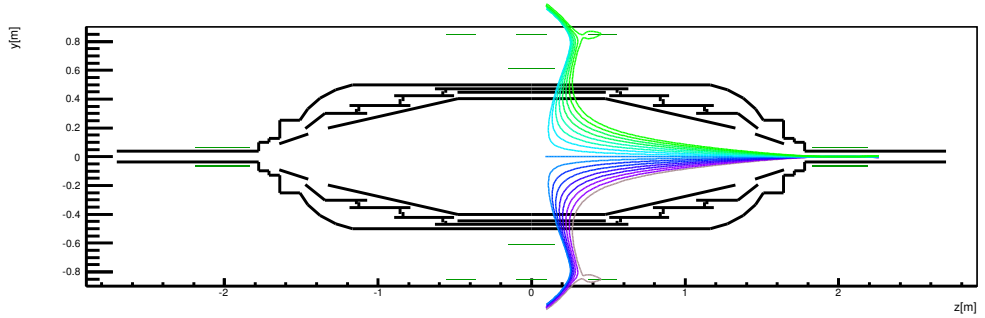

(b) specific "asymmetric FE" flux tube

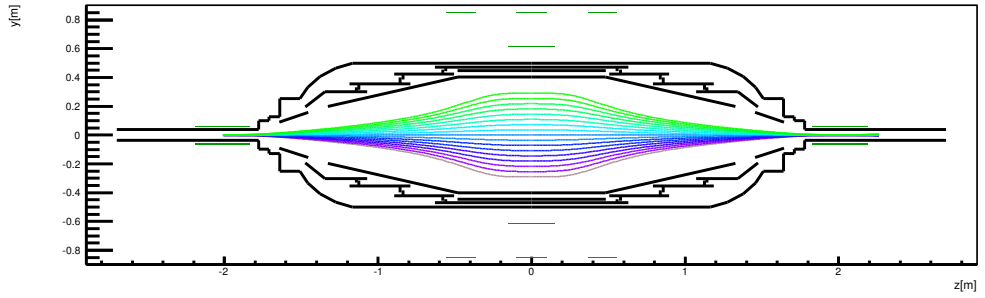

(c) "symmetric" flux tube

Figure 7.1.: **Magnetic flux tube configurations at the monitor spectrometer** Here, magnetic flux tubes for the configurations described in table 7.1 are visualized. The detector is located at z=2.27 m and has a radius of 0.7 cm. In (a) the muon-paddles (black) are shown above the spectrometer.

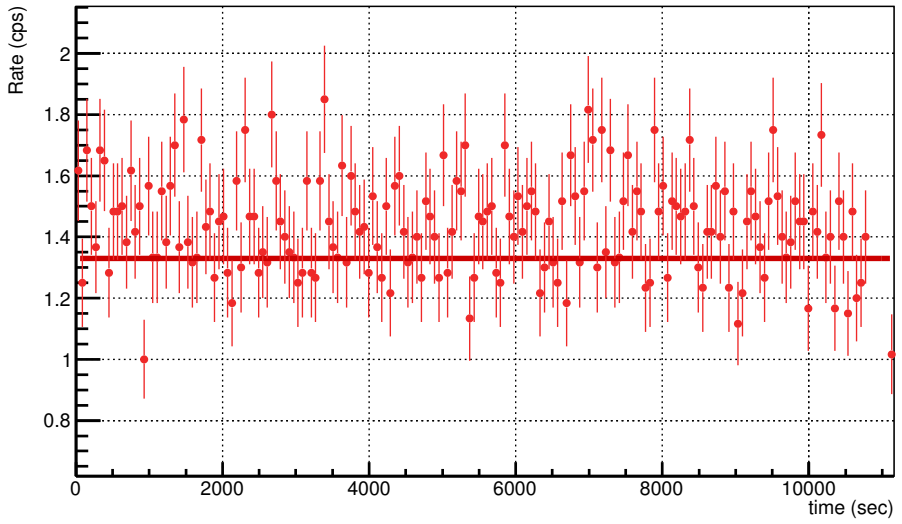

Figure 7.2.: **Secondary electron rate at the monitor spectrometer measurements with asymmetric B-field** Measured secondary electron rate in the "asymmetric" configuration. The average rate accounts to (1.33±0.01) cps.

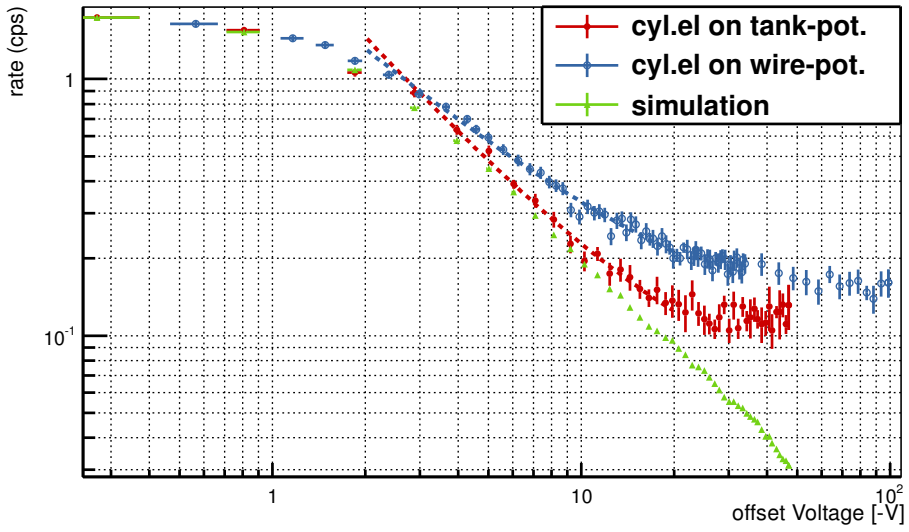

Figure 7.3.: **Secondary electron rate as a function of the wire offset voltage in asymmetric B-field configuration** Measurement of the secondary electron rate at the detector when varying the potential offset on the wire electrode. Two measurements are shown employing both (blue) and only the most inner layer of the wire electrode, together with the simulated rate for a single layer inner electrode (green). Here, the magnetic field setup was "asymmetric FE". Measurement time per voltage setting was 600 s.

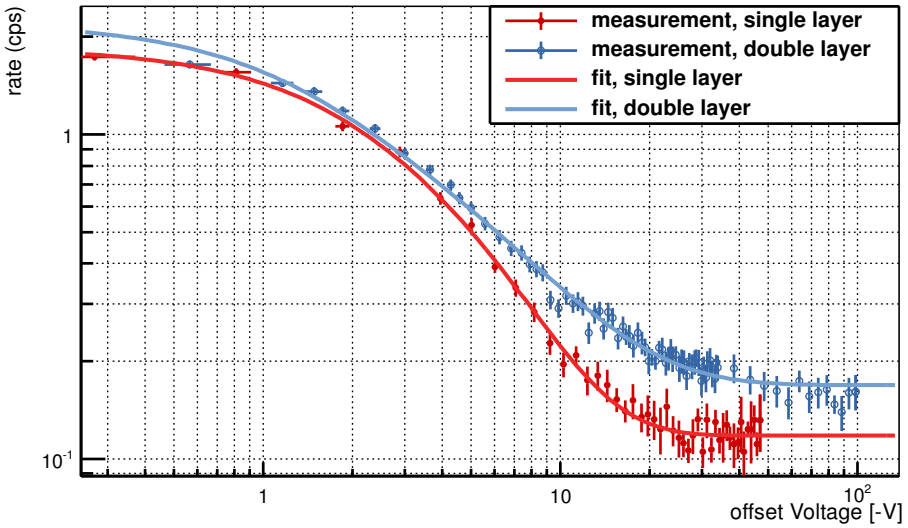

Figure 7.4.: **Fit to data of wire electrode measurement at the monitor spectrometer** Here a fit based on equation 7.3 was applied to the rate as a function of offset voltage measured at the monitor spectrometer.

energy-spectrum.

In figure 7.3 the shielding effect of the wires is shown. In one case the solid and outer wire electrode were short-circuited and elevated onto -30 kV and the potential of the inner wire electrode was varied. In the other case, inner and outer wire layer were short-circuited and their potential was varied. The magnetic field setup "asymmetric FE" was used in both cases.
For offset voltages over 3 V the measurements show a steep decrease of the rate with a power-law like distribution ($\lambda_1 = -(1.29 \pm 0.12)$, $\lambda_2 = -(1.02 \pm 0.01)$) and a plateau above about 20 V. The residual emission rate observed originates from the support structure of the wire electrode which is not shielded by the wires.
For the simulation, a simplified monitor spectrometer geometry was used, featuring only one layer of the wire electrode. The electrons were started at the solid electrode with an isotropic angular and a typical secondary electron energy distribution. Due to the fact that no electrons were started from the wires, the simulated spectrum at the detector features no characteristic plateau like the measured spectra.
The simulation further showed, that an electron from the wall has to overcome two barriers to reach the detector: First, its energy $E_\parallel$ parallel to the magnetic field has to be greater than the offset voltage:

$$U \leq E_\parallel = \cos^2\theta \cdot E \quad \Rightarrow \quad \cos\theta \geq \sqrt{\frac{U}{E}} \tag{7.1}$$

And second, its emission angle to the magnetic field θ has to be small enough to overcome the magnetic mirror effect ($\theta \leq \theta_{\text{lim}}$):

$$\alpha(U,E) = \int_{\theta_{\text{lim}}}^{1} \mathrm{d}\cos\theta \;\; \cos\theta \equiv 1 - \cos^2\theta_{\text{lim}} \equiv 1 - \frac{U}{E} \tag{7.2}$$

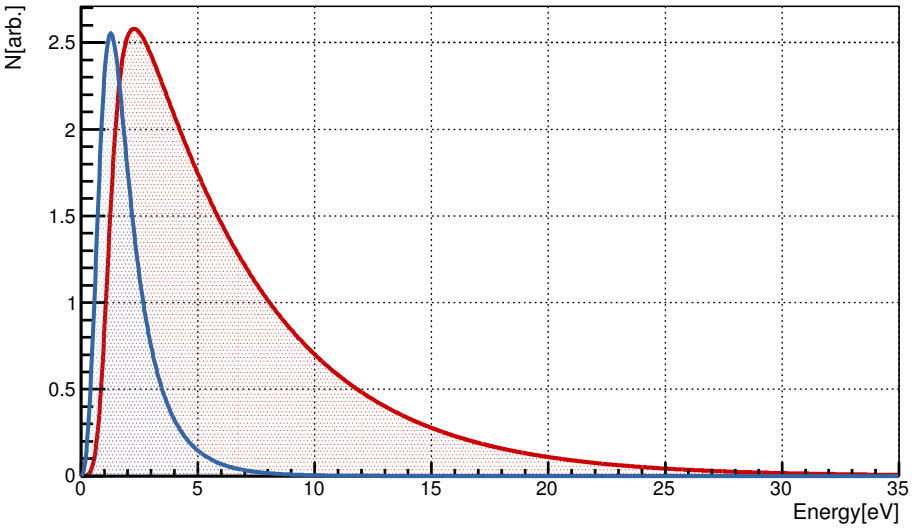

Figure 7.5.: **Approximated energy spectra $F(E)$ of secondary electrons from the solid electrode** Here the approximated secondary energy spectra obtained by fits of equation (7.4) to the experimental data are shown. The spectrum for the double wire layer (blue) shows a significantly narrower energy peak ($E_{\text{peak},1} = 1.3$ eV, $E_{\text{peak},2} = 2.2$ eV) than the spectrum of the single layer measurement (red).($p_1 = 4.26 \pm 0.11$, $\epsilon_1 = 5.3 \pm 0.41$, $s_1 = 4.22 \pm 0.12$, $p_2 = 2.42 \pm 0.07$, $\epsilon_2 = 1.79 \pm 2.02$, $s_2 = 3.50 \pm 0.07$).

For such a simplified case, the rate R at a certain offset Voltage U can be expressed by:

$$R(U) = \int_U^\infty \mathrm{d}E \left(1 - \frac{U}{E}\right) \cdot F(E) \tag{7.3}$$

Here $F(E)$ denotes the energy spectrum of the emitted secondary electrons, it is most commonly described by the approximation [108]:

$$F(E) = D(E) \cdot E^{(p-1)} \cdot e^{-\frac{E}{\epsilon}} \qquad \text{with} \quad D(E) = \frac{s \cdot E}{s - 1 + E^s} \tag{7.4}$$

where p, ϵ and s are adjustable parameters. By fitting equation 7.3 to the measured data, it was possible to fine-tune the energy spectrum so that simulated and measured data agree to each other. The fit to the data is shown in figure 7.4 and the resulting energy spectrum is shown in figure 7.5. As expected from the theory (see section 3.3) the distribution shows a peak at low Energies (E_{peak} =(1.3 - 2.2) eV) and a steep decrease towards higher energies.

7.2.3. Muon coincidence with secondary electrons

During the measurements with the "asymmetric" magnetic field-configuration , the muon-detector was continuously taking data. This allows tp search for coincidences between incident muons in the paddles and secondary electrons at the detector. In order to define an optimized coincidence time window, a tracking simulation was done. Here, μ-induced electrons were started evenly distributed on the surface of the solid electrode with isotropic starting-angles and energies from 0.1-50 eV. Figure 7.6

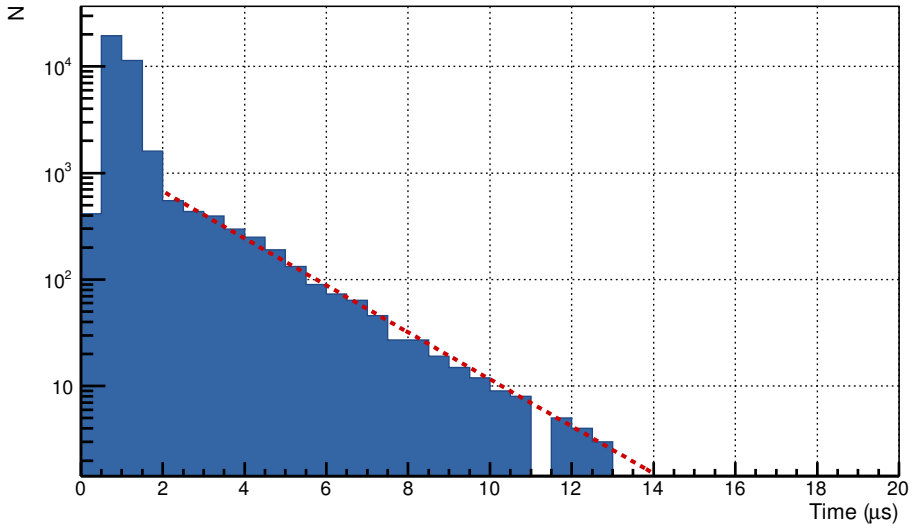

Figure 7.6.: **Simulation of electron travel times** Calculated travel times of electrons originating at the solid electrode and reaching the detector. Start energies in the interval 0.1-50 eV, starting angles were distributed isotropically. The tail of the distribution decreases exponentially($\lambda = -(0.51 \pm 0.01)$).

shows the travel time of these simulated secondaries starting from the solid electrode. The average travel time is 0.94 µs (Full Width Half Maximum (FWHM)=0.56 µs), while the slowest electrons take up to 20 µs to reach the detector.

Based on this information, a coincidence search between muons and secondary electrons was performed by looking for electron events at the detector in a time window of τ_c =20 µs after each muon event. Figure 7.7 shows the resulting distribution of time differences observed in a 4 h time interval. A clear peak is visible with a FWHM=2.1 µs which is shifted by 2.08 µs in comparison to the simulation. This effect arises from the limited timing accuracy of the monitor-spectrometer DAQ system causing the signal broadened and shifted.

Interestingly, a total of 9 muon-electron coincidences was observed where two electrons were registered by the detector within the coincidence time window τ_c =20 µs. These events can either be two electrons that were created by the same muon or stem from accidental coincidences. The probability for an accidental coincidence can be estimated: The average electron rate during the coincidence measurements was N_2 =1.33 cps, meaning that the average time-interval between two electrons was 0.75 s. We now calculate the probability p_{acc} for an accidental coincidence between a true muon-electron sequence with a second, accidental electron according to:

$$p_{acc} \sim N_1 \cdot N_2 \cdot \tau_c \tag{7.5}$$

with a true coincidence rate of $N_1 = 1.5 \times 10^{-2}$ cps (see figure 7.8), the average electron rate N_2 =1.33 cps, and the coincidence time window $\tau_c = 2 \times 10^{-4}$ s we derive $p_{acc} = 4 \times 10^{-7}$, so that for a 4 h measurement time the number of accidental coincidences is expected to be 5.7×10^{-3}.

Figure 7.8 shows a number of double electron hits that clearly exceeds the expected accidental electron coincidences. These double electron hits originate from interac-

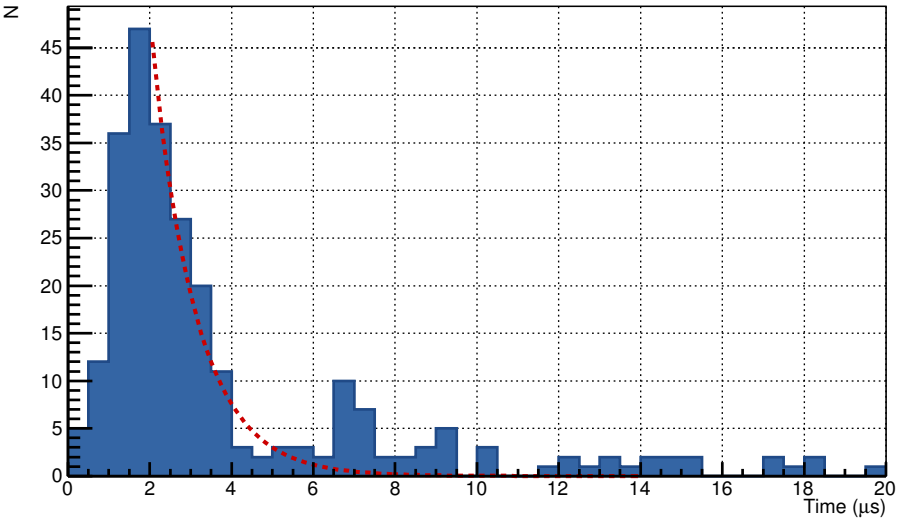

Figure 7.7.: **Mesured electron travel-times** Measured time difference of electron-detector signal after hit in the muon-paddles. As for the simulation, the tail of the distribution decreases exponentially ($\lambda = -(0.93 \pm 0.12)$).

tions, where one muon created two electrons simultaneously that were able to reach the detector.
If we assume an isotropic angular distribution of secondary electrons and a vanishing angular correlation between the electrons of a multi-hit sequence, we would expect a ratio of $1 : 2.5 \times 10^{-2}$ of single electron coincidences to multi electron coincidences. In fact we measure a ratio of $1 : 4.4 \times 10^{-2}$ which is in good agreement to the simulation.

7.3. Field emission

To test the characteristics of field-emission of the wire electrode of the monitor spectrometer, measurements with high offset voltage between the wire and solid electrode of the monitor spectrometer were performed. In these measurements, the tank voltage was set to -30 kV and the wire offset voltage was varied up to -3.1 kV. The goal was to provoke field-emission at the wires, thereby getting a handle on the a priori unknown electric field strengths that induce such a process. Measurements with both asymmetric and symmetric magnetic field configurations were performed, and in both cases field emission of electrons was clearly visible.
At first, we discuss the measurements with the asymmetric magnetic field set-up, where the detector looks directly onto the surface of the solid electrode ("asymmetric FE"). In figure 7.9 the measured rate over the difference voltage is shown. The onset of field-emission is localized at about -2 kV and produces an almost exponential rise of the rate.
It is possible to calculate the local surface electric field F at the emission point using the rate-trend over voltage. The F-N-equation (3.3) can be modified to be applicable to our data, using the substitutions:

$$\begin{aligned} J &= c_1 R \qquad \text{and} \\ F &= c_2 \Delta U \end{aligned} \tag{7.6}$$

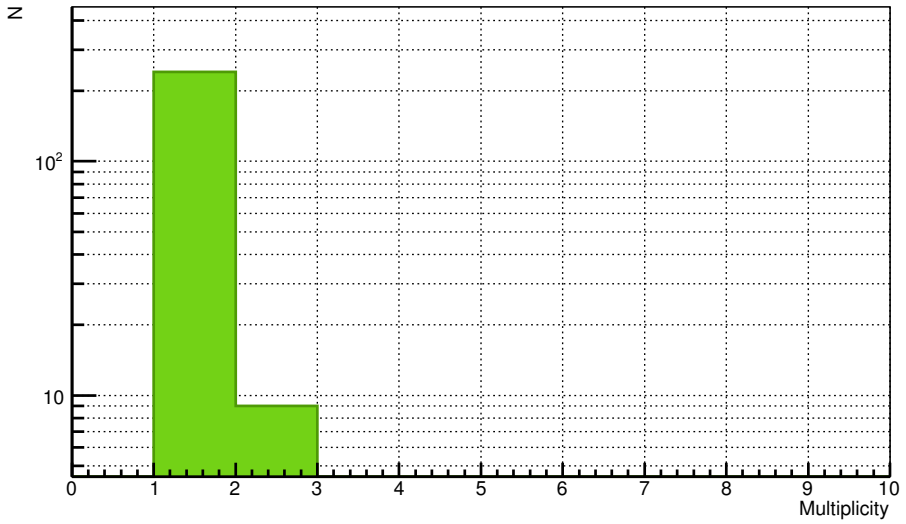

Figure 7.8.: **Electron-cluster-sizes** Number of electrons arriving in the 20 µs-window after a muon hit.

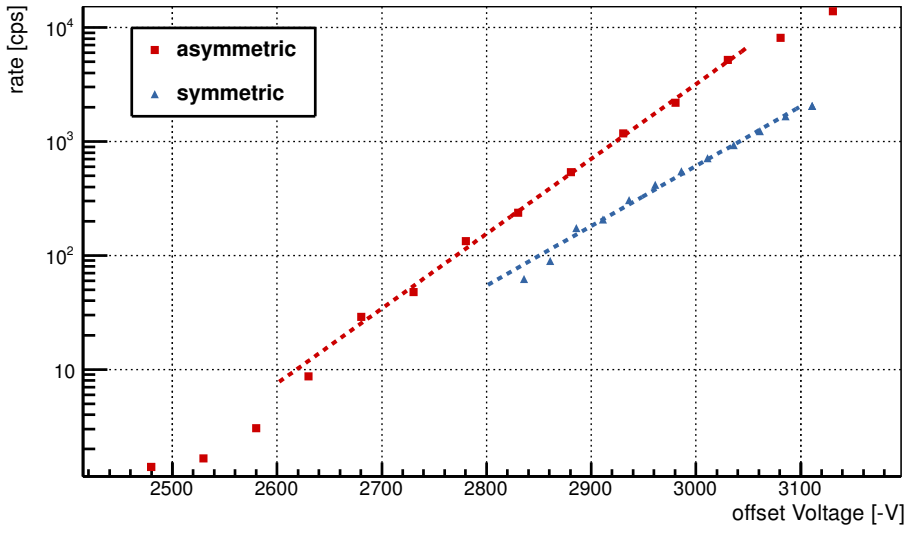

Figure 7.9.: **Field electron emission rate for asymmetric and symmetric set-up** Here the rate at the detector as a function of voltage offset between the solid and the wire electrode is displayed. The process of field emission starts above -2 kV and causes an exponential rise ($\sim e^{\lambda \cdot \Delta U}$) of the electron-rate ($\lambda_{\text{symm}} = (1.51 \pm 0.01) \times 10^{-2}$, $\lambda_{\text{asymm}} = (1.21 \pm 0.02) \times 10^{-2}$).

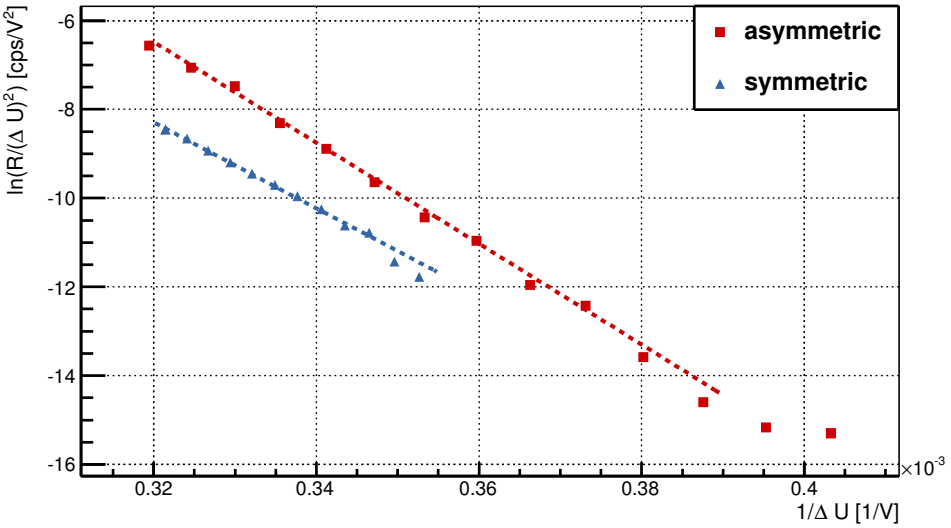

Figure 7.10.: **Fowler-Nordheim type plot** of the rate as a function of the offset voltage with asymmetric and symmetric magnetic field.

This allows for the theorem to be rewritten in a way, so that it follows a linear progression:

$$\ln\left(\frac{R}{\Delta U^2}\right) = -\frac{b\phi^{3/2}}{c_2} \cdot \frac{1}{\Delta U} \ln\left(\frac{c_1\phi}{ac_2}\right) \tag{7.7}$$

In figure 7.10 we see the measurement with asymmetric magnetic field in a F-N-type plot. From the slope of the linear fit to the data and employing an unreduced thermodynamic work function of stainless steel ϕ =4.4 eV we deduce an emission electric field strength of $F = (1.54 \pm 0.03)$ GV/m. This value of F is characteristic for F-N-type field emission.
If we compare this fit value to simulations of the electric field near the wires, shown in figure 7.11, we find a maximum $\mathcal{E}$ =1.5 MV/m, 3 orders of magnitude below the value of F.
The reason for this discrepancy can be traced to surface condition, which is not considered in the field-simulations. Surface roughness and irregularities on the surface amplify the emission field strength $F = \beta \cdot \mathcal{E}$. The enhancement factor for the electric field $\mathcal{E}$ can account to up to $\beta = 10^3$ [175], which is in good agreement with the observed amplification in this measurement.
The measurement was then repeated with a symmetric magnetic field configuration. To increase statistics, the field of the solenoids was lowered, so that a larger part of field emission electrons from the wires can penetrate through the magnetic shielding. Again, in figure 7.9 the rate is shown as a function of the offset voltage. Now, the detector is screened by magnetic shielding the rates typically are a factor 5-10 lower than in the asymmetric configuration. Interestingly however, the same exponential rate-rise is visible in the plot.

The representation described in equation 7.7 can also be applied to the data with symmetrical magnetic field. In figure 7.10 the plot is shown, the corresponding fit results into a emission field strength of $F = (1.81 \pm 0.04)$ GV/m which is slightly larger than in the asymmetric measurement. It is unlikely that this is caused by

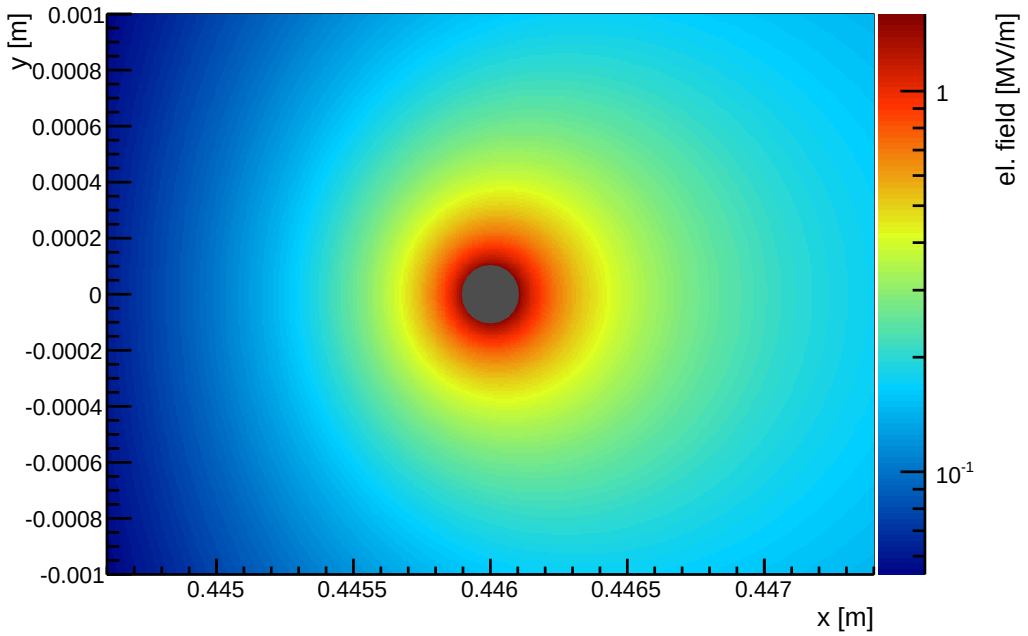

Figure 7.11.: **Electric field simulation of an inner electrode wire** Simulated map of the electric field strength around a wire of the inner wire electrode ($\varnothing = 0.3$ mm) of the monitor spectrometer. The potential difference between the outer solid and inner wire-based electrode was set to -3 kV.

non-field-emission processes but rather points to a slightly larger value of β when averaging over the entire spectrometer setup.

In conclusion, it has been demonstrated that electron field emission can be generated between the solid and the wire electrode of the monitor spectrometer. The rather high surface factors that result from the F-N-plots point to a fact already stated in the literature [176] that the F-Ntheorem in its elementary form can over-predict the field emission strength by a large factor between 10^3 and 10^9 in comparison to the technical complete form. However the complete form can not be applied to our data to calculate the emission-field-strength as it presumes detailed knowledge of the surface structure on a microscopic scale. The general F-N theorem gives however a qualitative estimation and in particular it allows to detect, if electron field-emission is present as background component or not.

8. Measurements at the main spectrometer

In the course of the SDS-Comissioning Phase I [95] of the KATRIN main spectrometer a specific focus was on the detailed study and characterization of secondary electrons coming from the vessel walls and electrodes. Various measurements were carried out employing both symmetric and asymmetric magnetic field configurations. In addition, the muon detector system described in chapter 6 was taking data to gather complementary data on the origin of the secondary electrons. In the following chapter these measurements will be presented together with simulations of the experimental setup. All simulations were relying on the computation methods described in chapters 4 and 5 and which have been implemented in the Kassiopeia software [146]. The analyses were performed using the BEANS-Software [177].

8.1. Magnetic field-setup

The magnetic setup of the main spectrometer contains not less than four superconducting solenoids (S_{PS1}, S_{PS2}, S_{PCH}, S_{DET}), the 14 individual coils (AC_{1-14}) of the LFCS air coil system and 8 current loops each of the vertical and horizontal EMCS ($EMCS_{hor}$, $EMCS_{ver}$). In table 8.1 a survey of the most commonly used magnetic field setups for operation with symmetric and asymmetric magnetic field is given.

The field configurations implemented differ mostly in the absolute field strength on the surface of the electrode, as well as on the monitored area of the spectrometer surface. In view of background-generating processes this implies a variation of the starting angle acceptance of secondary electrons that are able to reach the detector.

8.1.1. Misaligned magnetic flux-tube

At the beginning of the SDS-I measurement phase, the detector system including the Pinch (PCH) and Detector (DET) magnet was aligned with respect to the main spectrometer. Due to limitations in the alignment hardware it was not possible to

Table 8.1.: **Magnetic setups of the SDS-I phase** Here, solenoid- and LFCS-current settings are given. Settings A and B denote asymmetric setups. The current values are defined so, that a positive value generates a magnetic-field pointing towards the FPD.

	current [A]					
coil/solenoid	A	B	1.5G	3.8G	5G	9G
S_{PS1}	0	0	104.67	104.67	104.67	104.67
S_{PS2}	0	0	148.61	148.61	148.61	148.61
S_{PCH}	72.63	72.63	72.63	72.63	72.63	72.63
S_{DET}	54.59	54.59	54.59	54.59	54.59	54.59
AC_1	100	-50	0	28.6	60.1	95.2
AC_2	100	-50	0	24.0	15.4	99.8
AC_3	100	0	0	17.3	24.3	48.9
AC_4	100	100	0	22.1	41.8	98.8
AC_5	100	100	6	33.5	47.4	100
AC_6	100	100	9	36.4	77.4	74
AC_7	100	100	11	35.8	29.7	98.2
AC_8	100	100	19	54.1	52.1	96.6
AC_9	100	100	13	10.2	58	80.9
AC_{10}	100	100	13	52.1	48.6	90.4
AC_{11}	100	100	5	32	54.8	61.3
AC_{12}	100	100	0	20.1	23.8	99
AC_{13}	100	100	0	29.8	46	97.6
AC_{14}	0	70	-50	-51.8	-50.9	-36.2

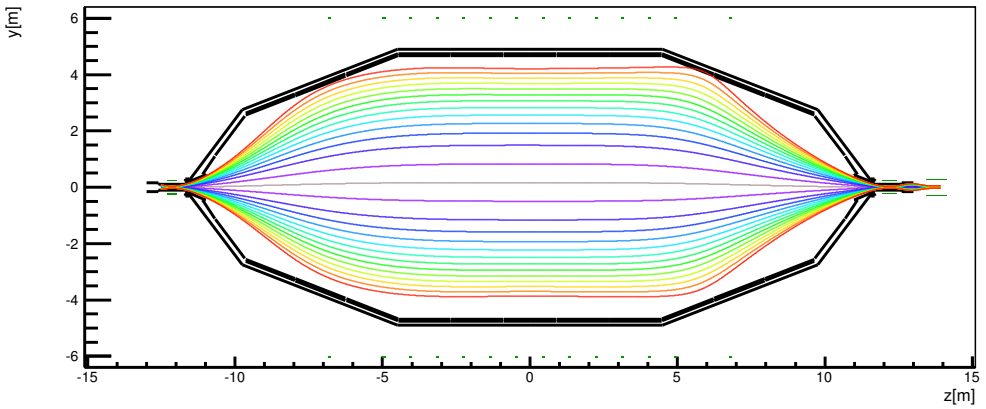

Figure 8.1.: **Misalignment of the flux tube at 3.8 G** Magnetic flux tube of the 3.8 G configuration, which touches the wall.

align the FPD to a precision better than 3.3 mm in x/y-position and 1° in the horizontal and vertical plane.

Due to the fact that the flux-tube at the detector has a dimension of only 90 mm this apparently small misalignment is responsible for a rather noticeable displacement of the magnetic flux tube near the analyzing plane. In figure 8.1 it is shown that the misalignment even leads to the flux tube touching the vessel wall. Apart from limited alignment precision this was caused by the Pinch magnet working with only 5 T and not its nominal field of 6 T. As a consequence, several pixels of the FPD in the top part had to be excluded in the analysis, see also section 2.4.

When examining secondary electron emission, it is important to include any misalignment into the field calculations. This is due to the effect that the surface area of the spectrometer then is mapped incorrectly onto the detector pixels in the asymmetric configurations. Figure 8.2 shows this mapping of the steep- and flat-cone surface on the FPD-pixels for asymmetric configuration A. The projection is shifted to the upper left. The second parameter that is affected by the misalignment is the actual magnetic field strength on the inner surface. However, this effect is only rather small for the source side surface, where we are interested in during asymmetric measurement. The magnetic field there is almost exclusively formed by the air coil system.

8.2. Secondary emission without high-potential

The first measurements of the SDS-Comissioning Phase I were performed with asymmetric field configurations and no potential on the electrodes, to test functionality of the FPD system and the spectrometer together. In contrast to the monitor spectrometer, the main spectrometer beamline features a PAE which allows to detect electrons with very low energies. This is of great value when characterizing the background due to secondary electrons from the walls even when no electric potential is applied to the electrodes.

In preparation to the measurements, extensive simulations of the magnetic flux tube

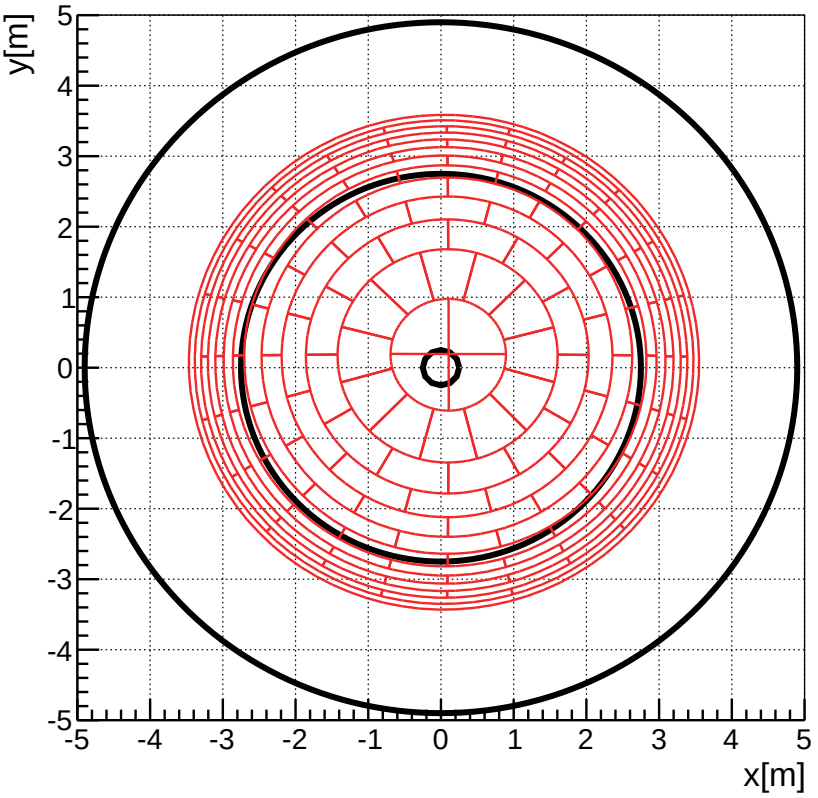

Figure 8.2.: **Misalignment of the flux tube during asymmetric B-field** Mapping of the spectrometer surface to the detector for configuration A. Upstream view.

as well as tracking simulations were carried out. The objective of the simulations was to maximize the detection efficiency of secondaries from the wall by maximizing the magnetic field strength there as well as to calculate the surface area that was actually mapped onto the detector pixels.

8.2.1. Magnetic mirror effect

With no electric potential applied, the probability for an electron created at the vessel wall to reach the detector only depends on the magnetic field strength at the point of creation B_{start} and its gyration angle relative to the magnetic field. The maximum acceptance angle θ_{lim} that allows an electron to overcome the magnetic mirror effect then is only defined by the maximum magnetic field strength B_{max} on its path:

$$\sin^2\theta_{\text{lim}} = \frac{B_{\text{start}}}{B_{\text{max}}} \quad \rightarrow \quad \theta_{\text{lim}} = \arcsin\sqrt{\frac{B_{\text{start}}}{B_{\text{max}}}} \tag{8.1}$$

Each electron created with an angle $>\ \theta_{\text{lim}}$ will be reflected due to the magnetic mirror effect. In a first approximation, we assume the distribution of starting angles of a secondary electron to be isotropic. As for flat solid angle distributions the $\cos\theta$ is equally distributed, so that the probability for an electron to be created with an angle smaller or equal to θ_{lim} accounts to:

$$P_{\text{isotropic}} = 1 - \cos\theta_{\text{lim}} \tag{8.2}$$

For a cosine angular distribution, the function $\cos^2\theta$ is equally distributed. Hence, the probability for an electron to be created with an angle smaller or equal to θ_{lim} is given by:

$$P_{\text{cosine}} = 1 - \cos^2\theta_{\text{lim}} \tag{8.3}$$

The starting magnetic field B_{start} on the wall of the source-side steep and flat cone parts of the main spectrometer for configuration A is shown in figure 8.3.

Finally, the maximal field in the Pinch-magnet is 5 T, meaning that only a very small fraction of between 3×10^{-5} and 9×10^{-5} of the started secondary electrons are able to reach the detector.

8.2.2. Secondary rate

The average rate measured in this setup accounted to (416±5) mpcs after pixel-cuts. In figure 8.4 fluctuations of the actual rate over the 4 h run over time periods of 10 minutes as well as the rate at individual pixels of the FPD and the rate trend during the measurement are shown.

There are no individual hot-spots being visible on the detector map and the rate-trend only shows small fluctuations. The average magnetic field strength on the starting surface is $B_{\text{start}} = 4.18 \times 10^{-4}$ T. Analytically, the probability for an electron started in this magnetic field with a gyration-angle small enough to overcome the magnetic mirror effect is $4.18{\times}10^{-5}$. The analytical probability is very close to the one estimated by tracking simulations which is $6.6{\times}10^{-5}$ using a cosine angular distribution. With a total surveyed area of 68.4 m^2 this corresponds to a secondary emission rate on the surface between 145 and 175 cps/m^2. This is in good agreement with measurements at the monitor spectrometer of 120 cps/m^2 (see 7.2.1) as well as

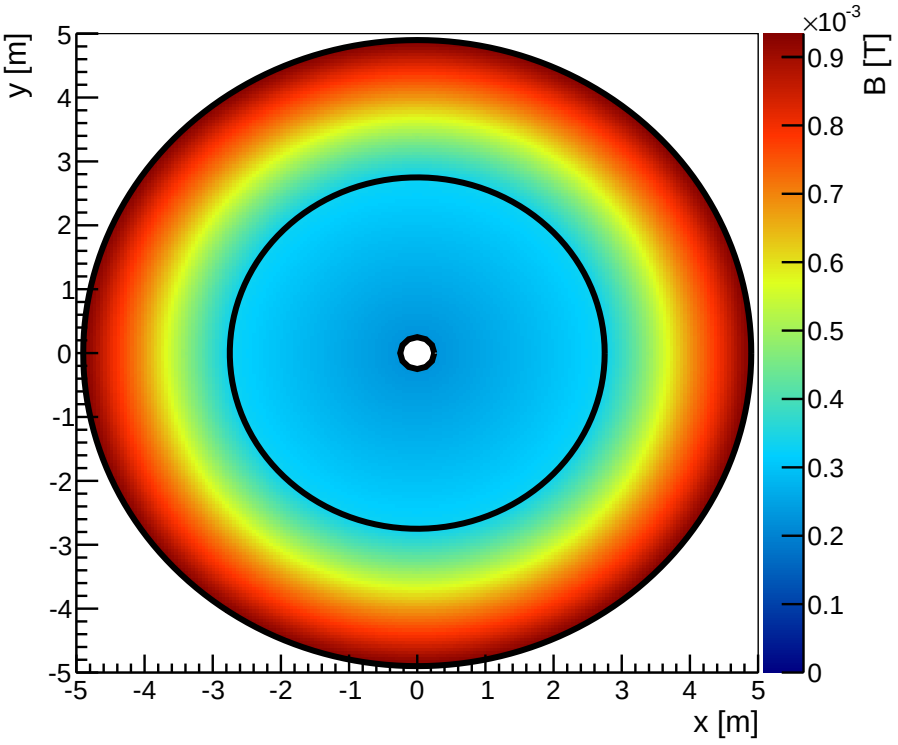

Figure 8.3.: $B_{\mathbf{start}}$ **on the surface of the electrodes at the source side of the spectrometer in an asymmetric field layout** Here, the magnetic field strength on the surface of the steep and flat cones for configuration A is given in a view from the detector to the source (upstream view).

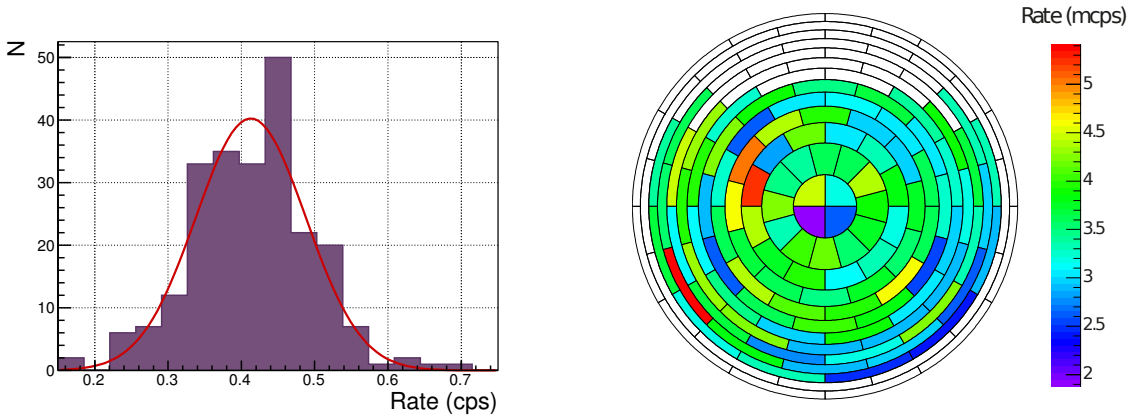

(a) Rate-histogram

(b) Detector view

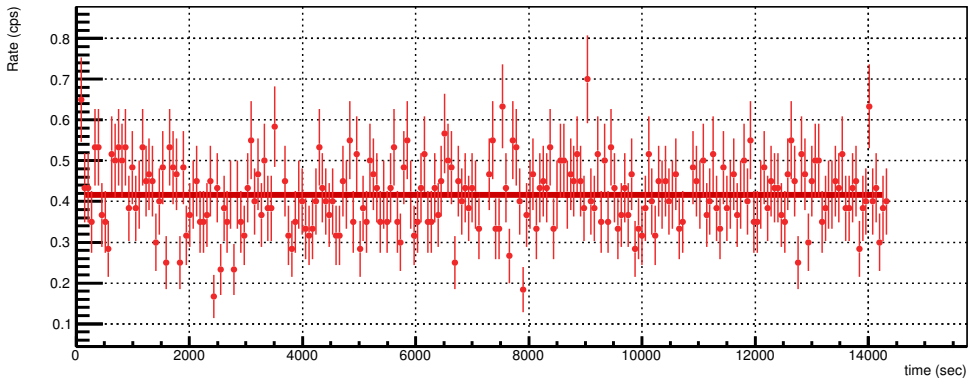

(c) Rate trend graph

Figure 8.4.: Characteristics of run fpd6308-6311 with an asymmetric configuration.

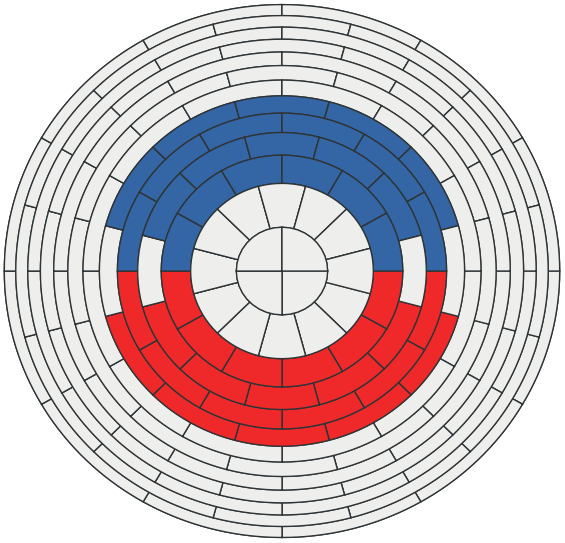

Figure 8.5.: **Pixel groups for an up-down comparison** Here, the FPD pixels are grouped in two areas the top region with 22 pixels (blue) and the bottom area with 22 pixels (red).

the pre-spectrometer [103] and measurements at predecessor experiments.
Of particular interest in this measurement is also the distribution of electron emission on the spectrometer surface. A first qualitative evaluation of this is a look on the detector pixel rate in figure 8.4(b) which shows no preferred direction. A more quantitative approach is to define groups of pixels, to then calculate the spectrometer surface area that is mapped on to them, and finally to compare the rate per unit area.
As the most muons come from above, a naïve expectation would be to expect a higher secondary electron rate from the top surface than from the surface on the bottom. Figure 8.5 shows a selection of 22 pixels each that look on the top and bottom area of the spectrometer. Due to the non-negligible misalignment of the detector-system and the associated magnets, different surface areas are mapped onto both pixel groups, namely 25.23 m^2 for the top-pixels, and 25.65 m^2 for the bottom ones. The rates account to (80.0 ± 0.4) mcps for the top group resulting into a rate of 3.17 mcps/m^2 and (79.9 ± 0.5) mcps for the bottom group resulting into a rate of 3.12 mcps/m^2 correspondingly. This represents a 1.5% effect that can easily be explained by the upward shift of the observed surface area due to the misalignment of the detector-system. This shift introduces non-equal magnetic fields on the particular starting surfaces and is most likely the cause for the very small top-bottom rate-asymmetry. The result contradicts expectations of an elevated rate from the top side of the spectrometer including that the secondary emission rate from the wall due to cosmic and environmental radiation can be regarded homogeneously distributed across the inner surface. This homogeneous distribution of secondary emission is well explained by cosmic ray muons that interact in the stainless steel both when entering and leaving the main spectrometer. Moreover, the slow secondary emission is independent of the direction of the primary particle. A small top-down asymmetry is expected due to muons stopping in th upper half of the spectrometer but this small effect was not detectable due to the alignment effects described above.

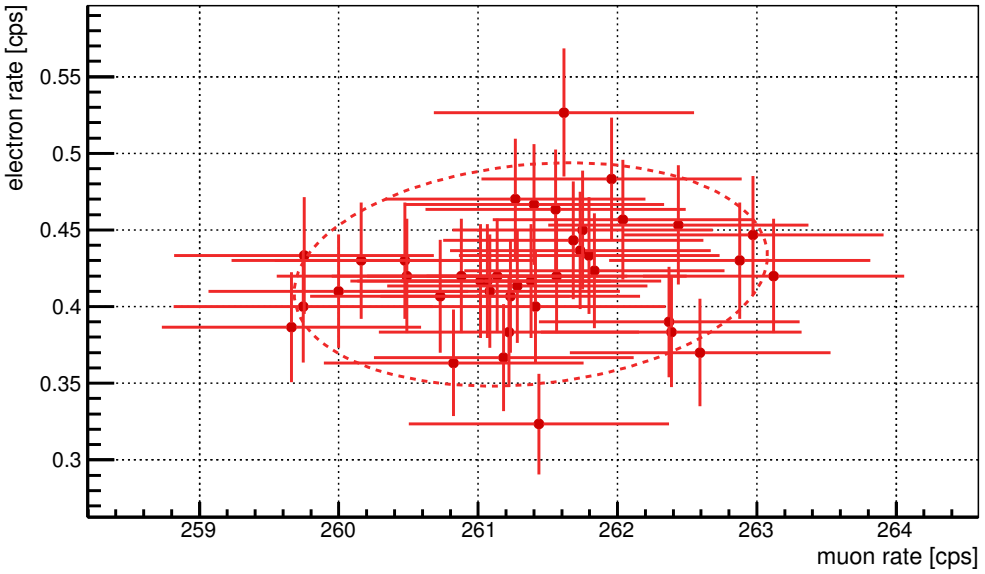

Figure 8.6.: **Correlation of the muon rate and the secondary electron rate in a configuration with no HV applied** Here, the electron rate over the muon rate in muon panel 6 is displayed. Each point represents an average rate over 300 s. The correlation factor is 0.17 with a statistical significance of 0.15.

8.2.3. Correlation and coincidences between secondary-electrons and muons

When assuming the cosmic ray muons interacting in the vessel walls to be the main source of the secondary electron emission a straightforward test is to look for a correlation between the electron rate at the FPD and the muon rate measured by the muon detection system.

As outlined in chapter 6, the flux of cosmic rays can vary by up to several percent over the timescale of several days. Unfortunately, no time slot for a week-long background measurement in the SDS-Phase-I was available. The longest time period for a secondary-emission measurement with no HV was only 4 hours. There, the mean muon-rate was (261.9 ± 0.5) cps and it featured a very small variation of only maximum 1.1%. The mean electron rate was (416 ± 5) mcps including spikes of up to 37% maximum variation. In figure 8.6 the secondary electron rate in this measurement is shown over the muon-rate in the muon-panel 6. The correlation between the two rates accounts to 0.17. This shows that both rates are only very weakly correlated in the measurement. To further evaluate the correlation factor, one usually looks at the statistical significance. It corresponds to the probability that a measurement of two uncorrelated values would result in the observed correlation factor. The sample size of the correlation measurement is only 40, so the statistical significance accounts to $p = 0.15$, implying that the obtained correlation factor is not very meaningful. The relatively weak correlation can also be explained by additional perturbations that influence the electron rate at the detector. It is highly probable that future measurements with a pure cosmic ray muon dominated background rate will show a much better correlation as here, where short-term nuclear-decay-induced back-

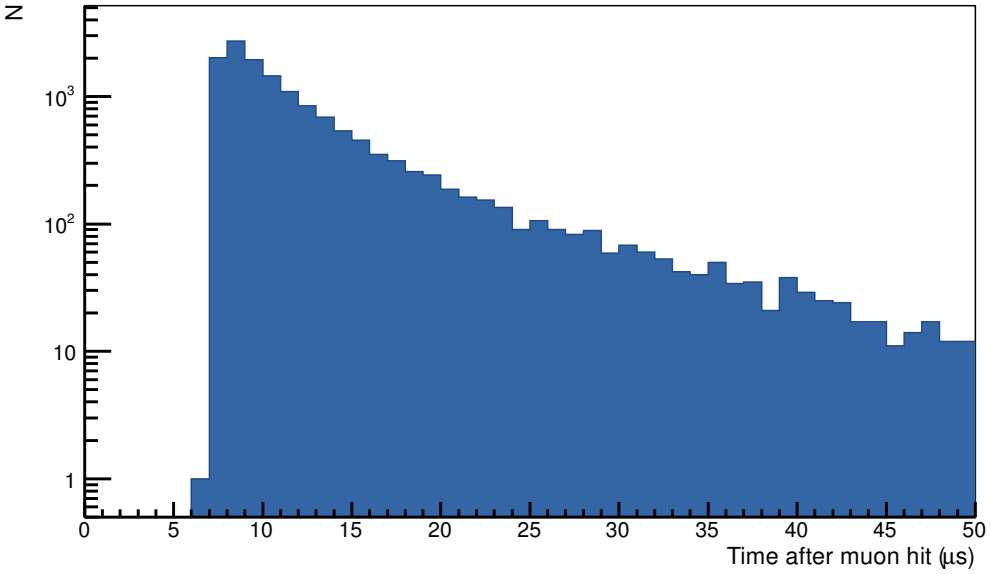

Figure 8.7.: **Simulated electron travel times after muon hits the vessel** Here, the time of flight from the vessel to the detector for electrons as calculated by KASSIOPEIA is shown. The magnetic field setup in this case was A, the starting energies were between 0.1 and 50 eV and the starting angles were cosine distributed.

ground fluctuations reduce the correlation. In so far, figure 8.6 is a valuable test grad for future investigations [178]. A far-reaching consequence of such a correlation for the KATRIN experiment would be a background rate that varies with the cosmic ray flux, making it necessary to closely monitor the incident muon rate during measurement operation.

The precise timing of the muon detection system and its synchronization with the FPD-DAQ make it possible to search for electron events that coincide with events in the muon panels. To search for these, a coincidence window of 40 µs was defined in accordance with the time-spectrum from simulations shown in figure 8.7.
In the framework of the coincidence search we look for detector events that occur in a time window of 40 µs after a muon hit a scintillator panel on each side of the main spectrometer.

Because of the rather small muon flux for the large azimuthal angles selected by the muon detectors, the average coincidence-rate was only 5×10^{-3} per second. In figure 8.8 the time differences of electron events at the detector after a muon hit are shown. There is no coincidence signal visible as expected from the simulation. This is due to the small coincidence rate as there are only muon detectors monitoring the lateral muon flux instead of the significantly higher vertical flux. This measurement will be repeated in the future with additional muon detectors on top and under the main spectrometer.

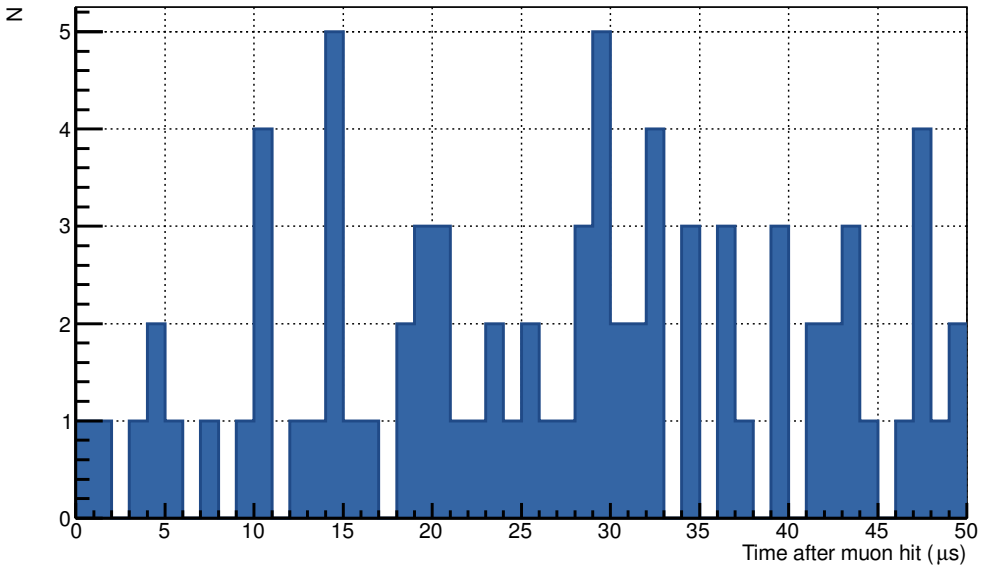

Figure 8.8.: **Measured time spectrum of hits in the FPD after muon hits in the muon detection system for configuration A.** A total of 80 events were measured in the coincidence time window (50 µs.

8.2.4. Multiplicity of secondary emission

In the low-rate measurements with asymmetric field configuration a number of coincidences were observed where multiple electrons within a time-window of 120 µs reached the detector. Figure 8.9 shows this time-clustering of the inter-arrival times of electrons at the detector in a 1 ms time window. The average rate accounted to 416 mcps, so for Poisson-distributed single electron events, the mean time difference between events is expected to be 2.5 s. The probability for an accidental coincidence of two electrons would then be:

$$p = 1 - \mathrm{e}^{-R \cdot \Delta t} = 4.2 \times 10^{-4} \tag{8.4}$$

where R denotes the rate and Δt the coincidence time window. For a total measurement time of 4 h we would expect 2.5 accidental coincidences in the time-window. The measured number of 50 events clearly indicates an underlying physical process which leads to the simultaneous emission of multiple electrons, where at least one electron follows another one at the detector in less than 120 µs.

In figure 8.10 the electron multiplicity in a 120 µs long window after detection of the first electron is shown. It is remarkable that the ratio of single- to double-electron hits is only of the order of 170 : 1. This is a further indication that many of the secondary emission events start with a rather large multiplicity of electrons.

Complementary measurements with a symmetric magnetic field setup at 3.8 G and no high-voltage were performed later in course of the baffle test measurements [179]. In these 20 h measurements the background due to nuclear decays from emanated radon atoms was strongly suppressed and background due to secondary electrons from the walls was dominating the background rate. Interestingly, the detector was

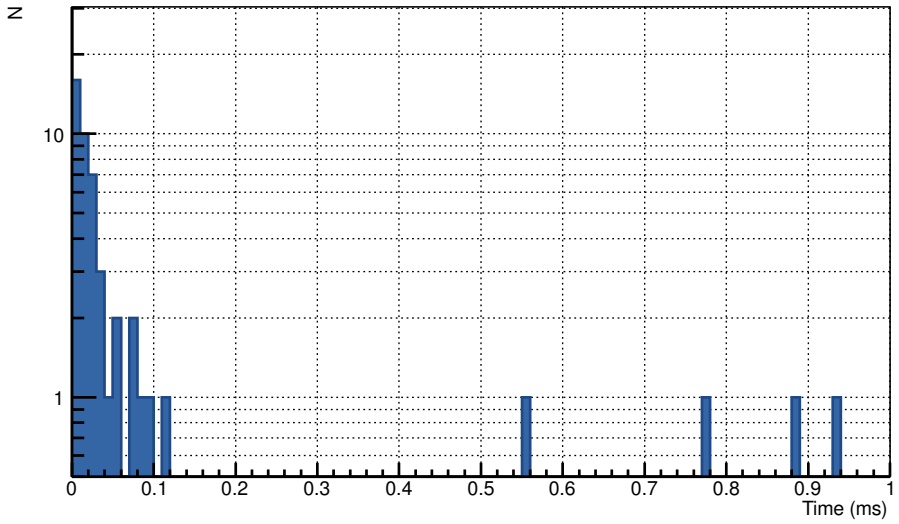

Figure 8.9.: **Distribution of inter-arrival times of electrons in an asymmetric B-field** Here, the nter-arrival times in a time-window of 1 ms from background electrons originating from the spectrometer surface in a measurement with asymmetric magnetic field are displayed.

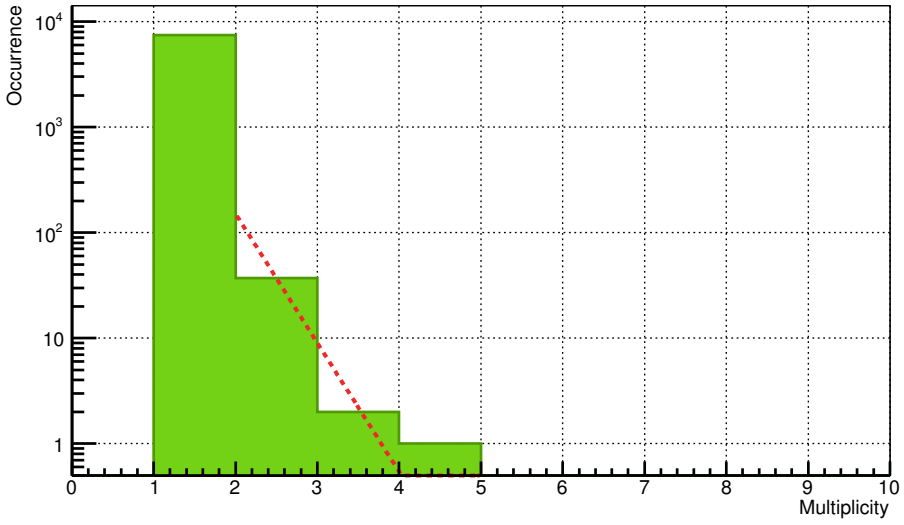

Figure 8.10.: **Multiplicity of electron hits** Measured multiplicity of background electrons in a 120 µs-window with asymmetric magnetic field and the detector viewing at the spectrometer surface. The slope of the exponential fit accounts to $\lambda = -2.82 \pm 0.71$.

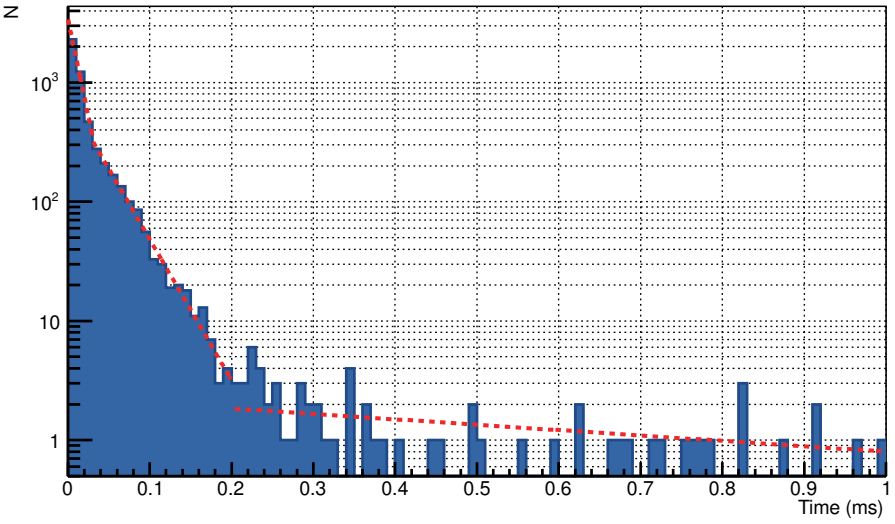

Figure 8.11.: **Distribution of inter-arrival times of electrons in a symmetric B-field** Inter-arrival times of background electrons from e-gun-gate-valve in a symmetric magnetic field configuration. The exponential slopes correspond to $\tau_1 = (75.5 \pm 2.1$ / µs), $\tau_2 = (27.2 \pm 0.9$ / µs) and $\tau_3 = (1.04 \pm 0.75$ / µs).

looking at the gate-valve on the e-gun-side due to the symmetric field. The sensitive flux-tube covered a circle 8 cm radius on the valve, accounting to an area of 0.02 m^2. The average measured background rate was (90.5±0.5) mcps.

In figure 8.11 the interarrival times between two detector events are shown. This figure shows that most secondary electrons there are correlated in time and arrive in a time window of up to 250 µs. Again, considering only Poisson-distributed single event electrons, the mean interval time would be about 10 s and the expected number of accidental coincidences 0.03. Summing over all electrons in this window results in the multiplicity distribution shown in figure 8.12. It is notable that a multiplicity of 18 has been observed at the detector, despite of the non-negligible suppression of electron transmission to the detector through the magnetic mirror effect.

The frequency of occurrence of multiplicities $\geq$ 2 is shown in figure 8.13. The exponential fit ($\tau = 0.0131 \pm 0.0003$) shows that the multi-electron clusters follow a Poisson distribution and are thereby uncorrelated. Their average rate of occurrence is 13.1 mcps.

To check the origin of these multi-electron events and whether the source is point-like or extended, one can take a look at FPD-pixel coincidences. In figure 8.14 the spatial correlation between the (exemplatory) FPD-pixel 23 and the other pixels is shown for the asymmetric and symmetric measurements. In the symmetric case, the field of view is confined to a small area, in the asymmetric case this is much larger (see figure 8.2). Also, the acceptance angles are different. In both cases one observes that multi-electron events are localized, i. e. they occur at the same pixel. However, in some cases neighboring pixels are hit, pointing to an extended source.

In the case with a symmetric field, the magnetic field at the gate-valve is $B_{\text{start}} = 2.45$ T whereas the maximum magnetic field generated by the pinch magnet is

Figure 8.12.: **Multiplicity of electron hits with symmetric B-field** Multiplicity of background electrons within a 250 µs-window with the detector viewing the electron gun gate-valve. The number of single events is corrected for the expectation from background due to nuclear decays and shows an exponential decrease ($\lambda = -0.699 \pm 0.016$).

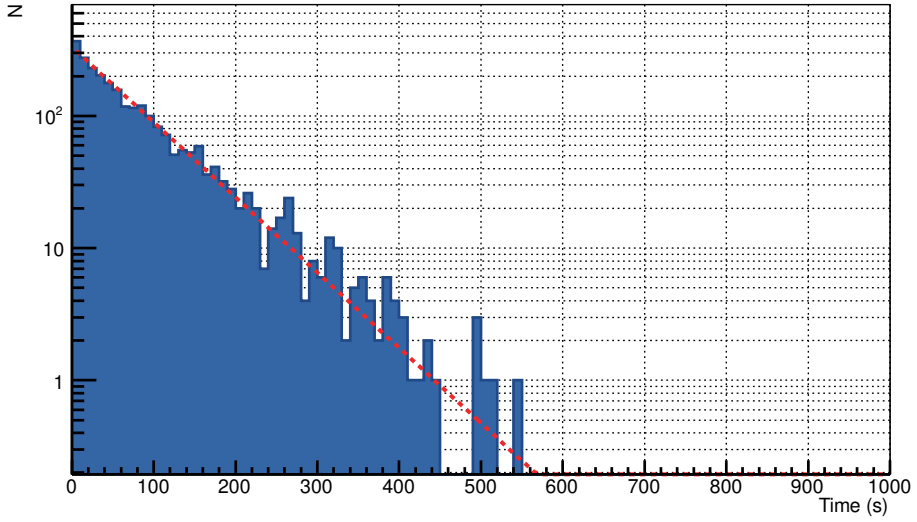

Figure 8.13.: **Distribution of inter-arrival times of multi-electron events in a symmetric B-field** Inter-arrival times of multi-electron clusters at the detector, where the first electron recorded during a multi-electron sequence is counted as the cluster time. The dashed line denotes an exponential fit with slope $\tau = 0.0131 \pm 0.0003\ \frac{1}{\mathrm{s}}$, corresponding to the average cluster-rate in cps.

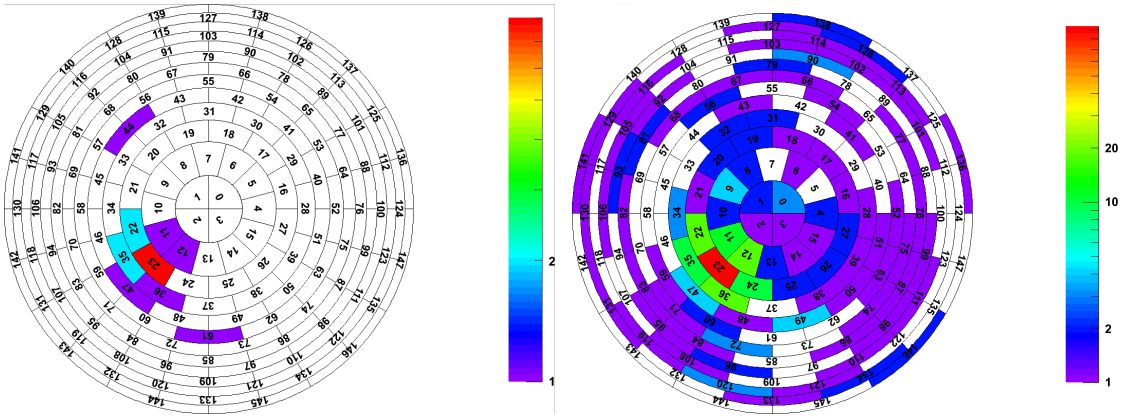

(a) FPD-pixel 23, asymmetric run

(b) FPD-pixel 23, symmetric run

Figure 8.14.: **Pixels coincident with pixel 23** Pixel correlation of pixel 23 with other FPD-pixels for multi electron events. The color-scale indicates the coincidence-rate with the particular pixel.

$B_{\max} = 5$ T. This translates into a maximal acceptance angle for an electron from the wall of the gate-valve to overcome the magnetic mirror effect of:

$$\theta_{\lim} = \arcsin\sqrt{\frac{B_{\text{start}}}{B_{\max}}} = \arcsin\sqrt{\frac{2.45\ \text{T}}{5\ \text{T}}} = 44.42° \tag{8.5}$$

Assuming a cosine start-angle distribution for electrons from the valve, a tracking simulation with KASSIOPEIA was performed for the geometry of the gate-valve. The simulation yields a probability for a single-event electron being created with an angle $\leq \theta_{\lim}$ and reaching the detector of:

$$p_{\text{MC}} = 0.632 \tag{8.6}$$

For multi-events, each electron of the cluster has to be created with an angle $\theta_i \leq \theta_{\lim}$ in order to be counted by the detector. Under the assumption of cosine-distributed, uncorrelated angles θ_i, we are able to correct for the magnetic mirror effect to obtain the primary multiplicity-distribution.
If n electrons are created and the probability for a single electron to reach the detector is p, then the probability to measure k electrons on the detector is given by a binomial distribution:

$$B_{n,k}(p) = \binom{n}{k} p^k (1-p)^{n-k} \tag{8.7}$$

The probability Q_k to measure a k-fold multiplicity is then related to the original probability P_n for an n-fold multiplicity through:

$$Q_k = \sum_n P_n \cdot B_{n,k}(p) = \sum_{n \geq k} B_{n,k}(p) \cdot P_n \tag{8.8}$$

This can be expressed in terms of a linear equation system:

$$Q_k = \sum_{n=1}^{12} M_{kn}\ P_n \quad ; \quad M_{kn} = \begin{cases} 0 & \text{for} \quad n < k \\ B_{n,k}(p) & \text{else} \end{cases} \tag{8.9}$$

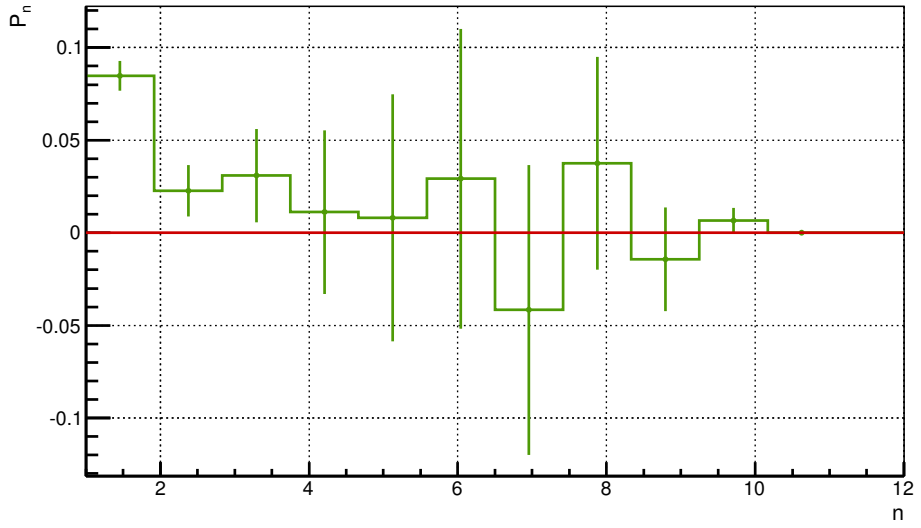

Figure 8.15.: Calculated primary multiplicities of electrons at their point of origin at the gate-valve.

This linear equation system can now be solved for P_n. However, the inversion of M_{kn} for the measured values Q_k yields unphysical results with some elements of P_n smaller than zero. Therefore the error of the cluster sizes has to be determined by a MC calculation. The values of Q_k are diced in a Gaussian-distribution with mean Q_k and the error $\sqrt{Q_k}$. The equation system is then solved for P_n. In the calculation this is repeated 10^5 times.
Figure 8.15 shows the resulting mean values P_n and their errors that were obtained. Now, all P_n are greater than zero within their error-interval. The distribution seems to have a maximum between the cluster size of 6 and 9. This result supports the hypothesis that in some cases cosmic μ-induced secondary emission events are short bursts featuring a high number of electrons. Potential sources of high-multiplicity events are deep-inelastic muon scatterings, the electromagnetic component of a shower, or Auger electrons from nuclear muon capture.

8.3. Secondary emission with high-potential

When elevating the spectrometer on a high potential the rate of secondaries from the wall at the detector increases quite substantially. This is caused by the electric retarding field that helps the electrons to overcome the magnetic mirror effect by accelerating them in direction of the magnetic field-lines after passing the analyzing plane. The result of this acceleration is a collimation of the gyration-angle that leads to a drastically increased probability for secondary electrons to overcome the magnetic mirror effect and reach the detector.

8.3.1. Secondary rate

To measure the secondary rate from the spectrometer walls in a field setup with nominal HV, the asymmetric magnetic field setup A was used. The tank and inner electrode were both elevated on -18600 V to first measure the unshielded rate from

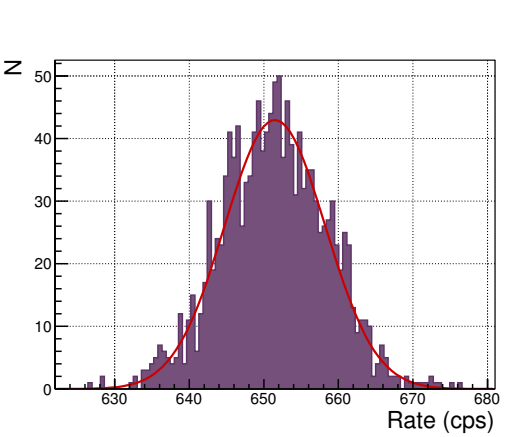

(a) Rate histogram

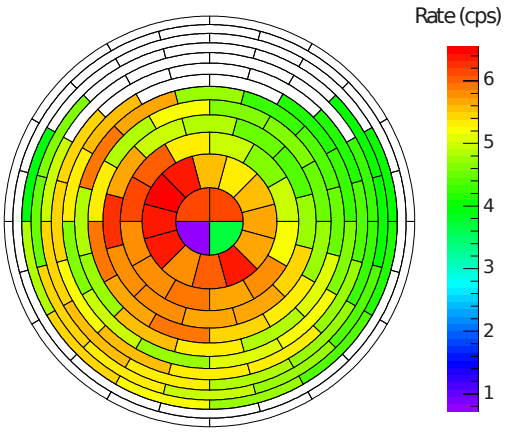

(b) Detector view

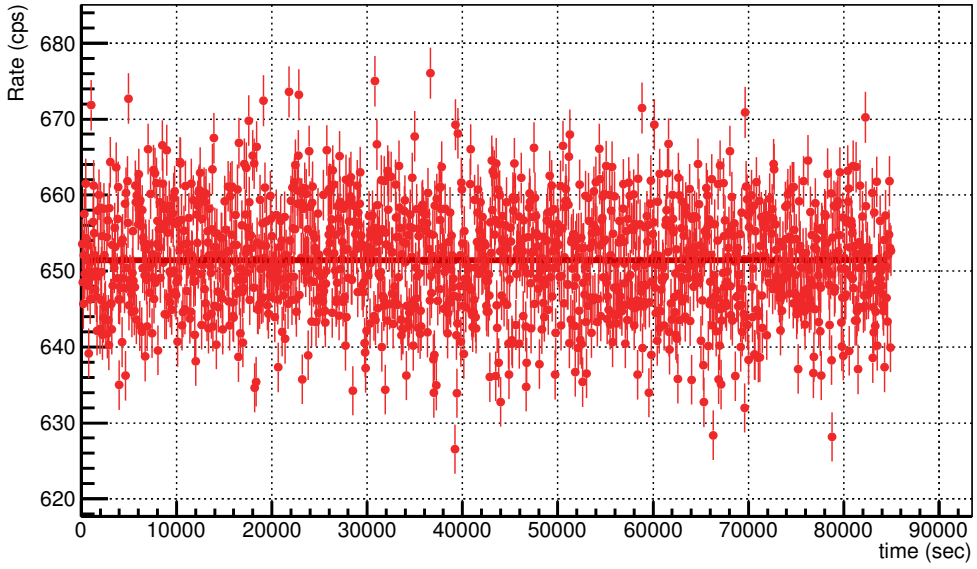

(c) Rate trend graph

Figure 8.16.: Rate analysis of run fpd7111-7134.

the wall. In figure 8.16 the rate fluctuations (a), the pixel distribution (b) and rate trend (c) of this measurement are shown. The average rate accounted to (653.4 ± 6.8) cps.

As for the zero-potential measurements, a tracking simulation with KASSIOPEIA was executed in preparation to the HV measurements. The starting parameters for the simulated electrons were identical to the ones in 8.2 with only the electric field of the main spectrometer electrodes to be added to the simulation. A total of 2×10^5 electrons, of which a fraction of 6.28×10^{-2} was able to reach the detector. Using this detection probability and the surveyed area of 68.4 m^2 this results into an average emission rate of 131 cps/m^2, which is in good agreement with the rate obtained from the zero-potential measurements, the measurements at the monitor spectrometer and previous measurements at the pre-spectrometer [103].

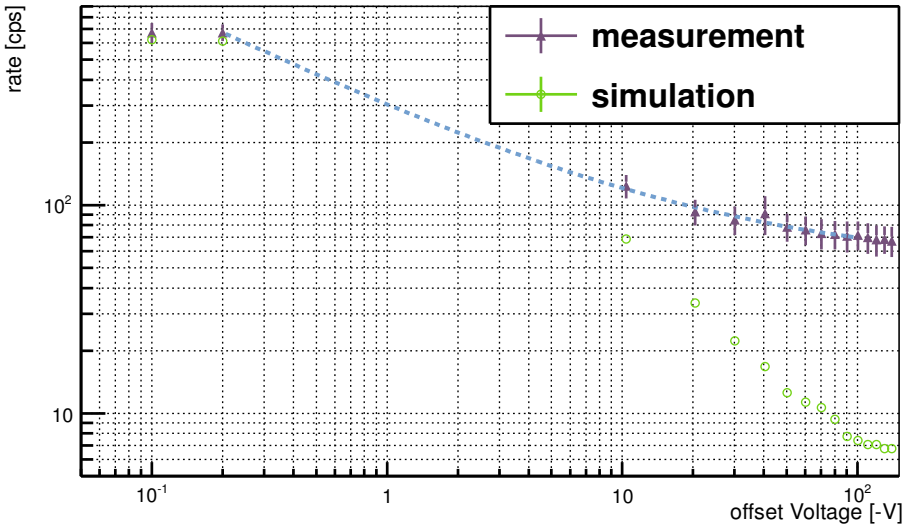

Figure 8.17.: **Measured and simulated secondary electron rate as a function of the wire potential offset** The measured secondary electron rates at the detector are displayed for various offset potentials on the wire-electrode. The magnetic field setup was A and the measurement time per point was 600 s.

8.3.2. Dependence of the secondary electron rate from the wire-voltage

For the next measurement, the potential of the both layers of the wire-electrode was varied with respect to the vessel potential. Analogous to the measurement at the monitor spectrometer described in section 7.2.2, the goal was to measure an integrated energy spectrum, by reflecting all secondary electrons with less longitudinal energy than the wire potential.

Figure 8.17 shows the rate at the detector as a function of the offset voltage between the wire electrode and the tank. The measurement time per voltage setting was 600 s. The rate shows a steep decrease for larger voltage offsets ($\lambda_{\mathrm{MS}} = -(0.56 \pm 0.09)$). Again, the simulation was done with a simplified main spectrometer geometry, featuring only one wire layer and with no inclusion of the holding structure of the wire electrode. Electrons were started with an isotropic angular distribution and the energy distribution that was obtained from the comparison of simulations and measurements at the monitor spectrometer (see figure 7.5).
As the simulated electrons were only started from the wall and not from the wire electrode or its holding structure, the values of measurement and simulation differ in the plateau-area, where almost all electrons from the vessel wall are shielded and only the emission from the wire electrode and its holding structure is visible.
When comparing figure 8.17 with the measurement at the monitor spectrometer the constant plateau is now reached only at higher difference voltages. This is due to two reasons: First of all, for this measurement at the main spectrometer a smaller angle-acceptance occurs. This means that the electrons that reach the detector have a higher fraction of their kinetic energy in the longitudinal component, right

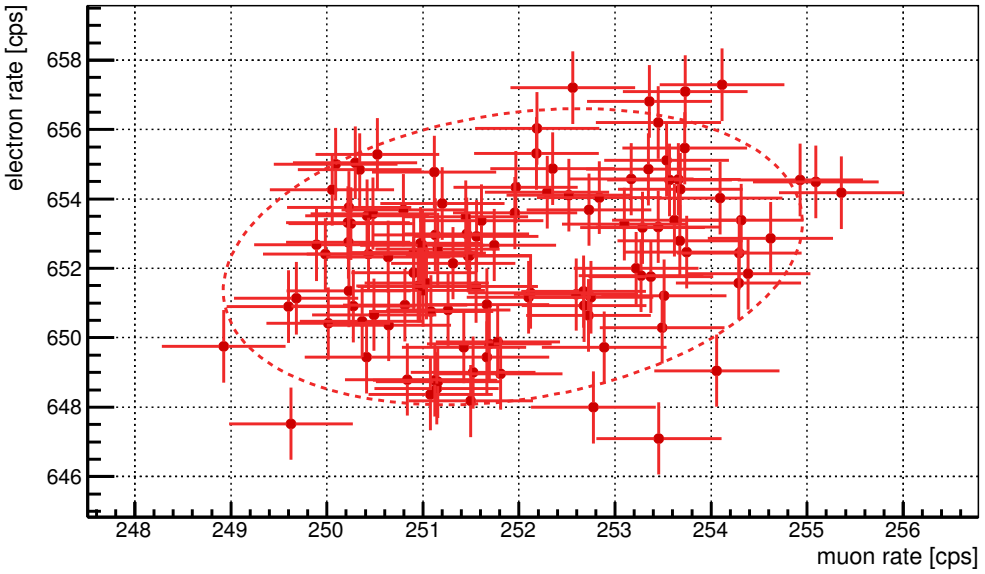

Figure 8.18.: **Correlation of muon and secondary electron rate** Here, the electron rate over muon rate in muon-panel 6 is displayed. The points represent rates averaged over 600 s. The correlation factor is 0.28 with a statistical significance of 1.12×10^{-2}. The measurement lasted 20 h.

from their start. And, as the wire potential only scans the longitudinal part of the kinetic energy, the spectrum is expected to exhibit a harder spectrum extending towards higher energies. And secondly, the wire electrodes of the main spectrometer has been implemented with a far more massive holding structure. In the single offset-configuration of the SDS-I phase the electrons from the holding structure are unshielded and thus cause a quite high rate extending to the plateau-region.
From this behavior we can estimate an electric shielding factor in the asymmetric case, of the non-fully-functional wire-electrode to be $s_{\text{electric, asymmetric}} \approx 10$. This shielding factor is smaller than expected from previous experiments [180]. Also, the measurement confirms, that electrons from secondary emission have rather small energies, on average below 20 eV.
In summary the measurements at the main spectrometer and the monitor spectrometer reveal, within errors, a energy spectrum corresponding to the expectations for true secondary electron emission from stainless steel.

8.3.3. Correlation between secondary and muon rate

Assuming the secondary electron emission to be mainly caused by cosmic ray muons interacting in the vessel wall, one can again look for a correlation between the rate of the muon detector and the rate of secondary electrons recorded at the FPD. Here, the measurement time was increased to 20 hours in order to cover a potentially stronger variation of the muon flux to obtain a clearer correlation.

Figure 8.18 shows the electron rate over the muon rate, where each point represents an average over 600 s measurement time. The mean muon rate over the entire measurement was 252 cps and the mean electron rate 652 cps. Both rates show small

variations of less than about 0.5 to 1%. A correlation factor of 0.28 is found with a sample size of 117 and a resulting statistical significance of p=1.12 × 10^{-2}. This result is decidedly more reliable than the shorter measurements with no electric field. It indicates a moderate correlation between the emission rate of secondary electrons and the rate of incident muons. Again it has to be noted that the 600 s sampling time is not long enough to mitigate rate fluctuations due to other sources. Ultimately this measurement again points to the fact during future long-term measurements a time-dependent background rate has to be expected due to cosmic-induced secondary electron emission. As a consequence, the muon rate on the experiment will have to be monitored in the whole measurement period of KATRIN and the fluctuation in the background rate will have to be taken into account for the neutrino mass analysis.

8.3.4. Background due to secondary electrons

During operation with symmetric magnetic field and with HV appliedto the vessel a suite of measurements was performed with varying potential offset on the wire electrode. Figure 8.19 shows the summarized results of the measurements. In comparison to the asymmetric measurements (see figure 8.17) the rate-drop is much smaller. This is explainable by two factors. First, in this configuration other background components are present that contribute to the total background that react in a different way than secondary electrons from the wall (as seen in figure 8.17) to the electric shielding. An example for this is the background due to stored electron originating from radon α-decays. Secondly, due to the magnetic shielding most particles from the wall will be suppressed, so that they contribute only sub-dominantly to the rate suppression for different offset voltages. The magnetic field will lead electrons from the wall to hit the wire electrode, whereas secondary electrons emitted from the wires will have an unobstructed trajectory towards the sensitive flux tube. The wire electrode can only screen secondary emission from the tank. However, with the symmetric magnetic field these are already highly suppressed due to the magnetic shielding. Thus the electric shielding seems to have a much lower effect on the background rate.

To investigate an optimized setting with regard to the background rate at the detector, HV measurements with active wire shielding and symmetric magnetic field (3.8 G) were done. As mentioned in chapter 2 the main spectrometer is equipped with a LN2 cooled baffle system that strongly suppresses background due to radon decays inside the sensitive volume of the flux tube. To investigate this, series of measurements with warm and cold baffles were performed, allowing to discriminate background contributions due to secondary electron emission and nuclear decays.

In figure 8.20 the projected rates for the measurements with warm and cold baffles are shown. As 30 of 148 detector-pixels were cut-out in the analysis, we have to upscale the rates by 20%. This results in an average rate of 893 mcps with warm and 557 mcps with cold baffles for the full detector. If we assume a 100% efficiency in suppressing background from radon for operating cold baffles, the average rate of the cold-baffle measurement corresponds to the background due to secondary emission. Consecutively, we obtain an average background rate due to radon decays of 336 mcps.

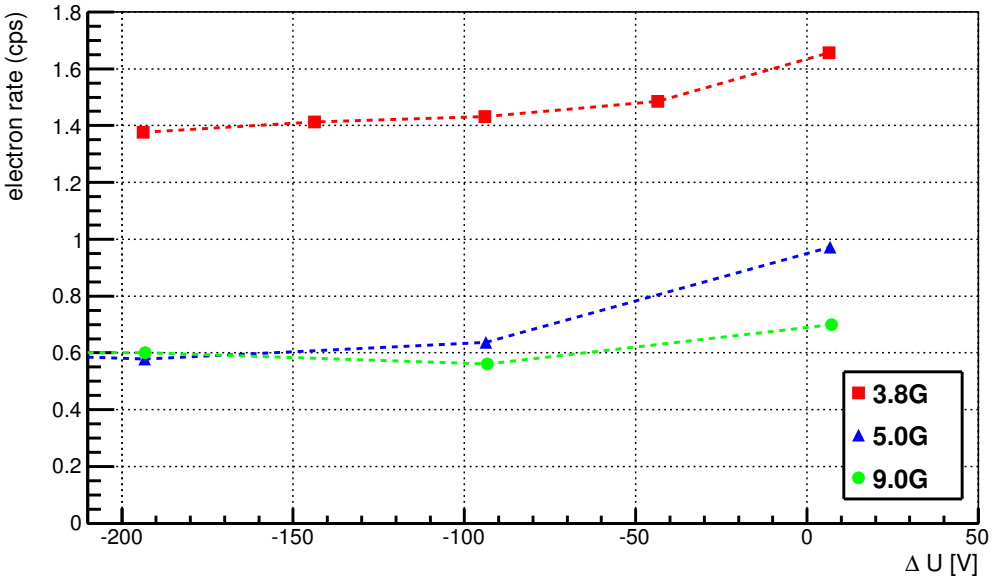

Figure 8.19.: **Background rate as a function of the voltage offset voltage between wire electrode and tank** Three different magnetic field settings were measured. Figure taken from [79].

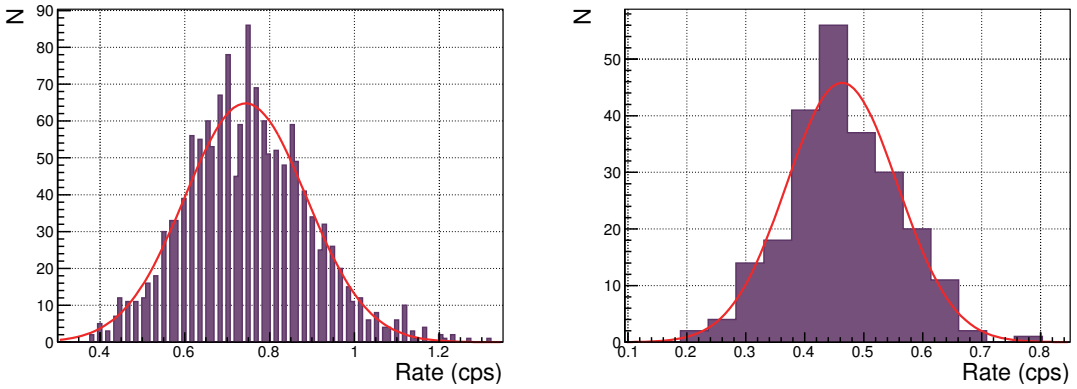

(a) warm baffles (b) cold baffles

Figure 8.20.: **Comparison of background rates for cold and warm baffles** Here, the rate projections for symmetric background measurements with warm and cold baffles are displayed with a mean rate of (743±4) mcps and (463±6) mcps, respectively.

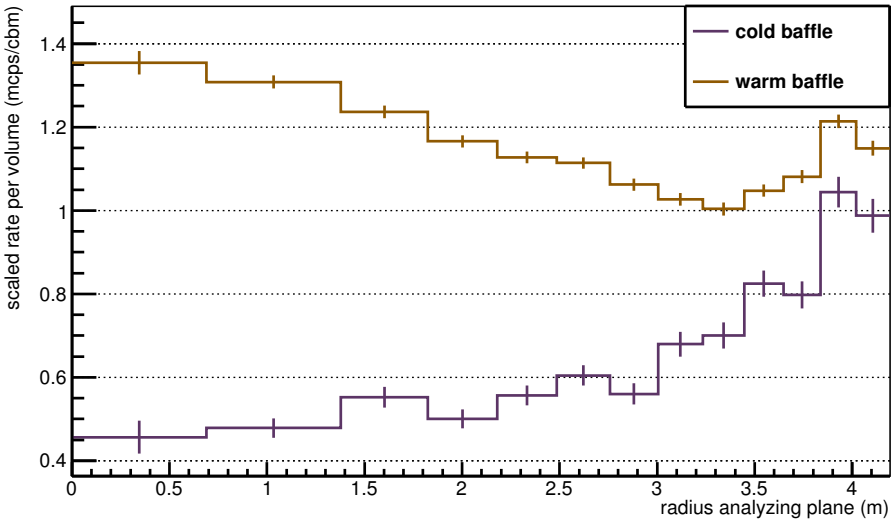

Figure 8.21.: **Comparison of the radial background distribution with warm and cold baffle** Background rates are given per unit volume (m^3).

Another possibility to (partly) discriminate the two background components is given by their radial distribution at the detector. The background due to nuclear decays originates exclusively from stored high-energetic electrons that are generated during the decay and from subsequent processes in the daughter-atom (see section 3.2). In the analyzing plane, the cyclotron radii of electrons with energies larger than 30 keV (where the magnetic field drops to 380 µT) exceed 1.20 m. Thus, they can only be stored in the inner parts of the flux tube, otherwise they would hit the wall due to their large cyclotron radius and get absorbed there. Also, the inner flux-tube has better storing conditions for high-energy electrons [170]. On the other hand, electrons from secondary emission originate from the electrode surfaces. As outlined in section 3.6, these electrons can reach the sensitive flux tube through radial drifts as a result of non-axisymmetric magnetic field configurations. As their average radial velocity is quite small, they will generate background at rather large flux tube radii, by an ionization collision and thus are less likely to migrate to the inner parts of the flux tube.

In figure 8.21 the radial distributions of both background components is visualized. The background rate per unit volume as a function of the radius in the analyzing plane is given. In the warm baffle measurement, the rate at small radii is higher than for large radii, indicating the presence of background-producing stored electrons. However the rate rises again in the last two radius-bins, showing the contribution of the secondary electron emission to the background-rate. In the cold baffle measurement the rate drops significantly for small radii, implying that there are no longer any stored electrons present. The background rate rises again towards the outer flux-tube, in agreement with the expectation that the background due to secondary electron emission is unmodified by the LN2-cold baffle.

Finally, one can estimate the magnetic shielding factor for the 3.8 G setup. In a measurement with warm baffle and 0 V wire-potential the rate was 1377 mcps.

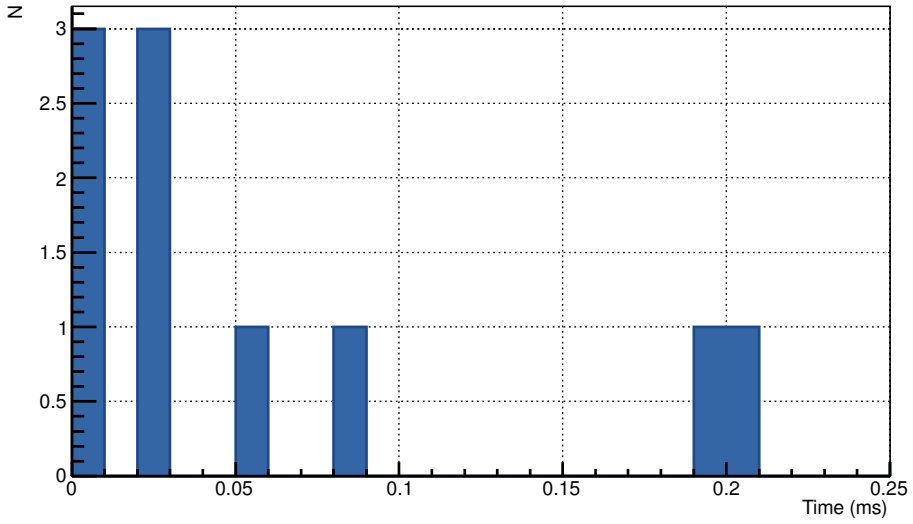

Figure 8.22.: **Inter-arrival times between electrons for the measurements with cold baffle** for the symmetric magnetic field configuration with HV applied.

If we subtract the expected background due to nuclear decays, the remaining rate accounts to 1097 mcps. The average secondary electron emission rate is found to be 145 - 175 electrons m^{-2} s^{-1}. In view of the surface of the tank of 610 m, the total secondary emission rate is expected to be (8.8 - 10.7)$\times 10^4$ per second over the entire tank-surface. From this a magnetic shielding-factor of $s_{\text{mag, measured}}$ =(8.0 - 9.7)$\times 10^4$ can be deduced which is in good agreement with the expectation of $s_{\text{mag, expected}} = 10^5$ [141].

8.3.5. Multiplicity in background due to secondary electrons

Similarly to the measurements of secondary emission with asymmetric field, we now discuss an analysis of inter-arrival times of background electrons during the cold-baffle measurements.
As mentioned before, the average background rate at the detector was 463 mcps. This corresponds to an average time of 2.16 s between two background electrons. If we choose a time-window of 250 µs, we can again calculate the probability for accidental coincidences to $p = 1.16 \times 10^{-4}$. This corresponds to an expectation of 0.8 accidental coincidences during a 4 h measurement.

Figure 8.22 shows the inter-arrival times of subsequent electrons in a 1 ms window during the measurement. There is a total of 10 coincidences within an interval of 250 µs, a number that clearly exceeds the expectation for accidental coincidences. The average cluster rate accounts to 0.69 mcps. In figure 8.23 it is shown that all ten events are double-electron events, where one electron follows another within 250 µs.

The source of this double-hits remains unclear. If they are caused by stored particles, the two electrons should lie on the same detector ring. In figure 8.24 the pixels for two different double-events are shown. It is evident that the coincident pixels can not originate from a stored particle. It is more likely that these double

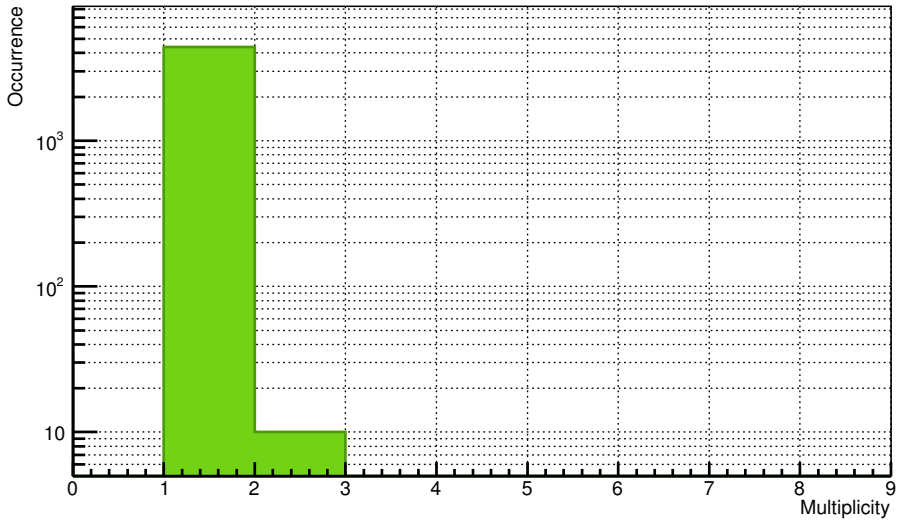

Figure 8.23.: **Multiplicity of electron events with cold baffle, symmetric B-field configuration with HV applied** Measured electron-cluster-sizes of background electrons within a 250 µs-window from e-gun-gate-valve.

events are secondary emission due to cosmic ray muons. In some interactions, a high number of electrons can be emitted simultaneously where two of them are being able to overcome the magnetic shielding to reach the detector in a relatively small time-interval.
As a consequence, we observe a cosmic-induced non-Poissonian background-component of 1.4 mcps at the detector under nominal conditions in the experiment (this is 1/7 of the nominal background rate). On the other hand, this result is reassuring with regard to the operation of the LN2-cold baffle as no indication for a stored particle background is discernible.

8.3.6. Impact of background due to secondary electrons on KATRIN

The background characteristics observed in the main spectrometer strongly influences the neutrino mass sensitivity of KATRIN. If the experiment measures a number of N Poisson-distributed background events, the statistical uncertainty on $m^2_{\bar{\nu}_e}$ scales approximately with $\sigma_{\mathrm{stat}} \sim N^{\frac{1}{6}}$. However, there is a background component with multiple background electrons which is not Poisson-distributed.
If these non-Poissonian background events would not be eliminated by a cut on the inter-arrival times but would be included in the sensitivity calculation they can be incorporated in two ways: by either a Gaussian distribution with a fixed average rate including a broadening corresponding to the fluctuations, or by a a Gaussian distribution with a fluctuating average, which would be the worst case for KATRIN. In either case the statistical error of the measured neutrino mass σ_{stat} is obtained by a fit of the theoretical integral β-spectrum to 10^4 simulated KATRIN-measurements that assume $m_{\bar{\nu}_e} = 0$. This ensemble test is implemented in the KaFit-program package [181] which allows for easy use and manipulation of the input background

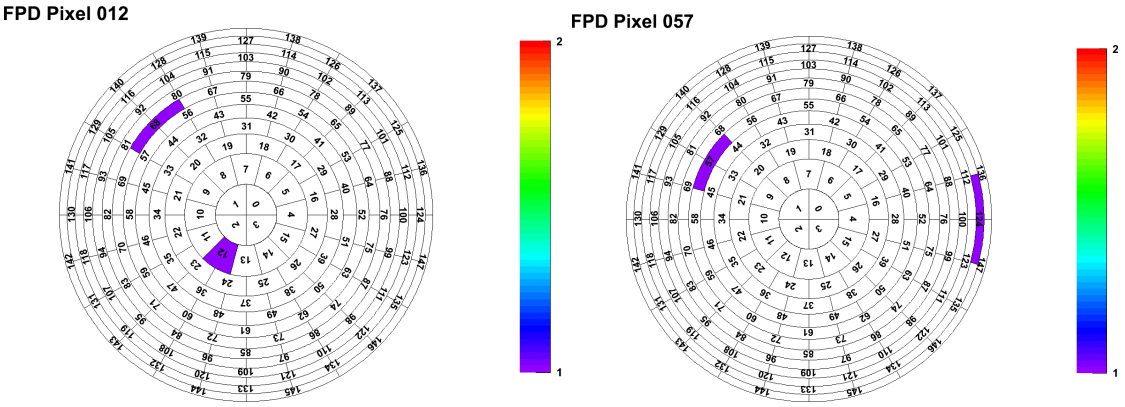

(a) FPD-pixel 12, cold-baffle measurement (b) FPD-pixel 57, cold-baffle measurement

Figure 8.24.: **Event topologies of double coincidences for cold baffles** The pixels are located on separate rings, discarding the hypothesis that they were created by a single stored particle undergoing magnetron motion.

rates.

Figure 8.25 shows the neutrino-mass sensitivity of KATRIN as a function of the background-rate. It allows to compare the sensitivities of different background models. The original assumption is based on a purely Poisson-distributed background. In addition the sensitivities with different non-Poissonian-components are shown. It is evident that a non-Poissonian background component with a constant average of the background rate would only slightly worsen the sensitivity of KATRIN, whereas a background component with a non-constant average rate would seriously endanger the sensitivity-goal.
In the case of multi-hit events as observed repeatedly throughout the SDS-I measurement, a simple cut on the inter-arrival times of events of larger than 250 µs (or longer, depending on the integral measurement time) suffices to eliminate these rather dangerous background classes.

8.4. Field emission measurements at the main spectrometer

In 3.3.4 it was discussed that cold field emission of electrons from electrodes elevated on a high negative potential can occur as a source of strong background in the experiment. During the SDS-I-commissioning phase this effect was observed already during the early measurements, as soon as the offset voltage applied to the wires exceeded −160 V.
The effect is visible with asymmetric magnetic field setting as well as with symmetric setting. In figure 8.26(b) map of the pixel rates for of an early measurement run is shown. It is notable that the field emission mainly originates from two ring-like structures. As shown in figure 8.26(a) these areas of high rate coincide with the position of the wire electrode holding structures. This fact was used to align the FPD with respect to the spectrometer axis. In the scope of this thesis it is nevertheless more interesting to study the nature of the field-emission electrons.

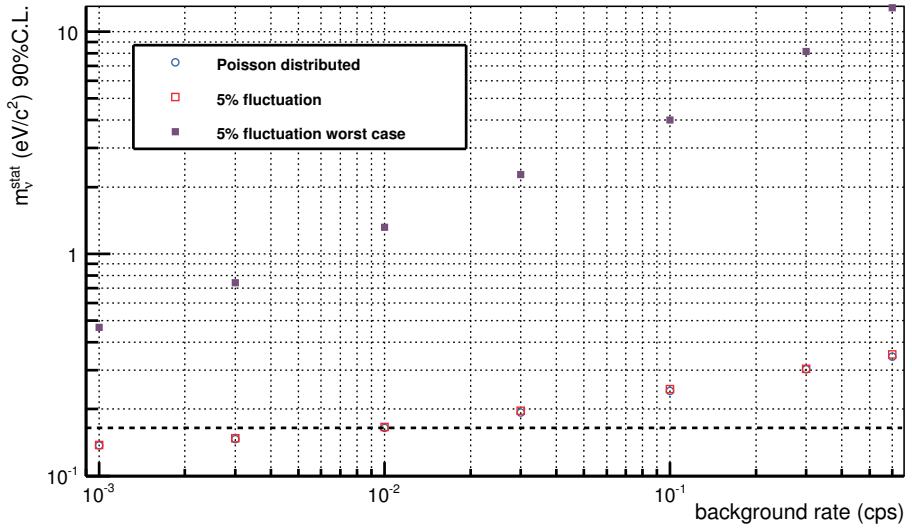

Figure 8.25.: **KATRIN neutrinomass sensitivity (90% C.L.) as a function of the background rate** The dashed line marks the reference statistical sensitivity of $m_\nu^{\text{stat}} = 0.165\ \frac{\text{eV}}{\text{c}^2}$. Sensitivities calculated with the KaFit-program package [181].

In figure 8.27 the observed rate as a function of the offset voltage of the wires is shown for an asymmetric setting. In the following we discriminate between the rate of the pixels that directly map the holding structure, labeled with *combs*, and those pixels that view an area that is shielded by the wire electrode, labeled *wires*. If we analyze at the full rate, we see the typical, strong decrease at very small offset voltages, where electrons from secondary emission are more and more shielded. Between 70 and 160 V a plateau of the rate is observed, where all secondaries from the wall are suppressed and only the residual secondary emission of unshielded surfaces remains. The steep increase of the rate at offset voltages exceeding 160 V is clearly visible in the full and comb rate. Even the wire rate shows a small increase at high offset voltages that is due to the presence of the so-called C-profiles that are part of the wire module units. They connect the wire-spanning combs to give the electrode units stability (they are on the same potential as the outer wires and the combs).

Analogous to chapter 7, the rates can be displayed in a F-N plot. This is done in figure 8.28 where the same data is plotted as $\ln\left(\frac{\text{Rate}}{\Delta U^2}\right)$ over $\frac{1}{\Delta U}$. In this form the electric field at the emission location can be deduced by a linear fit to the data. The fit yields an emission field strength of F =26.8 GV/m. This field strength seems surprisingly high, therefore we will take a closer look at the emission geometry.

The holding structure for the wires is made of stainless steel. It features a rather sharp edge that has a direct line of sight into the sensitive spectrometer volume. In figure 8.29 a 3D-drawing of the so-called *wire-combs* and a test-notch is shown that images the radius at the marked edge. The radius of the edge was measured to be between 0.1 and 0.03 mm [182].
An electric field simulation for both edge radii and a 200 V voltage offset is shown

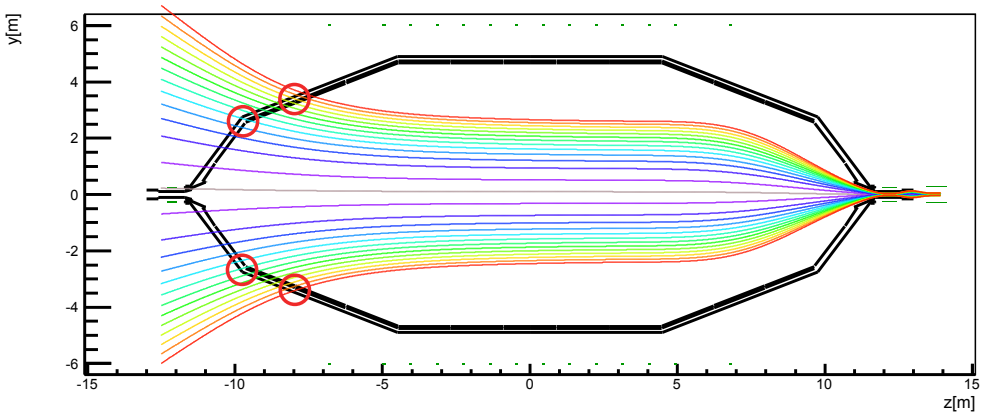

(a) magnetic field lines for an investigation of field emission

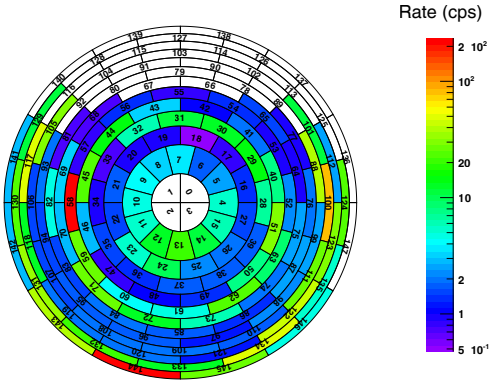

(b) FPD pixel view

Figure 8.26.: **Characteristics of field emission from holding structures of the inner electrode system** In (a) the magnetic flux tube imaging the comb structure (circle) of the inner electrode system shown. The pixel view in (b) images the ring structures of the holding structures of the electrode system via field emission from the wire combs. In addition, two *hot-spots* are visible with a substantially elevated rate. The potential offset between inner electrode and tank was -250 V in this case.

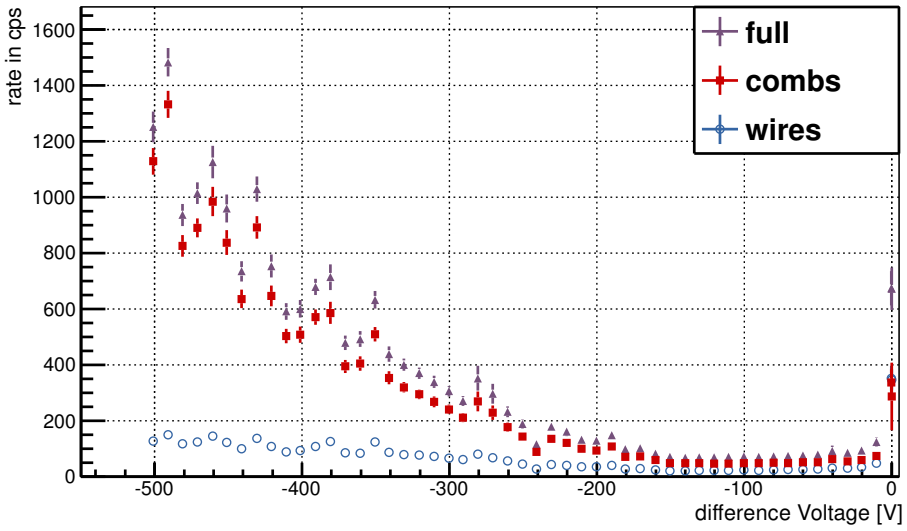

Figure 8.27.: **Rate of background electrons from the spectrometer wall as a function of the offset voltage of wires relative to the main spectrometer tank** In addition, a discrimination is made between pixels that image the holding structure of the wire electrode directly (combs) and pixels, where the holding structure and tank are screened by the wires (wires).

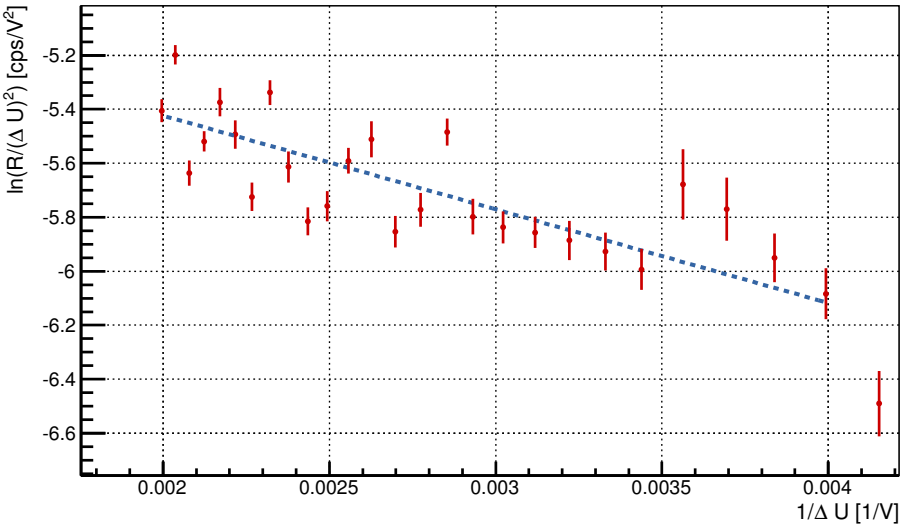

Figure 8.28.: F-N plot for high offset voltages applied to the inner electrode with an asymmetric magnetic field configuration A to provoke field-emission.

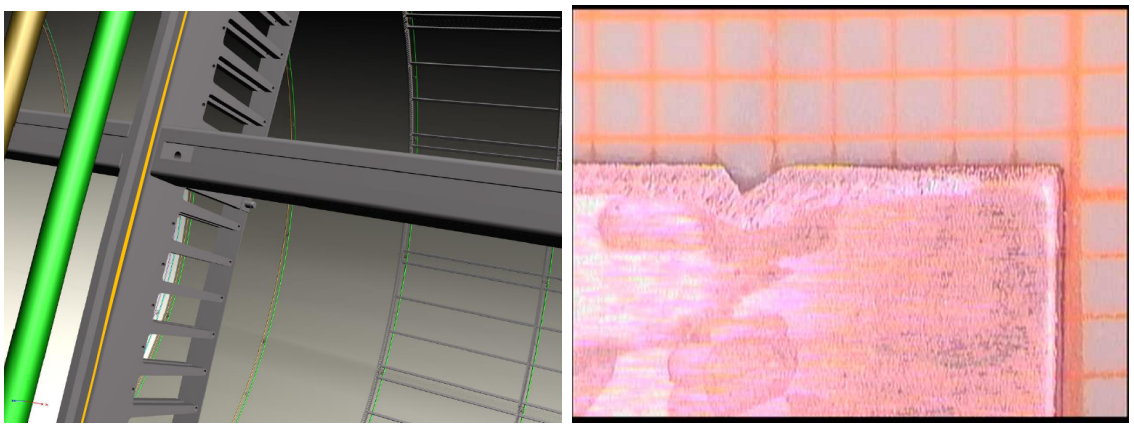

(a) 3D-CAD-drawing of the wire-combs (b) edge-negative in copper

Figure 8.29.: **Pictures of the wire holding structure** CAD-drawing of the holding-structure of the wire-electrode (a) and test-notch used to estimate the highlighted edge (b).

in figure 8.30. The electric field reaches a value of up to 0.3 MV/m near the edge.
The discrepancy between the simulated electric field strengths and the ones obtained by the fit would imply exceedingly large surface enhancement factors of $\beta = 10^5$ to 10^6. Although the surfaces of the holding-structure of the wire-electrode are not electro-polished, such surface enhancement factors border unphysical values. Probably this factor is due to the above-mentioned over prediction of the F-N theorem in its elementary form when applied to large area emitters. In general, the successful fitting of the data to the elementary form can be seen as a qualitative indicator that field-emission is present.
As a result of these investigations the offset voltages applied to the inner electrodes have to be set in such a way as to minimize the flux of incoming secondary electrons from the wall as well as to minimize field electron emission.

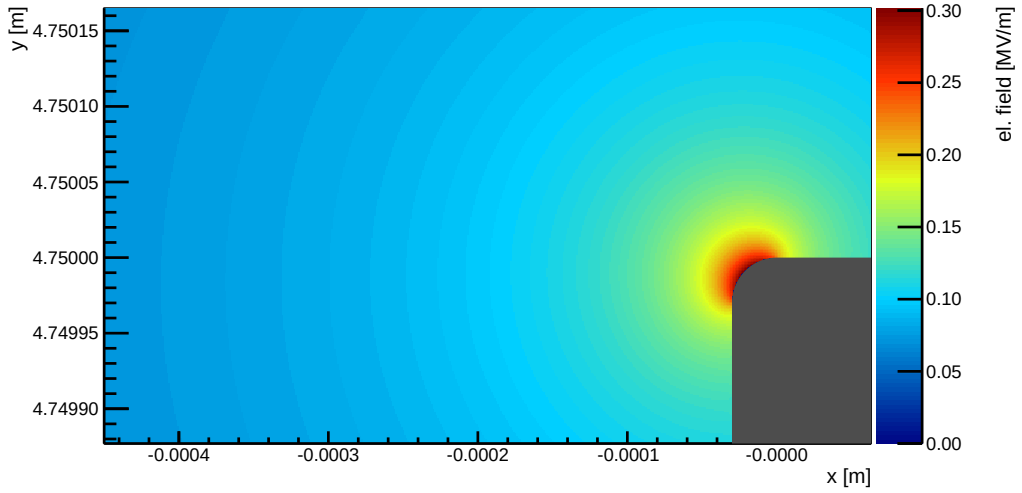

(a) field-simulation for an 0.03 mm edge

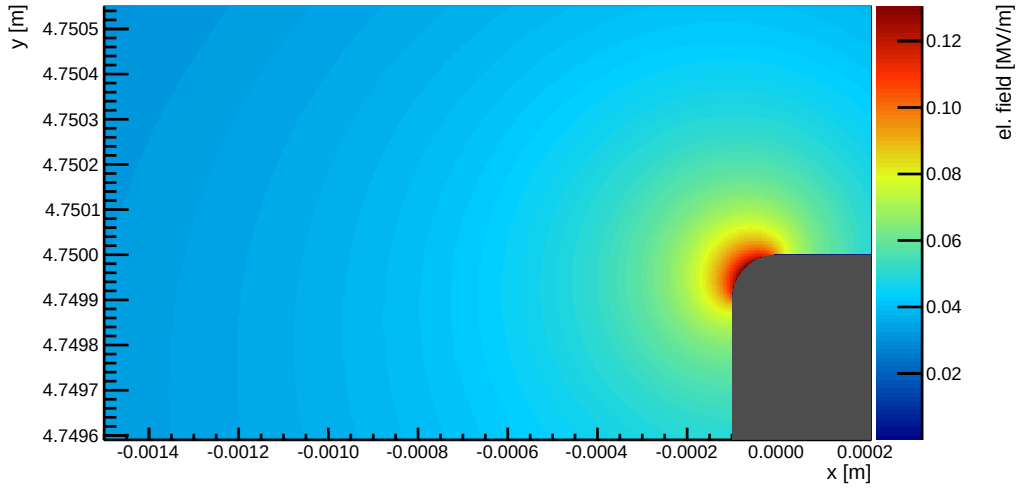

(b) field-simulation for an 0.1 mm edge

Figure 8.30.: **Electric field simulations of the wire combs** Displayed is the electric field strength as calculated by KASSIOPEIA near the edge of the wire-combs. The wire electrode is on -200 V compared to the main spectrometer tank. The radial distance between the edge and the tank is 15 cm. Note the different scales in (a) and (b)

9. Summary and Conclusion

The observation of neutrino oscillations has provided incontestable evidence for non-zero neutrino masses. This evidence for physics beyond the SM is a strong motivation for experiments to determine the absolute neutrino mass scale and not only to infer mass splittings, as do oscillation studies. The KATRIN experiment will determine the effective mass of the electron anti-neutrino with a sensitivity of 200 meV (90%C.L.) by performing a precision measurement of the tritium-β-spectrum close to the endpoint energy at 18.6 keV. The experiment makes use of two MAC-E filter type spectrometers based on the principle of magnetic adiabatic collimation with an electrostatic filter. To achieve the design sensitivity, a background rate of 10 mcps is necessary.
Measurements at predecessor experiments revealed secondary electron emission caused by environmental radiation and cosmic ray muons to account for the majority of the expected background rate. It is therefore important to obtain a good understanding of this background component in KATRIN as well.
The focus of this work has been on the development of methods and tools to study the electromagnetic properties especially with regard to background electrons emitted from the large 690 m^2 inner spectrometer surface of the KATRIN spectrometers. An important tool to understand complex background processes has been the Kassiopeia software package. Without the detailed field calculation and particle tracking options provided by Kassiopeia, the extensive test measurements with different types of spectrometers could not have been analyzed. Whenever possible Kassiopeia calculations were compared to measurement data as a complementary tool to refine background models.
The thesis at hand thus provides a thorough study of the characteristics, the formation as well as the complex transport mechanisms of secondary electrons in the spectrometers. The main results of the interrelated work packages consisting of simulations, models and measurements can be summarized as follows:

- For the first time, a complete description of the nature of secondary electron emission following muon interactions in stainless steel sheets is presented. To do so, geometry-related issues for complex electron trajectories and computations of scattering and attenuation processes were performed allowing to decompose different sources of secondary electron emission. A crucial role in this

regard is played by transport mechanisms of secondary electrons enabling them to penetrate electric and magnetic shielding mechanism of a MAC-E filter, and this work allowed for the first time to understand the complex phenomena in th KATRIN main spectrometer.

- This thesis has contributed significantly to providing new techniques for the calculation of electric and magnetic fields in the experiment. Here, the focus was put on methods that are highly suited to the computation of non-axially symmetric field-contributions. The methods introduced for particle-tracking allowed for the first time for a precise qualitative and quantitative study of secondary electrons in the KATRIN experiment.

- In addition to these works, measurements with dedicated muon detector systems were performed at the monitor and main spectrometer. Special interest and care was given to signal-processing and the uncertainties related to it. This work is the first to consider variations of the cosmic ray flux due to atmospheric conditions with regard to a time-dependent secondary emission rate for direct neutrino mass experiments at sea level.

- An ensemble of interconnected test measurements was carried out at the monitor and main spectrometer to obtain a reliable estimate of the absolute secondary electron emission rate induced by muons and to characterize these background events by their energy- and angular-distributions and multiplicity. The measurements give clear proof that secondary electron emission is induced dominantly by muons and not by intrinsic or environmental radioactivity of or around the spectrometer vessel. The distinct, non-Possion-distributed emission time characteristics of this background class can have an impact on the KATRIN sensitivity if left unconsidered.

The works of this thesis are of vital importance in optimizing the active suppression methods against background due to cosmic-induced secondary electron emission. It could be demonstrated that the vast majority of secondary electrons from the vessel wall is of low energy ($E < 20$ eV) nature and, somewhat counterintuitive but fully supported by trajectory calculations, able to overcome the magnetic shielding by adiabatic drift (see 3.6). Also, a first hint of the correlation of the secondary emission rate with the flux of cosmic ray muons could be provided.
With a limited electrostatic shielding factor due to the not yet fully-functional wire electrode, and with non-existing shielding of the holding structures if the inner wire electrode, the secondary emission dominates the background rate with a value of of $\sim$560 mcps, of specific interest in this context is a small but distinct non-Poissonian component that amounts to 1.4 mcps for normal operation conditions. In the case, that this non-Possion-distributed component would be left unconsidered, it would lead to a noticeable reduced sensitivity of KATRIN. Once the wire electrode is fully operational, however, the remaining background due to secondary electrons from walls is expected to drop by a factor of 10.
Analyses reveal, a total background of $\sim$60 mcps would still remain, which is considerably larger than the design goal of KATRIN. Further suppression of the secondary electron emission from the vessel wall could be achieved by a stronger magnetic shielding. This can either be done by increasing the minimum magnetic field in the analyzing plane, which however would soften the energy resolution of the spectrometer, or by minimizing of the magnetic stray fields from structural materials in the

spectrometer hall by a system of compensation coils [183]. Finally, by application of cyclic pulses of an electric dipole and a magnetic pulse the trapped electrons can be ejected from the sensitive part of the flux tube.

To conclude, this thesis has provided crucial insight into one of the dominant background classes in electrostatic spectrometers; secondary electron emission following muon interactions in the large spectrometer vessel. Only by combining an extensive suite of test experiments with advanced modeling and simulation tools is it possible to achieve the stringent limit of 10 mcps for background processes to measure the fundamental mass scale of neutrinos with unprecedented sensitivity.

List of Figures

List of Tables

List of Acronyms

BEM Boundary Element Method

CMB Cosmic Microwave Background

CN Campus North

CPS Cryogenic Pumping Section

DAQ data acquisition

DPS Differential Pumping Section

DPS1-R Differential Pumping Section 1-Rear

DPS1-F Differential Pumping Section 1-Forward

EMCS Earth Magnetic field Compensation System

F-N Fowler-Nordheim

FLT first level trigger

FPD focal plane detector

FWHM Full Width Half Maximum

GPS global positioning system

HV high-voltage

KIT Karlsruhe Institute of Technology

LBNL Lawrence Berkeley National Laboratory

LFCS low-field coil system

LN2 Liquid Nitrogen

MC Monte-Carlo

MS main spectrometer

NEG non-evaporable getter

NIM Nuclear Instrumentation Module

PAE post-acceleration electrode

PMT photomultiplier

PSI Paul-Scherrer-Insitut

ORCA object-oriented real-time control and acquisition

SDS spectrometer and detector section

SDSS Sloan Digital Sky Survey

SLT second level trigger

SM Standard Model

SN supernovae

SSM Standard Sun Model

TMP turbo-molecular pump

UHV ultra-high vacuum

WGTS Windowless Gaseous Tritium Source

Appendices

A. Determination of tritium-acitivity in the pre-spectromter

To determine the tritium-flux from the DPS into the pre-spectrometer, a dedicated measurement is planned. The pre-spectrometer will be set on -19 kV, to block decay-electrons from the source. The main spectrometer will not be operated with high-voltage, so that no background due to stored particles within it occurs. The goal of the experimental setup will be the measurement of secondary electrons due to particles that are stored in the pre-spectrometer. These will be caused by tritium-decays inside the pre-spectrometer, allowing for a calculation of the tritium-partial-pressure and -flux based on the secondary-rate.

A.1. Simulation

In order to estimate the fraction of secondary electrons that are able to reach the detector and which factors influence this fraction, a tracking simulation was done. Electrons with a typical secondary-electron spectrum (see figure A.1) were started equally distributed in the volume of the pre-spectrometer. To save computation-time, only the sensitive volume of the pre-spectrometer, which is determined by the magnetic flux-tube that is mapped onto the detector, was considered. In figure A.2 a longitudinal-section of this volume is shown.
As the main spectrometer is not on high-voltage and the secondary electrons that are created in the pre-spectrometer have energies around 19 keV, they show non-adiabatic trajectories in areas of small magnetic field ($\approx$550 µT). The non-adiabatic trajectories lead to electrons that do not follow the magnetic field-lines or suddenly change their gyration-angle to the magnetic-field. Electrons affected by these effects are not able to reach the detector as they either hit the spectrometer-wall or are stored in the main spectrometer (see figure A.3)
To suppress these non-adiabatic effects, the magnetic field-strength in the analyzing plane of the main spectrometer can be increased to 11 G. With the higher magnetic field, more than 90% of the secondary electrons, created in the pre-spectrometer can

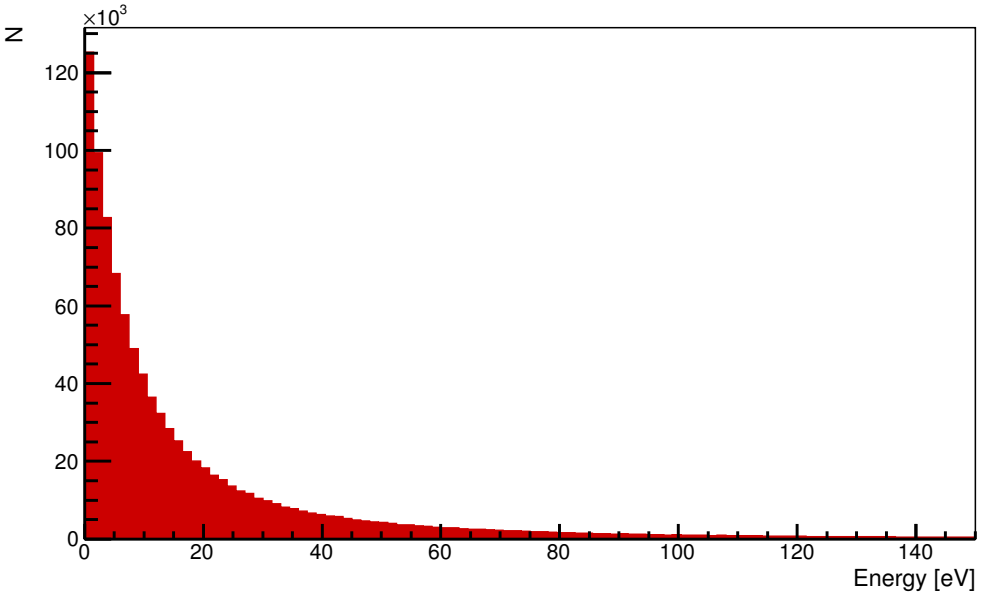

Figure A.1.: Energy spectrum of secondary electrons created by stored electrons.

reach the detector. Only a small fraction of them gets absorbed on the wall of the spectrometer, presumably due to their large cyclotron-radii.

A.2. Determination of tritium-activity

The mean electron-energy of a tritium-decay accounts to:

$$\langle E_e \rangle = 5.7 \text{ keV} \tag{A.1}$$

The number of secondary electrons is closely correlated with the energy of the primary electron [102]:

$$N_s \sim {E_e}^{0,97\pm0,02} \quad \Rightarrow \langle N_s \rangle = 174\ e^- \rightarrow 32 \text{ mcps} \equiv \mathcal{R}_0 \tag{A.2}$$

So, on average, 174 electrons are created per decay. This corresponds to a rate of 32 mcps over a time of 90 min, if the pressure is 10^{-11} mbar (this scales linear with the pressure).
So if we measure a certain rate $\mathcal{R}$ at this pressure, the activity in the flux-tube results to:

$$A_{\text{PS}} = \frac{\mathcal{R}}{\mathcal{R}_0} \cdot \frac{1}{0.473} \cdot \frac{1}{0.95} \tag{A.3}$$

Using this result and the decay-constant of tritium λ (=3.568 109 $\times 10^{-9}$ s), we can calculate the number of tritium molecules N_{T_2} in the sensitive volume of the pre-spectrometer. And finally, derive the tritium density n_{T_2} in this volume:

$$A_{\text{PS}} = \lambda \cdot N_{T_2} \quad \Rightarrow \quad N_{T_2} = \frac{A_{\text{PS}}}{\lambda} \quad \Rightarrow \quad n_{T_2} = \frac{N_{T_2}}{V_{\text{PS}}} \tag{A.4}$$

with V_{PS} (=1.6954 m^3) denoting the volume of the flux tube in the pre-spectrometer.

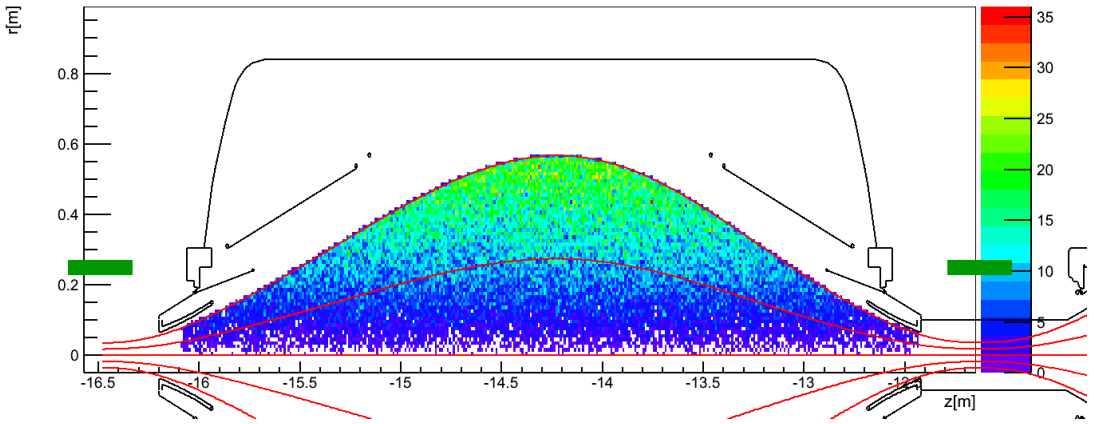

Figure A.2.: $z - r$-distribution of 10^5 simulated secondary-electrons in the pre-spectrometer

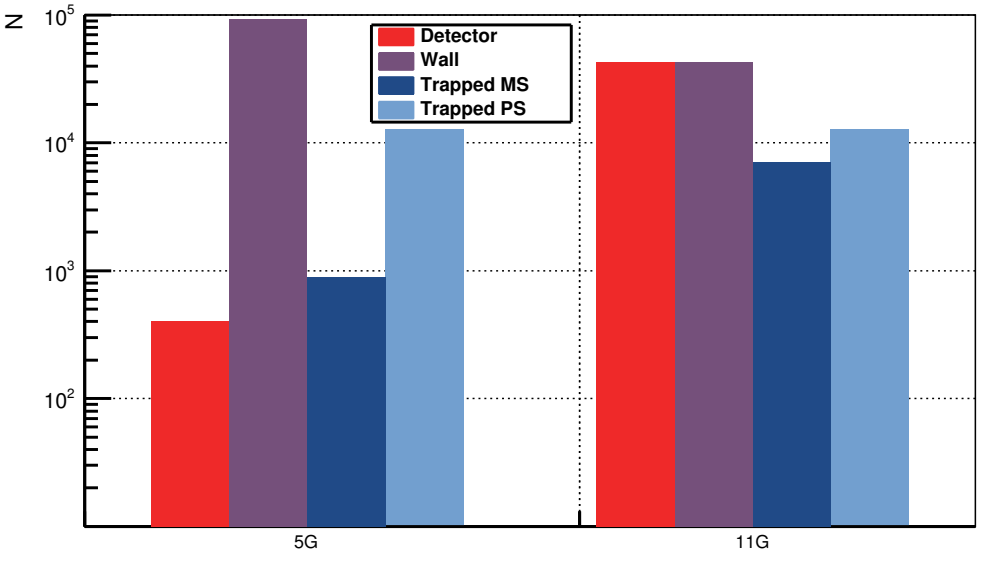

Figure A.3.: **Simulated fates of secondary electrons** "Detector" means they were able to reach the detector, "Wall" means they hit the spectrometer walls, "TrappedMS" means they were stored in the main spectrometer and "TrappedPS" means they were stored in the pre-spectrometer. Trapped particles will eventually reach the detector after they changed their gyration-angle due to scattering.

Bibliography

[1] J. Chadwick. Intensitätsverteilung im magnetischen Spektrum von β-Strahlen von Radium B+C. *Verh. d. Deutsch. Phys. Ges.*, 15:383, 1914.

[2] W. Pauli. Letter to Gauvereinstagung in Tübingen: "Sehr geehrte radioaktive Damen und Herren". *published in R. Kronig and V. Weisskopf (Eds.), Wolfgang Pauli, Collected scientific Papers, Vol.2, Interscience, New York (1964)*, 1930.

[3] J. Chadwick. Possible Existence of a Neutron. *Nature*, 312:312, 1932.

[4] E. Fermi. Versuch einer Theorie der β-Strahlen. *Zeitschrift für Physik A*, 88:161–177, 1934. 10.1007/BF01351864.

[5] C. L. Cowan, F. Reines, F. B. Harrison, H. W. Kruse, and A. D. McGuire. Detection of the Free Neutrino: a Confirmation. *Science*, 124(3212):103–104, 1956.

[6] F. Reines, C. L. Cowan, F. B. Harrison, A. D. McGuire, and H. W. Kruse. Detection of the Free Antineutrino. *Phys. Rev.*, 117(1):159–173, Jan 1960.

[7] J-M. Gaillard, K. Goulianos, L. M. Lederman, N. Mistry, M. Schwartz, J. Steinberger, and G. Danby. Observation of High-Energy Neutrino Reactions and the Existence of Two Kinds of Neutrinos. *Phys. Rev. Lett.*, 9:36–44, 1962.

[8] K. Kodama et al. Observation of tau neutrino interactions. *Phys. Lett. B*, 504(3):218–224, 2001.

[9] D. Decamp et al. A precise determination of the number of families with light neutrinos and of the Z boson partial widths. *Phys. Lett. B*, 235(3-4):399–411, 1990.

[10] D. Decamp et al. Determination of the number of light neutrino species. *Phys. Lett. B*, 231(4):519–529, 1989.

[11] J. N. Bahcall, A. M. Serenelli, and S. Basu. New Solar Opacities, Abundances, Helioseismology, and Neutrino Fluxes. *Astrophys. J.*, 621(1):85–88, 2005.

[12] B. T. Cleveland et al. Measurement of the solar neutrino flux with the Homestake chlorine detector. *Astrophys. J.*, 496(1):505–526, 1998.

[13] R. Davis. A review of the Homestake solar neutrino experiment. *Prog. Part. Nucl. Phys.*, 32:13–32, 1994.

[14] GALLEX Collaboration. GALLEX solar neutrino observations: results for GALLEX IV. *Phys. Lett. B*, 447(1-2):127–133, 1999.

[15] GNO Collaboration. Complete results for five years of GNO solar neutrino observations. *Phys. Lett. B*, 616(3-4):174–190, 2005.

[16] SAGE Collaboration. Solar neutrino flux measurements by the Sovjet-American gallium experiment (SAGE) for half the 22-year solar cycle. *J. Exp. Theo. Phys.*, 95:181–193, 2002.

[17] Kamiokande Collaboration. Solar Neutrino Data Covering Solar Cycle 22. *Phys. Rev. Lett.*, 77:1683–1686, 1996.

[18] Q. R. Ahmad et al. (SNO Collaboration). Direct Evidence for Neutrino Flavor Transformation from Neutral-Current Interactions in the Sudbury Neutrino Observatory. *Phys. Rev. Lett.*, 89(011301), 2002.

[19] B. Aharmim et al. (SNO Collaboration). Determination of the ν_e and total ^8B solar neutrino fluxes using the Sudbury Neutrino Observatory Phase I data set. *Phys. Rev. C*, 75(4):045502, 2007.

[20] SNO Collaboration. Independent Measurement of the Total Active ^{8}B Solar Neutrino Flux Using an Array of ^{3}He proportional counters at the Sudbury Neutrino Observatory. *Phys. Rev. Lett.*, 101(111301), 2008.

[21] K. S. Hirata et al. Experimental Study of the Atmospheric Neutrino Flux. *Phys. Lett.*, B205:416, 1988.

[22] Y. Fukuda at al. (Super-Kamiokande Collaboration). Evidence for Oscillation of Atmospheric Neutrinos. *Phys. Rev. Lett.*, 81:1562–1567, Aug 1998.

[23] W. W. M. Allison et al. Measurement of the atmospheric neutrino flavour composition in Soudan 2. *Physics Letters B*, 391:491, 1997.

[24] C. Berger et al. Study of Atmospheric Neutrino Interactions with the Frejus Detector. *Phys. Lett.*, B227:489, 1989.

[25] G. Battistoni et al. Fully contained events in the Mont Blanc Nucleon decay detector. *Phys. Lett.*, B118:461, 1982.

[26] The Super-Kamiokande Collaboration. Study of the atmospheric neutrino flux in the multi-GeV energy range. *Physics Letters B*, 436:33, 1998.

[27] Particle Data Group. Review of particle physics. *Phys. Rev. D*, 86(010001), 2013.

[28] M. C. Gonzalez-Garcia and Y. Nir. Neutrino masses and mixing: evidence and implications. *Rev. Mod. Phys.*, 75(2):345–402, Mar 2003.

[29] G. Altarelli and K. Winter eds. *Neutrino Mass.* Springer Tracts in Modern Physics. Springer, 2003.

[30] R. Wendell et al. (Super-Kamiokande Collaboration). Atmospheric neutrino oscillation analysis with subleading effects in Super-Kamiokande I, II and III. *Phys. Rev. D*, 81, 2010.

[31] S. Abe et al. (KamLAND Collaboration). Precision Measurement of Neutrino Oscillation Parameters with KamLAND. *Phys. Rev. Lett.*, 100(22):221803, Jun 2008.

[32] Y. Abe et al. (Double Chooz Collaboration). Indication for the disappearance of reactor electron antineutrinos in the Double Chooz experiment. *Phys. Rev. Lett.*, 108, 2012.

[33] Y. Abe et al. (Double Chooz Collaboration). Reactor electron antineutrino disappearance in the Double Chooz experiment. *Phys. Rev. D*, 86, 2012.

[34] J. K. Ahn et al. (RENO Collaboration). Observation of reactor electron antineutrino disappearance in the RENO experiment. *Phys. Rev. Lett.*, 108, 2012.

[35] F. P. An et al. (DAYA-BAY Collaboration). Observation of electron-antineutrino disappearance at Daya Bay. *Phys. Rev. Lett.*, 108, 2012.

[36] M. H. Ahn et al. (K2K Collaboration). Measurement of neutrino oscillation by the K2K experiment. *Phys. Rev. D*, 74, 2006.

[37] K. Abe et al. (T2K Collaboration). Indication of Electron Neutrino Appearance from an Accelerator-Produced Off-Axis Muon Neutrino Beam. *Phys. Rev. Lett.*, 107:041801, 2011.

[38] G. Feldman et al. NoVa Technical Design Report. Technical Design Report, 2007.

[39] H. Murayama. Oscillation Parameter Plots. web plot, 2014.

[40] E. N. Alexeyev, L. N. Alexeyeva, I. V. Krivosheina, and V. I. Volchenko. Detection of the neutrino signal from SN 1987A in the LMC using the INR Baksan underground scintillation telescope. *Physics Letters B*, 205(2–3):209 – 214, 1988.

[41] C. B. Bratton et al. Angular Distribution of Events From Sn1987a. *Phys.Rev.*, D37:3361, 1988.

[42] K. S. Hirata, T. Kajita, M. Koshiba, M. Nakahata, Y. Oyama, et al. Observation in the Kamiokande-II Detector of the Neutrino Burst from Supernova SN 1987a. *Phys.Rev.*, D38:448–458, 1988.

[43] T. J. Loredo and D. Q. Lamb. Bayesian analysis of neutrinos observed from supernova SN 1987A. *Phys. Rev. D*, 65(6):063002, Feb 2002.

[44] E. W. Kolb, A. J. Stebbins, and M. S. Turner. How reliable are neutrino mass limits derived from SN1987A? *Phys. Rev. D*, 35(12):3598–3606, Jun 1987.

[45] J. Ellis, H. T. Janka, N. E. Mavromatos, A. S. Sakharov, and E. K. G. Sarkisyan. Prospective constraints on neutrino masses from a core-collapse supernova. *Phys. Rev. D*, 85:105028, May 2012.

[46] L. Bergström and A. Goobar. *Cosmology and Particle Astrophysics*. Springer, 2006.

[47] J. C. Mather et al. A preliminary measurement of the cosmic microwave background spectrum by the cosmic background explorer (COBE) satellite. *Astrophys. J.*, 354:37–40, 1990.

[48] A. A. Penzias and R. W. Wilson. A Measurement of Excess Antenna Temperature at 4080 Mc/s. *Astrophys. J.*, 142(1):419–421, 1965.

[49] Planck Collaboration. Planck 2013 results. XVI. Cosmological parameters. 2013. Submitted to Astron. Astrophys.

[50] J. Lesgourgues and S. Pastor. Massive neutrinos and cosmology. *Physics Reports*, 429(6):307 – 379, 2006.

[51] A. Faessler et al. Search for the Cosmic Neutrino Background and KATRIN. 2013.

[52] E. Giusarma, R. de Putter, S. Ho, and O. Mena. Constraints on neutrino masses from Planck and Galaxy Clustering data. *Phys.Rev.*, D88(6):063515, 2013.

[53] H. Aihara and others (SDSS Collaboration). The Eighth Data Release of the Sloan Digital Sky Survey: First Data from SDSS-III. *Astrophys. J. Suppl. S.*, 193(2):29, 2011.

[54] M. Vogelsberger, S. Genel, V. Springel, P. Torrey, D. Sijacki, D. Xu, G. Snyder, S. Bird, D. Nelson, and L. Hernquist. Properties of galaxies reproduced by a hydrodynamic simulation. *Nature*, 509(7499):177–182, May 2014.

[55] V. Springel, S. D. M. White, A. Jenkins, C. S. Frenk, N. Yoshida, L. Gao, J. Navarro, R. Thacker, D. Croton, J. Helly, et al. Simulations of the formation, evolution and clustering of galaxies and quasars. *Nature*, 435(7042):629–636, 2005.

[56] S. Hannestad. Structure formation with strongly interacting neutrinos—implications for the cosmological neutrino mass bound. *Journal of Cosmology and Astroparticle Physics*, 2005(02):011, 2005.

[57] M. Fukugita, G. C. Liu, and N. Sugiyama. Limits on neutrino mass from cosmic structure formation. *Physical Review Letters*, 84(6):1082, 2000.

[58] E. Majorana. Teoria symmetrica dell elettrone e del positrone. *Il Nuovo Cimento (1924-1942)*, 14:171–184, 1937.

[59] K. H. Ackermann et al. The GERDA experiment for the search of $0\nu\beta\beta$ decay in 76ge. *The European Physical Journal C*, 73(3), 2013.

[60] M. Agostini et al. Results on neutrinoless double-β decay of ^{76}Ge from phase i of the GERDA experiment. *Phys. Rev. Lett.*, 111:122503, Sep 2013.

[61] C. E. Aalseth et al. Comment on 'Evidence for Neutrinoless Double Beta Decay'. *Mod. Phys. Lett. A*, 17(22):1475–1478, 2002.

[62] H. V. Klapdor-Kleingrothaus, A. Dietz, H. L. Harney, and I. V. Krivosheina. Evidence for Neutrinoless Double Beta Decay. *Mod. Phys. Lett. A*, 16:2409–2420, 2001.

[63] R. Beuselinck, J. Sedgbeer, and Y. Shitov. The Supernemo Experiment.

[64] M. Hötzel. Berechnung von KATRIN Messspektren unter Einbeziehung der Eigenschaften der fensterlosen gasförmigen Tritiumquelle. Diploma thesis, KIT, 2009.

[65] M. Daum, R. Frosch, D. Herter, M. Janousch, and P. R. Kettle. Measurements of the muon-neutrino mass. *Zeitschrift für Physik C Particles and Fields*, 56(1):S114–S116, 1992.

[66] K. Assamagan et al. Upper limit of the muon-neutrino mass and charged pion mass from momentum analysis of a surface muon beam. *Phys. Rev.*, D53:6065–6077, 1996.

[67] R. Barate et al. An upper limit on the tau neutrino mass from three- and five-prong tau decays. *Eur. Phys. J.*, C2:395–406, 1998.

[68] J. Angrik et al. KATRIN Design Report (FZKA Report 7090). internal report, 2004.

[69] N. Doss and J. Tennyson. Excitations to the electronic continuum of $^3HeT^+$ in investigations of T_2 β-decay experiments. *Journal of Physics B: Atomic, Molecular and Optical Physics*, 41(12):125701, 2008.

[70] W. W. Repko and C.-E. Wu. Radiative corrections to the end point of the tritium β decay spectrum. *Phys. Rev. C*, 28(6):2433–2436, Dec 1983.

[71] R. B. Firestone, S. Y. F. Chu, and C. M. Baglin. Table of Isotopes, 8th Edition. 1999.

[72] MARE Collaboration. MARE homepage. http://mare.dfm.uninsubria.it/frontend/exec.php [last update: 18-Mar-2011].

[73] MARE Collaboration. MARE-1 in Milan: Status and Perspectives. *J. Low Temp. Phys.*, 167:1035–1040, 2012.

[74] M. Galeazzi et al. The Electron Capture Decay of ^{163}ho to Measure the Electron Neutrino Mass with sub-eV Accuracy. 2012. arXiv:1202.4763v3 [physics.ins-det].

[75] J.-P. Porst et al. Low temperature magnetic calorimeters for high precision measurements of ^{163}Ho and ^{187}Re spectra. *Nucl. Phys. B (Proc. Suppl.)*, 446:229–232, 2012.

[76] P. C.-O. Ranitzsch et al. Development of Metallic Magnetic Calorimeters for High Precision Measurements of Calorimetric ^{187}Re and ^{163}Ho Spectra. *J. Low Temp. Phys.*, 167(5-6):1004–1014, 2012.

[77] HoLMES Collaboration. HoLMES homepage. https://artico.mib.infn.it/nucriomib/experiments/holmes [last update: 04-Jun-2014].

[78] J. F. Amsbaugh et al. Focal-plane detector system for the KATRIN experiment. *NIM A*, 2014.

[79] J. Schwarz. *Detector-System Implementation for the KATRIN Experiment.* PhD thesis, KIT, 2014.

[80] J. Beamson et al. The collimating and magnifying properties of a superconducting field photoelectron spectrometer. *J. Phys. E*, 13(64), 1980.

[81] V. M. Lobashev and P. E. Spivak. A method for measuring the electron antineutrino rest mass. *Nucl. Instrum. Methods Phys. Res., Sect. A*, 240(2):305–310, 1985.

[82] A. Picard et al. A solenoid retarding spectrometer with high resolution and transmission for keV electrons. *Nucl. Instrum. Methods Phys. Res., Sect. B*, 63(3):345–358, 1992.

[83] J. Bonn et al. The mainz neutrino mass experiment. *Nucl. Phys. B Proc. Suppl.*, 91(1-3):273–279, 2001. Neutrino 2000.

[84] Ch. Kraus et al. Final results from phase II of the Mainz neutrino mass search in tritium. *Eur. Phys. J. C*, 40:447–468, 2005.

[85] M. Erhard. Untersuchung der Langzeitstabilität des nuklearen Standards für die Energieskala des KATRIN-Expriments. Diploma thesis, KIT, 2012.

[86] J. Goullon. Installation and commissioning of the monitor spectrometer. Diploma thesis, KIT, 2010.

[87] M. Erhard et al. High-voltage monitoring with a solenoid retarding spectrometer at the KATRIN experiment. *JINST*, 2014. accepted for publication.

[88] M. Prall et al. The KATRIN pre-spectrometer at reduced filter energy. *New J. Phys.*, 14(073054), 2012.

[89] S. Görhardt et al. Commissioning of a liquid nitrogen cooled baffle for radon trapping in the KATRIN main spectrometer. 2014. in preparation.

[90] S. Görhardt. *Background Reduction Methods and Vacuum Technology at the KATRIN Spectrometers*. PhD thesis, KIT, 2014.

[91] F. Glück and A. Osipowicz. Air coil design at the main spectrometer. KATRIN Collaboration meeting, April 2008, `http://fuzzy.fzk.de/bscw/bscw.cgi/d443733/95-TRP-4440-D1-FGlueck-AOsipovicz.ppt`, 2009.

[92] F. Glück, G. Drexlin, B. Leiber, S. Mertens, A. Osipowicz, et al. Electromagnetic design of the large-volume air coil system of the KATRIN experiment. *New J.Phys.*, 15:083025, 2013.

[93] N. Wandkowsky et al. Technical design and commissioning of the KATRIN large volume air coil system. 2013. in preparation.

[94] F. Glück et al. Air coil system and magnetic field sensor system. Internal KATRIN report, `http://fuzzy.fzk.de/bscw/bscw.cgi/d530439/Air%20Coil%20System%20and%20Magnetic%20Field%20Sensor%20System.pdf`, 2009.

[95] F. Fränkle et al. Results of the first KATRIN SDS measurement phase. Internal KATRIN report, 2014.

[96] F. Glück F. Fränkle and K. Valerius et al. Penning discharge in the KATRIN pre-spectrometer. *New Journal of Physics*, 2014.

[97] M. J. Berger and J. H. Hubbell. XCOM: Photon Cross Section Database (version 1.5), 2010. [Online; accessed 04-April-2014].

[98] F. M. Fränkle et al. Radon induced background processes in the KATRIN pre-spectrometer. *Astropart. Phys.*, 35(3):128–134, 2011.

[99] N. Wandkowsky, G. Drexlin, F. M. Fränkle, F. Glück, S. Groh, et al. Modeling of electron emission processes accompanying radon-α-decays within electrostatic spectrometers. *New J.Phys.*, 15:083040, 2013.

[100] N. Wandkowsky, G. Drexlin, F. M. Fränkle, F. Glück, S. Groh, et al. Validation of a model for Radon-induced background processes in electrostatic spectrometers. *J.Phys.*, G40:085102, 2013.

[101] H. Tawara et al. Cross sections and related data for electron collisions with hydrogen molecules and molecular ions. *J. Phys. Chem. Ref. Data*, 19(3):617–636, 1990.

[102] S. Mertens et al. Background due to stored electrons following nuclear decays at the KATRIN experiment. *Astropart. Phys.*, 41:52–62, 2013.

[103] F. Glück. Secondary electron emission in the pre-spectrometer and in the Mainz spectrometer. KATRIN Collaboration meeting, March 2009, `http://fuzzy.fzk.de/bscw/bscw.cgi/540728/95-TRP-4652-A5-FGlueck.ppt`.

[104] B. L. Henke, J. A. Smith, and D. T. Attwood. 0.1-10-keV X-ray-induced electron emissions from solids-models and secondary electron measurements. *Journal of Applied Physics*, 48(5):1852–1866, 1977.

[105] S. V. Chuklyaev and O. I. Shchetinin. Emission of slow secondary electrons under the influence of ionizing radiation. *Soviet Atomic Energy*, 63(1):560–562, 1987.

[106] M. Ya. Grudskii, N. N. Roldugin, and V. V. Smirnov. Regularities in γ-ray-initiated emission of true secondary electrons. *Soviet Physics-Technical Physics*, 27(6):701 – 704, 1982.

[107] P. A. Wolff. Theory of secondary electron cascade in metals. *Phys. Rev.*, 95:56–66, Jul 1954.

[108] M. A. Furman and M. T. F. Pivi. Probabilistic model for the simulation of secondary electron emission. *Phys. Rev. ST Accel. Beams*, 5:124404, Dec 2002.

[109] T. E. Burlin and S. R. Husain. The low energy portion of the electron spectrum established within and emitted from irradiated conducting materials. *Physics in Medicine and Biology*, 13(2):169, 1968.

[110] D. E. Groom, N. V. Mokhov, and S. I. Striganov. Muon stopping power and range tables 10 MeV–100 TeV. *Atomic Data and Nuclear Data Tables*, 78(2):183–356, 2001.

[111] D. F. Measday. The nuclear physics of muon capture. *Physics Reports*, 354(4–5):243 – 409, 2001.

[112] C. S. Wu and L. Wilets. Muonic atoms and nuclear structure. *Annual Review of Nuclear Science*, 19(1):527–606, 1969.

[113] G. Drexlin. private communication, 2014.

[114] C. Castagnoli, P. Picchi, A. Castellina, B. D'Ettorre Piazzoli, G. Mannocchi, and S. Vernetto. Energy spectrum and angular distribution of prompt cosmic-ray muons. *Il Nuovo Cimento A*, 82(1):78–92, 1984.

[115] S. I. Klimushin, E. V. Bugaev, and I. A. Sokalski. Parametrization of atmospheric muon angular flux underwater. *Phys. Rev. D*, 64:014016, May 2001.

[116] B. Jung. Simulation des Myon-induzierten Untergrundes und dessen Speicherwahrscheinlichkeit am KATRIN Hauptspektrometer. Diploma thesis, KIT, 2011.

[117] S. Agostinelli and J. Allison. Geant4—a simulation toolkit. *Nucl. Instrum. Meth. A*, 506(3):250–303, 2003.

[118] J. Allison et al. Geant4 developments and applications. *IEEE Transactions on Nuclear Science*, 53(1):270 –278, Feb. 2006.

[119] J. Baró, J. Sempau, J. M. Fernández-Varea, and F. Salvat. PENELOPE: An algorithm for Monte Carlo simulation of the penetration and energy loss of electrons and positrons in matter. *Nuclear Instruments and Methods in Physics Research Section B: Beam Interactions with Materials and Atoms*, 100(1):31–46, 1995.

[120] PENELOPE homepage. http://www.oecd-nea.org/tools/abstract/detail/nea-1525 [last update: 23-May-2011].

[121] B. Flatt. *Voruntersuchungen zu den Spektrometern des KATRIN-Experiments*. PhD thesis, University of Mainz, 2004.

[122] H. Arlinghaus. Investigation of the muon-induced secondary electron background in the KATRIN Experiment. Diploma thesis, University of Münster, 2009.

[123] M. Eisenbud and T. Gesell. *Environmental Radioactivity*. Elsevier, 4th edition, 1997.

[124] M. Lammers. Untersuchung der Untergrundrate des KATRIN Vorspektrometers im Bereich hoher Feldstärken. Diploma thesis, KIT, 2009.

[125] K. Schlösser. Gamma background measurements at KATRIN and Mainz. KATRIN Collaboration meeting, April 2008, `http://fuzzy.fzk.de/bscw/bscw.cgi/d443774/95-TRP-4446-D2-KSchloesser.ppt`.

[126] A. Sonzogni. Interactive Chart of Nuclide. National Nuclear Data Center: Brookhaven National Laboratory, http://www.nndc.bnl.gov/chart/.

[127] M. Ya. Grudskii, N. N. Roldugin, V. V. Smirnov, A. F. Adadurov, and V. T. Lazurik. Experimental investigation and Monte Carlo calculation of photon-induced electron emission from solids. *Nuclear Instruments and Methods in Physics Research Section A: Accelerators, Spectrometers, Detectors and Associated Equipment*, 227(1):126 – 134, 1984.

[128] A. Poon, A. Smith, and J. Wolf. Radon Emanation in the KATRIN Main Spectrometer. KATRIN internal report 430-DOC-3-0000-1, `http://fuzzy.fzk.de/bscw/bscw.cgi/d898720/LBNL-MainSpec_SST_Avtivity-Report-2013-v0.pdf`.

[129] R. H. Fowler and L. Nordheim. Electron emission in intense electric fields. *Proceedings of the Royal Society of London. Series A*, 119(781):173–181, 1928.

[130] R. G. Forbes and J. H. B. Deane. Reformulation of the standard theory of fowler–nordheim tunnelling and cold field electron emission. *Proceedings of the Royal Society A: Mathematical, Physical and Engineering Science*, 463(2087):2907–2927, 2007.

[131] R. G. Forbes. Description of field emission current/voltage characteristics in terms of scaled barrier field values (f-values). *Journal of Vacuum Science & Technology B*, 26(1):209–213, 2008.

[132] B. Bonin. Field emission and surface conditioning. *Vacuum*, 46(8–10):907 – 912, 1995.

[133] J.L. Delcroix. *Plasma Physics*, volume 1. John Wiley and Sons, 1968.

[134] E. Otten. The Mainz neutrino mass experiment. *Prog. Part. Nucl. Phys.*, 32:153–171, 1994.

[135] F. M. Fränkle. *Background Investigations of the KATRIN Pre-Spectrometer*. PhD thesis, KIT, 2010.

[136] F. Glück. Background theory: radial motion of electrons from spectrometer electrodes into the fluxtube. Internal KATRIN report, `http://fuzzy.fzk.de/bscw/bscw.cgi/d174403/background_theory_Glueck.pdf`, 2005.

[137] A. Torro. Background Study: Radial Motion of electrons in a spectrometer. Internal EXAKT report, 2005.

[138] J. Hergenhahn. Das KATRIN-Luftspulensystem: Messungen des Feldverlaufs und Überwachung mit einem Sensorsystem. Diploma thesis, KIT, 2010.

[139] J. Reich. *Magnetic Field Inhomogeneities and Their Influence on Transmission and Background at the KATRIN Main Spectrometer*. PhD thesis, KIT, 2013.

[140] A. Müller. Field Alignment Studies at the KATRIN Pinch Magnet. Bachelor's thesis, KIT, 2014.

[141] B. Leiber. Non-axially symmetric field and trajectory calculations for the KATRIN-experiment. Diploma thesis, KIT, 2009.

[142] F. Glück. Axisymmetric magnetic field calculation with zonal harmonic expansion. *Progress In Electromagnetics Research B*, 32:351–388, 2011.

[143] F. Glück. Axisymmetric electric and magnetic field calculations with zonal harmonic expansion. *PIER Proceedings, Kuala Lumpur*, pages 1698–1702, 2012.

[144] M. Hötzel. *Simulation and analysis of source-related effects for KATRIN*. PhD thesis, KIT, 2012.

[145] P. Renschler. *KESS - A new Monte Carlo simulation code for low-energy electron interactions in silicon detectors*. PhD thesis, KIT, 2011.

[146] D. Furse et al. Kassiopeia - the simulation package for the KATRIN experiment. in preparation.

[147] T. Fließbach. *Elektrodynamik*. BI-Wiss.-Verlag, 1994.

[148] F. Glück. Steel in the KATRIN buildings and the magnetic field in the main spectrometer. Internal KATRIN report, `http://fuzzy.fzk.de/bscw/bscw.cgi/d176563/steel_buildings_Glueck.pdf`, 2005.

[149] J. D. Jackson. *Classical Electrodynamics*. John Wiley and Sons, Ltd, 1998.

[150] W. H. Press et al. *Numerical Recipes 3rd Edition: The Art of Scientific Computing*. Cambridge University Press, New York, NY, USA, 3rd edition, 2007.

[151] R. J. LeVeque. *Finite Difference Methods for Ordinary and Partial Differential Equations: Steady-State and Time-Dependent Problems*. SIAM, 2007.

[152] S. C. Brenner and L. R. Scott. *The mathematical theory of finite element methods*. Springer Texts in Applied Mathematics. Springer, 2008.

[153] P. W. Hawkes and E. Kasper. *Principles of Electron Optics*, volume 1. Academic Press, 1989.

[154] G. Engel-Müllges and F. Uhlig. *Numerical Algorithms with C*. Springer, 1996.

[155] F. Durand. *Electrostatique*. Masson, 1964.

[156] M. Eupper. *Eine verbesserte Integralgleichungsmethode zur numerischen Lösung dreidimensionaler Dirichletprobleme und ihre Anwendung in der Elektronenoptik*. PhD thesis, Eberhard-Karls-Universität zu Tübingen, 1985.

[157] F. Glück. Axisymmetric electric field calculation with zonal harmonic expansion. *Progress In Electromagnetics Research B*, 32:319–350, 2011.

[158] S. Filippi and J. Gräf. New Runge Kutta Nystroem formula-pairs of order 8(7), 9(8), 10(9) and 11(10) for differential equations of the form $y'' = f(x, y)$. *Journal of Computational and Applied Mathematics*, 14(3):361 – 370, 1986.

[159] L. Papula. *Mathematik für Ingenieure und Naturwissenschaftler*, volume 2. Vieweg + Teubner, 1996.

[160] J. H. Verner. Explicit Runge-Kutta methods with estimates of the local truncation error. *SIAM J. Numer. Anal.*, 15(4):772–790, August 1978.

[161] P. W. Sharp. Numerical comparisons of some explicit Runge-Kutta pairs of orders 4 through 8. *ACM Trans. Math. Softw.*, 17:387–409, September 1991.

[162] F. Glück. Runge-Kutta method for numerical solution of differential equation system. `http://fuzzy.fzk.de/bscw/bscw.cgi/d479152/rungekutta.pdf`.

[163] Th. Thümmler. Entwicklung von Methoden zur Untergrundreduzierung am Mainzer Tritium β-Spektrometer. Diploma thesis, Johannes Gutenberg Universität Mainz, 2002.

[164] P. Rovedo. Muon induced secondary electrons at the KATRIN experiment: Detector installation and setup & data analysis. Diploma thesis, KIT, 2013.

[165] J. Reichenbacher. *Final KARMEN-Results on Neutrino-Oscillations and Neutrino-Nucleus-Interactions in the Energy-Regime of Supernovae*. PhD thesis, KIT, 2004.

[166] BC-400,BC-404,BC-408,BC-412,BC-416 - Premium Plastic Scintillators - Datasheet. `http://www.crystals.saint-gobain.com/uploadedFiles/SG-Crystals/Documents/SGC%20BC400-404-408-412-416%20Data%20Sheet.pdf`.

[167] Hamamatsu Photonics K.K. *Photomultiplier Tubes - Basics and Applications*, 3rd edition, 2006.

[168] H. Gemmeke. The Auger Fluorescence Detector Electronics. *27th International Cosmic Ray Conference*, 27:737 – 740, 2001.

[169] M. Howe. ORCA - Object-oriented Real-time Control and Acquisition. `http://orca.physics.unc.edu/~markhowe/Orca_Help/About_Orca.html`.

[170] N. Wandkowsky. *Study of background and transmission properties of the KATRIN spectrometers*. PhD thesis, KIT, 2013.

[171] CAEN SY127 - Technical Information Manual. `http://www.tunl.duke.edu/documents/public/electronics/CAEN/caen_sy127.pdf`.

[172] S. Enomoto and B. Leiber. Time-sync between Detector- and Muon-DAQ. Electronic Logbook Entry, `https://neutrino.ikp.kit.edu:8080/SDS-Measurements+Phase+2/1`.

[173] R. Rink. Master's thesis, KIT, 2014. in preparation.

[174] O.C. Allkofer. *Introduction to Cosmic Radiation*. Karl Thiemig, 1975.

[175] R. C. Smith, R. D. Forrest, J. D. Carey, W. K. Hsu, , and S. R. P. Silva. Interpretation of enhancement factor in nonplanar field emitters. *Appl. Phys. Lett.*, 87, 2005.

[176] R. G. Forbes. Extraction of emission parameters for large-area field emitters, using a technically complete fowler–nordheim-type equation. *Nanotechnology*, 23(9):095706, 2012.

[177] Center for Experimental Nuclear Physics and Astrophysics. 2014 Annual Report. *University of Washington*, 2014.

[178] J. Lapp. Master's thesis, KIT, 2015. in preparation.

[179] S. Görhardt, F. Harms, and M. Kraus. Baffle on high voltage. Electronic Logbook Entry, `https://neutrino.ikp.kit.edu:8080/SDS-Measurements/238`.

[180] F. Schwamm. *Untergrunduntersuchungen für das KATRIN-Experiment*. PhD thesis, KIT, 2004.

[181] M. Kleesiek. *A Data-Analysis and Sensitivity-Optimization Framework for the KATRIN Experiment*. PhD thesis, KIT, 2014.

[182] R. Gumbsheimer. private communication, 2013.

[183] F. Glück. Electromagnetic design of the magnetic material compensation system (MMCS). KATRIN Collaboration meeting, March 2014, `http://fuzzy.fzk.de/bscw/bscw.cgi/d876853/95-TRP-5625-A1-FGlueck.pptx`.

Acknowledgments

An dieser Stelle möchte ich all denjenigen Danken, die zum guten Gelingen dieser Arbeit zugetragen haben. Mein Dank gebührt hierbei besonders folgenden Personen:

- Prof. Dr. G. Drexlin für die Möglichkeit meine Doktorarbeit bei KATRIN durchzuführen zu können und ganz besonders für die Unterstützung und die gute Betreuung während der gesamten Zeit,
- Prof. Dr. H. Blümer der sich freundlicherweise als Korreferent für diese Arbeit zur Verfügung gestellt hat,
- Dr. F. Glück für das Bereitstellen und Erklären seiner zahlreichen Programme, auf denen diese Arbeit basiert, sowie auch für die zahlreichen physikalischen Diskussionen, die beispielhafte Betreuung und das Korrekturlesen meiner Arbeit,
- Dr. K. Schlösser für die Unterstützung und Geduld bei den Messungen am Monitorspektrometer,
- Prof. Dr. Sanshiro Enomoto für die Entwicklung der Analysesoftware BEANS und die Beantwortung all meiner Fragen über eben diese,
- Marco Kleesiek für seine Hilfe bei der Sensitivitätsberechnung mit KaFit,
- Dr. Stefan Görhardt und Johannes Schwarz für die Motivation auf den letzten Metern,
- allen jungen Wissenschaftlern des KATRIN Experiments für die schöne Zeit, sowohl während als auch außerhalb der Arbeitszeit,
- allen Kollegen an den Instituten für Kernphysik und für Technische Physik am Karlsruher Institut für Technologie für die angenehme Arbeitsatmosphäre und die stets vorhandene Hilfsbereitschaft, sowie jedem, der nicht namentlich erwähnt ist.

Außerdem möchte ich Kathrin Eckerlin, einem besonderen Menschen, der immer für mich da war, danken, sowie meinen Freunden und meiner Familie.